SUNSHINE DURATION AS A PROXY OF THE ATMOSPHERIC AEROSOL CONTENT

Alejandro Sanchez Romero

Per citar o enllaçar aquest document:
Para citar o enlazar este documento:
Use this url to cite or link to this publication:

http://hdl.handle.net/10803/394045

ADVERTIMENT. L'accés als continguts d'aquesta tesi doctoral i la seva utilització ha de respectar els drets de la persona autora. Pot ser utilitzada per a consulta o estudi personal, així com en activitats o materials d'investigació i docència en els termes establerts a l'art. 32 del Text Refós de la Llei de Propietat Intel·lectual (RDL 1/1996). Per altres utilitzacions es requereix l'autorització prèvia i expressa de la persona autora. En qualsevol cas, en la utilització dels seus continguts caldrà indicar de forma clara el nom i cognoms de la persona autora i el títol de la tesi doctoral. No s'autoritza la seva reproducció o altres formes d'explotació efectuades amb finalitats de lucre ni la seva comunicació pública des d'un lloc aliè al servei TDX. Tampoc s'autoritza la presentació del seu contingut en una finestra o marc aliè a TDX (framing). Aquesta reserva de drets afecta tant als continguts de la tesi com als seus resums i índexs.

ADVERTENCIA. El acceso a los contenidos de esta tesis doctoral y su utilización debe respetar los derechos de la persona autora. Puede ser utilizada para consulta o estudio personal, así como en actividades o materiales de investigación y docencia en los términos establecidos en el art. 32 del Texto Refundido de la Ley de Propiedad Intelectual (RDL 1/1996). Para otros usos se requiere la autorización previa y expresa de la persona autora. En cualquier caso, en la utilización de sus contenidos se deberá indicar de forma clara el nombre y apellidos de la persona autora y el título de la tesis doctoral. No se autoriza su reproducción u otras formas de explotación efectuadas con fines lucrativos ni su comunicación pública desde un sitio ajeno al servicio TDR. Tampoco se autoriza la presentación de su contenido en una ventana o marco ajeno a TDR (framing). Esta reserva de derechos afecta tanto al contenido de la tesis como a sus resúmenes e índices.

WARNING. Access to the contents of this doctoral thesis and its use must respect the rights of the author. It can be used for reference or private study, as well as research and learning activities or materials in the terms established by the 32nd article of the Spanish Consolidated Copyright Act (RDL 1/1996). Express and previous authorization of the author is required for any other uses. In any case, when using its content, full name of the author and title of the thesis must be clearly indicated. Reproduction or other forms of for profit use or public communication from outside TDX service is not allowed. Presentation of its content in a window or frame external to TDX (framing) is not authorized either. These rights affect both the content of the thesis and its abstracts and indexes.

Universitat de Girona

DOCTORAL THESIS

SUNSHINE DURATION AS A PROXY OF THE ATMOSPHERIC AEROSOL CONTENT

Alejandro Sanchez Romero

2016

DOCTORAL THESIS

SUNSHINE DURATION AS A PROXY OF THE ATMOSPHERIC AEROSOL CONTENT

Alejandro Sanchez Romero

2016

Doctoral Programme in Experimental Sciences and Sustainability

Supervisors:

Josep Calbó Angrill

José Abel González Gutiérrez

Presented in partial fulfilment of the requirements for a doctoral degree from the University of Girona

Dr. Josep Calbó Angrill and Dr. José Abel González Gutiérrez, of Department of Physics Universitat de Girona,

WE DECLARE:

That the thesis entitled "Sunshine duration as a proxy of the atmospheric aerosol content", presented by Alejandro Sanchez Romero to obtain a doctoral degree, has been completed under our supervision and meets the requirements to opt for an International Doctorate.

For all intents and purposes, we hereby sign this document.

Dr. Josep Calbó Angrill Dr. José Abel González Gutiérrez

Girona, May 2nd, 2016.

List of publications

This Ph.D. thesis includes one review paper and three research papers that have been published in peer-reviewed journals. The complete references of the papers comprised in this thesis and the corresponding impact factor of the journals, according to the 2014 Journal Citation Reports (JCR), are:

1. Sanchez-Romero, A., Sanchez-Lorenzo, A., Calbó, J., González, J.A., and Azorin-Molina, C. (2014), The signal of aerosol-induced changes in sunshine duration records: A review of the evidence, *Journal of Geophysical Research Atmosphere*, 119, 4657–4673, doi:10.1002/2013JD021393.

   (Impact factor: 3.426; position 19/175; Category: Geosciences, Multidisciplinary; 1st quartile).
2. Sanchez-Romero, A., González, J. A., Calbó, J., and Sanchez-Lorenzo, A. (2015), Using digital image processing to characterize the Campbell–Stokes sunshine recorder and to derive high-temporal resolution direct solar irradiance, *Atmospheric Measurement Techniques*, 8, 183-194, doi:10.5194/amt-8-183-2015.

   (Impact factor: 2.929; position 20/77; Category: Meteorology & Atmospheric Sciences; 2nd quartile).
3. Sanchez-Romero, A., González, J. A., Calbó, J., and Sanchez-Lorenzo, A., and Michalsky, J. (2016), Aerosol optical depth in a western Mediterranean site: an assessment of different methods, *Atmospheric Research*, 174-175, 70-84, doi:10.1016/j.atmosres.2016.02.002.

(Impact factor: 2.844; position 22/77; Category: Meteorology & Atmospheric Sciences; 2nd quartile)

4. Sanchez-Romero, A., Sanchez-Lorenzo, A., González, J.A., and Calbó, J. (2016), Reconstruction of long-term aerosol optical depth series with sunshine duration records, *Geophysical Research Letters*, 43, 1296–1305, doi:10.1002/2015GL067543.

   (Impact factor: 4.196; position 9/175; Category: Geosciences Multidisciplinary; 1st quartile)

Two other articles related with the subject of the thesis have also been co-authored by the author of this thesis, but are not included in it:

1. Sanchez-Lorenzo, A., Calbó, J., Wild, M., Azorin-Molina, C., and Sanchez-Romero, A. (2013), New insights into the history of the Campbell-Stokes sunshine recorder. *Weather*, 68: 327-331, doi: 10.1002/wera.2130.
2. Sanchez-Lorenzo, A., Enriquez-Alonso, A., Wild, M., Trentmann, J., Vicente-Serrano, S.M., Sanchez-Romero, A., Posselt, R., and Hakuba, M. (2016), Trends in downward surface solar radiation from satellites and ground observations over Europe during 1983-2010, *Remote Sensing of Environment* (in progress).

There is nothing so stable as change

Bob Dylan

Acknowledgments

Com en una marató, aquest ha estat un llarg camí per recórrer. Aquesta tesi posa punt i final a una de les etapes més maques de la meva vida. Tancar etapes sempre genera certa tristesa, però sé que després vindran nous reptes i això sempre es motivador. M'he pres la llibertat d'escriure aquesta secció en la meva llengua, per tal de poder expressar la més sincera gratitud a un nombre de persones (tot i que no dubto que algú em deixaré), sense les quals aquesta tesi mai hagués estat completada.

En primer lloc, m'agradaria agrair als meus directors de tesi, en Josep Calbó i en Josep-Abel González (o com són més coneguts en el departament, els *Joseps*), per la seva dedicació i suport durant aquests anys. Així mateix, per haver-me transmès el rigor, esperit científic i honestedat intel·lectual necessaris per moure'm en un món, el de la investigació científica, cada vegada més competitiu.

Arturo, la burocràcia, les normatives i els papers no entenen ni reflecteixen les relacions humanes, però està clar que la confiança, el suport i el coneixement que m'has aportat des del primer dia reflectirien, i de sobres, el teu paper com a codirector d'aquesta tesi. A més, ningú m'ha aportat tantes hores de lectura com els teus correus. Agrair també en César que ha aconseguit encomanar-me la seva passió per un instrument tan simple i rudimentari com és l'heliògraf Campbell-Stokes.

A continuació, vull donar les gràcies a totes les companyes i companys del grup i de despatx en general: Aaron, Victor, Montse, Ios, Conxi, Alex, Bruna, Dani, etc. Sou genials! Gràcies per tot el que hem compartit, pels milers de cafès, per totes les hores de pensar, llegir, d'escriure….No voldria oblidar-me del Servei Personal Administratiu del Departament de Física, sobretot de l'Anna Espígol, en Xevi Baca, i en Xicu Gómez, que han fet que els problemes administratius i tècnics (que no han estat pocs) hagin estat pura anècdota.

Agrair també a Joseph Michalsky i John Augustine, que van fer de la meva estada a Estats Units una gran experiència. Sobre el paper, investigadors de renom mundial amb molta experiència en el món de la recerca. En la realitat, això i més, persones properes, directes, honestes i que mai tenen un no per resposta. Moltes gràcies per la vostra ajuda. No m’oblido tampoc dels meus companys en la casa de la sra. Lorna Pollard (la nostra petita representació de la ONU), poques coses hi ha més gratificants que les xerrades multiculturals que vam compartir.

He de recordar a tots aquells amics amb qui he compartit trajecte vital durant aquests anys, molt especialment, Robert, Tates, Carlos, Ali, Puxi, Tresa, David, Sònia, Javi, Estefania, Adri, Nàndez, Sarita, així com molts altres, espero que es donin per al·ludits. A tots aquells que alguna vegada em van dedicar 5 minuts del seu temps perquè els expliqués què dimonis estava investigant, sincerament, gràcies!

Finalment i no per això menys important, no hi ha paraules de agraïment als meus pares, per la vostra estima incondicional, per la immensa llibertat que m’heu donat i per respectar sempre les meves decisions. També vull donar les gràcies a la meva germana, la Silvia, qui sempre m’ha animat a superar-me a mi mateix, tot i el meu passotisme i la distància que ens separa. Sara, per acabar vull donar-te les gracies a tu, espero poder dedicar-te tot el temps que et mereixes i que aquesta tesi t’ha robat.

List of abbreviations and symbols

α	Ångström aerosol Exponent
AE	Ångström aerosol Exponent
AEMET	Agencia Estatal de Meteorología
AERONET	Aerosol Robotic Network
AOD	Aerosol Optical Depth
AOD_{CSSR}	Estimation of AOD using burn width from CSSR cards
API	Air Pollution Index
AR4	IPCC Fourth Assessment Report
AR5	IPCC Fifth Assessment Report
β	AOD at 1 μm
BAOD	Broadband Aerosol Optical Depth
CALIOP	Cloud-Aerosol Lidar with Orthogonal Polarization
CSSR	Campbell-Stokes Sunshine Recorder
δ_{CD}	Optical thickness of the clean dry atmosphere
DSI	Direct Solar Irradiance
DSI_{CS}	Threshold irradiance value when burn starts on CSSR cards
DSI_{SD}	Estimation of DSI using hourly SD, i.e., counting the minutes with burn within each hour
DSI_{W}	Estimation of DSI using burn width from CSSR cards
EARLINET	European Aerosol Research Lidar Network
ERFaci	Effective radiative forcing from aerosol-cloud interactions
ERFari	Effective radiative forcing from aerosol-radiation interactions

GHG	Greenhouse gases
GSI	Global Solar Irradiance
h	Burn width for a CSSR card
h’	Normalized burn width for a CSSR card
I_0	Extraterrestrial solar irradiance
IPCC	Intergovernmental Panel on Climate Change
λ	Wavelength
LCC	Low Cloud Cover
LST	Local Solar Time
m_A	Relative optical air mass
MB	Mean bias
MBE	Mean bias error
MFRSR	Multifilter Rotating Shadowband Radiometer
MISR	Multi-angle Imaging SpectroRadiometer
MODIS	Moderate Resolution Imaging Spectroradiometer
OMI	Ozone Monitoring Instrument
R	Coefficient of correlation
R^2	Coefficient of determination
RGB	Red Green Blue
RFaci	Radiative forcing from aerosol-cloud interactions
RFari	Radiative forcing from aerosol-radiation interactions
RMSE	Root mean square error
RMSD	Root mean square deviation
RRMSE	Relative root mean square error

SBDART	Santa Barbara Discrete ordinates radiative transfer Atmospheric Radiative Transfer model
SD	Sunshine Duration
SDaut	SD obtained by applying the semi-automatic method
SDman	SD obtained by reading the cards manually
SDpyr	SD obtained counting the minutes when DSI is greater than 120 W m^{-2}
SMARTS2	Simple Model of the Atmospheric Radiative Transfer of Sunshine
SNHT	Standard Normal Homogeneity Test
SURFRAD	Surface Radiation Budget network
τ	total atmospheric optical depth
τ_A	Aerosol optical depth
τ_R	Rayleigh optical depth
τ_{O3}	Ozone optical depth
τ_{NO2}	NO_2 optical depth
τ_W	Water optical depth
TCC	Total Cloud Cover
T_L	Linke’s turbidity factor
TOMS	Total Ozone Mapping Spectroradiometer
TST	True Solar Time
V	Response of the radiometer at the surface
V_0	Response of the radiometer at the top of the atmosphere
WMO	World Meteorological Organization

List of figures

Figure 1.1. Global mean energy budget under present-day climate conditions. Numbers state magnitudes of the individual energy fluxes in W m^{-2}, adjusted within their uncertainty ranges to close the energy budgets. Numbers in parenthesis attached to the energy fluxes cover the range of values in line with observational constraints [figure adapted from *Wild et al.*, 2013]. With permission of Springer International Publishing. 4

Figure 1.2. Schematic of the new terminology used in IPCC Fifth Assessment Report (AR5) for aerosol-radiation and aerosol-cloud interactions and how they relate to the terminology used in IPCC Fourth Assessment Report (AR4). The blue arrows depict solar radiation, the grey arrows terrestrial radiation and the brown arrow symbolizes the importance of couplings between the surface and the cloud layer for rapid adjustments [figure from *Boucher et al.*, 2013]. 8

Figure 1.3. Changes in surface solar radiation observed in regions with good station coverage during three periods. Numbers denote typical literature estimates for the specified region and period in W m^{-2} per decade [figure from *Wild*, 2012]. ©American Meteorological Society. Used with permission. 10

Figure 1.4. Mean annual trends of SD series of Western Europe stations between 1938 and 2004 (thin line), calculated by least squares linear fitting, and plotted together with a low-pass filter (thick line). The series are expressed as relative deviations from the 1961-90 mean [figure from *Sanchez-Lorenzo et al.*, 2008]. ©American Meteorological Society. Used with permission. 18

Figure 1.5. Comparison between the solar data extracted from a CSSR card and that from the collocated pyheliometer [figure from *Horseman et al.*, 2013]. 23

Figure 1.6. Long-term measurements and trends in relative SD and clear days (>92% sunny) for the Blue Hill Meteorological Observatory in Milton, Massachusetts (United States). 1-year (red) and 10-year (black) moving averages of moving weekly relative SD measurements, overlaid on raw daily relative SD observations (blue points). Right axis displays the number of clear days (purple) in a moving 365-day interval [figure from *Magee et al.*, 2014]. ©American Meteorological Society. Used with permission...24

Figure 4.1. The large quantity of aerosol, emitted during the night of 24 December 1977 in Mexico City, produced a reduction of direct solar irradiance in the morning of the next day, and in consequence, the paper strip of the CSSR started to burn later than the other days. The solar radiation unit refers to Langley·hour^{-1}, which equals to 11.63 W m^{-2}. Adapted from *Galindo and Chavez* [1978]. © Geofísica Internacional. Used with permission. 40

Figure 4.2. (a) Parts of a CSSR and (b) an example of the three types of cards used during summer, winter, and equinoctial seasons, respectively. 43

Figure 4.3. Turbidity Linke factor, T_A, determined with a pyrheliometer as a function of that computed with the burned trace method by Helmes and Jaenicke (1984), T_{CS}, which is calculated using the individual threshold values DSI_{CS} for each type of the card determined by comparison with pyrheliometer. Similar results are obtained using a fixed value of DSI_{CS} = 20 mWcm^{-2} for all cards. From *Helmes and Jaenicke* [1984]. © American Meteorological Society. Used with permission. 49

Figure 4.4. Counts of mornings and evenings within the analyzed solstice periods when burn(s) below 2° solar elevation was/were observed in each year. The totals are grouped into summer and winter. Note that after the early 1990s, there was an increase in the number of mornings and evenings per year when bright sunshine was recorded at sub-2º elevations. Note also that most of the increase was contributed by the winter period. From *Horseman et al.* [2008]. © Elsevier. Used with permission. 52

Figure 4.5. Thin lines represent the annual evolution of both sunshine duration (solid lines, labeled as SD) and total cloud cover (dashed lines, labeled as TCC; note the reversed axis) series for the whole Iberian Peninsula during the period 1961-2004. Thick lines are the smoothed (11 year averaging) evolution. Note that there is a clear disagreement between both series, especially from the 1960s to the mid-1980s. Adapted from *Sanchez-Lorenzo et al.* [2009]. 56

Figure 4.6. Average daily sunshine hours under conditions with low-medium aerosol loading (air pollution index ≤ 80) and high aerosol loading (API > 80) across China for the 2001-2005 period. Note that the plots are only for clear-sky conditions (i.e. days with 0 mm precipitation and total cloud cover ≤ 10%) and that SD is shorter at times of higher API (high aerosol loading). From *Wang et al.* [2012b]. 57

Figure 5.1. Solar path for the 21st of each month (red lines) and horizon height for each azimuth angle (blue line). 75

Figure 5.2. (Top) Details of the two different CSSRs mounted in Girona (NE Spain), and (bottom) an example of the 3 types of cards used during summer, winter, and equinoctial seasons, respectively (the longer the daylight hours, the longer the card): (1) summer card of Thies Clima; (2) summer card of Mod.98; (3) equinoctial card of Thies Clima (note that although the card edges are not symmetric, the markings are); (4) equinoctial card of Mod.98; (5) winter card of Thies Clima; and (6) winter card of Mod.98. 76

Figure 5.3. Steps of the semiautomatic method for retrieving information from the CSSR burned cards and for a certain day: (a) captured image, (b) treated image, (c) positioned image, and (d) measured burn width over time. 79

Figure 5.4. Scatter plots of the (a) daily SD obtained for CSSR1 from both SDaut (blue crosses) and SDman (red points) methods against SDpyr, considering the threshold of 120 W m^{-2} in DSI; and (b) the daily SD obtained by the two CSSR using the automatic method. In each graphic we also represent the 1:1 line (black line). 84

Figure 5.5. (a, b) Daily evolution of burn width (blue line for CSSR1 and red line for CSSR2) and DSI (green line) for 2 different days. (c) Scatter plot of the burn width in CSSR2 (H2) versus that of CSSR1 (H1) at hourly resolution. We also represent the 1:1 line (black line) and the linear regression fit (green line). 88

Figure 5.6. (a) Scatter plots at hourly resolution of the DSI against normalized width for CSSR1. The fitted logistic function and the correlation coefficient are also shown (black line). (b) The same but for CSSR2. 90

Figure 5.7. (a) Scatter plots at hourly resolution of the DSI against SD for CSSR1. The exponential regression (black line) and the correlation coefficient are also displayed. (b) The same but for CSSR2. 90

Figure 5.8. Box plots of the differences between estimated and true DSI for (a) estimation based on burn width and (b) estimation based on SD. It is applied for CSSR1. 93

Figure 6.1. Map of the western Mediterranean showing the region of study, the main site (Girona, where MFRSR is measuring) and the complementary site (Barcelona, where the AERONET Cimel instrument is measuring). Solid and dotted yellow lines represent the MISR and MODIS cells, respectively. 101

Figure 6.2. Summary of the steps to obtain AOD and AE from MFRSR. The references for each step are also shown in the figure. 105

Figure 6.3. Time patterns of V_0 in the 500-nm channel of the MFRSR from June 2012 to June 2014. The black dots are the retrieved Langley plot intercepts. The red dots are robust estimates of V_0 based on a moving window of 20 Langley plot intercepts. The red line is a smooth curve fit to these data, based on Gaussian filter of 30-day width, from which daily V_0 values may be obtained. 108

Figure 6.4. An example of the cloud screening results using the technique described in the paper. Red points were deemed true AOD, and black points were considered cloud contaminated. Sample images from the Whole Sky Camera show clear sky and cirrus clouds, respectively. 111

Figure 6.5. (a) Daily averages of AOD at 500 nm anc (c) of AE (black points). Smoothing in windows of ten years (red line) and three months (green line) are also shown. (b) Monthly boxplots of AOD in the 500 nm channel and (d) of AE red; red points represent the monthly mean values, whiskers correspond to 5 and 95 percentiles. 115

Figure 6.6. (a) Density representation of the scatterplot of simulated solar direct normal irradiance (DSI) using AOD and AE from MFRSR with respect to measurements (1-min averages); the 1:1 line (black line) and the linear regression fit (red line) are also represented. (b) Histogram of the differences between simulated and observed direct solar irradiance, using bins of 1.3 W m^{-2} (blue line for simulated data using AE from MFRSR and green line for simulated values using the rural aerosol model); dashed lines represent the mean bias. 118

Figure 6.7. (a,c) Behavior of AOD at 500 nm and AE, respectively. Values from MFRSR are in red, those from Cimel are in blue. Solid lines correspond to smoothing in windows of ten days, dashed lines represent fits in windows of three months. (b,d) Scatterplots of the daily values of AOD at 500 nm and AE, respectively, obtained by Cimel versus obtained by MFRSR. The 1:1 line (black lines) and the linear regression fits (red lines) are also shown. 122

Figure 6.8. (a) Behavior of AOD at 500 nm derived from MFRSR (black line), MISR (red line), and MODIS Terra/Aqua (green/blue lines), in windows of ten days. (b) Scatterplots of daily AOD derived from MISR and MODIS Terra/Aqua against those from MFRSR; the 1:1 line (black lines) and the linear fits (red lines) for each case are also represented. 126

Figure 6.9. (a) Image of MODIS Terra (corrected reflectance) for 23 July 2012, 10.30 LST, showing the plume caused by the forest fire. (b) Geopotential height at 850 hPa for 25 July 2012 at 12 UTC according NOAA-CIRES Climate Diagnostics Center. 128

Figure 6.10 (next page). (a,b) Evolution of AOD (at 500 nm) and AE, from MFRSR (red), during the episode of the end of July 2012; bid dots correspond to 1-minute AOD and AE values; small dots correspond to cloud contaminated to 1-minute AOD and AE values; small dots correspond to cloud contaminated values; the green line corresponds to AOD (at 550 nm) and AE from MODIS Terra and blue line to MODIS Aqua. Several images of the Whole Sky Camera for these days are included to illustrate different sky conditions. (c) Direct solar irradiance evolution during the whole episode, directly measured (red line), calculated using a rural aerosol model (green line) and calculated using AE obtained by MFRSR in the model (blue line). (d) Relative differences between model and observed direct irradiance. Note that for large solar zenith angles, very high relative differences (beyond the represented scale) are reached when the rural aerosol is used (green line). 128

Figure 7.1. Scatterplot of AOD at 500 nm against burn width, in two different ranges of air mass. The colors of the points are related to the range of water vapor. 137

Figure 7.2. Four examples of daily evolution of AOD obtained from MFRSR (black points) or estimated from burn width (red triangles), at 10-min resolution..........141

Figure 7.3 (next page). (a) Scatterplot of AOD_{CSSR} versus $\text{AOD}_{\text{MFRSR}}$ at 10-minutes resolution. We also represent the 1:1 line (dotted line) and the linear regression fit (black line). (b) Boxplot of the differences between estimated and true AOD (centered in the values of the x-axis), where the top and bottom lines of the rectangle are the 3rd and 1st quartiles, and the line in the middle is the median (or the 2nd quartile); red triangles refer to mean values, and numbers on the top of each rectangle refer to the number of points of each box. (c) The same boxplot of (b) but depending on solar elevation. 142

Figure 7.4. (a) Scatterplot of AOD_{CSSR} versus $\text{AOD}_{\text{MFRSR}}$ on 10-minutes resolution (solar elevation < 15º); we also represent the 1:1 line (dotted line) and the linear regression fit (black line). (b) Scatterplot of mean burn width versus $\text{AOD}_{\text{MFRSR}}$ (solar elevation < 15º) for each evening; we also represent the linear regression fit (black line). 145

Figure 8.1. Map of the distribution of the 16 sites studied in our research. Each number is associated with one AEMET and one AERONET station, as defined in Table 8.1. 152

Figure 8.2. Scatterplot of SD fraction versus AOD_{440} for summer (June, July and August) at eight sites. Each point represents one day of measurements. We also show the correlation coefficients and slope values. 156

Figure 8.3. Scatterplot of AOD estimated from SD and AOD measured by Cimel for the eight selected stations and for summer values (average of the available days of June, July and August). Each point represents one summer mean value for one site. The fitted line and the correlation coefficient illustrate the remarkable agreement. 159

Figure 8.4. (a) Evolution (1961-2014 period) of the mean relative anomalies of estimated AOD_{440} for summer (black line) for eight sites distributed throughout Spain (including two in the Canary Isles); smoothing by a moving window of 11 years (red line) is also shown; blue area refers to range between the maximum and minimum values of the different series for each year. (b) Evolution (1920-2007 period) of the relative anomalies of estimated AOD_{440} (black line) for Madrid in summer; smoothing by a moving window of 11 years (red line) is also shown. 161

Figure 8.5 (previous page). (a) Evolution of the mean relative anomalies of estimated AOD_{440} for summer for the two Canary Isles sites (1961-2014 period, black line). (b) Evolution of the relative anomalies of estimated AOD_{440} for summer for the six sites distributed throughout the Iberian Peninsula and Mallorca (1961-2014 period, black line). In both panels, smoothing by a moving window of eleven years (red line) is also shown; blue are refers to the range between the maximum and minimum values of the different series for each year. 164

Figure 9.1. Two different CSSR cards for two different cases. Black lines separate the days, as we change the CSSR card near midday: the afternoon data is for the previous day of the morning data. 175

List of tables

TABLE 1.1. SUMMARY OF THE CURRENT OPERATIONAL AOD NETWORKS [ADAPTED FROM *MICHALSKY ET AL.*, 2010] 12

TABLE 1.2. THE HISTORY OF CURRENT PLATFORMS AND SENSORS USED TO DERIVE AEROSOL PROPERTIES FROM SPACE [*LEE ET AL.*, 2009] 12

TABLE 4.1. SUMMARY OF WORKS THAT FIND DISCREPANCIES BETWEEN TRENDS OF SD AND TRENDS OF CLOUD COVER AND/OR SURFACE SOLAR RADIATION[A]. THE COLUMNS OF SD, TCC, LCC, GSI (GLOBAL SOLAR IRRADIANCE), DIF (DIFFUSE SOLAR IRRADIANCE), AND DSI (DIRECT SOLAR IRRADIANCE) REFERS TO TRENDS OF THESE VARIABLES. 55

TABLE 5.1. THE FIRST TWO COLUMNS ARE THE MEAN VALUE OF SD BY MANUAL AND SEMIAUTOMATIC METHOD, RESPECTIVELY. THE THIRD COLUMN IS THE VALUE OF SD FROM PYHELIOMETRIC METHOD BY USING A DSI THRESHOLD (IN PARENTHESIS) THAT WOULD APPROACH THE CONSIDERING MEAN SD USING THE SEMIAUTOMATIC METHOD. RECALL THAT THE "TRUE" MEAN SD (BY USING 120 WM^{-2} AS THE DSI THRESHOLD) IS 7.16H. 83

TABLE 5.2. STATISTICAL PARAMETERS OF ESTIMATIONS OF HOURLY DSI WHEN COMPARED WITH DSI MEASUREMENTS BY DIFFERENT METHODS AND INSTRUMENTS (FROM MEAN BURN WIDTH, H1, H2 AND HOURLY SUNSHINE DURATION, SD1, SD2; *STANHILL*, 1998A). MBE IS THE MEAN BIAS ERROR; RMSE IS THE ROOT MEAN SQUARE ERROR; RRMSE IS THE RELATIVE ROOT MEAN SQUARE ERROR; R^2 IS THE COEFFICIENT OF DETERMINATION; A IS THE SLOPE OF THE REGRESSION LINE; AND B IS THE Y INTERCEPT OF THE REGRESSION LINE. 92

TABLE 6.1. STATISTICAL COMPARISON OF DAILY AOD/AE RETRIEVALS FROM CIMEL (IN BARCELONA) AND SATELLITE INSTRUMENT (MISR AND MODIS ONBOARD TERRA/AQUA, FOR THE CELLS CONTAINING GIRONA) RETRIEVALS WITH THAT FROM MFRSR (IN GIRONA). N IS THE NUMBER OF DAYS USED IN EACH COMPARISON; MB IS THE MEAN BIAS OF CIMEL OR SATELLITE DATA WITH RESPECT TO MFRSR; RMSD IS THE ROOT MEAN SQUARE DEVIATION; R, A AND B REFER RESPECTIVELY TO THE CORRELATION COEFFICIENT, SLOPE AND INTERCEPT OF THE REGRESSION LINE. 123

TABLE 7.1. LOOK-UP-TABLE OF AOD VALUES FROM BURN WIDTH AND AIR MASS. 140

TABLE 8.1. SUMMARY OF LOCATIONS OF THE 16 STATIONS IN SPAIN[A] 150

TABLE 8.2. RECONSTRUCTED TIME SERIES OF AVERAGE SUMMER AOD FOR SPAIN FROM 1961 TO 2014, OBTAINED FROM 8 SITES DISTRIBUTED THROUGHOUT SPAIN (INCLUDING TWO IN THE CANARY ISLES). 162

CONTENTS

ABSTRACT .... **xxvii**

RESUM .... **xxxi**

RESUMEN .... **xxxv**

PART I. INTRODUCTION AND METHODOLOGY **1**

Chapter 1. Introduction **3**

1.1. Atmospheric aerosols 6

1.1.1. Effects of aerosols 7

1.1.2. Measurement of aerosol properties 11

1.1.3. Atmospheric turbidity and other proxies 15

1.2. Sunshine duration 17

1.2.1. Campbell-Stokes sunshine recorder 19

1.2.2. Current instruments and methods 21

1.2.3. Sunshine duration as a proxy for cloudiness and solar irradiance 21

1.2.4. Sunshine duration as a proxy for aerosol 23

Chapter 2. Goals **27**

Chapter 3. Instruments and Methodology **31**

3.1. Sunshine duration data 32

3.2. Aerosol content data 32

3.3. Other instruments and data 33

Chapter 4. Review about aerosol traces in sunshine observations **35**

4.1. Introduction 36

4.2. Sunshine duration measurements 41

4.2.1. From the pioneering designs to the current methods 42

4.2.2. Variability of the burning thresholds 45

4.3. Evidence of aerosol/turbidity effects on sunshine duration measurements 47

4.3.1. Assessing turbidity from CSSR cards 47

4.3.2. Aerosol effects on SD variability and trends 53

4.4. Conclusions and future perspectives 63

PART II. RESULTS 67
Chapter 5. Characterization of CSSR and derivation of direct solar irradiance from burn width 69
5.1. Introduction 70
5.2. Instruments and data 75
5.3. Semi-automatic method for reading the burnt traces 77
5.3.1. Image capture 78
5.3.2. Image treatment 80
5.3.3. Image positioning 81
5.3.4. Measurement of burning width 81
5.4. Applications of the measurements of the burn width 82
5.4.1. Assessment of the measurement of sunshine duration 83
5.4.2. Burn width and its relationship with direct solar irradiance 87
5.5. Conclusions and future research 93
Chapter 6. Aerosol optical depth in a western Mediterranean site: an assessment of different methods 97
6.1. Introduction 98
6.2. Data and method 103
6.2.1. Calibration of the MFRSR 104
6.2.2. Computing AOD and AE 108
6.2.3. Cloud screening 110
6.2.4. Uncertainty of the derived aerosol properties 112
6.3. Results and discussion 113
6.3.1. Evolution of AOD and AE at Girona 113
6.3.2. Radiative closure experiment 116
6.3.3. Assessment of other aerosol products 119
6.3.4. High aerosol event 127
6.4. Conclusions and future research 131
Chapter 7. Effect of aerosols on burn width 135
7.1. Data and method 136
7.2. Results and discussion 139
7.3. Conclusions 145

Chapter 8. Reconstruction of long-term aerosol optical depth series with sunshine duration records 147

8.1. Introduction 148
8.1. Data and methods 150
8.1. Results and discussion 155
  8.1.1. Effect of AOD on SD 155
  8.1.2. Reconstruction of AOD series 158
8.2. Conclusion 165

PART III. DISCUSSION AND CONCLUSIONS 167

Chapter 9. Discussion 169

9.1. Aerosol characterization at high temporal resolution 169
9.2. Aerosol characterization in long temporal scales 176

Chapter 10. General conclusions 181

REFERENCES 185

ABSTRACT

Atmospheric aerosols play a significant and central, albeit complex, role in the Earth's radiation budget. Knowledge of long-term changes in particle load and in induced atmospheric turbidity is therefore fundamental for a better understanding of climate change. Owing to the heterogeneity of the sources, the short lifetime and the dependence of sinks on the meteorology, aerosol distribution shows large variations, not only on a daily and seasonal basis, but also at inter-annual scales. Furthermore, little available information exists on changes in aerosol concentration in the atmosphere, especially prior to the 1980s. On the contrary, we do avail of long time series of sunshine duration (SD) measurements. In the past, the Campbell-Stokes sunshine recorder (CSSR) has been the most common instrument for measuring SD, which it accomplishes by means of the burn length of a card; thus, it has given rise to long historical series of SD records. The principal goal of the present thesis is to investigate the suitability of sunshine observations for detecting changes in atmospheric aerosol load for both high time resolution and long time scales.

There is abundant evidence that one cause of the decadal changes observed in sunshine duration records involves variations in atmospheric aerosol loading. Some of the studies reviewed propose methods for estimating aerosol-related magnitudes, such as turbidity, based upon sunshine deficit at approximately sunrise and sunset, when the impact of aerosols on the solar beam is more easily observed. Despite the simple idea that the stronger the sunshine, the wider the burn, very few previous studies have considered the burn width of CSSR cards, rather than burn length.

In the present thesis, we first checked the use of the burn width registered by CSSR in order to create time series of atmospheric aerosol loading metrics at high temporal resolution (e.g., sub-daily). For this purpose, a set of measurements was performed in Girona, a city in the northeast of the Iberian Peninsula. We characterized CSSRs and their cards, developed a method of analysis based on image processing of digitally scanned images of burnt cards in order to obtain burn width at a 1-min resolution, and used a technique that enables aerosol optical depth (AOD) to be estimated at the same resolution. Before comparing with AOD, we found that there is a strong relationship between burn width and direct solar irradiance (DSI); the method therefore provides a practical way to exploit sets of CSSR cards to create series of DSI. As DSI is affected by atmospheric aerosol content, it is confirmed that burn width from CSSR records may also become a proxy measurement for turbidity and atmospheric aerosol loading. Thus, we used concurrent high-resolution (10 minutes) cloud-screened data on AOD with burn width. The non-linear relationship we found depends closely upon air mass. In addition, this relationship is stronger for low values of solar elevation (high values of air mass).

With the aim of performing a long-term reconstruction of AOD, we also study the relationship between AOD and daily SD at long temporal scales (e.g., seasonal). We employ a linear relationship between AOD and SD for cloudless days and for some stations on the Iberian Peninsula and on the Balearic and Canary Isles. The variables SD and total cloud cover (TCC) were taken from stations of the Spanish Meteorological Agency, whereas AOD data were provided by close stations of the AERONET network. We established that an increase in AOD reduces the measurement of SD. We then studied the long-term change in AOD for those stations showing homogeneous SD series. The reconstructed AOD series show a clear increase from the mid-1960s to the 1980s, with a maximum during the 1982-1984 period, followed by a subsequent recovery until the present. These reconstructions are compatible with the dimming and brightening phenomenon. For Madrid, the reconstructed AOD series dates back to 1920; this series shows a decrease in AOD from mid-1940s to 1960, which is compatible with the early brightening phenomenon observed in other parts of Europe.

In conclusion, our thesis has demonstrated that sunshine observations performed by means of CSSR instruments can be used to estimate AOD and its variability and trends both quantitatively and at high temporal resolution and for long timescales. As CSSR has been one of the instruments most commonly used for measuring SD with series longer than 100 years (which are available at some historical meteorological stations), the present thesis provides the possibility to determine variations in atmospheric aerosol loading and therefore to assess the possible influence of human activities on the Earth radiation budget, with the resulting climatological implications.

RESUM

Els aerosols atmosfèrics juguen un paper important però complex en el balanç de radiació de la Terra. El coneixement dels canvis a llarg termini en la càrrega d'aerosols i en la terbolesa atmosfèric induïda és, per tant, fonamental per una millor comprensió del canvi climàtic. Degut a la heterogeneïtat de les seves fonts, el seu curt temps de vida, i la dependència dels embornals en la meteorologia, la distribució d'aerosols mostra grans variacions, no només a escales diàries i estacionals, sinó que també a escales interanuals. No obstant, hi ha poca informació disponible sobre els canvis en la concentració d'aerosols en l'atmosfera, especialment per abans del 1980. Per altra banda, existeixen llargues series temporals d'insolació (SD). En el passat, l'heliògraf Campbell-Stokes (CSSR) ha estat l'instrument més comú per la mesura de SD, a través de la longitud de la cremada en la banda, donant lloc a llargues series històriques de SD. L'objectiu principal de la present tesi és investigar la idoneïtat de la utilització de mesures de SD per detectar canvis en la càrrega d'aerosols atmosfèrics, tant en alta resolució temporal com en llargues escales temporals.

Existeixen nombroses evidències de que una de les causes dels canvis decennals observats en els registres de SD implica variacions en la càrrega d'aerosols atmosfèrics. Alguns dels estudis revisats proposen mètodes per estimar les magnituds relacionades amb aerosols, tals com la terbolesa, a partir del dèficit de SD durant l'alba i el capvespre, que és quan s'observa més fàcilment l'impacte dels aerosols en els raigs solars. Tot i la simplicitat de la hipòtesis, "quant més intensa sigui la llum solar, major serà la cremada", molt pocs estudis consideren l'amplitud de la cremada en bandes de CSSR en comptes de la longitud de la cremada.

En la present tesi, primer hem estudiat l'ús de l'ample de la cremada amb l'objectiu de crear series temporals de càrrega d'aerosol atmosfèric en alta resolució temporal (per exemple, sub-diària). Amb aquesta finalitat, un conjunt de mesures es van dur a terme a Girona, ciutat al nord-est de la Península Ibèrica. Vam caracteritzar el CSSR i les seves bandes, desenvolupant un mètode d'anàlisis basat en el processament digital d'imatges escanejades de les bandes cremades amb l'objectiu d'obtenir l'ample de la cremada en resolució de 1 minut, i vam utilitzar una tècnica que permet estimar l'espessor òptic d'aerosols (AOD) en la mateixa resolució. Abans de fer la comparació amb AOD, es va trobar que existeix una alta correlació entre l'ample de la cremada i la radiació solar directa (DSI); per tant, el mètode ofereix una forma pràctica d'explotar un conjunt de bandes de CSSR per crear sèries de DSI. Degut a que la DSI es veu afectada pel contingut d'aerosol atmosfèric, es confirma que els registres de cremada en bandes de CSSR poden convertir-se en una mesura representativa de la terbolesa i la càrrega d'aerosols atmosfèrics. Llavors, hem concorregut dades de moments serens de AOD amb amples de cremada en alta resolució (10 minuts). La relació no lineal que hem trobat depèn, en gran mesura, de la massa d'aire. A més, aquesta correlació és més alta per valors baixos d'elevació solar (és a dir, valors alts de massa d'aire).

Amb l'objectiu de realitzar una reconstrucció a llarg termini de AOD, també hem estudiat la relació entre valors diaris de AOD i SD a llargues escales temporals (per exemple, estacional). Hem utilitzat una relació lineal entre la AOD i SD per dies serens i per algunes estacions en la Península Ibèrica, les Illes Balears i Canàries. SD i la nuvolositat total (TCC) es prenen de les estacions de la Agència Estatal de Meteorologia, mentre que les dades de AOD es prenen de les estacions més properes de la xarxa AERONET. Hem obtingut que un augment de AOD redueix la mesura de SD. Per tant, per aquelles estaciones que la seva sèrie de SD va resultar ser homogènia, hem estudiat el canvi a llarg termini de AOD. Les series de AOD reconstruïdes mostren un clar augment des de mitjans de la dècada de 1960 fins a la dècada de 1980, amb un màxim durant el 1982-1984, seguit d'una posterior recuperació fins el present. Aquestes reconstruccions són compatibles amb el fenomen de *Dimming & Brightening*. Per a Madrid, la sèrie reconstruïda de AOD es remunta fins el 1920; aquesta sèrie mostra una disminució de AOD des de mitjans dels anys 1940 a 1960, que és compatible amb el fenomen de *Early Brightening* observat en altres parts d'Europa.

En conclusió, hem demostrat en aquesta tesi que les observacions realitzades amb CSSR poden fer-se servir per estimar quantitativament la AOD i la seva variabilitat i tendència, tant en alta resolució temporal com en llarga escala temporal. Com CSSR ha estat un dels instruments més utilitzats per mesurar SD, amb sèries de més de 100 anys (que estan disponibles en algunes estaciones meteorològiques històriques), aquesta tesi ofereix la possibilitat de determinar les variacions en la càrrega d'aerosols atmosfèrics i, per tant, d'avaluar la possible influència de les activitats humanes sobre el balanç de radiació de la Terra, amb les resultants conseqüències climatològiques.

RESUMEN

Los aerosoles atmosféricos juegan un papel importante pero complejo en el balance de radiación de la Tierra. El conocimiento de los cambios a largo plazo en la carga de aerosoles y en la turbidez atmosférica inducida es, por lo tanto, fundamental para una mejor comprensión del cambio climático. Debido a la heterogeneidad de sus fuentes, su corto tiempo de vida, y la dependencia de los sumideros en la meteorología, la distribución de aerosoles muestra grandes variaciones, no sólo a escalas diarias y estaciones, sino que también en escalas interanuales. Sin embargo, hay poca información disponible sobre los cambios en la concentración de aerosoles en la atmósfera, especialmente para antes del 1980. Por otra parte, existen largas series temporales de insolación (SD). En el pasado, el heliógrafo Campbell-Stokes (CSSR) ha sido el instrumento más común para la medición de SD, a través de la longitud de la quemada en la banda, dando lugar a largas series históricas de SD. El objetivo principal de la presente tesis es investigar la idoneidad de la utilización de medidas de SD para detectar los cambios en la carga de aerosoles atmosféricos, tanto en alta resolución temporal como en largas escalas temporales.

Hay cuantiosas evidencias de que una de las causas de los cambios decenales observados en los registros de SD implica variaciones en la carga de aerosoles atmosféricos. Algunos de los estudios revisados proponen métodos para estimar las magnitudes relacionadas con aerosoles, tales como la turbidez, a partir del déficit de SD durante el amanecer y el atardecer, que es cuando se observa más fácilmente el impacto de los aerosoles en los rayos solares. A pesar de la simpleza de la hipótesis, a saber, “cuanto más fuerte sea la luz solar, mayor será la quemada”, muy pocos estudios consideran el ancho de la quemada en bandas de CSSR en lugar de la longitud de la quemada.

En la presente tesis, primero hemos estudiado el uso del ancho de quemada con el objetivo de crear series temporales de la carga de aerosol atmosférico en alta resolución temporal (por ejemplo, sub-diaria). Para este fin, un conjunto de mediciones se llevaron a cabo en Girona, ciudad al noreste de la Península Ibérica. Caracterizamos el CSSR y sus bandas, desarrollando un método de análisis basado en el procesamiento digital de imágenes escaneadas de las bandas quemadas con el fin de obtener la anchura de la quemada en resolución de 1 minuto, y utilizamos una técnica que permite estimar el espesor óptico de aerosoles (AOD) en la misma resolución. Antes de hacer la comparación con AOD, se encontró que existe una fuerte relación entre la anchura de quemada y la radiación solar directa (DSI); por consiguiente, el método ofrece una forma práctica de explotar un conjunto de bandas de CSSR para crear series de DSI. Debido a que la DSI se ve afectada por el contenido de aerosol atmosférico, se confirma que los registros de quemada en bandas de CSSR pueden convertirse en una medida representativa de la turbidez y la carga de aerosoles atmosféricos. Entonces, hemos concurrido datos de momentos despejados de AOD con ancho de quemada en alta resolución (10 minutos). La relación no lineal que hemos encontrado depende en gran medida de la masa de aire. Además, esta relación es más fuerte para valores bajos de elevación solar (es decir, valores altos de masa de aire).

Con el objetivo de realizar una reconstrucción a largo plazo de AOD, también estudiamos la relación entre valores diarios de AOD y SD a escalas temporales largas (por ejemplo, estacional). Utilizamos una relación lineal entre la AOD y SD para los días despejados y para algunas estaciones en la Península Ibérica, las Islas Baleares y Canarias. SD y la nubosidad total (TCC) se toman de las estaciones de la Agencia Estatal de Meteorología, mientras que los datos de AOD se toman de las estaciones más cercanas de la red AERONET. Obtenemos que un aumento de AOD reduce la medida de SD. Por lo tanto, para aquellas estaciones que su serie de SD resultó ser homogénea, se estudia el cambio a largo plazo de AOD. Las series de AOD reconstruidas muestran un claro aumento desde mediados de la década de 1960 hasta la década de 1980, con un máximo durante el 1982-1984, seguido de una posterior recuperación hasta el presente. Estas reconstrucciones son compatibles con el fenómeno de *Dimming & Brightening*. Para Madrid, la serie reconstruida de AOD se remonta hasta 1920; esta serie muestra una disminución de AOD desde mediados de los años 1940 a 1960, que es compatible con el fenómeno de *Early Brightening* observado en otras partes de Europa.

En conclusión, hemos demostrado en esta tesis que las observaciones realizadas con CSSR pueden usarse para estimar cuantitativamente la AOD y su variabilidad y tendencia, tanto en alta resolución temporal como en larga escala temporal. Como CSSR ha sido uno de los instrumentos más utilizados para medir SD, con series de más de 100 años (que están disponibles en algunas estaciones meteorológicas históricas), esta tesis ofrece la posibilidad de determinar las variaciones en la carga de aerosoles atmosféricos y, por lo tanto, de evaluar la posible influencia de las actividades humanas sobre el balance de radiación de la Tierra, con las resultantes consecuencias climatológicas.

PART I.

INTRODUCTION
AND
METHODOLOGY

Chapter 1.

Introduction

The Earth's climate system is driven by the balance between the solar shortwave radiation absorbed by the atmosphere and the surface of the Earth and the thermal longwave radiation emitted to space [see, for example, *Sellers*, 1965]. On average, radiative processes warm the surface and cool the atmosphere, which is balanced by the hydrological cycle and sensible heating. Spatial and temporal energy imbalances due to radiation and latent heating produce the general circulation of the atmosphere and oceans. In Figure 1.1 there is a schematic of the global mean energy budget under present-day climate conditions. The averaged values (in time and space) of the solar shortwave radiation incident on the top of the atmosphere and on the Earth surface are about 340 and 185 W m^{-2}, respectively.

In this research we focus on this first component, saying for short "solar radiation". Distribution and variation of incoming solar radiation is important for a wide range of applications in meteorology, engineering, agricultural sciences, as well in the health sector and in research in many fields of the natural sciences. However, the processes that control the net solar radiation absorbed by the planet are complex and involve the multiple scattering and absorption of solar radiation by atmospheric molecules, clouds, aerosols, as well as characteristics of the surface such as the albedo.

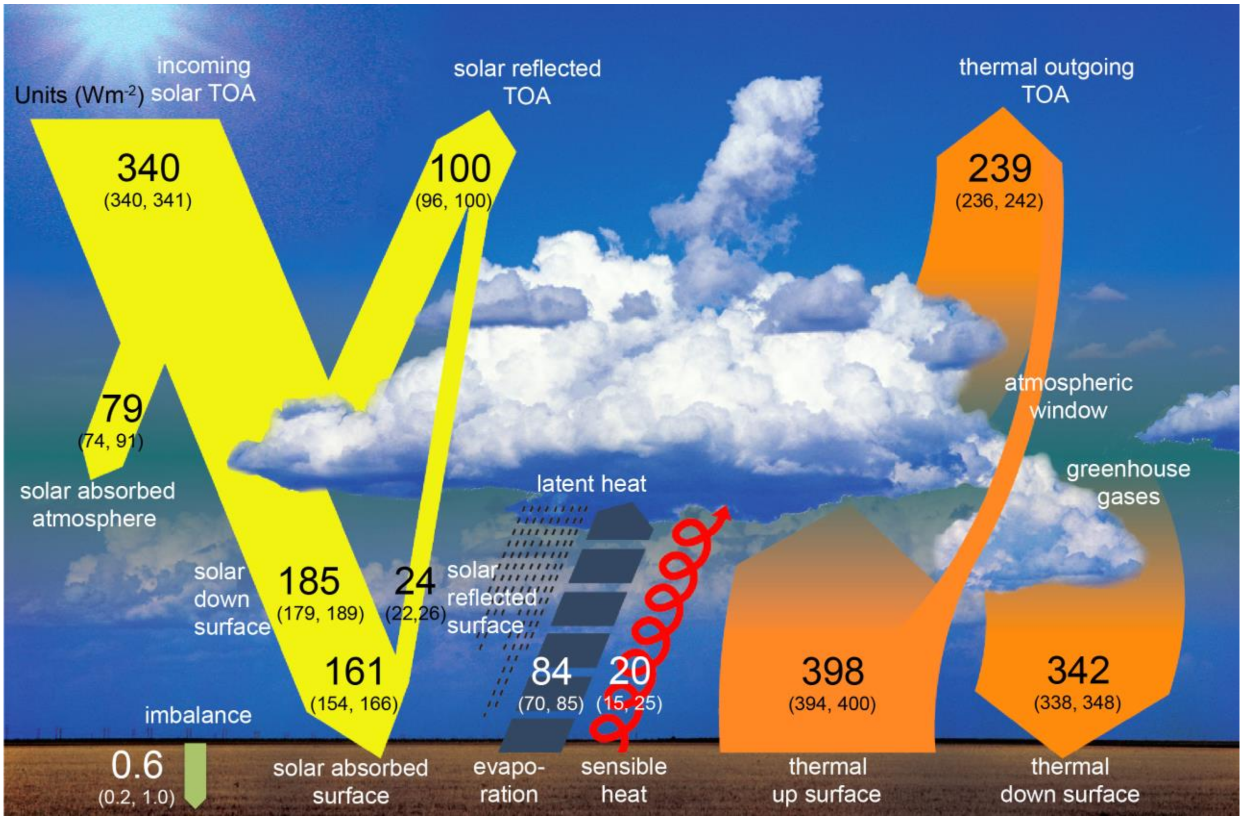
Units (Wm-2)
incoming solar TOA
340
(340, 341)
solar reflected TOA
100
(96, 100)
thermal outgoing TOA
239
(236, 242)
79
(74, 91)
solar absorbed atmosphere
atmospheric window
greenhouse gases
latent heat
solar down surface
185
(179, 189)
24
(22,26)
solar reflected surface
161
(154, 166)
84
(70, 85)
20
(15, 25)
398
(394, 400)
342
(338, 348)
imbalance
0.6
(0.2, 1.0)
solar absorbed surface
evapo-ration
sensible heat
thermal up surface
thermal down surface

Figure 1.1. Global mean energy budget under present-day climate conditions. Numbers state magnitudes of the individual energy fluxes in W m^{-2}, adjusted within their uncertainty ranges to close the energy budgets. Numbers in parenthesis attached to the energy fluxes cover the range of values in line with observational constraints [figure adapted from *Wild et al.*, 2013]. With permission of Springer International Publishing.

The response to any change affecting the radiative properties of the atmosphere is ultimately a change in the surface temperature of the planet and, if maintained over time, in its climate. The term radiative forcing is used to denote the result of an externally imposed perturbation in any component of the radiative energy budget of the climate system. Radiative forcing is a measure of the change in radiative fluxes within the atmosphere-surface system, especially those of the net solar and terrestrial (that is, the thermal longwave radiation) fluxes at the top of the atmosphere and at the Earth's surface. Clouds and aerosols are one of the main factors that modulate the planetary energy balance [e.g., *Iqbal*, 1983]. Another factors that affect the radiative transfer of shortwave and longwave radiation through the atmosphere are the atmospheric gases (including greenhouse gases, GHG) and albedo.

Thus, clouds and aerosols significantly contribute to the Earth's climate and its change, as well as, at regional scales, may produce warming or cooling effects depending on their characteristics [e.g., *Ramanathan et al.*, 1989; *Hartmann et al.*, 1992]. Clouds act as reflectors of solar radiation and absorbers of terrestrial radiation. They constitute one of the biggest uncertainties in climate-change predictions because of difficulties in simulating changes in cloud cover and cloud type, the radiative properties of the many types of cloud, and their high variability both temporally and spatially.

Uncertainties on aerosols, and their effect on Earth's climate and its change, are also very important. These effects are complex, include interactions with radiation and clouds [*Charlson et al.*, 1992; *Moosmüller et al.*, 2009], and are hard to simulate with current models. Because of their short lifetime and uneven distribution in the atmosphere, the abundance of aerosols –and their climate effects– have varied over time and place [*Hartmann et al.*, 2013]. Concretely, in this thesis we are interested in studying the evolution of aerosols based upon their effects on solar radiation, which may become detectable in sunshine duration series.

1.1. Atmospheric aerosols

Atmospheric aerosols are small liquid or solid particles suspended in the atmosphere, other than larger cloud and precipitation particles. The size of particles in aerosol ranges from about 0.001 to about 100 μm. They occur naturally (e.g., originating from volcanoes, dust storms, sea spray, wildfires) or are generated by human activities (e.g., burning of fossil fuels, mining activities). The term “atmospheric aerosol” encompasses a wide range of suspended particles with different compositions, sizes, shapes, and optical properties. In the present thesis, we consider the singular form (“aerosol”) to refer the phenomenon of the suspended particles, whereas the plural form (“aerosols”) to refer as a synonym of particles.

Atmospheric aerosols, whether natural or anthropogenic, originate from two different pathways: emissions of primary particulate matter and formation of secondary particulate matter from gaseous precursors. For example, mineral dust and sea salt are introduced into the atmosphere as primary particles, whereas non-sea salt sulfate, nitrate and ammonium are predominantly from secondary aerosol formation processes. Primary and secondary organic aerosols are influenced by both natural and anthropogenic sources and have a typical lifetime of one day to two weeks in the troposphere, and about one year in the stratosphere [*Boucher et al.*, 2013].

The inclusion of aerosols is now necessary in climate change studies that examine changes in surface and atmospheric temperatures, snow and ice-cover extent, sea-level, precipitation patterns, frequency and intensity of extreme weather events, and desertification, since aerosols crucially affect the radiation budget at the top of the atmosphere, in the atmosphere and at the surface. In addition, aerosols modify the water cycle as they may act as condensation nuclei.

1.1.1. Effects of aerosols

The aerosol influence on the Earth radiative budget is produced in several ways. First, aerosols may scatter and absorb solar and terrestrial radiation; these are called as "direct effects" [e.g., *Charlson et al.*, 1992; *Hansen et al.*, 1997]. Second, aerosols act as cloud condensation nuclei (i.e. can accumulate water vapor during cloud droplet formation), and any change in concentration or hygroscopic properties of aerosol particles has the potential to modify the physical and radiative properties of clouds, affecting the cloud formation, lifetime, and decay; these mechanisms are referred as "indirect effects" [e.g., *Twomey*, 1977; *Ramanathan et al.*, 2001; *Rosenfeld et al.*, 2014]. Finally, absorption of solar radiation by aerosol particles increases atmospheric stability, reducing cloudiness and amplifying the warming influence of absorbing aerosols; these are referred to as the "semi-direct effect" [*Hansen et al.*, 1997]. A detailed overview of these aerosol radiative mechanisms is provided by *Haywood and Boucher* [2000].

However, *Boucher et al.* [2013] have reformulated the former terminology of aerosol direct, semi-direct and indirect effects (Figure 1.2). The radiative forcing from aerosol-radiation interactions (RFari) encompasses radiative effects from anthropogenic aerosols before any adjustment takes place and corresponds to what was usually referred to as the aerosol direct effect. Rapid adjustments induced by aerosol radiative effects on the surface energy budget, the atmospheric profile and cloudiness contribute to the effective radiative forcing from aerosol-radiation interactions (ERFari). They include what was earlier referred to as the semi-direct effect. The radiative forcing from aerosol-cloud interactions (RFaci) refers to the instantaneous effect on cloud albedo due to changing concentrations of cloud condensation and ice nuclei. All subsequent changes to the cloud lifetime and thermodynamics are rapid adjustments, which contribute to the effective radiative forcing from aerosol-cloud interactions (ERFaci).

Most studies agree that the overall aerosol radiative forcing is negative (i.e., it has a cooling influence) [*Stocker et al.*, 2013]. However, in spite of these well-known mechanisms, and compared with GHG, aerosols still present a major uncertainty when estimating their radiative forcing of climate due to their non-uniform chemical and physical properties, and spatial and temporal variations in the atmosphere [*Boucher et al.*, 2013]. In addition, due to the differences in its shortwave and longwave forcing, the net effect of aerosols on Earth's climate does not involve a global offsetting of the warming impact of anthropogenic GHG emissions [*Charlson et al.*, 1992; *Power*, 2003b]. Although many observational studies have quantified local radiative effects of anthropogenic and natural aerosols, determining their global impact requires satellite data and models.

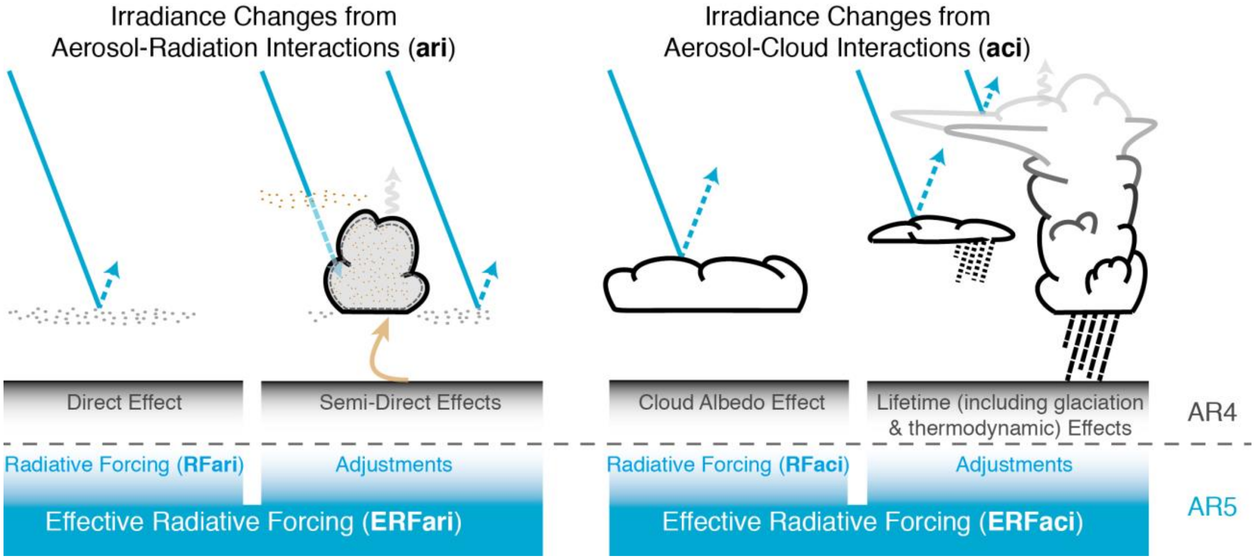
Irradiance Changes from
Aerosol-Radiation Interactions (**ari**)
Irradiance Changes from
Aerosol-Cloud Interactions (**aci**)
Direct Effect
Semi-Direct Effects
Cloud Albedo Effect
Lifetime (including glaciation & thermodynamic) Effects
AR4
Radiative Forcing (**RFari**)
Adjustments
Radiative Forcing (**RFaci**)
Adjustments
Effective Radiative Forcing (**ERFari**)
Effective Radiative Forcing (**ERFaci**)
AR5

Figure 1.2. Schematic of the new terminology used in IPCC Fifth Assessment Report (AR5) for aerosol-radiation and aerosol-cloud interactions and how they relate to the terminology used in IPCC Fourth Assessment Report (AR4). The blue arrows depict solar radiation, the grey arrows terrestrial radiation and the brown arrow symbolizes the importance of couplings between the surface and the cloud layer for rapid adjustments [figure from *Boucher et al.*, 2013].

One of the major pieces of evidence supporting the crucial role played by the direct effects of aerosols upon the climate system is provided by the dimming and brightening phenomenon, represented in Figure 1.3 [e.g., *Stanhill and Cohen*, 2001; *Stanhill*, 2005; *Wild*, 2012]. Both terms refer to a widespread decrease (dimming) in downward solar radiation from the 1950s to the 1980s [*Stanhill and Cohen*, 2001], while a reversal of this trend (brightening) has been seen since the late 1980s, particularly in the developed countries [*Wild et al.*, 2005; *Wild*, 2012]. Similar trends have also been observed when only cloudless conditions are considered [e.g., *Qian et al.*, 2007; *Ruckstuhl et al.*, 2008]. The causes of the dimming/brightening are not yet completely understood, although changes in atmospheric transmissivity since the mid-20th century resulting from variations in anthropogenic aerosol emissions are considered as the main factor causing the observed trends in solar radiation [*Stanhill and Cohen*, 2001; *Wild*, 2009, 2012]. In particular, an increase in these emissions was observed from the 1950s to the 1980, i.e. during the period when the global dimming is detected. A subsequent decrease in anthropogenic aerosol emissions from the 1980 to the 2000s has been reported, resulting from actions aimed at regulating air pollution in the developed countries, which coincide with the period of brightening [e.g., *Wild*, 2009; *Smith et al.*, 2011]. In addition, recent trends in aerosol optical depth derived from satellites indicate a decline in Europe since 2000, in line with evidence from solar radiation observations at the surface.

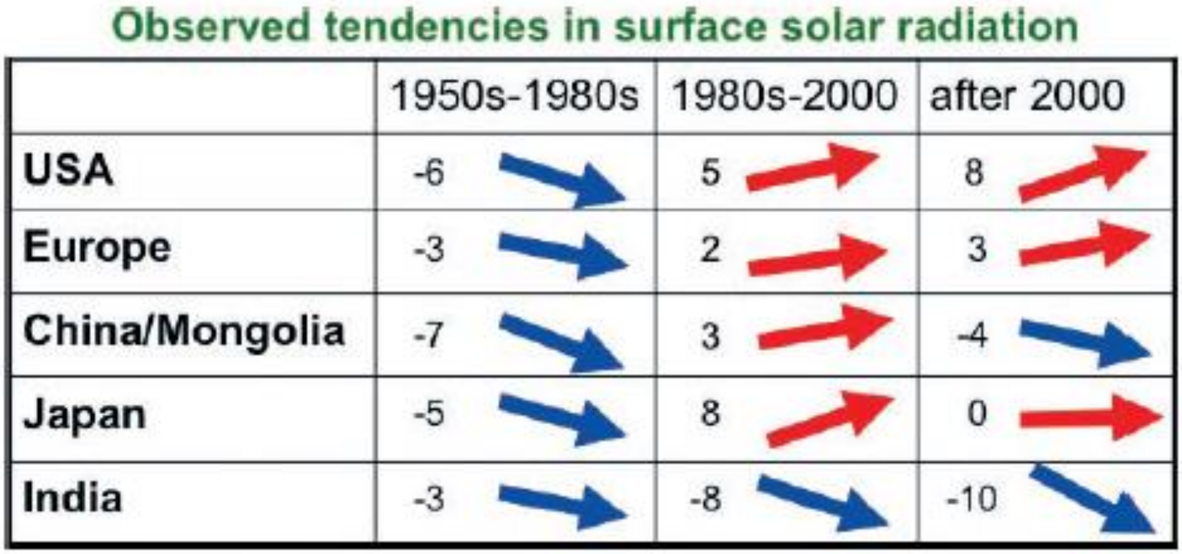

Observed tendencies in surface solar radiation

	1950s-1980s	1980s-2000	after 2000
USA	-6 ↘	5 ↗	8 ↗
Europe	-3 →	2 →	3 →
China/Mongolia	-7 ↘	3 ↗	-4 ↘
Japan	-5 ↘	8 ↗	0 →
India	-3 →	-8 ↘	-10 ↘

Figure 1.3. Changes in surface solar radiation observed in regions with good station coverage during three periods. Numbers denote typical literature estimates for the specified region and period in W m^{-2} per decade [figure from *Wild,* 2012]. ©American Meteorological Society. Used with permission.

Nevertheless, there exist certain uncertainties regarding the causes of the global dimming/brightening phenomenon [e.g., *Wild*, 2012]. Widespread quantification of the aerosol load in the atmosphere (or at least of its radiative characteristics) had not commenced until the late 1970s, with the development of ground and satellite-based instruments. In addition, there is little availability of long-term measurement of downward shortwave radiation prior to the mid-20th century. In the frame work of the International Geophysical Year (1957-1958), measurements of surface solar radiation were initiated and, much more recently, were generalized worldwide. All these factors limit the spatial and temporal representativeness of the observed trends.

1.1.2. Measurement of aerosol properties

One of the most important aerosol radiative properties is the aerosol optical depth (AOD), which is an indirect measure of the integrated columnar aerosol load and is an important parameter for evaluating aerosol-radiation interactions [*Ångström*, 1929]. The typical way of representing these interactions is to account for the spectral transmitted solar radiation:

$$DSI(\lambda) = I_0(\lambda)e^{-\tau(\lambda)m_A} \qquad \text{(Eq. 1.1)}$$

where I_0 is the extraterrestrial solar irradiance in a certain wavelength (that is the solar constant with the correction from the mean distance Sun-Earth), DSI is the measured broadband direct normal solar irradiance in cloudless conditions, λ is the wavelength, τ the vertical total atmospheric optical depth due to scattering and absorption by the different components of the atmosphere, and m_A the air mass traversed by the direct solar beam relative to the air mass in the zenith direction. Subtracting the contributions of water vapor, ozone, NO_2 and Rayleigh scattering to the total optical depth, it is possible to obtain AOD (denoted τ_A in the equations):

$$\tau_A = \tau - (\tau_R + \tau_{O3} + \tau_{NO2} + \tau_W) \qquad \text{(Eq. 1.2)}$$

where $\tau_R, \tau_{O3}, \tau_{NO2}, \tau_W$ refer to the Rayleigh or molecular scattering (i.e., scattering from the main atmospheric gases), absorption by ozone, NO_2, and water vapor optical depths, respectively. Furthermore, the spectral dependence of AOD, which is typically described by the Ångström exponent (AE or α) is often used as a qualitative indicator of aerosol particle size, with large particles having AE values near zero (e.g., desert dust) and smaller particles (e.g., urban, industrial, or biomass burning aerosols) exhibiting larger AE values. AE can be computed from spectral values of AOD in two different wavelengths:

$$\alpha = -\frac{\Delta \ln AOD_\lambda}{\Delta \ln \lambda} \qquad \text{(Eq. 1.3)}$$

Many methods and instruments are developed to measure AOD from ground-based networks (see Table 1.1) and satellite platforms (see Table 1.2). Both are based on radiative measurements to retrieve values of aerosol properties.

Table 1.1. Summary of the current operational ground-based AOD networks [adapted from *Michalsky et al.*, 2010]

Reference	**Coverage**	**Started**	**Instruments**
AGSNET *www.csiro.au*	Australia	1997	Cimel
AERONET *aeronet.gsfc.nasa.gov*	Global	1993	Cimel
SKYNET *atmos2.cr.chiba-u.jp*	East Asia	1996	MFRSR
USDA *uvb.nrel.colostate.edu*	United States	1995	MFRSR
SURFRAD *www.srrb.noaa.gov*	United States	1997	MFRSR
ARM *www.arm.gov*	United States, South Pacific Ocean	1992	MFRSR, Cimel
AEROCAN *aerocanonline.com*	Canada	1997	Cimel
ARFINET *www.spl.gov.in*	India	1985	Other

Ground-based optical observations of atmospheric aerosols may be usually used to obtain AOD and AE [*Ångström*, 1929, 1964; *Masmoudi et al.*, 2003], and involve measurements of solar radiation in distinct spectral bands using pyrheliometer or sunphotometers [*Iqbal*, 1983]. For example, we can highlight the Aerosol Robotic Network (AERONET) of ground based Cimel Sun-photometers that are designed to perform automated direct solar and sky-scanning spectral radiometric measurements every 15 min throughout the day for different channels between 0.34

and 1.64 μm [*Holben et al.*, 1998; *Dubovik et al.*, 2000]. Another example is the Surface Radiation Budget Network (SURFRAD) of ground based Multifilter Rotating Shadowband Radiometers (MFRSR), which employs an automated rotating band which periodically shadows the diffuses of a radiometer to make quasi-simultaneous measurements of the global and diffuse (and derive the direct-normal) components of the solar spectral irradiance [*Harrison et al.*, 1994] also at several wavelengths.

Table 1.2. The history of current platforms and sensors used to derive aerosol properties from space [*Lee et al.*, 2009]

Platform	**Instrument**	**Launch**	**Reference**
GOES-1~12	VISSR	1975	[*Knapp*, 2002]
NOAA-6~16	AVHRR	1979	[*Mishchenko et al.*, 1999]
TRMM	VIRS	1997	[*Ignatov and Stowe*, 2000]
ERS-2	ATSR-2 GOME	1995	[*Veefkind et al.*, 1999]
Earth Probe	TOMS	1996	[*Torres et al.*, 2002]
OrbView-2	SeaWiFS	1997	[*Gordon and Wang*, 1994]
SPOT-4	POAM-3	1998	[*Randall et al.*, 2001]
TERRA	MODIS MISR	1999	[*Remer et al.*, 2005]
PROBA	CHRIS	2001	[*Barnsley et al.*, 2004]
Odin	OSIRIS	2001	[*Bourassa et al.*, 2007]
AQUA	MODIS	2002	[*Remer et al.*, 2005]
ENVISAT	AATSR MERIS SCIAMACHY	2002	[*Grey et al.*, 2006]
MSG-1	SEVIRI	2002	[*Popp et al.*, 2007]
AURA	OMI HIRDLS	2004	[*Torres et al.*, 2007]
PARASOL	POLDER-3	2004	[*Fan et al.*, 2009]

Among the great number of satellite onboard instruments it is worth mentioning the Multi-Angle Imaging SpectroRadiometer (MISR) and the Moderate Resolution Imaging Spectroradiometer (MODIS). Both instruments give a very complete set of variables related to atmospheric aerosol (including AOD and AE), which are derived from various measurement channels. They give low temporal resolution as compared to ground based observations; the latter being generally regarded as more accurate aerosol retrievals for the place they are operating. Specifically, MISR is an instrument onboard the Terra satellite operated by NASA that measures in 4 spectral bands between 0.45 and 0.87 μm [*Diner et al.*, 1998, 2005]. On the other hand, MODIS is an instrument onboard satellites Terra and Aqua of NASA's Earth Observing System, and its detectors measure in 36 spectral bands between 0.40 and 14.39 μm [*Salomonson et al.*, 1989; *King et al.*, 1992].

All the previous instruments are based on passive sensors, which detect radiation that is emitted or reflected by the object or scene being observed. On the other hand, there are instruments that emit radiation in the direction of the target to be investigated; these instruments are called active sensors, and detect and measure the radiation that is reflected or backscattered from the target. In this group, it is important to mention Lidar (light detection and ranging) devices, which are instruments that use a laser source to transmit a light pulse and a receiver with sensitive detectors to measure the backscattered or reflected light. There are various instruments for observation of atmospheric aerosols based on Lidar, both for ground-based networks, e.g., European Aerosol Research Lidar Network (EARLINET), and satellite instruments, e.g., Cloud-Aerosol Lidar with Orthogonal Polarization (CALIOP).

Ground measurements present the inconvenient of their scarcity. The increasing spatial resolution of satellite instruments should help for a better characterization of the regional conditions, but the low temporal resolution of their measurements is an issue. So, each AOD retrieval by satellite sensors shows certain skill against more accurate sunphotometer measurements such as those of AERONET, but there are still large differences among satellite products in regional and seasonal patterns because of differences and uncertainties in calibration, sampling, cloud screening, treatment of the surface reflectivity and aerosol microphysical properties [*Li et al.*, 2009; *Kokhanovsky et al.*, 2010].

Another aerosol property required to evaluate their effect on radiation is the single scattering albedo, which describes the fraction of light scattered by the particle, in relation with the total that is scattered and absorbed; values range from 0 for totally absorbing (dark) particles to 1 for purely scattering ones; an overall representative value is around 0.97, but much lower values are observed in strongly polluted areas with large amounts of absorbing aerosols (e.g., emitted from forest fires and other combustion processes). Another quantity, the asymmetry parameter, reports the first moment of the cosine of the scattering angle; this parameter ranges from –1 for entirely back-scattering particles to +1 for entirely forward-scattering. Forward-backward symmetrical scattering (as isotropic or Rayleigh) has asymmetry parameter equal to zero, but common values range from 0.55 to 0.75. All these quantities are dimensionless, and are in general wavelength-dependent. In addition, they usually need in situ observations, which mean a limited spatial coverage.

1.1.3. Atmospheric turbidity and other proxies

According with the IPCC, little high-accuracy information on AOD changes exists prior to 1995. In order to derive long-term series of aerosols characteristics, which are linked to global aerosol effects, different turbidity coefficients were proposed instead. The optical effect resulting from the absorption and scattering by aerosols, along with water in the liquid/ice phases, is known as atmospheric turbidity, which is an important atmospheric property in climate and pollution studies, as well as in aspects relating to solar energy [*Power*, 2003b]. Atmospheric turbidity can be referred to spectral (wavelength-specific) or to broadband solar radiation. If measurements at some specific wavelength are available, it is possible to distinguish the contribution to attenuation of water vapor from that of aerosols. Several atmospheric turbidity indices have been used for almost one century to quantify the influence of atmospheric aerosol content on the radiation received at the Earth's surface [for an overview, see *Eltbaakh et al.*, 2012].

One of the most known indices is the Linke turbidity factor (T_L), introduced by F. Linke in 1922 [*Linke*, 1922]. This turbidity factor is an indicator of the number of clean dry atmospheres (δ_{CD}) that would be necessary to produce the same attenuation effect as the real atmosphere (Eq 1.2):

$$DSI = I_0 e^{-T_L \delta_{CD} m_A} \qquad \text{(Eq. 1.4)}$$

However, T_L cannot be used as a pure indicator of column aerosol content because it also depends on other atmospheric parameters such as water vapor amount and solar zenith angle. Other authors introduced different techniques using radiative transfer models to determine the so-called "broadband AOD" from broadband pyrheliometric data [*Gueymard*, 1998; *Qiu*, 1998; *Ohvril et al.*, 2009], after the first proposals by *Unsworth and Monteith* [1972]. In addition, some authors used broadband pyranometer data [*Kudo et al.*, 2010b; *Lindfors et al.*, 2013]. All of these techniques are based on radiative transfer models but have the problem that, as we said before, measurements of global solar radiation started only after the International Geophysical Year 1957-1958, and have been generalized worldwide much more recently.

Visibility has often been employed as another proxy for atmospheric aerosol characterization [*Wang et al.*, 2009b; *Zheng et al.*, 2011; *Van Beelen and Van Delden*, 2012]. The problem with visibility is its subjectivity and that few available long-term series exist [e.g., *García et al.*, 2015]. Finally, as we will see in next Section, sunshine duration, which is affected by atmospheric conditions, has also been proposed as a proxy for atmospheric turbidity [see *Sanchez-Romero et al.*, 2014 for a review]. Series of sunshine duration are longer than those of surface solar radiation and more objective and widely-used than visibility.

1.2. Sunshine duration

Sunshine duration (SD) for a given period (usually a day) is currently defined as the sum of those sub-periods for which the direct solar irradiance exceeds 120 W m^{-2}; so SD can be affected by aerosols as they modify direct solar irradiance. This variable was defined according to the World Meteorological Organization, WMO [*WMO*, 2008]. The units used are “hours per day”, as well as relative quantities, such as “relative daily sunshine duration”, where SD is divided by the maximum possible SD (i.e., as if sky was clear all the time), which is computed by using astronomical formulas and an elevation angle of the sun higher than some selected threshold (e.g. 3 degrees).

The first SD recorders started to appear in the late 19th century [*Sanchez-Lorenzo et al.*, 2013b]. Therefore, the existing long time series of SD measurements have a remarkable historical value. Several studies have analyzed the spatial and temporal behavior of SD in different regions during the last few decades, and the possible causes of the variability (see for example the Figure 1.4). These studies used long-term series of SD obtained from different sites across the world such as, e.g., the United States [e.g., *Stanhill and Cohen*, 2005; *Magee et al.*, 2014], Canada [e.g., *Cutforth and Judiesch*, 2007], South America [e.g., *Raichijk*, 2012], Australia [e.g., *Jones and*

Henderson-Sellers, 1991], China [e.g., *Zheng et al.*, 2008; *Li et al.*, 2012], Japan [e.g., *Stanhill and Cohen*, 2008], Taiwan [e.g., *Liu et al.*, 2002], India [e.g., *Jaswal*, 2009; *Soni et al.*, 2012], South-Eastern Europe [e.g., *Brázdil et al.*, 1994], Western Europe [e.g., *Pallé and Butler*, 2001; *Sanchez-Lorenzo et al.*, 2008], and Central Europe [e.g., *Liepert*, 1997; *Sanchez-Lorenzo and Wild*, 2012].

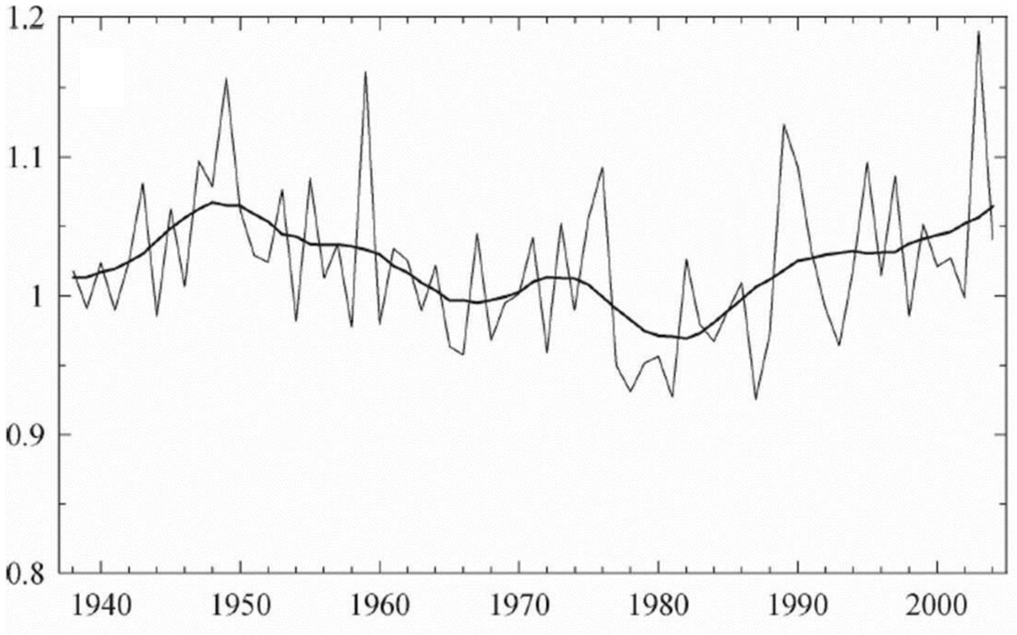

Figure 1.4. Mean annual trends of SD series of Western Europe stations between 1938 and 2004 (thin line), calculated by least squares linear fitting, and plotted together with a low-pass filter (thick line). The series are expressed as relative deviations from the 1961-90 mean [figure from *Sanchez-Lorenzo et al.*, 2008]. ©American Meteorological Society. Used with permission.

The problem of using such long-term series is that a change of the instrument used to measure SD can affect the homogeneity of the dataset. In some cases, entire networks of measurements changed their instruments (for example, in the United States, optic/photographic instruments were changed to thermometric instruments and, later, to electronic instruments). This may lead to significant errors when evaluating trends and may hinder the possibility of determining long-term secular trends [*Powell*, 1983; *Steurer and Karl*, 1991; *Brázdil et al.*, 1994; *Stanhill and Cohen*, 2008]. Among the studies that analyze long series of SD, some works choose to restrict the period in order to avoid instrumental changes, therefore not encompassing the entire period of observation [*Angell et al.*, 1984; *Kerr and Tabony*, 2004; *Sanchez-Lorenzo et al.*, 2007; *Xia*, 2010]. The results of these studies point towards the need for further research, including homogenization of the long-term SD series and the necessity of simultaneous measurements by different instrumentation [*Aguilar et al.*, 2003].

1.2.1. Campbell-Stokes sunshine recorder

One of the instruments used to measure SD is the Campbell-Stokes sunshine recorder (CSSR). It was invented in the late nineteenth century to provide a measurement of the duration of bright sunlight by making a burn mark on a piece of specially treated cardboard. The measurement of the length of the burn for a given card gives daily SD. For details on the history of the CSSR, we refer to *Stanhill* [2003] and *Sanchez-Lorenzo et al.* [2013b]. In brief, the main parts of a current CSSR are a sphere made of transparent glass and a rounded metal frame placed behind the sphere (see Figure 4.2 in Chapter 4). The glass sphere is designed to focus the Sun's rays onto a piece of recording cardboard. The metal frame part has three overlapping sets of grooves to hold the recording cards for the winter, summer, and spring/autumn periods. The recording card has to be replaced daily after sunset. Different designs of cards exist with hourly and half-hourly divisions marked across these cards, enabling determination of the times of sunshine, at an estimated resolution of 0.1 h. For further details on the instrument and instructions for obtaining uniform results, as well as other traditional instruments for measuring SD, see *Middleton* [1969] and Chapter 4.

As the longer SD series are generally measured using CSSR, the errors connected with this instrument are well-described [*Painter*, 1981; *Brázdil et al.*, 1994]. The two major problems with CSSR when comparing their measurements with other methods or instruments lie in the variability of the level of direct irradiance which produces a burn and the overburning of the card in conditions of intermittent high irradiance [*Stanhill*, 2003]. These difficulties can be added to the obvious element of subjectivity in measuring the burn length on the CSSR cards [*Brázdil et al.*, 1994]. The problem of overburning is very difficult to evaluate as one small burst of high direct irradiance causes a burn apparently lasting far longer than the few seconds of its actual duration; standard methods have therefore been proposed to take into account this fact when evaluating the burn lengths [*WMO*, 2008]. Despite these rules, during events of very broken cloudiness a measurement of SD by means of CSSR can be significantly overestimated [*Painter*, 1981; *Kerr and Tabony*, 2004].

Regarding the first problem, defining the direct irradiance value that produces burning ("burning threshold") is a well-known issue. A value of 120 W m^{-2} was recommended [*WMO*, 2008], even if *Bider* [1958], *Jaenicke and Kasten* [1978] and *Roldán et al.* [2005] showed a large variety of burning thresholds for different CSSR. Similarly, *Helmes and Jaenicke* [1984] described the effects of using different types of recording cards. In addition, the measurement of threshold values indicated that there were notable losses of record, which must be attributed to dew or other water deposits on the glass sphere [*Painter*, 1981]. From the above discussion it is clear that long time series of SD include errors of several kinds and that their removal is a complicated issue. See Chapter 4 to know more about the problem of thresholds in CSSR devices.

1.2.2. Current instruments and methods

Over the last years, various automated instruments and other methods for obtaining SD have been developed, which are summarized in *WMO* [2008]. One of these is the pyrheliometric method, which is based on direct irradiance measurements [e.g., *Hinssen*, 2006; *Hinssen and Knap*, 2007; *Vuerich et al.*, 2012]. Another way of determining SD is by means of automatic instruments specifically designed to this end, which have become commercially available [*Wood et al.*, 2003; *Kerr and Tabony*, 2004; *Matuszko*, 2014a]. These instruments count the time interval during which the direct solar irradiance exceeds a certain threshold. Progressively, many weather stations have changed traditional manual instruments (such as CSSR and Jordan photographic recorders) to these automatic systems. Moreover, different methods exist nowadays to estimate SD from geostationary satellite data, which potentially provide improved spatial coverage and representativeness [*Olseth and Skartveit,* 2001; *Good*, 2010; *Kothe et al.*, 2013].

Despite the fact that new models of sunshine recorders do not require daily attention by an observer and their data reduction (i.e., the process of recording and storing the SD data) is faster and more accurate, there is a consensus with regard to preserving traditional instruments (as CSSR) at long-established (in some cases more than 120 years ago), well-maintained, and freely exposed meteorological stations [*Stanhill*, 2003; *Wood and Harrison*, 2011; *Sanchez-Lorenzo et al.*, 2013b].

1.2.3. Sunshine duration as a proxy for cloudiness and solar irradiance

SD provides additional embedded information on cloudiness and solar irradiance [*Stanhill*, 2003; *Wood and Harrison*, 2011]. Regarding the first phenomenon, relationships between both variables have been studied since the early 20th century [e.g., *van der Stok*, 1913; *Haurwitz*, 1948; *Fox*, 1961]. The two quantities were considered as a complement of each other: in general an increase (decrease) in cloudiness is accompanied by a decrease (increase) in SD. Regarding the solar radiation and with the use of Ångström-Prescott type formulas, many authors relate SD during a period of time with direct or global irradiance [e.g., *Martínez-Lozano et al.*, 1984; *Stanhill*, 1998a; *Suehrcke*, 2000; *Power*, 2001; *Bakirci*, 2009], which were first proposed by *Ångström* [1924] and further modified by *Prescott* [1940]. Moreover, as with the long-term measurements of downward shortwave radiation, most of the papers that have addressed the variability in SD, the trends thereof, and the possible causes of these, found a widespread decrease in SD between the 1950s and 1980s, i.e. the "global dimming" period. Equally, most of these studies also showed a partial recovery of SD since the 1980s, i.e. "brightening" period.

Burn width in CSSR cards has also been used as a proxy of direct solar irradiance [*Wright*, 1935]: the size of the burn at any point is related to the strength of the direct solar irradiance focused on the card at that time (Figure 1.5). *Galindo Estrada and Fournier d'Albe* [1960] applied a similar approach: they compared daily values of the mass loss of burned cards (which is related to the perforation of the card and thus to mean burn width besides to burn length – sunshine duration) with pyrheliometer readings. The hypothesis of using the burn width of CSSRs to obtain direct solar irradiance data has recently been revisited, and several studies have shown the potential of the burn width of CSSR cards as a proxy for DSI [e.g., *Wood and Harrison*, 2011; *Horseman et al.*, 2013]. In addition, *Sanchez-Romero et al.* [2015], which constitutes Chapter 5 of the present thesis, proves whether the relationship between burn width and DSI depends on the type of CSSR and burning card. The method offers a practical way to exploit long-term sets of CSSR cards to create long time series of DSI. As we will see in the next section, since DSI is affected by atmospheric aerosol content, CSSR records may also become a proxy measurement for turbidity and atmospheric aerosol loading.

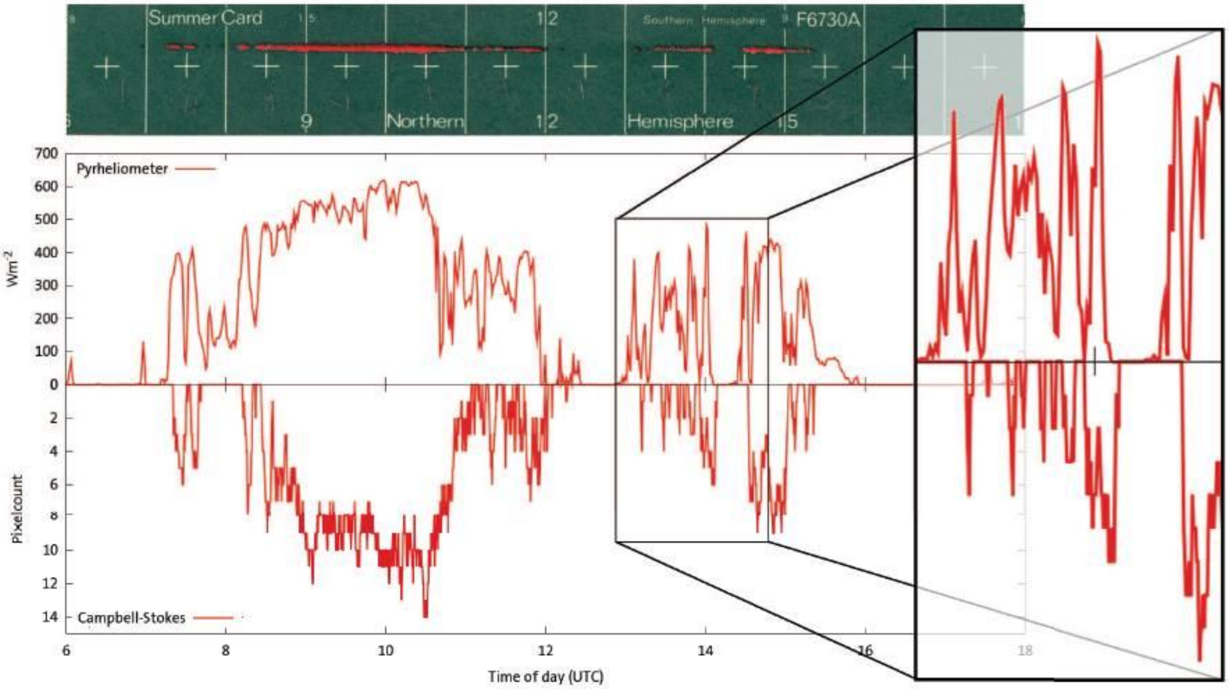

Figure 1.5. Comparison between the solar data extracted from a CSSR card and that from the collocated pyheliometer [figure from *Horseman et al.*, 2013].

1.2.4. Sunshine duration as a proxy for aerosol

The possibility that SD records can be affected by the changes in atmospheric turbidity and thus by the aerosol loading was proposed by various authors. According to the reviewed literature, there is evidence that SD records contain signals of the direct effects of aerosols on the solar beam, and in consequence, SD records can be used as a proxy for studying aerosol trends and their radiative forcing. A detailed review of the state-of-the-art on this matter is performed in Chapter 4, which is already published [*Sanchez-Romero et al.*, 2014].

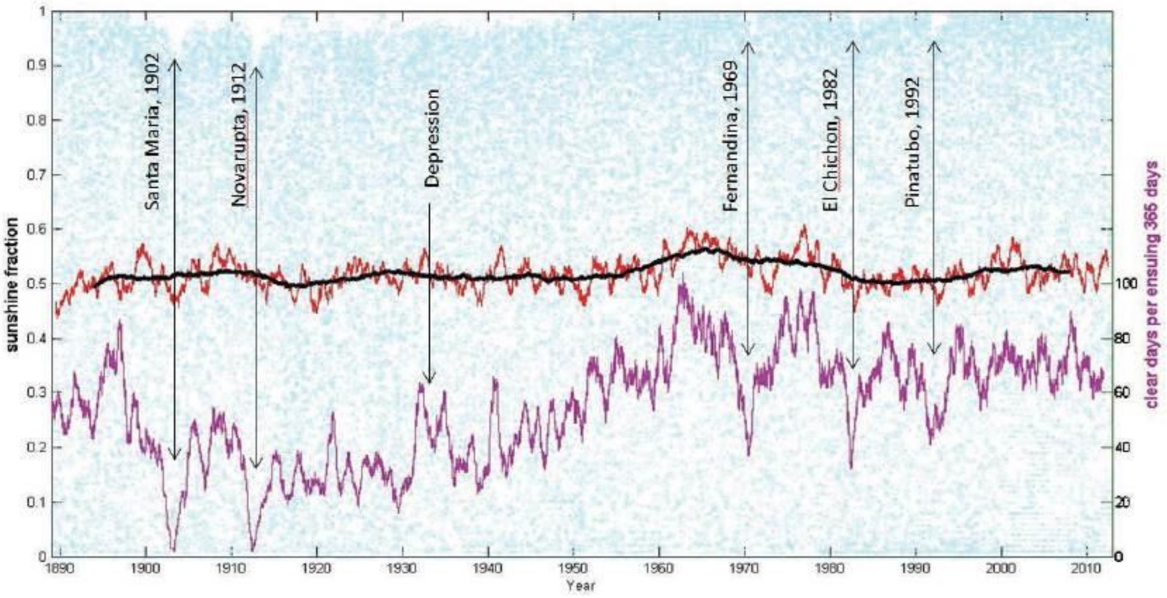

Figure 1.6. Long-term measurements and trends in relative SD and clear days (>92% sunny) for the Blue Hill Meteorological Observatory in Milton, Massachusetts (United States). 1-year (red) and 10-year (black) moving averages of moving weekly relative SD measurements, overlaid on raw daily relative SD observations (blue points). Right axis displays the number of clear days (purple) in a moving 365-day interval [figure from *Magee et al.*, 2014]. ©American Meteorological Society. Used with permission.

If the effect of atmospheric aerosols on SD records is to be determined, the effects of cloudiness should be previously removed from SD measurements. On the other hand, aerosol modifies cloud amount and properties; this indirect effect is difficult (if not impossible) to quantify by means of SD data. Therefore, the aerosol direct effect has been the only one considered by researchers when quantifying the signal of aerosols within SD data. For example, *Magee et al*. [2014] observed that SD is linked with a wide variety of natural and anthropogenic processes, e.g., industrial activity and regional air quality (Figure 1.6). In particular, the impacts of several volcanic eruptions are apparent in its series. The impacts of the El Chichón (April 1982) and Pinatubo (June 1991) volcanic eruptions are also evident in other SD series, which present clear minima during the periods 1982-1983 and 1992-1993, hypothetically due to the impact of the big increase in sulfate aerosols in the lower stratosphere, which reduces incoming solar radiation [e.g., *Sanchez-Lorenzo et al.*, 2009; *Sanchez-Lorenzo and Wild*, 2012].

In general, studies showing links between changes in SD and aerosols do not focus upon proving and quantifying the causal relationship. In fact, few studies focus on estimating the effect of aerosols in SD: *Jaenicke and Kasten* (1978), *Helmes and Jaenicke* (1984, 1985, 1986). These articles are based on the fact that aerosols reduce SD at low solar elevations (i.e. at the beginning and the end of the day): high aerosol content can reduce the incident direct solar irradiance to a level such that no burn appears in CSSR cards. It is not expected that aerosol contribute to reduce SD for high sun elevation periods (e.g., at noon for not very high latitudes), when the DSI is well above the burn threshold. As a particular example, *Cohen and Kleiman* [2005] observed that, in cloudless mornings and afternoons, the Sun appeared and disappeared from the sight well after and before of the calculated sunrise and sunset. Thus, the length of the day had apparently become shorter due to an increase of aerosol content. These methods are simple and give a coarse estimation of atmospheric turbidity, but pose the major problem that this estimation is not only affected by aerosols but also by water vapor.

Chapter 2.

Goals

Aerosols play an important role in the global climate balance, and might therefore have a significant effect on climate. However, there is little available information on changes in aerosol concentration in the atmosphere, especially prior to the 1980s. Since long time series of SD measurements exist, **the principal goal of the present thesis involves assessing the suitability of historical series of SD and CSSR cards with regard to detecting changes in atmospheric aerosols for long time periods, as well as the appropriateness of using burn width from CSSR cards to estimate AOD at sub-daily resolution.**

Firstly, we reviewed studies addressing the possibility of employing SD measurements to detect changes in atmospheric turbidity, as well as articles focusing on quantifying the causal relationship [*Sanchez-Romero et al.*, 2014 or Chapter 4]. We concluded that there is abundant evidence that one cause of the decadal changes observed in SD records involves variations in atmospheric aerosol loading, and that very few articles study the burn width of CSSR cards. Having established the state of the art, and within the framework of the above mentioned general goal, our research has focused on the following specific goals:

1) To prove and quantify the effect of aerosols on burn width of CSSR cards at a high temporal resolution (e.g., sub-daily).
    a) To characterize the CSSR and its cards, especially in relation to burn threshold and SD measurement [*Sanchez-Romero et al.*, 2015; Section 5.4.1].
    b) To develop a method based on image processing of digitally scanned images of burnt cards in order to obtain burn width at high temporal resolution [*Sanchez-Romero et al.*, 2015; Section 5.3].
    c) To show the relationship between burn width and direct solar irradiance at high temporal resolution, and to prove whether this relationship depends upon the type of CSSR and/or burning card [*Sanchez-Romero et al.*, 2015; Section 5.4.2].
    d) To obtain reliable AOD measurements at high temporal resolution, as well as a comparison between ground-based and satellite data [*Sanchez-Romero et al.*, 2016a; Chapter 6].
    e) To relate the measurements of AOD and burn width at sub-daily resolution, and specifically to show whether the increase in aerosol content causes a decrease in the burn width of CSSR cards [Chapter 7].

2) To prove, quantify and exploit the effect of atmospheric aerosol on SD in cloudless conditions, at long temporal scales (e.g., seasonal).
    a) To establish a relationship between SD and AOD from synchronic observations [*Sanchez-Romero et al.*, 2016b; Section 8.3].
    b) To reconstruct long-term AOD series [*Sanchez-Romero et al.*, 2016b; Section 8.4].

This research was made possible by a pre-doctoral scholarship grant from the FPU program (FPU AP2010-0917) of the Spanish Ministry of Education. The research was conducted under the umbrella of the NUCLIEREX and NUCLIERSOL projects, funded by the former Spanish Ministry of Science and Innovation, and was developed at the Department of Physics of the University of Girona. The overall aim of these projects is to contribute to reducing uncertainties associated with clouds and aerosols in the radiation models employed to describe climate and in studies on climate change. In particular, this thesis involved tasks intended to increase our knowledge of the effects upon climate of atmospheric aerosol loading, as well as to test the hypothesis that SD measurements with the CSSR can constitute a proxy for aerosol loading.

Chapter 3.

Instruments and Methodology

In this thesis we are concerned mainly with measurements of SD and aerosol loading. For both magnitudes, we use data from a weather and radiometric station located on the roof of a building of the University of Girona (41.962ºN, 2.829ºE, 115 m asl), besides data of some AEMET and AERONET stations, and data from satellite MISR and MODIS instruments. Girona is a city located in the northeast of the Iberian Peninsula, about 30 km from the Mediterranean Sea, 100 km northeast of Barcelona and 40 km from the Pyrenees, and an average elevation of 75 meters above sea level. It has almost 100,000 inhabitants.

General information about the data used will be briefly provided in the next sections. Also, a short introduction on some methods used in this research, namely a semi-automatic method developed to retrieve information from the burnt cards and, and a method applied to determine AOD and AE at a high temporal resolution, will be also commented. However, most details about instruments, data, and methods, will be given in each of the corresponding chapters 5 to 8.

3.1. Sunshine duration data

The SD measurements used in this research come from the weather and radiometric station in the University of Girona and from 16 stations of the Spanish Meteorological Agency (AEMET).

In the case of University of Girona data, two different models of CSSR have been used. One of the CSSR (including cards) is from Thies Clima; the other CSSR is from Negretti & Zambra manufactured in the 1980s, with cards of the model Mod.98, formerly used by AEMET. Apart of visually reading the cards to obtain SD, a semi-automatic method to retrieve information from the burnt cards was developed. With this, we obtained daily evolution of the burn width at a resolution of 1-minute; the length of the burn (i.e. sunshine duration) was easily determined too (see Section 5.3 for a detailed explanation of the method).

In the case of AEMET data, daily records of SD (in hours) were available. SD was measured mainly by using CSSR, although some stations have recently changed to an automatic sensor (more details in Section 4.2.1.). SD fraction, which is the ratio of SD to the total length of daytime, is also calculated for these data.

3.2. Aerosol content data

AOD and AE data used in this thesis have been obtained from ground-based and from satellite instruments. For the first case, we use data from MFRSR and Cimel spectrophotometers and, for the second one, those from MODIS and MISR instruments.

The MFRSR ground-based data come from an instrument installed at the University of Girona, which continuously measures the global and diffuse solar horizontal irradiance in six wavelengths (415, 500, 615, 673, 870 and 940 nm), using the first five of these to derive optical depth and its spectral dependence. In order to obtain AOD and AE at a high temporal resolution (1-minute), we implemented a method that is explained with detail in Section 6.2. On the other hand, Cimel data is from the archives of the Aerosol Robotic Network (AERONET). Cimel sunphotometers measure in 8 different channels between 0.34 and 1.64 μm. Specifically, we calculated mean daily values of AOD by using the level 2.0 data, i.e. cloud-screened and quality-assured data from AERONET. Although MFRSR and Cimel are different instruments (spectral channels, sampling frequency, etc.), and algorithms applied to extract aerosol characteristics are also somewhat different, the uncertainty in the retrieved aerosol properties is similar.

As far as satellite instruments are concerned, MISR and MODIS provide global coverage at the expense of relatively low temporal resolution. For Girona location (a mid-latitude site), and due to its orbital cycle, MISR will generally observe it only 3 to 5 times every 16 days; on the contrary, MODIS instruments scan the entire Earth’s surface every 1 to 2 days. So, more cases are available from MODIS than from MISR.

3.3. Other instruments and data

DSI, which is another important variable, is measured in the University of Girona by a CH-1 pyrheliometer from Kipp & Zonen, mounted on a Sun tracker. The DSI is measured every second, and is stored as 1-minute averages. The weather and radiometric station of University of Girona is also equipped with meteorological sensors to measure temperature, humidity, pressure, wind speed, precipitation, etc., as well as other radiometric sensors to measure global and diffuse broadband solar irradiances, and in selected spectral bands. In addition, a ceilometer allows obtaining the height of cloud layers, and a whole sky camera is continuously taken pictures of the sky dome at 1-minute resolution.

When needed, total cloud cover (TCC) records, in oktas, have been obtained for 16 stations of the AEMET. These stations are constituted by ground level visual observations and available for 3-daily observations, taken at 7, 13 and 18 UTC.

We are interested in assessing how accurate are our AOD estimations, so we compare calculated clear-sky shortwave broadband irradiance using retrieved AOD with measurements in a closure experiment. For this purpose, we use the Simple Model of the Atmospheric Radiative Transfer of Sunshine (SMARTS2) to calculate the aerosol effects on the direct broadband shortwave irradiance at the surface. SMARTS2 is a parameterized spectral model for calculating the direct beam, diffuse, and global irradiances incident on the Earth's surface. Different inputs are used in the modeling. Surface pressure, relative humidity and air temperature are obtained from the University of Girona station. Integrated water vapor for the column above the site is taken from the ERA-Interim reanalysis, which is a global atmospheric reanalysis from 1979 to present [*Dee et al.*, 2011]. Finally, the total ozone column above the site is taken from the Ozone Monitoring Instrument (OMI); this instrument is on board the NASA Aura, and is continuing the Total Ozone Mapping Spectrometer (TOMS) record for total ozone and other atmospheric parameters related to ozone chemistry and climate (more details in Chapter 6).

Chapter 4.

Review about aerosol traces in sunshine observations

This chapter is a transcription of the paper:

Sanchez-Romero, A., A. Sanchez-Lorenzo, J. Calbó, J. A. González, and C. Azorin-Molina (2014), The signal of aerosol-induced changes in sunshine duration records: A review of the evidence, *J. Geophys. Res. Atmos*., 119, 4657–4673, doi:10.1002/2013JD021393.

The chapter deals with establishing the state-of-the-art regarding studies that investigate whether aerosol changes may be noticed in sunshine duration records. Some of the reviewed studies propose methods for estimating aerosol-related magnitudes, such as turbidity, from sunshine deficit at approximately sunrise and sunset, when the impact of aerosols on the solar beam is more easily observed. In addition, there is abundant evidence that one cause of the decadal changes observed in sunshine duration records involves variations in atmospheric aerosol loading.

4.1. Introduction

Solar radiation reaching the Earth's surface, also known as surface downward shortwave radiation, plays a key role in the global energy balance and therefore in modulating climate [see for example, *Sellers*, 1965]. Apart from the atmospheric gases (including GHG) affecting the radiative transfer of shortwave and longwave radiation through the atmosphere, clouds and aerosols are the main factors modulating the planetary energy balance [e.g., *Twomey*, 1977; *Iqbal*, 1983]. Thus, clouds and aerosols significantly contribute to the global albedo, and, at regional scales, may produce warming or cooling effects depending on their characteristics [e.g., *Ramanathan et al.*, 1989; *Hartmann et al.*, 1992].

An atmospheric aerosol involves suspension of solid and/or liquid particles in the air [*D'Almeida et al.*, 1991]. The term "atmospheric aerosol" encompasses a wide range of particles (aerosols) with different compositions, sizes, shapes, and optical properties. Both natural and human processes contribute to the presence of aerosols in the atmosphere. The concentration of aerosols alters the intensity of solar radiation scattered back to space, absorbed in the atmosphere, and reaching the earth's surface [e.g., *McCormick and Ludwig*, 1967; *Charlson et al.*, 1992; *Moosmüller et al.*, 2009]. The optical effect resulting from the absorption and scattering by aerosols, along with water in the liquid/ice phases, is known as atmospheric turbidity, which is an important atmospheric property in climate and pollution studies, as well as in aspects relating to solar energy [*Power*, 2003a]. Atmospheric turbidity is determined by measuring spectral (wavelength-specific) or broadband solar radiation. Several atmospheric turbidity indices have been used for almost one century to quantify the influence of atmospheric aerosol content on the radiation received at the Earth's surface [for an overview, see *Eltbaakh et al.*, 2012].

On a global average basis, aerosol radiative forcing is negative (i.e., it has a cooling influence) [*Solomon et al.*, 2007]. However, because of the spatial and temporal non-uniformity of the aerosol radiative forcing, and due to the differences in its shortwave and longwave forcings, the net effect of aerosols on Earth's climate does not involve a global offsetting of the warming impact of anthropogenic GHG emissions [e.g., *Charlson et al.*, 1992; *Power*, 2003a]. More specifically, aerosols affect Earth's energy budget in several ways [e.g., *Ramanathan et al.*, 2001; *Rosenfeld et al.*, 2008], which are referred to as direct, semi-direct and indirect aerosol effects. A detailed overview of these aerosol radiative mechanisms is provided by *Haywood and Boucher* [2000].

One of the major pieces of evidences supporting the crucial role played by the direct and indirect effects of aerosols upon the climate system is provided by the dimming and brightening phenomenon [e.g., *Stanhill and Cohen*, 2001; *Stanhill*, 2005; *Wild*, 2009, 2012]. Both terms refer to a widespread decrease (dimming) in downward shortwave radiation from the 1950s to the 1980s [*Stanhill and Cohen*, 2001], while a reversal of this trend (brightening) has been seen since the late 1980s, particularly in the developed countries [*Wild et al.*, 2005; *Wild*, 2012]. Similar trends have also been observed when only cloudless conditions are considered [e.g., *Qian et al.*, 2007; *Ruckstuhl et al.*, 2008]. The causes of the dimming/brightening are very complex, although changes in atmospheric transmissivity since the mid-20th century resulting from variations in anthropogenic aerosol emissions are considered as the main factor causing the observed trends in solar radiation [*Stanhill and Cohen*, 2001; *Wild*, 2009, 2012]. In particular, an increase in these emissions was observed from the 1950s to the 1980s, i.e., during the period when the global dimming is detected. A subsequent decrease in anthropogenic aerosol emissions from the 1980s to the 2000s has been reported, resulting from actions aimed at regulating air pollution in the developed countries, which coincides with the period of brightening [e.g., *Stern*, 2006; *Streets et al.*, 2009; *Wild*, 2009; *Folini and Wild*, 2011; *Smith et al.*, 2011].

Nevertheless, uncertainties remain regarding the causes of the global dimming/brightening phenomenon [e.g., *Wild*, 2012]. In addition, there is little availability of long-term measurements of downward shortwave radiation prior to the mid-20th century when widespread measurements were initiated within the framework of the International Geophysical Year (1957-1958). Measurements of atmospheric turbidity are even scarcer, and instrumentation for observations of aerosols has been developed more recently. All these factors limit the spatial and temporal representativeness of the observed trends. It would therefore be useful to find a proxy for these magnitudes with greater spatial and temporal coverage.

Since long time series of SD measurements exist, they have a remarkable historical value. According to the *WMO* [2008], the SD for a given period is currently defined as the sum of those sub-periods for which the direct solar irradiance exceeds 120 W m^{-2}. For climatological purposes, the units used are “hours per day”, as well as percentage quantities, such as “relative daily sunshine duration” where SD is divided by the maximum possible SD (i.e., as if sky was clear all the time). SD is affected by atmospheric conditions, and consequently it could serve as a proxy for atmospheric turbidity. Another proxy of atmospheric turbidity that has often been employed is visibility [*Wang et al.*, 2009a; *Zheng et al.*, 2011; *Van Beelen and Van Delden*, 2012]. The problem with visibility is, apart from being a magnitude even more subjective than SD, that few available long-term series.

One of the instruments used to measure SD is CSSR. It was invented in the late 19th century to provide a measurement of the duration of bright sunlight by making a burn mark on a piece of specially treated cardboard. The measurement of the length of the burn for a given card gives daily SD, and also provides additional embedded information on cloudiness and solar irradiance [*Stanhill*, 2003; *Wood and Harrison*, 2011]. Regarding the latter possibility, many authors relate SD during a period of time with direct or global (which is the sum of the solar direct and diffuse contributions) irradiance, with the use of Ångström-Prescott type formulas [e.g., *Martínez-Lozano et al.*, 1984; *Stanhill*, 1998a; *Suehrcke*, 2000; *Power*, 2001; *Bakirci*, 2009], which were first proposed by *Ångström* [1924] and further modified by *Prescott* [1940]. Moreover, several studies have analyzed the spatial and temporal behavior of SD in different regions during the last few decades [e.g., *Weber*, 1990; *Brázdil et al.*, 1994; *Pallé and Butler*, 2001; *Liu et al.*, 2002; *Stanhill and Cohen*, 2005, 2008; *Sanchez-Lorenzo et al.*, 2007; *Raichijk*, 2012; *Sanchez-Lorenzo and Wild*, 2012; *Wang et al.*, 2012a].

The possibility that SD records can be affected by changes in atmospheric turbidity and thus by the aerosol loading was proposed by J.F. Campbell, the inventor of the CSSR. Specifically, he claimed [*Campbell*, 1857; p. 1]: "The bowl, at the Board of Health -*downtown London*-, which is always in the smoke, was not nearly so much marked as the one at Campden Hill -*high ground in west London*-. One further from London would probably have been marked to a much greater extent and for much longer periods…" Later, other early studies found more evidence that air pollution can affect the measured SD. For example, *Whipple* [1878] compared SD data from two cities to the east and west of London, and found, by analyzing the reduction of the length of the burn, reductions in air transparency depending on wind direction. A large number of studies show a relationship between SD and smog in London during the last century [for an overview, see *Wheeler and Mayes*, 1997]. Equally, *Maurer and Dorno* [1914] already discussed how the eruption of Katmai (Alaska) in 1912 caused anomalous records of SD in various European observatories during 5 months following the eruption. *Galindo and Chavez* [1978] reported an increase in the aerosol loading the night of December 24th in Mexico City, caused by the burning of thousands of tires, causing a reduction by one hour in SD the next day. Specifically, on December 24th and 26th, the cardboard started to burn at 06:50; on December 25th, it started at 07:50 (Figure 4.1).

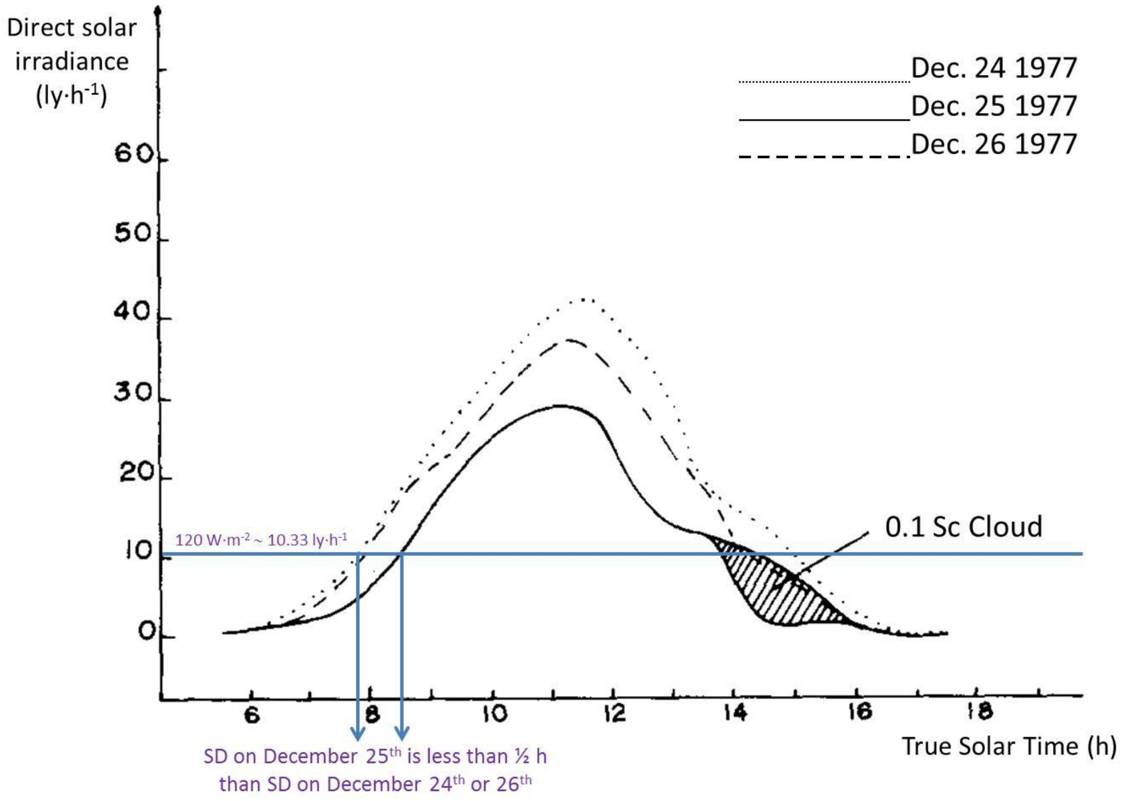

Figure 4.1. The large quantity of aerosol, emitted during the night of 24 December 1977 in Mexico City, produced a reduction of direct solar irradiance in the morning of the next day, and in consequence, the paper strip of the CSSR started to burn later than the other days. The solar radiation unit refers to Langley·hour^{-1}, which equals to 11.63 W m^{-2}. Adapted from *Galindo and Chavez* [1978]. © Geofísica Internacional. Used with permission.

R. Jaenicke and L. Helmes developed a series of pioneering studies presenting a method to determine atmospheric turbidity from SD records [*Jaenicke and Kasten*, 1978; *Helmes and Jaenicke*, 1984, 1985, 1986]. The same method was applied some years later [*Wu et al.*, 1990; *Balling and Idso*, 1991] but, to our knowledge, has not been used since then. However, the subject has recently aroused interest, and several studies have shown the potential of SD records for detecting changes in atmospheric turbidity, especially in clear-sky conditions and mainly during sunrises and sunsets [*Horseman et al.*, 2008; *Sanchez-Lorenzo et al.*, 2009, 2013b; *Xia*, 2010; *Wang et al.*, 2012b].

This article is based upon a number of studies that consider SD to be a good proxy for turbidity, as well as aerosol content in the atmosphere. Section 4.2 provides a brief description of the different instruments and methods for measuring SD, with particular focus on the CSSR. In Section 4.3, we review a number of works that show the effect of aerosols on the measurement of SD and other studies that point towards evidences of aerosol loading in SD data. Finally, in Section 4.4, we comment upon whether or not evidence of an aerosol signal from SD measurements is real, and propose further research in this sense.

4.2. Sunshine duration measurements

In Section 4.2.1 we present a brief summary of the main devices designed to measure SD, focusing on instruments developed since the late 19th century and the automation of SD measurements over the last few decades. The major problems when measuring burn lengths on CSSR sunshine cards are presented in Section 4.2.2.

4.2.1. From the pioneering designs to the current methods

As mentioned by *Stanhill* [2003], perhaps the first sketch of a design for measuring SD can be attributed to Athanasius Kircher, [*Kircher,* 1646, page 692, reproduced by *Stanhill,* 2003]. Kircher's design, which was never manufactured, showed a device with which the sun's rays are focused by a glass sphere to ignite a bowl that is in the shape of a wooden chalice. Almost 200 years later, Thomas Brown Jordan (1807-1890) designed and manufactured the first known sunshine recorder, which was presented in 1838. The device was based on the effect of sunlight on a sensitive photographic paper controlled by a clockwork mechanism, but no systematic observations were performed due to the high cost of the instrument [*Jordan and Gaster*, 1886; *Maring*, 1897].

Subsequently, in 1853, John Francis Campbell (1821-1885) constructed a new instrument to measure the duration of the sunlight. The original design by Campbell consisted of a glass sphere filled with water set into a wooden bowl that was charred by the sun's rays focused by the sphere. Four years later, in 1857, Campbell replaced the water lens by a compact spherical glass lens [*Campbell,* 1857]. In 1879, George Gabriel Stokes (1819-1903), a professor at the University of Cambridge, suggested changes in Campbell's original design, such as substituting the bowl with a metallic spherical segment with grooves to hold the cardboard cards used to make daily measurements. This revised instrument was adopted at the Meteorological Office, and in the 1880s more than 40 meteorological stations across the British Isles were reporting measurements of SD [*Scott,* 1885], most of them using Campbell's recorder with the modifications made by Stokes. For further details on the history of the CSSR, we refer to *Sanchez-Lorenzo et al.* [2013]. Figure 4.2a displays the main parts of a current CSSR, which involve a sphere (around 10 cm in diameter) made of high-quality, uniform, transparent glass, and a rounded metal plate placed behind the sphere. The glass sphere is designed to focus the Sun´s rays onto a piece of recording paper. The metallic spherical part has three overlapping sets of grooves of different length to hold the recording cards for the winter, summer and spring/autumn periods (Figure 4.2b). The recording card should be replaced daily after sunset. Hourly and half-hourly divisions are marked across it, enabling measurement of the times of sunshine (resolution of 0.1 hours). For further details on the instrument and instructions for obtaining uniform results, see *Middleton* [1969] and *WMO* [2008].

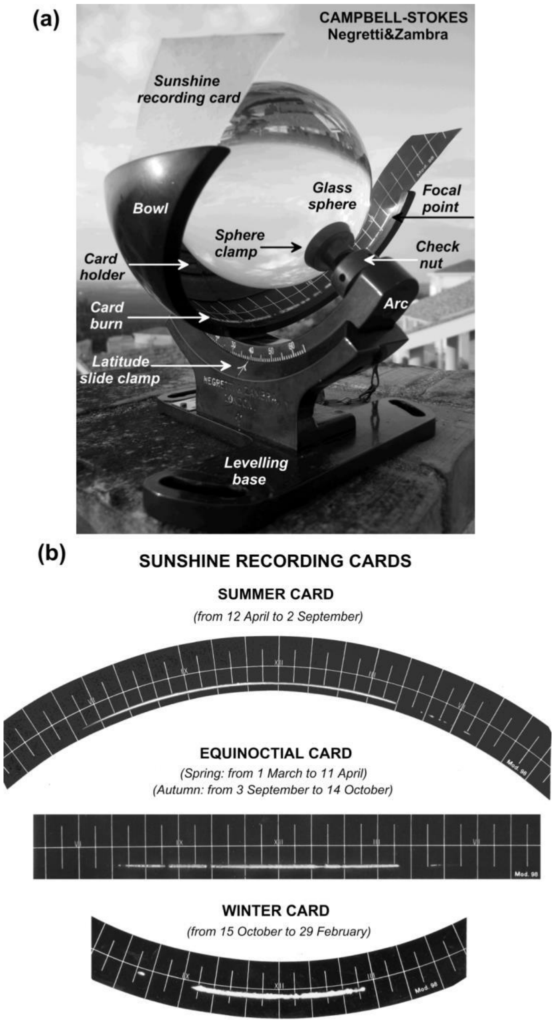
(a)
CAMPBELL-STOKES
Negretti&Zambra
Sunshine recording card
Glass sphere
Focal point
Bowl
Sphere clamp
Check nut
Card holder
Arc
Card burn
Latitude slide clamp
Levelling base
(b)
SUNSHINE RECORDING CARDS
SUMMER CARD
(from 12 April to 2 September)
EQUINOCTIAL CARD
(Spring: from 1 March to 11 April)
(Autumn: from 3 September to 14 October)
WINTER CARD
(from 15 October to 29 February)

Figure 4.2. (a) Parts of a CSSR and (b) an example of the three types of cards used during summer, winter, and equinoctial seasons, respectively.

In parallel to the development of the CSSR, during the mid-1880s James B. Jordan and Frederic Gaster improved the instrument developed by Jordan's father in the 1830s. They introduced the new photographic sunshine recorder in 1885 and subsequently, a new version of the device in 1888 [*Jordan*, 1888]. This latter instrument consisted of two hollow semicylinders used to contain the morning and the afternoon charts respectively. A hole to let the beam of sunlightenter is made in the center of the side of each semicylinder, which leaves a mark on a strip of paper sensitized with ferrocyanide. A version of the recorder, slightly modified by C.F. Marvin in 1888, was introduced into routine SD measurements at some meteorological stations run by the United States Weather Bureau [*Maring*, 1897]. The Jordan photographic recorders were gradually replaced at the beginning of the 20th century by the thermometric sunshine recorders designed by D.T. Maring and C.F. Marvin [*Brooks and Brooks*, 1947; *Stanhill and Cohen*, 2005]. The Maring-Marvin sunshine recorders were once again replaced in 1953 by new instruments based on a photoelectric switch, designed by N.B. Foster and L.W. [*Foster and Foskett*, 1953; *Michalsky*, 1992]. These, in turn, were removed from the meteorological stations in the late 1980s and early 1990s, which meant the end of the SD series in the United States.

During the last few years, various automated instruments and other methods for obtaining SD have been developed, which are summarized in *WMO* [2008]. First, we should mention the pyrheliometric and pyranometric methods [e.g., *Hinssen*, 2006; *Hinssen and Knap*, 2007; *Massen*, 2011]. The former are based on direct irradiance measurements, while the latter use global irradiance measurements. Another way of determining SD is by means of automatic instruments specifically designed to this end, which have become commercially available. These instruments are simple radiometers that detect direct solar radiation and count the time interval in which the irradiance exceeds a certain threshold. Progressively, many weather stations have changed traditional manual instruments (such as the CSSR and the Jordan photographic recorders) to these kinds of automatic sensors.

Kerr and Tabony [2004] compared SD from CSSR with automatic sensors, and found that CSSR records tend to overestimate SD because the burn on the card spreads, especially when cloud cover is broken and the sun is high in the sky. A change in the way to measure SD could therefore affect the homogeneity of the series and give rise to errors when evaluating trends [*Brázdil et al.*, 1994; *Stanhill and Cohen*, 2008]. Indeed, several studies assess the homogeneity of the SD series, such as research conducted in the Czech Republic [*Brázdil et al.*, 1994], Taiwan [*Liu et al.*, 2002], United Kingdom [*Kerr and Tabony*, 2004], Iberian Peninsula [*Guijarro*, 2007; *Sanchez-Lorenzo et al.*, 2007], Japan [*Katsuyama*, 1987; *Stanhill and Cohen*, 2008], China [*Xia*, 2010], and Switzerland [*Sanchez-Lorenzo and Wild*, 2012].

These new models of sunshine recorders do not require daily attention by an observer, data reduction (i.e., the process of filling and storing the SD data) is faster and more accurate, and routine and absolute calibration is possible [*Stanhill*, 2003]. All this appears to support the idea that automatic sensors will gradually replace the traditional instruments, but due to the additional information that can be extracted from burnt cards and their possible contribution to understanding climate change, there is a consensus with regard to preserving such instruments at long-established, well-maintained and freely exposed meteorological stations [*Stanhill*, 2003; *Wood and Harrison*, 2011; *Sanchez-Lorenzo et al.*, 2013b].

4.2.2. Variability of the burning thresholds

Differences between one type and another of SD measurements might be attributed to their particular characteristics and limitations. The two major problems with CSSR when comparing their measurements with other methods or instruments lie in the variability of the level of direct irradiance, which produces a burn and the overburning of the card in conditions of intermittent high irradiance [*Stanhill*, 2003]. These difficulties can be added to the obvious element of subjectivity in measuring the burn length on the sunshine cards [*Guijarro,* 2007].

The problem of overburning is very difficult to evaluate as one small burst of high direct irradiance causes a burn lasting far longer than the few seconds of its actual duration, and standard methods have therefore been proposed to take into account this fact when evaluating the burn lengths [*WMO*, 2008]. Despite these rules, during events of very broken cloudiness, a measurement of SD by means of CSSR can be significantly overestimated [*Painter*, 1981; *Kerr and Tabony,* 2004].

Regarding the first problem, the direct irradiance value that produces burning ("burning threshold") is usually considered constant, i.e. 120 W m^{-2} [*Gueymard*, 1993; *WMO*, 2008]. Nevertheless, *Jaenicke and Kasten* [1978] showed a large variety of burning thresholds for different CSSR. Similarly, *Helmes and Jaenicke* [1984] described the effects of using different types of recording cards. *Brázdil et al.* [1994] stressed the importance of using the same type of card in order to compare different SD series.

In order to homogenize the worldwide network, a specific design of the CSSR was recommended as the reference [*WMO*, 1962]. This, however, did not overcome all the problems. For example, *Bider* [1958] and *Painter* [1981] had observed that the burning threshold is on average higher in the early morning than in the late evening, thus producing notable losses of records, hypothetically attributed to dew or other water deposits on the glass sphere since more energy is required to burn a trace in the card when conditions are cold and damp than when these are warm and dry. Equally, absorption of water by the card can also affect the burning threshold. *Painter* [1981] also found that the burning threshold showed a marked seasonal effect; i.e., the burning threshold is higher in winter than in summer as a result of generally lower temperatures and higher relative humidity. Therefore, if global or direct radiation are to be estimated from SD records with the use of Ångström-Prescott type expressions, at the very least we need to become aware of the limitations of the CSSR, in particular the burning threshold issue, and, where possible, we must address and correct them [*Roldán et al.*, 2005]. This issue should also be taken into account on considering the possibility of using SD records as a proxy for aerosol loading.

4.3. Evidence of aerosol/turbidity effects on sunshine duration measurements

In this section, we have reviewed empirical investigations dealing with the direct effects of aerosol on SD. These studies suggest methods for estimating atmospheric turbidity (Section 4.3.1). In addition, we have also considered studies relating SD with meteorological and radiometric variables (clouds, global, direct and diffuse irradiance, wind speed and relative humidity) where aerosols are suggested as an intervening factor (Section 4.3.2).

4.3.1. Assessing turbidity from CSSR cards

Few articles focus on estimating the effect of aerosols in SD. Jaenicke, Kasten, and Helmes were the first authors to show interest in this sense. They proposed a method for quantifying atmospheric turbidity by means of data obtained from the readings of CSSR [*Jaenicke and Kasten*, 1978; *Helmes and Jaenicke*, 1984]. They based their arguments on the assumption that in the case of cloudless sunrises and sunsets, solar radiation is weakened because of the longer path it follows through the atmosphere. This weakening may such that the threshold value is not reached and therefore no trace is burnt on the card even if the sun is visible. Their method is based on the Linke factor, T_L, which represents the number of clean and dry atmospheres that would be necessary to produce the same attenuation of the extraterrestrial radiation produced by the real atmosphere. T_L can be derived from the measured direct normal irradiance over the whole solar spectrum DSI [*Linke*, 1922]:

$$T_L = \frac{1}{m_A \delta_{CD}} \ln\left(\frac{I_0}{DSI}\right) \qquad \text{(Eq. 4.1)}$$

where I_0 is extraterrestrial solar irradiance; δ_{CD} is the optical thickness of the clean dry atmosphere; and m_A the relative optical air mass. Then, from a CSSR cardboard, T_L can be approximated by the linear function (valid for solar elevation angles above 5°) [*Jaenicke and Kasten*, 1978]:

$$T_L = (0.154\varphi + 1.05) \ln\left(\frac{I_0}{DSI_{CS}}\right) \qquad \text{(Eq. 4.2)}$$

where φ is the solar elevation angle, calculated for the beginning or end of the burnt trace, and DSI_{CS} is the threshold value of the recorder. Equation (4.2) enables computation of the turbidity factor T_L from the solar elevation φ when burn starts, measured by any given SD recorder with known threshold irradiance DSI_{CS}. Experiments performed by *Jaenicke and Kasten* [1978] and *Helmes and Jaenicke* [1984] showed that Eq. (4.2) can be successfully used for SD data in cases of cloudless sunrises and sunsets (Figure 4.3).

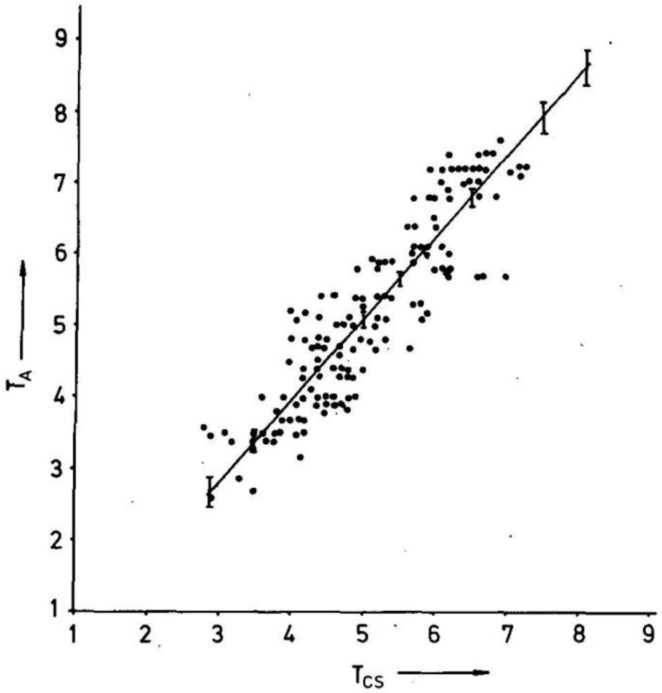

Figure 4.3. Turbidity Linke factor, T_A, determined with a pyrheliometer as a function of that computed with the burned trace method by Helmes and Jaenicke (1984), T_{CS}, which is calculated using the individual threshold values DSI_{CS} for each type of the card determined by comparison with pyrheliometer. Similar results are obtained using a fixed value of DSI_{CS} = 20 $mWcm^{-2}$ for all cards. From *Helmes and Jaenicke* [1984]. © American Meteorological Society. Used with permission.

Nevertheless, few sites provide information on cloudiness during sunrise and sunset, and therefore only few SD data can be used if cloudless conditions are to be guaranteed. Consequently, Helmes and Jaenicke developed another method for estimating atmospheric turbidity without requiring the condition of a cloudless sky [*Helmes and Jaenicke*, 1985, 1986]:

$$TCC + SD + T = 100\% \qquad \text{(Eq. 4.3)}$$

where TCC was defined as mean daily cloud cover in % of sky area; SD as sunshine duration in % of the astronomically possible; and T as mean daily turbidity in % as equivalent SD per astronomically possible SD [see *Helmes and Jaenicke*, 1985, 1986]. They found that the overall sum usually exceeded 100%, even if only TCC and SD were considered. They attributed this to an overestimation of cloud cover by most observers [e.g., *Karl and Steuer*, 1990; *Jones and Henderson-Sellers*, 1991]. In order to overcome this issue, *Helmes and Jaenicke* [1986] proposed the following modification:

$$TCC + SD + T\frac{100-TCC}{100} = f(TCC) \qquad \text{(Eq. 4.4)}$$

where atmospheric turbidity is weighted by a factor that depends on TCC in such a way that it ranges from one for cloudless days to zero for totally overcast days. The summation of the left-hand side terms is approximated by a linear function *f* (TCC) which is empirically derived.

Thus, availing of daily data of TCC and SD, a value for daily atmospheric turbidity can be obtained even for cloudy days, with similar results as when only cloudless days are used. Although these methods are simple and give us an idea of the atmospheric turbidity, they pose the major problem that the turbidity index is affected not only by aerosols but also by water vapor.

The development of new, more precise instruments (pyrheliometers, narrowband photometers, etc.), more remote sensing studies and the evolution of other methods have all caused discontinuity in the studies initiated by Jaenicke, Helmes, and their colleagues. Nevertheless, their methods have the advantage of being based on data which have been available for over 100 years; this justifies these methods for estimating atmospheric turbidity from SD in several studies. For instance, *Wu et al.* [1990] and *Balling and Idso* [1991], who were interested in volcanic material in the stratosphere, represented the variation of atmospheric turbidity obtained from sunshine records for Sonnblick (Austria) during the 20th century. Using this station at high altitudes and far from cities, where boundary layer aerosols are unlikely to dominate the record, they found a clear decrease in stratospheric sulfate aerosols from the 1900s to the mid-1980s.

Horseman et al. [2008] assumed that high, thin cirrus clouds, and aerosols, only reduce SD at low solar elevations when incident direct solar radiation would not be much higher than 120 W m^{-2}. Therefore, *Horseman et al.* [2008] described a method for extracting SD for cloudless periods at sunrise and sunset in order to track changes in pollution, using the cards of a CSSR from Lancashire (U.K.) during the 1976-2006 period. Unlike the method proposed by *Jaenicke and Kasten* [1978], this method is not a quantitative estimate of atmospheric turbidity; it does, however, provides a useful time series that can be interpreted in terms of changes of atmospheric opacity/pollution on daily basis. The method was proposed to test whether bright sunshine records at progressively lower solar elevation angles, corresponding to progressively longer path-lengths, indicate progressively lower amounts of sunshine. This involves splitting the daily record of low-elevation SD (solar elevation between 2 and 8 degrees) into a series of time subdivisions associated with increasing path-lengths of sunlight through the atmosphere, and measuring an "efficiency of burn" in each of these sub-divisions (three for winter and two for summer). Moreover, *Horseman et al.* [2008] divided the results into winter and summer periods because the origins of particulate air pollution could differ: more pollution caused by space-heating-related emissions and more generated by photochemical processes occur during winter and summer, respectively. The results of the efficiency of burn at these pollution-sensitive angles showed an increase from the late 1980s to the early 2000s which is in line with the widespread brightening found by *Wild et al*. [2005]. This brightening was more significant during winter than summer, which they related to a greater decrease in space-heating-related emissions than in photochemical pollution. Another interesting result involved the asymmetry of the daily burns between sunrise and sunset, which can be partly explained by the blocking of the morning horizon by topographic elevations, but may also be due in part to natural weather phenomena such as morning mist [*Bider*, 1958; *Painter*, 1981]. The current installation protocol for the sunshine recorders anticipates that no significant burns will be recorded below an elevation of 3º, but the results of *Horseman et al.* [2008] suggested that, although this assumption may have been true for most of the last century, there is now an increase in the number of the days when burns occur below a 2° elevation, associated with a decrease in pollution (Figure 4.4).

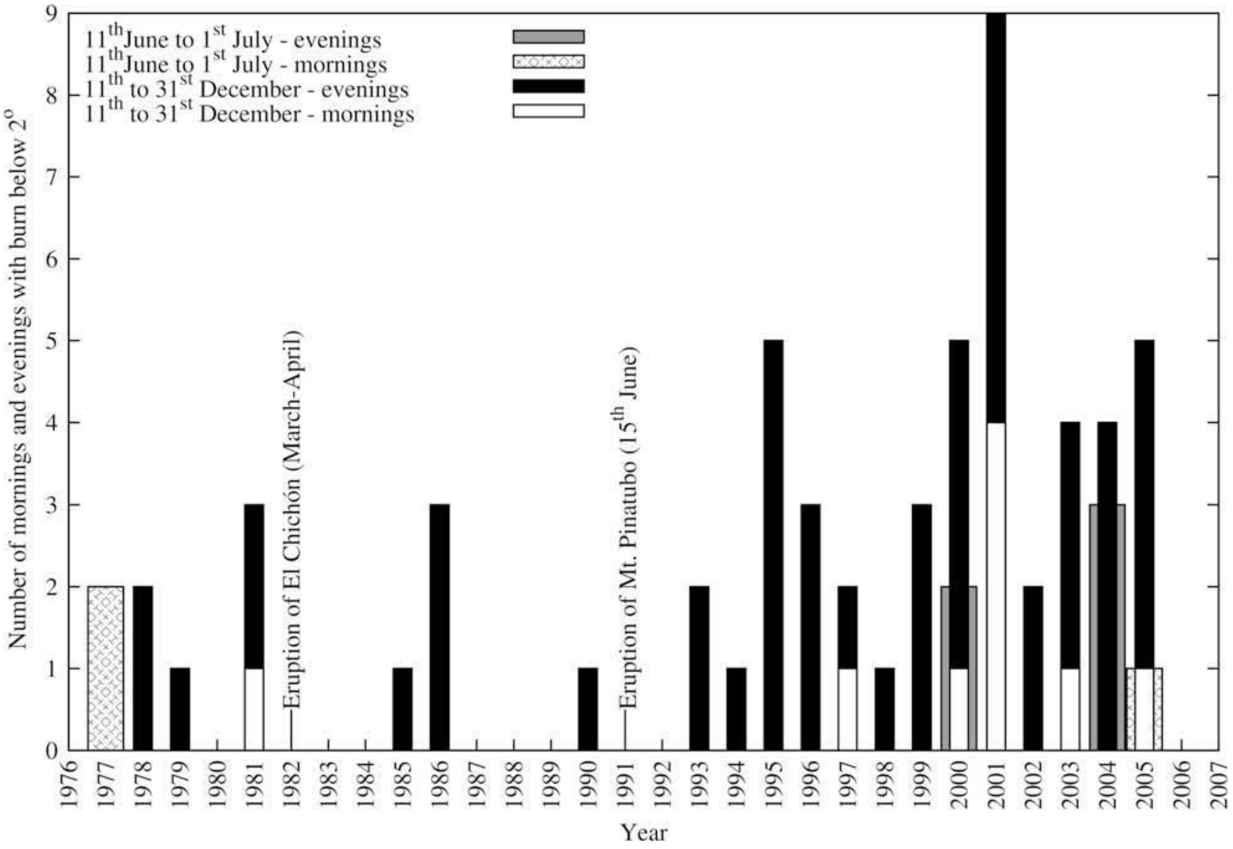

Figure 4.4. Counts of mornings and evenings within the analyzed solstice periods when burn(s) below 2° solar elevation was/were observed in each year. The totals are grouped into summer and winter. Note that after the early 1990s, there was an increase in the number of mornings and evenings per year when bright sunshine was recorded at sub-2º elevations. Note also that most of the increase was contributed by the winter period. From *Horseman et al.* [2008]. © Elsevier. Used with permission.

4.3.2. Aerosol effects on SD variability and trends

In the last two decades many papers have addressed the variability in SD, the trends thereof and the possible causes of these. These studies used long-term SD series obtained from different sites throughout the world as summarized by *Sanchez-Lorenzo et al.* [2007]. As with long-term measurements of downward shortwave radiation, most of the above mentioned studies found a widespread decrease in SD between the 1950s and 1980s, i.e., the “global dimming” period. Equally, most of these studies also showed a partial recovery of SD since the 1980s, i.e., the “brightening” period. The impacts of the El Chichón (April 1982) and Pinatubo (June 1991) volcanic eruptions are also evident in some of the SD series, which present clear minima during 1982-1983 and 1992-1993 periods, hypothetically due to the impact of the big increase in sulfate aerosols in the lower stratosphere which reduces incoming solar radiation [e.g., *Sanchez-Lorenzo et al.*, 2009; *Sanroma et al.*, 2010; *Sanchez-Lorenzo and Wild*, 2012]. Despite the fact that cloudiness is the most important factor affecting SD, some research detects the aerosol signal by combining simultaneous time series of cloudiness and SD. Other studies claim that the effect of aerosols can also be detected by comparing solar radiation series with SD series. These studies therefore point to a detectable direct effect of aerosols on SD [*Stanhill and Cohen*, 2001; *Stanhill*, 2005; *Wild*, 2009]. Table 4.1 shows an overview of these papers and also gives a rough idea of the role the authors attributed to atmospheric aerosols. The reviewed publications summarized in Table 4.1 are detailed below.

AUTHOR	SITE	STATIONS	PERIOD	TIME BASIS(b)	SD INSTRUMENT(c)	DISCREPANCY(d)	SD(e)	TCC	LCC	GSI	Diff	DSI	AEROSOLS? (f)
Morawska-Horawska, 1985	Cracow (Poland)	1	1861-1980	A	CSSR	1950s-1980s	— —	— —					D.E.
Kaiser, 2001	China	200	1954-1998	S, A	CSSR	1950s-1990s	— —	— —					D.E.
Zheng et al, 2008	Southwest China	184	1961-2005	A	Jordan	1960s-2000s	— —	=					D.E.
Sanchez-Lorenzo et al, 2009	Iberian Peninsula	69	1961-2004	S, A	CSSR	1960s-1980s	— —	=					D.E.
Jaswal, 2009	India	40	1970-2006	S, A	CSSR	1970s-2000s	— —	=					D.E.
Sanchez-Lorenzo and Wild, 2012	Switzerland	17	1930-2010	S, A	CSSR	1980s-2000s	+ +	=					D.E.
Wang et al, 2013	China	84	1955-2011	S, A	CSSR	1950s-2000s	— —	=					D.E.
Zheng et al, 2011	Southwest China	184	1961-2005	Annual	Jord	1960s-2000s	— —	=					D.E.
Kaiser and Qian, 2002	China	200	1954-1998	Annual	Jord	1950s-1990s	— —	— —					D.E.
Changnon, 1981	Midwestern EE.UU	36	1901-1977	S, A	CSSR	1960s-1970s	—	+ +					D.E. and I.E.
Kitsara et al, 2013	Athens (Greece)	1	1951-2001	S, A	CSSR	1980s-2000s	+ +	+ +					D.E.
Li et al, 2011	South China	147	1961-2005	Annual	CSSR	1960s-1990s	— —	— —	+ +				D.E. and I.E.
Xia, 2010	China	618	1955-2005	S, A	Jord and CSSR	1950s-1980s	— —	— —	+ +				D.E. and I.E.
You et al, 2010	Tibetan Plateau	71	1961-2005	S, A	?	1980s-2000s	— —	— —	+ +				D.E. and I.E.
Brunetti et al, 2009	Alpine Region	242	1886-2005	S, A	CSSR	1900s-1950s	+ +	+ +					NO
Plantico et al, 1990	EE.UU	94	1900-1987	S, A	Jord, M-M, Fost	1900s-1950s	—	+ +					NO
Liu et al, 2002	Taiwan (China)	25	1898-1999	S, A	CSSR, Jord, Eko	1960s-1990s	— —	=					NO
Yang et al, 2012	Tibetan Plateau	78	1984-2006	S, A	?	1980s-2000s	— —	— —					NO
Power, 2003b	Germany	13	1977-2000	Annual	CSSR	1970s-1990s	=			+ +	— —	+ +	D.E.
Zhang et al, 2004	Eastern China	3	1961-2000	Annual	?	1960s-1990s	—			— —	+	— —	D.E.
Che et al, 2005	China	64	1961-2000	Annual	?	1960s-1990s	—			— —	+	— —	D.E.
Stanhill and Kalma, 1995	Hong Kong (China)	1	1958-1992	Annual	?	1960s-1990s	—	=		— —			D.E. and I.E.
Stanhill and Cohen, 2005	EE.UU	106	1961-1990	Annual	Jord, M-M, Fost	1960s-1990s	=			— —			NO
Cutforth and Judiesch, 2007	Canada	7	1957-2005	S, A	CSSR	1950s-1990s	=			— —			NO
Liang and Xia, 2005	China	192	1961-2000	S, A	CSSR	1970s-1990s	— —	— —		— —		— —	D.E. and I.E.
Soni et al, 2012	India	12	1971-2005	Annual	CSSR	1970s-1990s	— —	— —	— —	— —			D.E. and I.E.
Qian et al, 2006	China	537	1955-2000	Annual	?	1970s-1990s	— —	— —	— —	— —			D.E. and I.E.
Liepert and Kukla, 1997	Germany	8	1964-1990	Annual	CSSR	1960s-1990s	=	=		— —			D.E. and I.E.
Stanhill, 1998a	Ireland	8	1955-1995	S, A	CSSR	1960s-1990s	— —	=		— —	— —		D.E. and I.E.

Table 4.1 (previous page). Summary of works that find discrepancies between trends of SD and trends of cloud cover and/or surface solar radiation[a]. The columns of SD, TCC, LCC, GSI (global solar irradiance), DIF (diffuse solar irradiance), and DSI (direct solar irradiance) refers to trends of these variables.

[a] The suggested role of aerosols in each case is also shown.
[b] S and A refers to Seasonal and Annual, respectively.
[c] Campbell–Stokes sunshine recorder (CSSR), Maring–Marvin thermometric recorder (M-M), Foster photoelectric Sun switch sunshine recorder (Fost), Jordan photographic recorder (Jord), and Eko sunshine duration sensor (Eko).
[d] Within the study period, the subperiod showing discrepancies between trends of SD and trends of clouds and/or solar radiation.
[e] Symbols indicate different degrees of trend in each case: nonsignificant (=), large positive (+ +), positive (+), large negative (— —), and negative (—).
[f] Discrepancies are attributed to the direct effect of aerosols (DE) and/or the indirect effect of aerosols (IE). Discrepancies are explained without the introduction of aerosols (NO).

Since long-term series of SD and total cloud cover (TCC) are widely available, the relationships between both variables have been studied since the early 20th century. The two quantities are considered to be mutually complementary (see Section 4.3.1): an increase (decrease) in TCC is generally accompanied by a decrease (increase) in SD [see for example the high correlation between SD and cloud cover at 1165 stations worldwide, in Figure 10 of *Wang et al.*, 2012a]. Therefore, a large literature record relating these two magnitudes and studying their annual, seasonal and monthly evolution is available [e.g., *Fox*, 1961; *Jones and Henderson-Sellers*, 1991; *Angell et al.*, 1984; *Angell*, 1990; *Weber*, 1990; *Pallé and Butler*, 2001]. But this relationship is not always simple and linear, and can be affected by several factors, such as changes in atmospheric transparency resulting from aerosols or changes in the properties of clouds.

The present paper specifically addresses studies that have demonstrated inconsistencies between trends of TCC and SD. For instance, a decrease (increase) in SD is not always accompanied by an increase (decrease) in TCC (Figure 4.5); this fact was revealed by several authors [*Morawska-Horawska*, 1985; *Kaiser*, 2001; *Zheng et al.*, 2008; *Jaswal*, 2009; *Sanchez-Lorenzo et al.*, 2009;

Sanchez-Lorenzo and Wild, 2012; *Kitsara et al.*, 2013; *Wang et al.*, 2013]. Most of these studies have proposed, as one important cause of decreases or increases in SD, an increase or decrease in emissions of carbon and sulfur compounds that scatter and absorb radiation, thus increasing (or decreasing) the turbidity of the atmosphere. *Zheng et al.* [2011] took a step forward: they found a significant declining trend in SD over South China with a non-significant trend in TCC and water vapor, while visibility (used as a proxy of aerosol concentration) exhibited a significant downward trend. They concluded that the decrease in SD was partially due to the enhanced aerosol loading resulting from anthropogenic activities. Equally, *Kaiser and Qian* [2002] found that a large portion of southeastern China, the region presenting the largest decrease in SD across this country, showed the biggest increases in aerosol extinction coefficient during the 1954-1998 period. Since a downward trend in TCC was also identified [*Kaiser*, 2000; *Xia*, 2013], the increase in aerosol extinction appears to support the theory that aerosol loading plays a major role in decreasing SD.

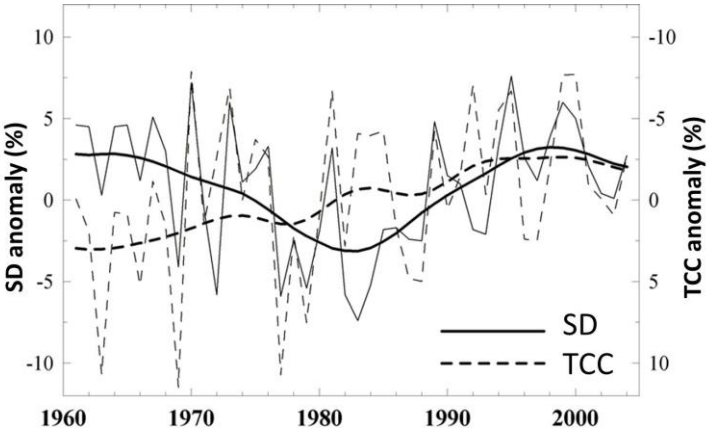

Figure 4.5. Thin lines represent the annual evolution of both sunshine duration (solid lines, labeled as SD) and total cloud cover (dashed lines, labeled as TCC; note the reversed axis) series for the whole Iberian Peninsula during the period 1961-2004. Thick lines are the smoothed (11 year averaging) evolution. Note that there is a clear disagreement between both series, especially from the 1960s to the mid-1980s. Adapted from *Sanchez-Lorenzo et al.* [2009].

Wang et al. [2012b] hypothesized that the SD trend in China was affected by TCC, precipitation and aerosols (quantified through the air pollution index, API). To isolate the impact of air pollution on SD, *Wang et al.* [2012b] selected clear-days (i.e., days with 0 mm of precipitation and TCC ≤ 10%) and grouped them into two categories: API ≤ 80 (low-medium aerosol loading) and API > 80 (high aerosol loading). They concluded that aerosols negatively affect SD in China (Figure 4.6). *Wang et al.* [2012a], analyzing data from more than 1100 stations over the world and filtering the cloud contribution, observed that approximately 58% percent of all stations had a correlation coefficient greater than 0.5 between SD and the aerosol optical depth (AOD) for a period of time from the 1980s to the 2000s (AOD is estimated by visibility data, supplemented with satellite data). They also found that some sites showed a low or even negative correlation. At these stations, cloud variability was the determining factor of long-term variation in SD.

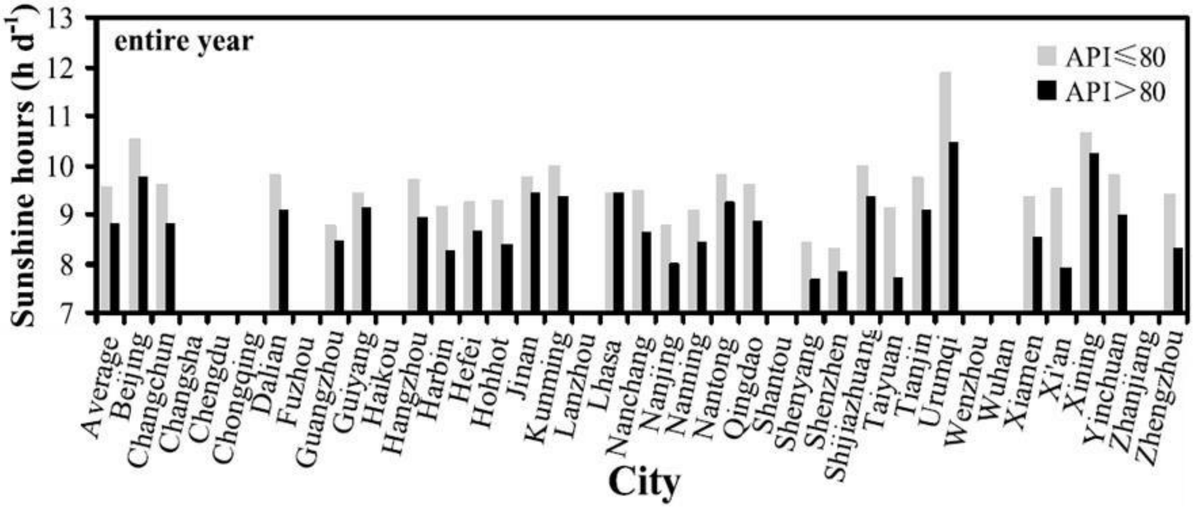

Figure 4.6. Average daily sunshine hours under conditions with low-medium aerosol loading (air pollution index ≤ 80) and high aerosol loading (API > 80) across China for the 2001-2005 period. Note that the plots are only for clear-sky conditions (i.e. days with 0 mm precipitation and total cloud cover ≤ 10%) and that SD is shorter at times of higher API (high aerosol loading). From *Wang et al.* [2012b].

SD trends can be better explained by trends of low cloud cover (LCC) than by TCC, as high clouds are more transparent than low and medium ones. For example, *Li et al.* [2011] and *Xia* [2010] found a significant increase in LCC combined with decreases in SD and TCC in China, as well as a higher LCC correlation with SD than with TCC. Both the trends and the correlation coefficients therefore suggest that LCC is the main factor of decreasing SD in their study area. Nevertheless, *Li et al.* [2011] also found a significant correlation between SD and visibility (used as a proxy of aerosol concentration), suggesting a link between SD and aerosols in their study area. *You et al.* [2010] obtained similar results on the Tibetan Plateau; i.e., SD has a significant correlation with LCC and a non-significant correlation with TCC. *Xu et al.* [2006] studied the annual variation trend in SD and LCC in Beijing city and its metropolitan area, and found that the decline in SD and the increase in LCC are more abrupt in the south peripheral area, where the highest concentration of aerosols occurs. The same behavior was found by *Shi et al.* [2008]who detected areas in Southeastern China where AOD derived from TOMS measurements correlated positively with LCC and negatively with SD. In summary, a decrease in SD appears to be related to the increase detected in LCC. On the other hand, LCC changes can be also linked to indirect aerosol effects.

Some studies do not consider aerosol changes on attempting to explain discrepancies between cloudiness and SD series. *Brunetti et al.* [2009] found significant disagreements in long-term trends of SD and TCC in some subregions of the Greater Alpine Region, but air pollution could not justify the same sign in the TCC and SD, as those subregions were less affected by air pollution. By way of an explanation, *Brunetti et al.* [2009] proposed a poor station density in the above mentioned subregions. *Plantico et al.* [1990] questioned the homogeneity of the long-term cloud and sunshine records, rather than attributing cloud/sunshine discrepancies to physical factors. Moreover, *Liu et al.* [2002], attempting to explain the observed ~15% reduction in SD in Taiwan from 1960 to 1990, found no significant trend in TCC. They attributed this discrepancy to the subjective nature and the well-known great uncertainty of cloud observations in the detection of trends in the order of 10% (similar to the reduction of SD). Finally, *Yang et al.* [2012] found a decreasing trend of both SD and TCC over the Tibetan Plateau. In light of this paradox, they initially suggested the increase in aerosol loading as a possible cause of the solar dimming over this area [*You et al.,* 2013], but they found that it was not sufficient to explain it. Instead, they proposed that the decrease in SD was mainly due to an increase in water vapor amount and greater cloud cover (due to low air density and strong surface heating), and that there was no need to introduce aerosols.

Trends in solar radiation can also be directly related to SD trends. Based on physical principles, an increase (decrease) in SD must reflect increases (decreases) in direct (DSI) and global (GSI) radiation and decreases (increases) in diffuse radiation. This means that high positive correlations are to be expected between SD and direct and global irradiation. Some studies explore deviations from these good correlations and attribute the inconsistencies to changes in aerosols.

For example, *Zhang et al.* [2004] and *Che et al.* [2005] found a decrease in SD in China, but with a lower rate than the reduction of GSI and DSI. Air pollution was suggested to be the possible cause of these decreases, as it absorbs and scatters solar radiation. According to *Stanhill and Kalma* [1995], the fact that the rate of decrease in SD was lower than the rate of decrease in GSI and DSI indicates that long-term increases in aerosols induce a more significant reduction in the intensity of solar radiation than in its duration.

Furthermore, some articles do not find SD trends, despite the existence of GSI or DSI trends. For some stations in Germany, *Power* [2003] found a non-significant trend in SD, while the long-term decreases in aerosols were the most likely cause of the observed increases in GSI and DSI and the decreases in diffuse radiation. Similarly, *Stanhill and Cohen* [2005] and *Cutforth and Judiesch* [2007] found no long-term SD trend but rather a significant reduction of GSI during the last 50 years of the 20th century in the United States and on the Canadian Prairie, respectively. They attribute this discrepancy to the different sensitivity of SD and GSI measurements to diurnal changes in cloud cover, and to the influence of other variables such as humidity, without needing to introduce aerosols. For example, an increase in midday cloud cover and air humidity would reduce annual values of GSI, without necessarily affecting SD, whereas the same increases occurring during the morning or evening hours would have the opposite effect. Moreover, *Stanhill and Cohen* [2008] found that the long series of atmospheric turbidity measurements available (used as an index of aerosol content) showed no long-term changes to explain the increase in GSI and SD in Japan, and they proposed that the most likely cause was the change in TCC, however, cloud data were unavailable. Thus, *Stanhill and Cohen* [2008] concluded that the causes of the increase in SD and GSI could not be established unequivocally, given the lack of TCC data.

Meanwhile, *Cohen and Kleiman* [2005] studied DSI and SD series in Jerusalem under stable synoptic summer conditions, which were characterized by negligible cloudiness during most hours of the day, and found a significant decrease in SD and DSI. Studying hourly SD data, they concluded that in the evening the sun cannot be seen with the naked eye before the calculated sunset, whereas the appearance of the sun came after the previously calculated sunrise. Thus, the length of the day has apparently become shorter during recent decades, due to a hypothetical increase in aerosol anthropogenic emissions. Previously, *Aksoy* [1999] had found the same effect in Ankara around sunset and sunrise as. In particular, he detected decreases in SD in each hour of the day that cannot be fully explained by changes in cloudiness, the longest reductions being at sunrise and sunset, i.e., at low solar elevation. Unlike *Cohen and Kleiman* [2005], who associated this change in SD with aerosol loading, Aksoy attributed the trend in SD to the trend in relative humidity, which causes changes in the burning threshold and consequently, reduces the hours of SD from sunrise to sunset. However, Aksoy also suggested that the weaker correlations between SD and relative humidity during the winter months may have arisen from aerosol anthropogenic emissions, which show an increase in the winter months.

Thus, both solar radiation and cloudiness data are required to obtain robust results on how aerosols affect long-term SD trends. *Liang and Xia* [2005] observed decreasing trends in SD, TCC, GSI and DSI over much of China. As trends in cloud amount and solar radiation were negative and quite similar, cloud amount was not the cause of the decrease in solar radiation. They suggested aerosol loading as the principal cause of the observed decline, due to the rapid increase therein as was revealed by means of visibility data. *Qian et al.* [2006] and *Soni et al.* [2012] observed that some stations in China and India, respectively, presented a decline in GSI, SD and TCC and also in LCC, so cloud cover changes could not serve as a "universal" explanation of solar dimming; they concluded that changes in the amount and optical properties of anthropogenic aerosols, as well as cloud properties, are the most probable causes of the reduction in surface solar radiation and, consequently, in SD. It is important to remark that the interactions between aerosols and cloud formation hinder complete separation of their effects on radiation and SD [e.g., *Rebetez and Beniston*, 1998; *Sanroma et al.*, 2010], since aerosols may either enhance [*Albrecht*, 1989] or inhibit [*Ackerman et al.*, 2000] cloud formation. For example, *Liu et al.* [2002] found that differences between the reductions of SD in urban centers and those of rural areas were substantially smaller than the differences in observed aerosol optical depths among those stations, so *Liu et al.* [2002] suggested that direct scattering by aerosols is not the major cause of the reductions in SD. Indeed, *Stanhill and Kalma* [1995] and *Liepert and Kukla* [1997] had already noted the importance of the effect of aerosol loading on cloud optical depth and on cloud type. *Stanhill* [1998b] could not explain the reduction in irradiance and SD at Valentia (Ireland), as it cannot be attributed to changes in TCC, and he concluded that more investigation was required on variation in cloud cover transmissivity associated with cloud type and/or aerosol load.

Some other authors have analyzed the effect of other meteorological variables on SD measurements. Firstly, *Oguz et al.* [2003], *Yang et al.* [2009a, 2009b], *Zongxing et al.* [2012] and *Wang et al.* [2012b] found that wind significantly influences aerosol loading and, in consequence, SD: on days with strong winds, the aerosol loading was lower than on days dominated by weak wind. Wind direction is also important because winds coming from deserts (dust winds), sea, or industrialized zones could increase aerosol loading and, thus, negatively influence SD. Secondly, atmospheric water vapor absorbs solar radiation in some bands, and thus can affect SD, as DSI could fall below the threshold level [*Oguz et al.*, 2003; *Yang et al.*, 2009b; *You et al.*, 2010]. For example, *Van Beelen and Van Delden* [2012] found an increase in SD and a decrease in relative humidity (which can be related to the columnar water vapor content in the atmosphere) in the Netherlands. Thus, the decline in humidity might have contributed to the clearing of the atmosphere, causing an increase in SD. A statistically negative correlation between SD and relative humidity was found by *Zongxing et al.* [2012], reflecting the significant influence of humidity on SD: increased (decreased) water vapor decreases (increases) received solar radiation. Finally, *Qian et al.* [2007] commented that a decrease in relative humidity may affect SD positively through reduced absorption and via the aerosol hygroscopic effect (i.e. particles take up water when relative humidity is high, increasing their diameters and changing their radiative properties [*Tang*, 1996; *Baynard et al.*, 2006]).

4.4. Conclusions and future perspectives

In the present paper we have reviewed studies addressing the possibility that SD measurements can be used to detect changes in atmospheric turbidity. According to the reviewed literature, there is evidence that SD records contain signals of the direct effects of aerosols on the solar beam and, in consequence, SD records can be used as proxy for studying aerosol trends and their radiative forcing. This finding may be crucial in the study of the dimming/brightening phenomenon and its causes.

If the direct effect of atmospheric aerosols on SD records is to be determined, the effects of cloudiness should be previously removed from SD measurements. Despite the fact that aerosol modifies cloud amount and properties, this indirect effect is difficult to quantify by means of SD data. Therefore, the aerosol direct effect has been the only one considered by researchers when quantifying the signal of aerosols with SD data.

Studies showing links between changes in SD and aerosols do not focus upon proving and quantifying the causal relationship. Indeed, the signal of aerosols on SD records is weak and instruments that measure SD present certain limitations. Moreover, changes in the way of measuring SD affect the homogeneity of the series and lead to errors when evaluating their trends. Moreover, water vapor in the atmosphere is important for two main reasons: firstly, apart from absorption of solar radiation by the vapor itself, as aerosols are normally hygroscopic, changes in humidity might contribute to the clearing/unclearing of the atmosphere, influencing SD measurements; secondly, the burning threshold of Campbell-Stokes sunshine recorders (CSSR) may be affected by relative humidity through modification of cardboard burning properties.

Despite all these difficulties, there is a need for further study of SD records, because a new method for determining information on aerosols prior to the 1980s would be very useful and would help us to understand the impact of aerosols on climate. For this reason, some authors have attempted to quantify the direct effect of aerosols on SD data. As pointed out by *Jaenicke and Kasten* [1978], *Helmes and Jaenicke* [1984, 1985, 1986] and *Horseman et al.* [2008], SD recorders do not differentiate a small change in direct solar radiation when it is well above the burning threshold. Therefore, the impact of aerosols on SD occurs particularly just after sunrise and before sunset because of the long distances that the direct beam travels to reach the earth's surface, so being much more affected by the presence of aerosols. These methods are simple but give only a coarse estimation of atmospheric turbidity, and pose the major problem of being affected not only by aerosols but also by water vapor.

Thus, the magnitude of the effect of aerosols on SD is a complex issue, but detailed studies of the burn (in particular during cloudless sunrises and sunsets) provides the possibility to determine variations in turbidity for both short and long time scales, and therefore, to assess the possible influence of human activities on the Earth radiation budget, with the resulting climatological implications.

Finally, we suggest some further research for further study of the suitability of SD records to detect changes in atmospheric turbidity and aerosols:

- In order to identify the impact of aerosol on SD records other variables such as cloud cover and visibility are recommended, especially data available at shorter time scales (e.g., daily or hourly), which can help to confirm the effect of aerosols on SD.
- To extract information on the trends of aerosol loading, a seasonal or monthly basis is more recommendable that an annual one because the origins of particulate air pollution can vary along the year. For example, in developed countries, more pollution is usually caused by space-heating-related emissions during winter, whereas photochemical processes dominate during summer.
- The method described by *Horseman et al.* [2008], which involves extracting sunshine amounts at low-elevation angles from cloudless sunrises and sunsets in order to track changes in pollution, could be improved by using measures of width of burn in CSSR cards [e.g., *Wright*, 1935; *Lally*, 2008; *Horseman et al.*, 2013], as this provides a way to create a time series of solar irradiance and atmospheric aerosol loading metrics reaching back over 120 years from the present day. Long-term records of SD cards are available at some historical meteorological stations, such as the Blue Hill Observatory in Milton, Massachusetts (US) where CSSR cards have been stored since the mid-1880s (Mike Iacono, personal communication). However, when these methodologies have been validated, they could be applied to long-term series of SD data without analysis of the original burnt cards. A limited number of sites with few years of burnt cards would be sufficient for the validation.

In conclusion, when the threshold drifts inherent to sunshine recorders have been well characterized, and when the length and widths of the burning can be determined in an objective manner, with the use of automated digital image processing techniques, we will likely be able to evaluate the historical aerosol content from SD records, which should be validated by comparing these estimates with atmospheric aerosol concentration derived from surface or satellite observations.

PART II.

RESULTS

Chapter 5.

Characterization of CSSR and derivation of direct solar irradiance from burn width

This chapter is transcription of the paper:

Sanchez-Romero, A., González, J.A., Calbó, J., and Sanchez-Lorenzo, A. (2015), Using digital image processing to characterize the Campbell–Stokes sunshine recorder and to derive high-temporal resolution direct solar irradiance. *Atmos. Meas. Tech.*, 8, 183-194, doi:10.5194/amt-8-183-2015.

The paper deals with developing a practical method in order to obtain burn width of CSSR cards at high temporal resolution, as well as with studying the relationship between the burn width and DSI. The method is based on image processing of digital scanned images and offers a practical way to exploit long-term sets of CSSR cards to create long time series of DSI.

5.1. Introduction

SD is a useful indicator of the amount of solar radiation arriving on the earth and a key variable for various sectors, including tourism, public health, agriculture, and energy. According to the WMO, the SD for a given period is defined as the total time length of those sub-periods for which the direct solar irradiance exceeds 120 W m^{-2}. For climatological purposes, the units used are “hours per day”, as well as percentage quantities, such as “relative daily sunshine duration” where SD is divided by the maximum possible SD (i.e., as if sky was clear all the time so a bright sun was present during the whole day, from sunrise to sunset).

One of the most used instruments to measure SD is CSSR. It was invented in the late 19th century to provide a measurement of the duration of bright sunlight by making a burn mark on a piece of specially treated cardboard. The measurement of the length of the burn for a given card gives daily SD. For details on the history of the CSSR, we refer to *Stanhill* [2003] and *Sanchez-Lorenzo et al.* [2013]. In brief, the main parts of a current CSSR are a sphere made of transparent glass, and a rounded metal frame placed behind the sphere. The glass sphere is designed to focus the Sun´s rays onto a piece of recording cardboard. The metal frame part has three overlapping sets of grooves to hold the recording cards for the winter, summer and spring/autumn periods. The recording card has to be replaced daily after sunset. Different designs of cards exist, with hourly and half-hourly divisions marked across these cards, enabling determination of the times of sunshine, with an estimated resolution of 0.1 hours. For further details on the instrument and instructions for obtaining uniform results, as well as other traditional instruments for measuring SD, see *Middleton* [1969] and *WMO* [2008].

Over the last few years, various automated instruments and other methods for obtaining SD have been developed, which are summarized in *WMO* [2008]. One of these is the pyrheliometric method, which is based on direct irradiance measurements [e.g., *Hinssen*, 2006; *Hinssen and Knap*, 2007; *Vuerich et al.*, 2012]. Another way of determining SD is by means of automatic instruments specifically designed to this end, which have become commercially available [*Wood et al.*, 2003; *Kerr and Tabony*, 2004; *Matuszko*, 2014a]. These instruments detect direct solar radiation and count the time interval during which the irradiance exceeds a certain threshold. Progressively, many weather stations have changed traditional manual instruments (such as CSSR and Jordan photographic recorders) to these automatic systems. Moreover, different methods exist nowadays to estimate SD from geostationary satellite data, which potentially provide improved spatial coverage and representativeness [*Olseth and Skartveit*, 2001; *Good*, 2010; *Kothe et al.*, 2013].

Despite the new models of sunshine recorders do not require daily attention by an observer and their data reduction (i.e., the process of recording and storing the SD data) is faster and more accurate, there is a consensus with regard to preserving CSSR type instruments at long-established (in some cases, more than 120 years ago), well-maintained and freely exposed meteorological stations [*Stanhill*, 2003; *Wood and Harrison*, 2011; *Sanchez-Lorenzo et al.*, 2013b].

A change of the instrument used to measure SD can affect the homogeneity of the data series. This may lead to significant errors when evaluating trends and may hinder the possibility of determining long-term secular trends [*Powell*, 1983; *Steurer and Karl*, 1991; *Brázdil et al.*, 1994; *Stanhill and Cohen*, 2008]. Among the studies that analyze long series of SD, some works choose to restrict the period in order to avoid instrumental changes, therefore not encompassing the entire period of observation [*Angell et al.*, 1984]. Other studies assess the homogeneity of the SD series, such as research conducted in the United States [*Cerveny and Balling*, 1990; *Stanhill and Cohen*, 2005], United Kingdom [*Kerr and Tabony*, 2004], Iberian Peninsula [*Guijarro*, 2007; *Sanchez-Lorenzo et al.*, 2007], Japan [*Katsuyama*, 1987; *Stanhill and Cohen*, 2008], China [*Xia*, 2010], and Switzerland [*Sanchez-Lorenzo and Wild*, 2012]. The results of these studies point towards the need for further research including homogenization of the long-term SD series and the necessity of simultaneous measurements by both traditional and automatic instrumentation [*Aguilar et al.*, 2003].

Differences between one type and another of SD measurements might be attributed to their particular characteristics and limitations. As the longer SD series are generally measured using CSSR, the errors connected with this instrument are well-described [*Painter*, 1981; *Brázdil et al.*, 1994]. The two major problems with CSSR when comparing their measurements with other methods or instruments lie in the variability of the level of direct irradiance which produces a burn, and the overburning of the card in conditions of intermittent high irradiance [*Stanhill*, 2003]. These difficulties can be added to the obvious element of subjectivity in measuring the burn length on the CSSR cards [*Brázdil et al.*, 1994]. The problem of overburning is very difficult to evaluate as one small burst of high direct irradiance causes a burn apparently lasting far longer than the few seconds of its actual duration, and standard methods have therefore been proposed to take into account this fact when evaluating the burn lengths [*WMO*, 2008]. Despite these rules, during events of very broken cloudiness, a measurement of SD by means of CSSR can be significantly overestimated [*Painter*, 1981; *Kerr and Tabony*, 2004].

Regarding the first problem, defining the direct irradiance value that produces burning ("burning threshold") is a well-known issue. One proof is the variability of values that the WMO has given:

in 1971, WMO suggested that the threshold can vary between 70 and 280 W m^{-2}; in 1976, WMO recommended a threshold value of 200 W m^{-2}; finally, in 1981, a value of 120 W m^{-2} was recommended [*WMO*, 2008]. *Gueymard* [1993] tried to give some scientific justification to this value. Nevertheless, *Bider* [1958], *Jaenicke and Kasten* [1978] and *Roldán et al.* [2005] showed a large variety of burning thresholds for different CSSR. Similarly, *Helmes and Jaenicke* [1984] described the effects of using different types of recording cards. In addition, the measurement of threshold values indicated that there were notable losses of record which must be attributed to dew or other water deposits on the glass sphere. *Painter* [1981] obtained monthly averaged threshold values ranging from 16 to 142 W m^{-2}, despite some thresholds up to 400 W m^{-2} were obtained in particular conditions. From the above discussion it is clear that long time series of SD include errors of several kinds and that their removal is a complicated issue. It is also important to stress that the problem of thresholds is not exclusive to the CSSR, as it has been studied for other instruments such as the Foster sunshine recorder [*Baker and Haines*, 1969; *Benson et al.*, 1984; *Michalsky*, 1992].

SD series also provide additional embedded information on other magnitudes. For example, many authors relate SD for a period of time with direct and global (which is the sum of the solar direct and diffuse contributions) irradiance, with the use of the so-called Ångström-Prescott type formulas [e.g., *Sears et al.*, 1981; *Benson et al.*, 1984; *Martínez-Lozano et al.*, 1984; *Stanhill*, 1998a; *Suehrcke*, 2000; *Power*, 2001; *Bakirci*, 2009], which were first proposed by *Ångström* [1924] and further modified by *Prescott* [1940]. In addition, R. Jaenicke and L. Helmes developed a series of pioneering studies presenting a method to determine atmospheric turbidity from SD records and cloud cover data [*Jaenicke and Kasten*, 1978; *Helmes and Jaenicke*, 1984, 1985, 1986], that has recently aroused interest [for a review, see *Sanchez-Romero et al.*, 2014].

SD data are also used in other fields such agriculture [*Monteith*, 1977; *Stanhill and Cohen*, 2001] or hydrological modeling [*Döll et al.*, 2003].

This paper describes an analysis method to derive direct solar irradiance from the CSSR burnt cards by using digital image processing. The idea we assume here was first proposed by *Wright* [1935]: the size of the burn at any point is related to the strength of DSI focused on the card at that time. *Galindo Estrada and Fournier d'Albe* [1960] applied a similar approach: they compared daily values of the mass loss of burnt cards (which is related with the perforation of the card so with mean burn width) with pyrheliomter readings. The hypothesis of using the burn width of CSSRs to obtain direct solar irradiance data has recently been revisited, and several studies have shown the potential of the burn width of CSSR cards as a proxy for DSI [e.g., *Wood and Harrison*, 2011; *Horseman et al.*, 2013], but here a more complete research is presented, comparing burn width and DSI for a relatively long period of time (2 years) and investigating results at high temporal resolution. As long-term records of SD cards are available at some historical meteorological stations, e.g., Blue Hill Observatory in United States [*Magee et al.*, 2014], the reconstruction of DSI for these sites can reach more than 100 years from the present day. Section 5.2 provides a description of data and instruments used in this research. In section 5.3, we describe the semi-automatic method proposed for determining the width of the burnt traces. In section 5.4, we show the application of the new treatment of the CSSR cards to, first, determine the daily SD, and second, estimate the DSI at hourly resolution. Finally, conclusions of this study and suggestions for further research are presented in Section 5.5.

5.2. Instruments and data

Exposed cards from CSSRs and meteorological and radiative measurements used in the present study come from a weather and radiometric station located on the roof of a building of the University of Girona (41.962ºN, 2.829ºE, 115 m asl). Girona is a city located in the North-East of the Iberian Peninsula, at about 30 km from the Mediterranean Sea. It has a Mediterranean climate, with moderate winters and hot summers, and maximum precipitation during autumn and spring. The mean height of the horizon for the CSSRs is 4.2º, with a minimum of 0.2º at azimuth angle 86ºW, and a maximum of 9.2º at azimuth angle 21ºE (Figure 5.1). Note that the Sun rises over the horizon at angular heights greater than 5º (except during summer period), while in the evening the Sun sets at much lower angular heights during most months. This means that the SD records and DSI measurements are slightly affected in the morning, but we assume that this issue does not affect the relationship between both variables.

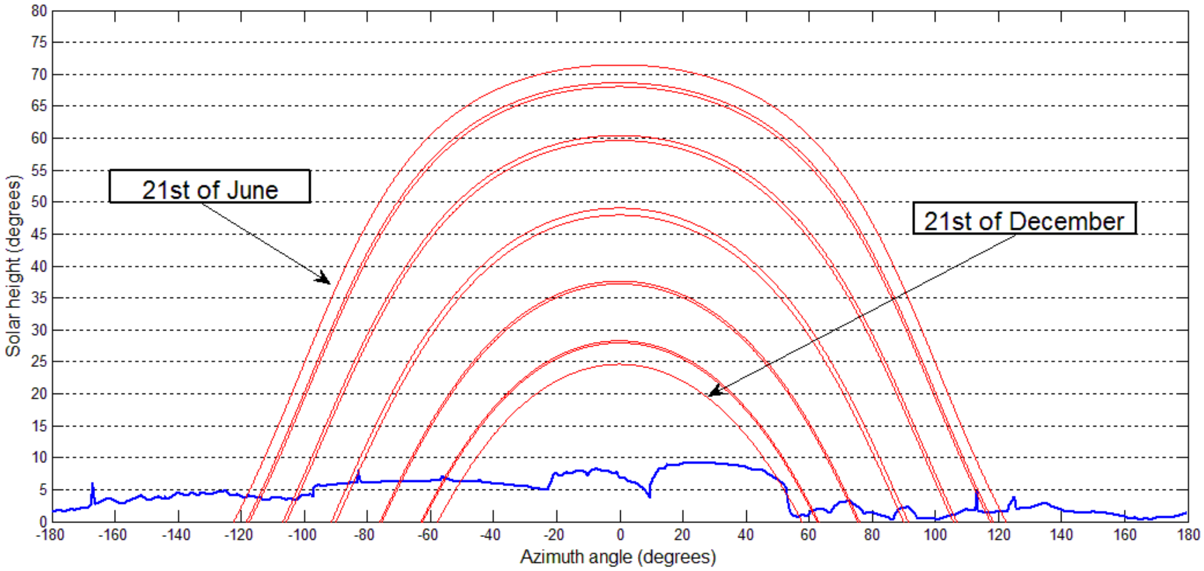

Figure 5.1. Solar path for the 21st of each month (red lines) and horizon height for each azimuth angle (blue line).

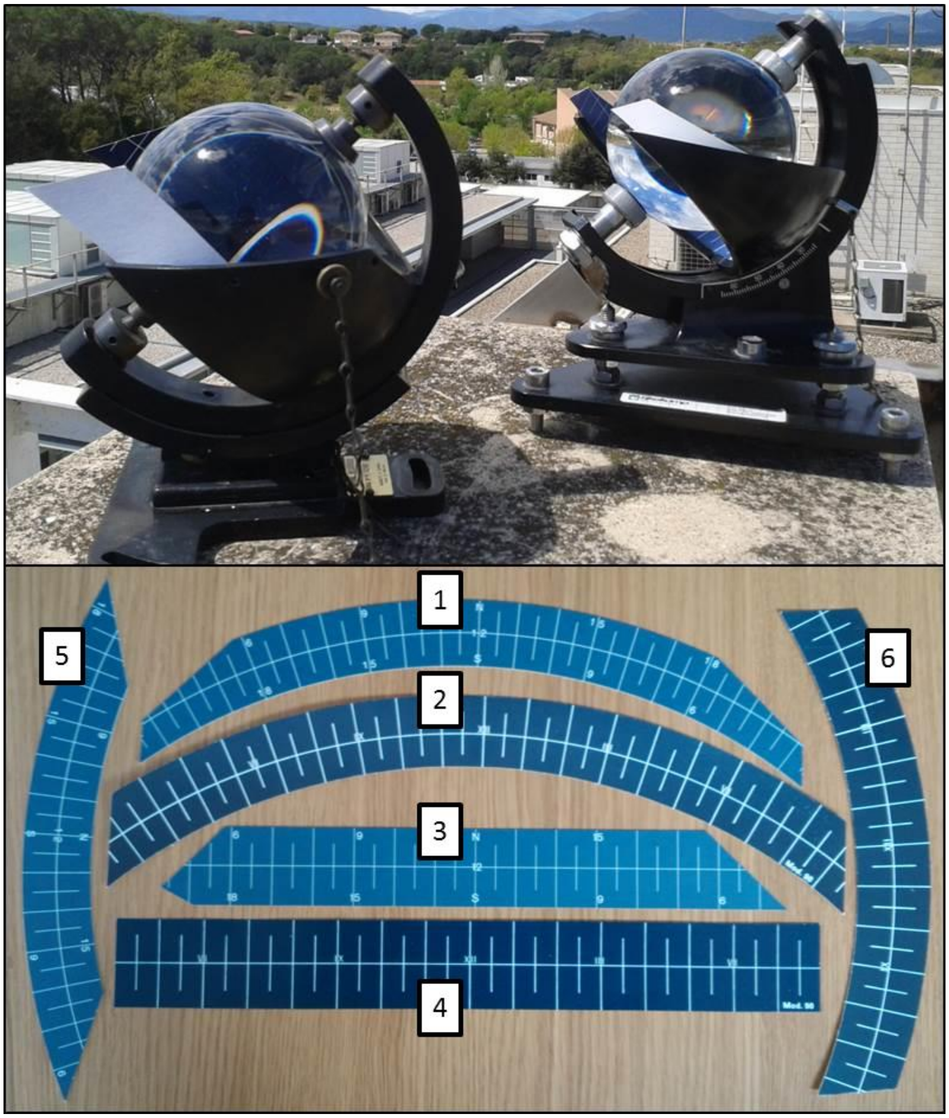

Figure 5.2. (Top) Details of the two different CSSRs mounted in Girona (NE Spain), and (bottom) an example of the 3 types of cards used during summer, winter, and equinoctial seasons, respectively (the longer the daylight hours, the longer the card): (1) summer card of Thies Clima; (2) summer card of Mod.98; (3) equinoctial card of Thies Clima (note that although the card edges are not symmetric, the markings are); (4) equinoctial card of Mod.98; (5) winter card of Thies Clima; and (6) winter card of Mod.98.

Two different models of CSSR have been used (Figure 5.2a), with three different cards for each CSSR (Figure 5.2b), which are used for different periods along the year. Hours and half-hours are printed in every card, as also shown in Figure 5.2b. One of the CSSR and cards are from Thies Clima (hereafter referred to as CSSR1); the other CSSR is from Negretti & Zambra manufactured in the 1980s with cards of the model Mod.98 (hereafter referred to as CSSR2), formerly used by the Spanish Meteorological Agency (AEMET). DSI is measured by a pyrheliometer (CH-1 model) from Kipp & Zonen, mounted on a Sun tracker. The DSI is measured every second, and values are stored as 1-minute averages. The station is also equipped with meteorological sensors to measure temperature, humidity, wind speed, precipitation, etc., as well as a ceilometer, a multifilter rotating shadowband radiometer and other radiometric sensors. In addition, a whole sky camera is continuously taken pictures of the sky dome.

We have processed 239 cards covering the period from January 2012 to January 2014, for each type of CSSR. We have 94 winter cards (from 16th October to 28/29th February), 56 equinoctial cards (from 1st March to 15th April and from 1st September to 15th October) and 89 summer cards (from 16th April to 31st August). The number of cards is limited because we do not put cards every day and we removed the cards that were too damaged due to the rain or with no trace of burnt.

5.3. Semi-automatic method for reading the burnt traces

We have developed a semi-automatic method to retrieve information from the burnt cards. We have considered “burnt” not only the perforated part, but also the black-grey area (scorched area) present on the edges of the burn. The method is very effective in detecting the burnt areas of the

CSSR cards and can be summarized in four steps. First, we scan each card on a suitable background. Second, we apply a digital process that increases the contrast of the burnt area. Thirdly, the center of the day, 12 true solar time (TST), on the card is determined. Finally, the burn width is measured, with the help of a computer program, along cross-sections spaced every minute. A schematic illustration of the different steps can be seen in Figure 5.3. With this, we obtain daily evolution of the burn width at a resolution of 1-minute; the length of the burn (i.e. sunshine duration) can be easily determined too. These four steps are detailed in the following sections. Our method presents similarities with the method by *Horseman et al.* [2013], but there are also significant differences, which will be highlighted below.

5.3.1. Image capture

As *Horseman et al.* [2013], scanning the burnt card is the first step of our method, and the manual part that consumes more time. For this purpose, we use a commercial scanner (model HP Scanjet 5590). As sensors in image scanners alter with time and use, a method to calibrate the scanner must be applied regularly [*Horseman et al.*, 2013]. On the other hand, we use a standard image format, 24-bit RGB BMP (bitmap), and the same dimension (2340 x 1700 pixels) for all scans. Unlike *Horseman et al.* [2013], for scanning the cards, we use a green background (Figure 5.3a) in order to obtain a contrast with the card, which is blue (face) and white (hour markers and other information). The positioning of the card on the scanner does not need to be precise, which simplifies and speeds up the card scanning process. Before the scanning, an evaluation has been done to remove those cards that do not present any burn or to control those that present any anomalies (stains on the card face, deformations due to the rain, etc.).

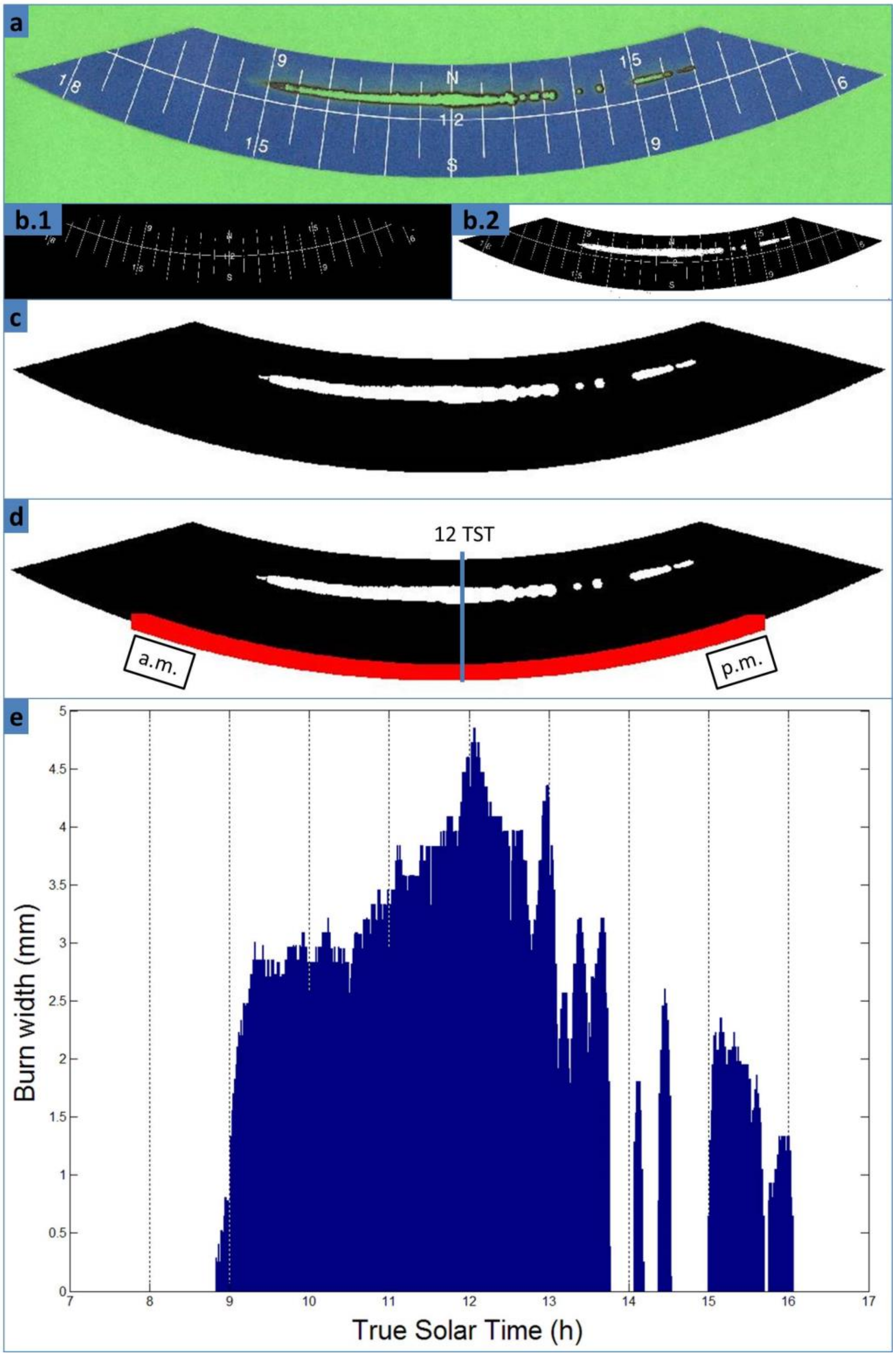

Figure 5.3. Steps of the semiautomatic method for retrieving information from the CSSR burned cards and for a certain day: (a) captured image, (b) treated image, (c) positioned image, and (d) measured burn width over time.

5.3.2. Image treatment

On used cards, the edges of the burnt or scorched traces are, for the most part, black-brown, occasionally with some grey ash. As stated by *Fan and Zhang* [2013], there are not abrupt changes in grey intensity between the weak scorch and the card face, but their signatures on the RGB color coordinates are noticeably different. This fact will be the basis to identify the burnt parts of the card, by using the Image Processing Toolbox from MatLab on the RGB image. First, we build an image called Im1 (Figure 5.3b.1), in which the pixels corresponding to the white markers in the card (hour and half-hour markers) have the value "1", and the rest of the pixels have "0". To distinguish the white pixels a threshold of $R>200$ is applied on the red component (which ranges from 0 to 255). Then, we build a second image, called Im2 (Figure 5.3b.2), distinguishing the blue area of the card. The selection is made applying the condition $B – R < 20$ on the red and blue components. In Im2, the pixels in blue areas are labeled as "0" and all the other pixels (green, black, grey and white) are labeled as "1". Next, by subtracting Im1 from Im2 and setting to 0 all pixels where the difference is negative, an image with pixels labeled "1" for the burn and the background (black, grey and green), and with pixels labeled "0" for the non-burnt part of the card (blue and white) is obtained. There is still some "noise" in this image (that is, pixels of one kind surrounded by eight pixels of the other kind); this noise is removed from the image to obtain the final processed image (Figure 5.3c, 1-pixels in white, 0-pixels in black). Note that all this process is automatic. The choice of the thresholds ($R > 200$ for Im1 and $B - R < 20$ for Im2) has been empirically determined after performing various checks and will certainly affect the identification of the burn but, as long as they are used consistently throughout the two card archives, their exact absolute values are not very important.

5.3.3. Image positioning

Unlike *Horseman et al.* [2013], the positioning of the card within the image requires also some manual intervention. This is convenient for checking the scan and the image treatment, and necessary to convert the image of the burnt pixels into length (millimeters of width) and into time (minutes along the day). Although this step slows down the process, it allows using our method for any type of card. We need to manually identify two or three points (depending on the shape of the card) to find the center of the day (12 TST). More specifically, in curved cards (summer and winter cards) we mark three points (two on the ends of the outer arc and the third close to the center of the outer arc) to find the center and the radius of the outer circumferences (the same process could be applied for the inner arc). Then, as these cards are symmetric about the midday marker, it is easy to find all points in the image belonging to the outer or inner arc and the point corresponding to noon (Figure 5.3d). In the equinoctial cards, the problem of finding the midday point is even easier than in the previous ones: knowing two points (at both ends of the outer -or inner- contour) provides sufficient information to locate the midday point.

5.3.4. Measurement of burning width

Horseman et al. [2013] method rectifies the image of each card (that is, images are transformed to a representation with a straight burnt trace) before extracting the burn width, thus simplifying geometrical calculations. Contrarily, we consider here continuous radial sections that cover the whole card and measure the burn width (i.e., the length from the first to the last “burnt” pixels) along each section. As the size and shape of each card type is known and standardized, we know the radii of the outer and inner boundaries and their distance, so there is no need to cross the whole image, but only the area where the card is placed. For the equinoctial cards, parallel sections are performed instead of radial sections.

We continue by defining the relation between angular (or linear) displacement and time: as we know the angle (or distance) between the two edges that we defined in the previous step and we also know the interval of time that corresponds to these two points (this time is fixed in each type of card), the relation between angle (or distance) and time is immediate. For example, for winter and summer cards, a 1-minute displacement corresponds to an angular displacement of 0.064º; in the case of equinoctial cards, 1-minute displacement corresponds to a linear displacement of 0.294 mm (0.317 mm) for CSSR1 (CSSR2). If we consider a resolution of one pixel, the resolution of the burn width is 0.126 mm in all cards (for the scanner used).

As we know the point corresponding with 12 TST, consecutive angular displacements (corresponding to a 1-minute temporal resolution) towards the left are applied, the radial sections between the inner radius to the outer radius are inspected, and the distance between the first "1" pixel to the last "1" pixel in the radial section is computed. Thus, we obtain the temporal evolution of the burn width for the morning. We do in a similar way (but towards the right) to obtain the afternoon evolution of the burn width. With this, the daily evolution of the burn width in each card is finally obtained (Figure 5.3e). Note that all processes in this last step are fully automatic.

5.4. Applications of the measurements of the burn width

The semi-automatic method proposed to process the burnt cards can help in the assessment of different types of errors that can affect the SD measurements (Section 5.4.1). The method can also be useful in order to provide a record of DSI, since the burn width can be used as a proxy for pyrheliometer measurements (Section 5.4.2).

5.4.1. Assessment of the measurement of sunshine duration

As summarized by *Brázdil et al.* [1994], the sources of errors in the SD series related to the use of CSSRs are i) the ageing of the glass ball, which with increasing operation time becomes less transparent, ii) the replacement of the recorder by a new device manufactured by different companies, and iii) the variability of the recording card (e.g., different quality, color, or material). In order to homogenize the worldwide measurements of SD, a specific design of the CSSR was recommended as the reference in the 1960s [*WMO*, 1962]. This, however, did not overcome all the problems, especially when long-term series with records before and after the 1960s are used to study SD trends. So, here we will quantify these errors/differences in the observations by using our digital method applied to two different CSSRs that use different burning cards.

Table 5.1. The first two columns are the mean value of SD by manual and semiautomatic method, respectively. The third column is the value of SD from pyheliometric method by using a DSI threshold (in parenthesis) that would approach the corresponding mean SD using the semiautomatic method. Recall that the "true" mean SD (by using 120 W m^{-2} as the DSI threshold) is 7.16h.

References	**Manual**	**Semiautomatic**	**DSI threshold**
SD1	7.31 h	7.53 h	7.49 h (55 W m^{-2})
SD2	7.10 h	7.22 h	7.21 h (110 W m^{-2})

One of the major problems when comparing SD measurements from different CSSR devices and card types is the variability of the level of DSI that produces a burn [e.g., *Stanhill*, 2003; *Sanchez-Romero et al.*, 2014]. We define here the SDpyr method as considering a threshold of 120 W m^{-2} in DSI in order to calculate SD, that is counting the minutes when DSI is greater than 120 W m^{-2}. By doing so, the mean value found for our database is 7.16 h, which can be taken as the reference (correct value) for other estimations. Table 5.1 shows the mean value obtained when using different methods of estimating SD applied both to CSSR1 and CSSR2. To obtain SD with the semi-automatic method described in Section 5.3 (SDaut), all minutes showing burn are counted. As shown in Figure 5.4a for CSSR1, retrieved SD using the SDaut and the SDpyr methods agree very well (correlation coefficients higher than 0.98 for both instruments), although a minor overestimation is apparent. Semi-automatic method gives a mean SD deviation with respect SDpyr of 0.37 h (4.9%) and 0.06 h (0.8%) for CSSR1 and CSSR2 respectively. Both instruments give a slight overestimation of SD, more pronounced for CSSR1, which shows a somewhat higher sensitivity than CSSR2. The instrument sensitivities can be also quantified by searching for the DSI threshold values that would give the corresponding mean SDaut: 55 W m^{-2} and 110 W m^{-2} respectively for CSSR1 and CSRR2; these threshold values are lower than the 120 W m^{-2} suggested by the WMO.

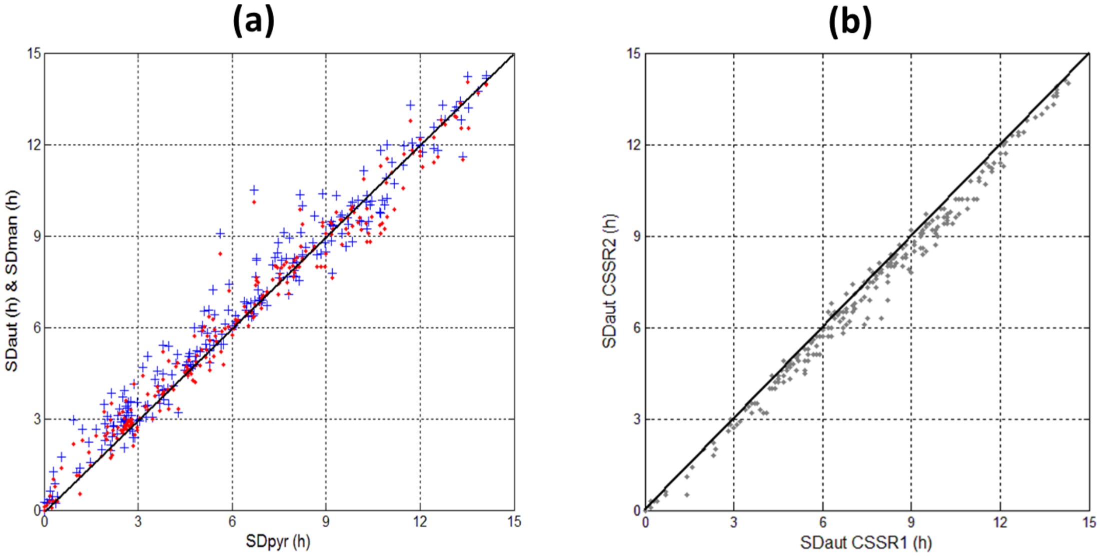

Figure 5.4. Scatter plots of the (a) daily SD obtained for CSSR1 from both SDaut (blue crosses) and SDman (red points) methods against SDpyr, considering the threshold of 120 W m^{-2} in DSI; and (b) the daily SD obtained by the two CSSR using the automatic method. In each graphic we also represent the 1:1 line (black line).

So, there is some overestimation in SD given by SDaut, which was expected because some instructions and recommendations [*WMO*, 2008] are not applied in the method. For example, when SD is retrieved by reading the cards manually (SDman), in the case of a clear burn with round ends, the time length is reduced at each end by an amount equal to half the radius of curvature of the end of the burn; or, in the case of a clear burn that is temporarily reduced in width by at least one third, an amount of 0.1h is subtracted from the total length of the burnt segment. Contrarily, SDaut accounts strictly for all minutes where a burn (or a scorch) is detected, without any further correction, so it tends to –slightly— overestimate SD. Among the possible improvements in the SDaut method, the introduction of the advice proposed by WMO [*WMO*, 2008] in the algorithm would reduce the differences between SDaut and SDpyr.

Table 5.1 also shows the mean SD that is obtained by SDman method (we processed all cards in the usual, visual way): as expected they are slightly lower than values found with SDaut method, but the general agreement between SDaut and SDman methods is very good for both instruments: the mean deviation of SDaut with respect SDman is 0.22 h (2.9%) for CSSR1 and only 0.12 h (1.7%) for CSSR2. Figure 5.4a shows (for CSSR1) the excellent agreement between daily SD obtained from both SDaut and SDman methods with SDpyr. It is important to notice that, for low values of SD, SDman gives also higher values than SDpyr (as it does SDaut): this must be related to the overburning of the card in conditions of broken cloudiness [*Stanhill*, 2003; *Sanchez-Romero et al.*, 2014].

From the above results, we confirm that 120 W m^{-2} is a suitable DSI threshold. Nevertheless, it is worth noting that there is a high variability in the exact threshold that gives the best agreement of SD for each particular card along the year (not shown). This large seasonal variability was pointed out by *Painter* [1981], *Michalsky* [1992] or *Roldán et al.* [2005]. The position of the card on the CSSR, the humidity conditions [*Bider*, 1958; *Painter*, 1981], and the poor horizon at the location of the instruments (especially in the morning between October and April) are factors that could explain such high variability.

The differences between instruments are evident in Figure 5.4b and in Table 5.1. CSSR1 gives slightly greater values than CSSR2 for both SDaut and SDman methods. It can be due to the ageing of the glass sphere as the latter is an instrument from the 1980s and the former was brand new at the beginning of our research, although it could also be related to the different quality and colors of the recording cards used for each device [*Brázdil et al.*, 1994]. In this sense, note that the semi-automatic method uses the same threshold values in the image segmentation when defining the burnt regions for both types of CSSR and cards; an improved method could tune a particular color threshold for each CSSR or card in order for SDaut to match almost exactly SDpyr (or SDman if pyrheliometric measurements are not available).

All mean differences found are similar to the uncertainty usually assigned to the measurement of SD (i.e., 0.1 h), and even in the case of the automatic method, the difference between CSSR is much lower than the maximum errors of around 7% suggested by *Brázdil et al.* [1994] referring to different instruments or to the ageing of the glass sphere. In fact, other radiometric variables have similar or even higher uncertainties: global solar radiation has instrumental errors of around 5% and 2% for the monthly and annual means, respectively [*Gilgen et al.*, 1998; for more information about instrumental errors of radiation data, see for example *Vignola et al.*, 2012]. With the improvements proposed above, not only the linear-relationship between SDman and SDaut would be even better, but also the differences between two different CSSR would be reduced to become almost nil.

5.4.2. Burn width and its relationship with direct solar irradiance

Figure 5.5a and 5.5b show the daily evolution of the burn width for the two CSSR and for two different days (one mostly sunny and the other with scattered and broken cloudiness). In this figure, and hereafter, we refer to the burn width for CSSR1 and CSSR2 as h1 and h2 respectively. It is evident that the evolution of the burn width shows an excellent agreement for both recorders (and also with DSI), with a correlation coefficient higher than 0.90 when all the 1-min records are taken. Nevertheless, for some days, there might be a shift of up to a few minutes between CSSR and DSI data. This is likely the result of a slight misalignment of the cards from their correct position in the CSSR device. Thus, if analysis with less than a few minutes resolution is to be performed, we would need to consider this misalignment; in the present study, hourly averages of burn width and of DSI will be used onwards. As an example of the strong relationship, Figure 5.5c shows the scatterplot, the linear fit, and the correlation coefficient of h2 against h1 on hourly basis. Note that the slope of the linear regression is lower than 1, i.e. burn width on CSSR1 is notably higher than that on CSSR2, as was expected given the higher sensitivity of CSSR1 found above. The same analyses have been performed separately for each set of seasonal cards (not shown) and it turns out that the correlation coefficients are almost 1 for all card types and the slopes of the linear regressions are also very similar for all seasons. In other words, the relationship between h1 and h2 is almost constant during the year.

The mean difference between h1 and h2 is 1.03 mm at 1-min resolution, which is a relative difference of 32% with respect h1 (much higher than the difference in daily SD). This value agrees with the slope of the fit of hourly averages (0.69) which points to a relative difference of 31%. *Wood and Harrison* [2011] already stated that the burns in one site could be thinner than those in another site although DSI conditions were the same (e.g., due to differences between instruments). Similarly, in our study we find that h1 and h2 are different (although highly correlated with each other). Then, when estimating the DSI from burn width data, it will be important to know which instrument has been used. This is similar to what happens with Ångström-Prescott equations that relate global solar radiation with SD, where parameters depend on local calibration and on time interval [*Martínez-Lozano et al.*, 1984]. Note, however, that the latter parameters must be adjusted because of different climates (typical atmospheric turbidity) while the former depend on the specific instrument.

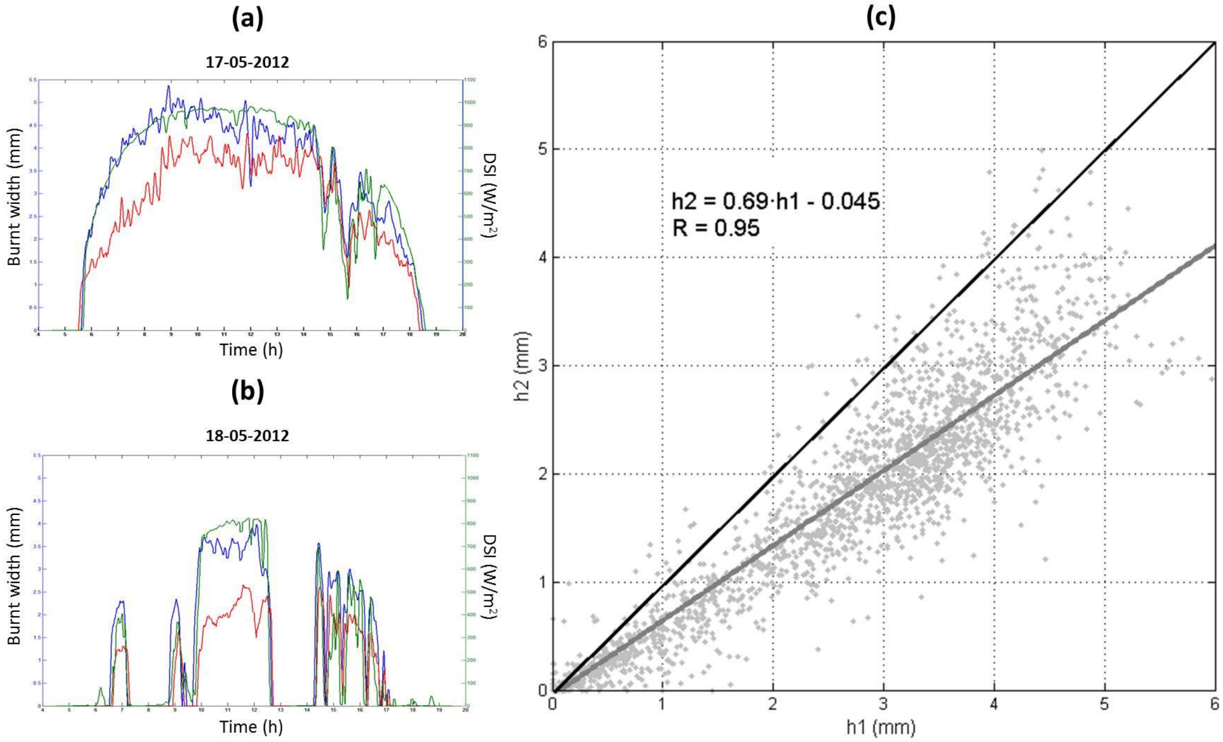

Figure 5.5. (a, b) Daily evolution of burn width (blue line for CSSR1 and red line for CSSR2) and DSI (green line) for 2 different days. (c) Scatter plot of the burn width in CSSR2 (h_2) versus that of CSSR1 (h_1) at hourly resolution. We also represent the 1:1 line (black line) and the linear regression fit (green line).

In Figure 5.5a and Figure 5.5b we can also see the daily evolution of DSI. The evolution of DSI and that of h1 and h2 shows a strong relationship, which is also displayed in Figure 5.6, that suggests a fit between burn width and DSI. *Wright* [1935] and *Lally* [2008] proposed an exponential fit for the estimation of DSI from burn width ($\mathrm{DSI_W}$). These studies did not consider many days and probably that is the reason why they did not find that increasing burn width tends to a certain maximum value of DSI, as a horizontal asymptote. The effect of DSI on burn width decreases and other factors have a role in the measure of burn width (e.g., the atmospheric or the card conditions). This is seen in Figure 5.6: from a certain value of burn width, the value of DSI does not vary too much and tends to a maximum value. So, in order to do a fit considering an exponential growing and a horizontal asymptote, a logistic function is proposed:

$$DSI_W = \frac{L}{1+ Ke^{-Gh'}} \qquad \text{(Eq. 5.1)}$$

In this equation, *h’* is the normalized burn width (i.e. the value of burn width divided by its 95-percentile value, for each CSSR). The function depends on some parameters having physical meanings: *L* is fixed to the 95-percentile value of DSI, *K* is related to the threshold DSI (i.e. the $\mathrm{DSI_W}$ value in the y-intercept), and *G* is related to the growth ratio. We consider *K* and *G* as the free-parameters for the fit. Figure 5.6 shows the scatterplot between burn width and DSI, the logistic fit ($\mathrm{DSI_W}$), and the correlation coefficient for the two CSSRs, on hourly basis. We can see that the growth ratio (*G* value) is similar in both CSSRs and that the *K* value is higher in CSSR1 than CSSR2, which agrees with the fact that CSSR1 has a lower DSI threshold than CSSR2 because CSSR1 is more sensitive than CSSR2.

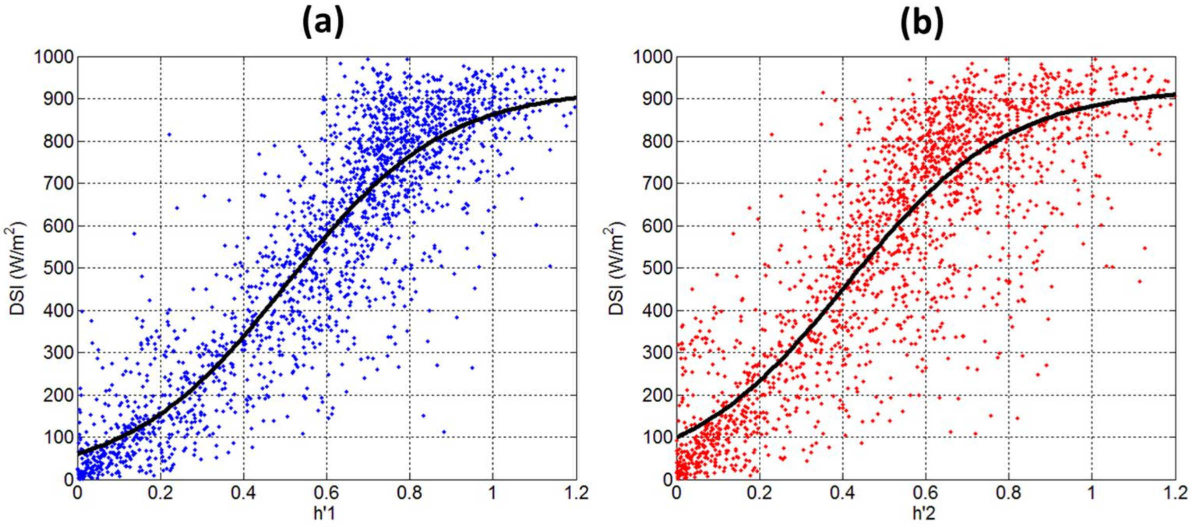

$\mathrm{DSI_W} = \frac{925}{[1+14.36\cdot\exp(-5.28\cdot h')]}$ $R = 0.899$

$\mathrm{DSI_W} = \frac{925}{[1+8.35\cdot\exp(-5.16\cdot h')]}$ $R = 0.863$

Figure 5.6. (a) Scatter plots at hourly resolution of the DSI against normalized width for CSSR1. The fitted logistic function and the correlation coefficient are also shown (black line). (b) The same but for CSSR2.

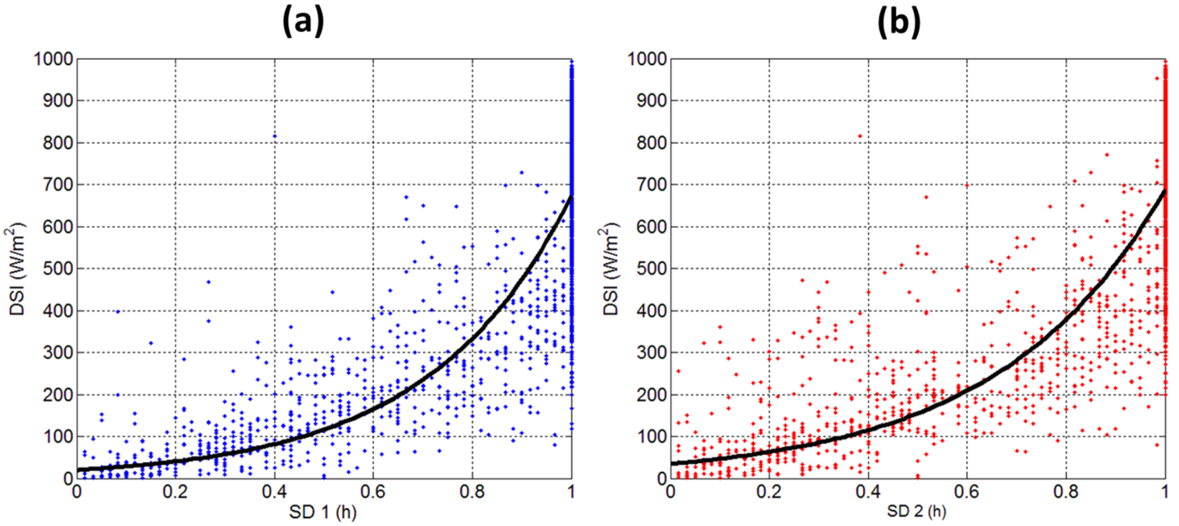

$\mathrm{DSI_{SD}} = 20.01 \cdot \exp(3.52 \cdot SD)$ $R = 0.838$

$\mathrm{DSI_{SD}} = 37.74 \cdot \exp(2.99 \cdot SD)$ $R = 0.847$

Figure 5.7. (a) Scatter plots at hourly resolution of the DSI against SD for CSSR1. The exponential regression (black line) and the correlation coefficient are also displayed. (b) The same but for CSSR2.

We compare our method based on measuring the burn width with the estimations of DSI using hourly SD, i.e., counting the minutes with burn within each hour (DSI_{SD}). *Stanhill* [1998a] presented a similar approach, and suggested both linear and quadratic regressions, but for our data we have found more appropriate to fit exponential functions, which are shown in Figure 5.7 for both CSSRs. It is important to note that values of DSI for SD equal to 1 h (that is, for sun shining along the whole hour) range from 200 to 1000 W m^{-2}, thus making it difficult to obtain a good estimation of DSI for completely clear-sky hours. In addition, the cases of SD equal to 1 h are the most probable (more than 62% of all the cases for the two CSSRs).

As seen in Figure 5.5a and 5.5b, DSI affects burn width at very short time scales (1 minute), but the advantages of using the burn width instead of SD to estimate DSI even at hourly resolution are shown in Table 5.2 and in Figure 5.8. In Table 5.2 we can see, for each method, different statistical indexes comparing the estimated DSI with the measured DSI, along with the parameters describing the relationship between both variables. It is clear that the method based on burn width gives better results, especially if we look the column of mean bias error and the intercept value, and also regarding the relative root mean squared error. These results show that the burn width gives more information about the variation of DSI high-resolution temporal data (1 hour) whereas counting the time length of the burn for short periods only gives information as to whether the sun is visible (i.e., whether DSI is higher than a certain value). It is remarkable that the correlation between DSI and burn width at hourly resolution is as good as other relationships found by other authors at lower temporal resolution (daily, monthly, seasonally or annually) using only SD and linear and quadratic correlations [*Benson et al.*, 1984; *Louche et al.*, 1991; *Nfaoui and Buret*, 1993; *Maduekwe and Chendo*, 1995; *Stanhill*, 1998a; *Power*, 2001].

Table 5.2. Statistical parameters of estimations of hourly DSI when compared with DSI measurements by different methods and instruments (from mean burn width, h_1, h_2 and hourly sunshine duration, SD1, SD2; *Stanhill*, 1998a). MBE is the mean bias error; RMSE is the root mean square error; RRMSE is the relative root mean square error; R^2 is the coefficient of determination; A is the slope of the regression line; and B is the y intercept of the regression line.

Method	**MBE ($W\ m^{-2}$)**	**RMSE ($W\ m^{-2}$)**	**RRMSE (%)**	**R^2**	**A**	**B ($W\ m^{-2}$)**
DSI_W CSSR1	-0.6	129	23.9	0.81	1.00	-3.20
DSI_W CSRR2	6.6	147	27.1	0.75	1.01	-1.23
DSI_{SD} CSSR1	-30.0	165	30.5	0.70	0.98	-16.7
DSI_{SD} CSSR2	-29.0	159	29.0	0.71	0.98	-20.7
Stanhill (linear)	-	-	48.4	0.74	-	-
Stanhill (quadratic)	-	-	44.7	0.78	-	-

In Figure 5.8, box plots for the residuals between the estimated and measured DSI, in bins of 100 W m^{-2} width, are represented for the two methods: (a) DSI_W and (b) DSI_{SD} (only results for CSSR1 are presented, as they are similar for CSSR2). Again, the burn width method gives better mean values and less dispersion than the SD method. Note that the burn width method can give values of DSI up to 925 W m^{-2} (the parameter L in Eq. 5.1) covering nearly the whole DSI range, while SD method cannot give values above 673 W m^{-2} (for CSSR1, and according to the exponential fit found for our data). This is a consequence of what it was said before: for hourly SD close to 1 h it is not possible to distinguish values of DSI ranging from 200 to 1000 W m^{-2}.

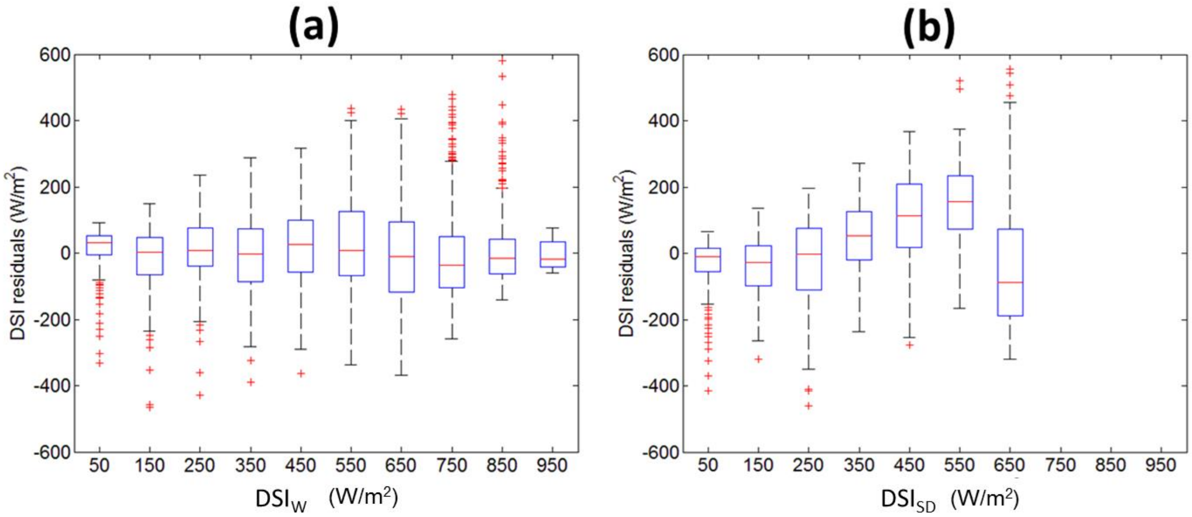

Figure 5.8. Box plots of the differences between estimated and true DSI for (a) estimation based on burn width and (b) estimation based on SD. It is applied for CSSR1.

5.5. Conclusions and future research

In this study we use a semiautomatic method to obtain the temporal evolution of the burn width in CSSR cards. This method is also capable to produce very good results as far as SD measurements are concerned. The mean overestimation in daily SD derived from this method, when compared with the value from a pyrheliometer by using the standard DSI threshold of 120 W m^{-2}, are less than 5%, which is very close to the accepted uncertainty of the traditional manual screening of cards. Differences could be reduced if advice proposed by WMO were taken into account regarding the rounded ends of the burnt areas, and the cases of intermittent burning. In addition, the thresholds applied in the image processing could be defined differently for each card type. These improvements, however, will be the subject of future research.

The two CSSRs studied here give almost the same SD, despite of different geometries and cardboard types, but CSSR1is slightly more sensitive than the CSSR2, therefore producing systematically longer SD: mean bias of 0.1-0.3 h depending on the method –manual or automatic. This difference is very small and of the same order of the instrumental uncertainty. Again, the different sensitivity of CSSR1 and CSSR2 is shown by the threshold values that should be applied to DSI for an exact match of CSSR SD values: 55 and 110 W m^{-2} respectively. The different sensitivity of the instruments is also reflected in the burn width measurements: the mean relative difference is about 30% (CSSR1 burns wider than CSSR2 burns). So, it is important to know which instrument has been used if we want to estimate other magnitudes such as DSI.

Hourly DSI can be satisfactorily estimated from the burn width measurements. The estimation based on burn width by using a logistic fit is better than that based on counting the time length of the burn (i.e. hourly SD). For example, in the case of CSSR1, we have obtained a mean bias error of -0.6 W m^{-2}, a coefficient of determination of 0.81 and a relative root mean squared error of 24%, when comparing hourly DSI estimations from burn width with actual measurements (the corresponding values for CSSR2 are 6.6 W m^{-2}, 0.75, 27%). These indexes are notably better than those obtained when SD is used (-30 W m^{-2}, 0.70, 30% approximately for the two instruments). This result shows that the burn width gives more information of the variation of DSI at high-resolution temporal data, meanwhile the other method is useful only for estimations for longer periods (e.g., daily). The parameters of the equation that relates burn width with DSI depend on the sensitivity of the instrument and the maximum DSI of the region.

Future research may consider taking into account the perforated part of the burn [*Roberts*, 2012] besides the burn width (perforated plus scorch parts); a priori, this would help in the estimation of DSI and give some light to explain the reason of the tail in the scatterplot of burn width versus DSI. Another point to consider is to use different threshold values when defining the burnt regions, depending on the type of CSSR and cards; the thresholding process is the most important factor if we are interested in relating the burn width with DSI, so it is crucial to define it correctly for each CSSR and card. Moreover, further analysis needs to consider the shift between the burn and DSI measurements if analyses with less than a few minutes resolution are to be performed.

Once this method is implemented, other magnitudes can be introduced. Since DSI is affected by atmospheric turbidity, especially at times near sunrise and sunset because of the longer optical path, having an estimation of DSI from the burn width may be used to estimate turbidity, i.e. CSSR records can become a proxy measurement for turbidity and atmospheric aerosol loading. This possibility has been proposed before by *Jaenicke and Kasten* [1978], *Helmes and Jaenicke* [1984, 1985, 1986], and more recently, by *Horseman et al.* [2008, 2013], as reviewed by *Sanchez-Romero et al.* [2014].

So, the measurements of burn width in CSSR cards obtained from the semi-automatic method described in this study can provide a way to create time series of solar irradiance in less than daily resolution, a fact that was proposed before by some authors [*Wright*, 1935; *Wood and Harrison*, 2011; *Horseman et al.*, 2013]. We have shown that it is possible to use readily available technology to mine the archives of a simple, reliable and widely used meteorological instrument to provide a proxy record of DSI. In our case, the process of scanning and manual intervention can last only 1.5 - 2 minutes for card, i.e. it is possible to process a year of exposed cards in about 12 hours of work. In fact, the reconstruction can reach as much as around 120 years from the present day as long-term records of SD cards are available at some historical meteorological stations such as, for example, the Blue Hill Observatory in Milton, Massachusetts (U.S.), where CSSR cards have been stored since the late-1880s [*Magee et al.*, 2014].

Chapter 6.

Aerosol optical depth in a western Mediterranean site: an assessment of different methods

This chapter is a transcription of the paper:

Sanchez-Romero, A., J. A. González, J. Calbó, A. Sanchez-Lorenzo, and J. Michalsky (2016), Aerosol properties in a western Mediterranean site: An assessment of different methods, *Atmospheric Research*, 174-175, 70-84, doi:10.1016/j.atmosres.2016.02.002.

The paper deals with obtaining reliable measurements of AOD at a high temporal resolution, as well as a comparison with ground-based (Cimel) and satellite data (MODIS and MISR). Measurements from a MFRSR at Girona are used to derive AOD at various wavelengths, and AE, at a maximum resolution of 1 minute. A radiative model is also used in a closure experiment to assess the accuracy of AOD retrievals from MFRSR.

6.1. Introduction

Aerosols are small particles suspended in the atmosphere that occur naturally (e.g., originating from volcanoes, dust storms, sea spray) or are generated by human activities (e.g., burning of fossil fuels). They have a profound impact on the climate system: the aerosol influence on the Earth radiative budget is related to a direct effect, due to scattering and absorption of solar and terrestrial radiation [e.g., *Charlson et al.*, 1992; *Hansen et al.*, 1997] and to an indirect effect connected to interaction with clouds [e.g., *Twomey*, 1977; *Ramanathan et al.*, 2001; *Rosenfeld et al.*, 2014].

In spite of these well-known mechanisms, and compared with greenhouse gases, aerosols still present a major uncertainty when estimating their radiative forcing of climate due to their non-uniform chemical and physical properties, and spatial and temporal variations in the atmosphere [*Boucher et al.*, 2013]. Improved knowledge of the aerosol loading and properties will help to reduce the uncertainties associated with aerosol effects in climate models and, in consequence, to improve climate change projections. Many studies are devoted to understanding the effects of aerosols on the climate system both from ground-based networks [see Table 1 in *Michalsky et al.*, 2010] and satellite platforms [see Table 1 in *Lee et al.*, 2009]. Both methods are based on radiative measurements to retrieve values of aerosol properties.

The most important of the aerosol radiative properties that can be retrieved from either ground or satellite-based methods is the aerosol optical depth (AOD), which is the degree to which aerosols prevent the transmission of light by absorption or scattering, and is much linked to the total aerosol burden in the atmosphere. The spectral dependence of AOD, typically described by the Ångström exponent (AE), is an indicator of particle size, with large particles having AE values near zero (e.g. desert dust) and smaller particles exhibiting larger AE values (e.g. urban, industrial, or biomass burning aerosols).

Among satellite onboard instruments, it is worth mentioning the multi-angle imaging spectroradiometer (MISR) and the moderate resolution imaging spectroradiometer (MODIS). Both instruments give a very complete set of variables related to atmospheric aerosol (including AOD and AE), which are derived from various measurement channels. Specifically, MISR is an instrument onboard the Terra satellite operated by NASA that measures in four spectral bands between 0.45 and 0.87 μm [*Diner et al.*, 1998, 2005]. On the other hand, MODIS is an instrument onboard two satellites of NASA's Earth Observing System (Terra and Aqua), and its detectors measure in 36 spectral bands between 0.40 and 14.39 μm [*Salomonson et al.*, 1989; *King et al.*, 1992]. Despite the satellite instruments providing global coverage, they give low temporal resolution as compared to ground based observations; the latter being generally regarded as more accurate aerosol retrievals for the place they are performed.

Ground-based optical observations of atmospheric aerosols usually involve measurements of direct solar radiation in distinct spectral bands using pyrheliometers or sunphotometers [*Iqbal*, 1983]. These measurements may be used to obtain AOD and AE [*Ångström*, 1929, 1964; *Masmoudi et al.*, 2003; *Ramachandran and Jayaraman*, 2003]. For example, we can highlight the Aerosol Robotic Network (AERONET) of ground based Cimel sun-photometers that measure in eight different channels between 0.34 and 1.64 μm [*Holben et al.*, 1998; *Dubovik et al.*, 2000]. In our research, we use the multifilter rotating shadowband radiometer (MFRSR), which continuously measures the global and diffuse solar horizontal irradiance in six narrowband wavelengths [*Harrison et al.*, 1994], using five of these to derive AOD and AE [*Harrison and Michalsky*, 1994; *Michalsky et al.*, 2001; *Alexandrov et al.*, 2002].

The MFRSR instrument has been extensively used to retrieve aerosol properties and study their climatology at different sites in the USA [e.g., *Augustine et al.*, 2008; *Michalsky et al.*, 2010; *Michalsky and LeBaron*, 2013], Europe [e.g., *Pace et al.*, 2006; *Mazzola et al.*, 2010; *Ciardini et al.*, 2012], Asia [e.g., *Janjai et al.*, 2008; *Lee et al.*, 2010], and Oceania [e.g., *Liley and Forgan*, 2009; *Bouya et al.*, 2010; *Bouya and Box,* 2011]; including the study of AOD and AE during fire and dust episodes [e.g., *Augustine et al.*, 2008; *Ge et al.*, 2010]. Nevertheless, it is worth noting that there are relatively few studies using this instrument in the western Mediterranean and in Spain in particular, where studies based upon Cimel sun-photometer measurements are much more common [e.g., *Toledano et al.*, 2007; *Bennouna et al.*, 2011, 2013; *Obregón et al.*, 2014].

Ground measurements present the inconvenience of their scarcity. Thus, for the western Mediterranean (Iberian Peninsula, southern France, Italy and North Africa), an area covering more than 1.5 million km^2, about 30 stations are currently measuring aerosol characteristics, with distances of hundreds of km between them. Given the geographical and meteorological complexity of the area (Figure 6.1), and the variability in the processes driving the aerosol behavior (emissions from different sources, transport subject to both synoptic and mesoscale meteorology), it can be argued that the network density should be improved in order to correctly describe the aerosol conditions in that area. On the other hand, the increasing spatial resolution of satellite instruments should help for a better characterization of the regional conditions, but the low temporal resolution of their measurements is an issue, besides the fact that satellite-derived records must be validated against reliable references (that is ground based).

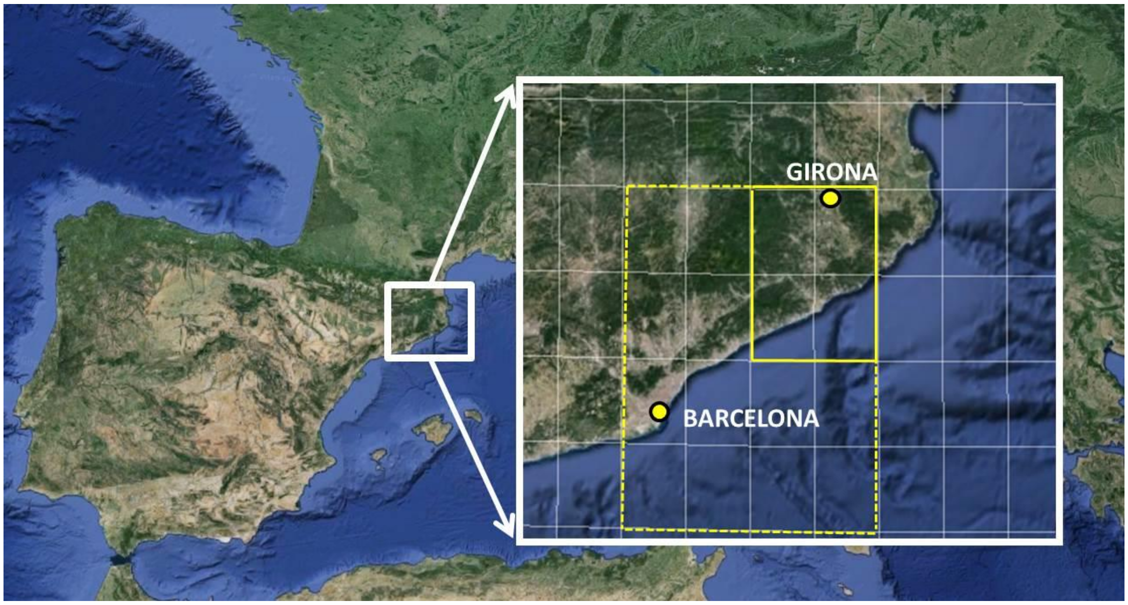

Figure 6.1. Map of the western Mediterranean showing the region of study, the main site (Girona, where MFRSR is measuring) and the complementary site (Barcelona, where the AERONET Cimel instrument is measuring). Solid and dotted yellow lines represent the MISR and MODIS cells, respectively.

This evident need of comparing the variety of methods and instruments usable to obtain information on aerosols has been partially covered by a number of studies. Comparisons between MFRSR and AERONET optical depth retrievals have been performed in the past giving good agreement between both devices [e.g., *Alexandrov et al.*, 2008; *Augustine et al.*, 2008]. However, comparison studies between MFRSR and satellite products are scarce [while there are a number of studies that relate AERONET data with MODIS and MISR retrievals, e.g., *Cheng et al.*, 2012; *Qi et al.*, 2013; *Kanniah et al.*, 2014]. As satellite products are on the rise, it is important to compare satellite instruments with ground based aerosol observations in order to understand deviations, if any, between the two kinds of measurements [*Kharol et al.*, 2011]. In the case of Spain, there are several articles that compare AERONET data with MODIS [e.g., *Bennouna et al.*, 2011, 2013; *Segura et al.*, 2015] and a few include a comparison with MISR [e.g., *de Meij* *and Lelieveld*, 2011], but no one for the specific region of the northeast corner of Spain (a region which, unlike other regions of Spain, is rarely affected by desert dust intrusions) and using MISR data.

In the present study, we use two years of MFRSR measurements taken at Girona, northeast Spain, to establish a reference dataset for AOD and AE for this area. A closure experiment is performed to help the assessment of the quality of the AOD and AE retrievals: we use the MFRSR retrieved aerosol properties as input of a radiative transfer model to determine the direct irradiance and compare it with pyrheliometer measurements [*Michalsky et al.*, 2006; *Ricchiazzi et al.*, 2006; *McFarlane et al.*, 2009]. The MFRSR-based dataset is then used as a reference for other alternative methods (ground and satellite-based) in order to assess the aerosol properties in the area, taking measurements from: (1) a 100 km away AERONET station (Barcelona), (2) MISR onboard Terra, and (3) MODIS onboard Terra and Aqua. The comparison is performed for the two years covered by the dataset, but particular attention is given to a wildfire event and a Saharan dust outbreak that occurred in Girona in July 2012. The general aim of the study is to add some knowledge about the performance of the methods when assessing aerosol behavior at some specific site.

Section 6.2 describes the characteristics of the site, the instruments used in this research, and the method applied to the raw measurements (including calibration, AOD and AE determination, cloud screening, and the evaluation of uncertainties). A detailed examination of the MFRSR retrieved AOD and AE is presented in Section 6.3.1; the radiative closure experiment in Section 6.3.2; a comparison with other products available to estimate aerosol properties in the area (AERONET, MISR, and MODIS data) in Section 6.3.3; and the episode with smoke and dust is examined in Section 6.3.4. Finally, conclusions of this study and suggestions for further research are presented in Section 6.4.

6.2. Data and method

The reference measurements were carried out in Girona, which is a small city located in northeastern Spain (Southern Europe), about 30 km from the Mediterranean Sea, 100 km northeast of Barcelona, and 40 km from the Pyrenees (Figure 6.1). It has a population of almost 100,000 inhabitants and an average elevation of 75 m above sea level (asl). Girona enjoys a Mediterranean climate, with mild winters and hot summers, and maximum precipitation during autumn and spring. The measurements for the present work are performed at the weather and radiometric station (41.96 N, 2.83 E, 115 m asl) located on the roof of a building of the University of Girona.

Data used cover the period from June 2012 to June 2014. The MFRSR, which is fully described in the work of *Harrison et al.* [1994], measures global and diffuse irradiances at six channels with nominal wavelengths 415, 500, 615, 673, 870 and 940 nm, and with 10 nm full width at half maximum. The radiometer also has a sensor for the measurement of the broadband solar irradiance (300–1100 nm). Measurements of the global and diffuse components are performed every 15 s and averaged over 1 min intervals. As both irradiances are measured using the same detector for a given wavelength, this guarantees that the calibration coefficients apply for both components. The direct normal irradiance is obtained by subtracting the diffuse from the global irradiance, and is used to derive AOD for all narrowband channels, with the exception of the 940 nm channel, which is strongly influenced by water vapor.

At the station, global, diffuse, and direct broadband irradiances are also measured with thermopile sensors (CM11 pyranometers and CH1 pyrheliometer from Kipp & Zonen). Images from a Whole Sky Camera [*Calbó and Sabburg*, 2008] are available at 1-minute resolution. Other meteorological and radiometric variables are also stored.

In order to have an overview of the method used for determining the AOD and the AE at a high temporal resolution, we have summarized it in Figure 6.2 (its different steps are described and discussed in the specified references). In brief, the radiometric calibration of the MFRSR and the total optical depths are obtained through Langley regression, which are generated twice-daily [*Harrison and Michalsky*, 1994]. With a robust estimate of top-of-the-atmosphere responses, 1-min time series of total optical depths for each of five spectral channels at 415, 500, 615, 673, and 870 nm are calculated, as well as AOD (by removing the effect of ozone absorption and Rayleigh scattering) and AE (by using the Ångström formula for 500 and 870 nm wavelengths). Then, the resulting AODs and AEs are flagged to indicate cloud contamination. Lastly, we evaluate the uncertainty affecting AOD and AE. These steps are described in the following subsections.

6.2.1. Calibration of the MFRSR

The full width at half maximum of the MFRSR channels is narrow enough to apply the so-called Langley plot method to find the absolute calibration. We can express the signal corresponding to the direct normal irradiance incident on the sensor by the well-known Bouguer-Lambert-Beer law:

$$V(\lambda) = V_0(\lambda) e^{-\tau(\lambda) m_A} \qquad \text{(Eq. 6.1)}$$

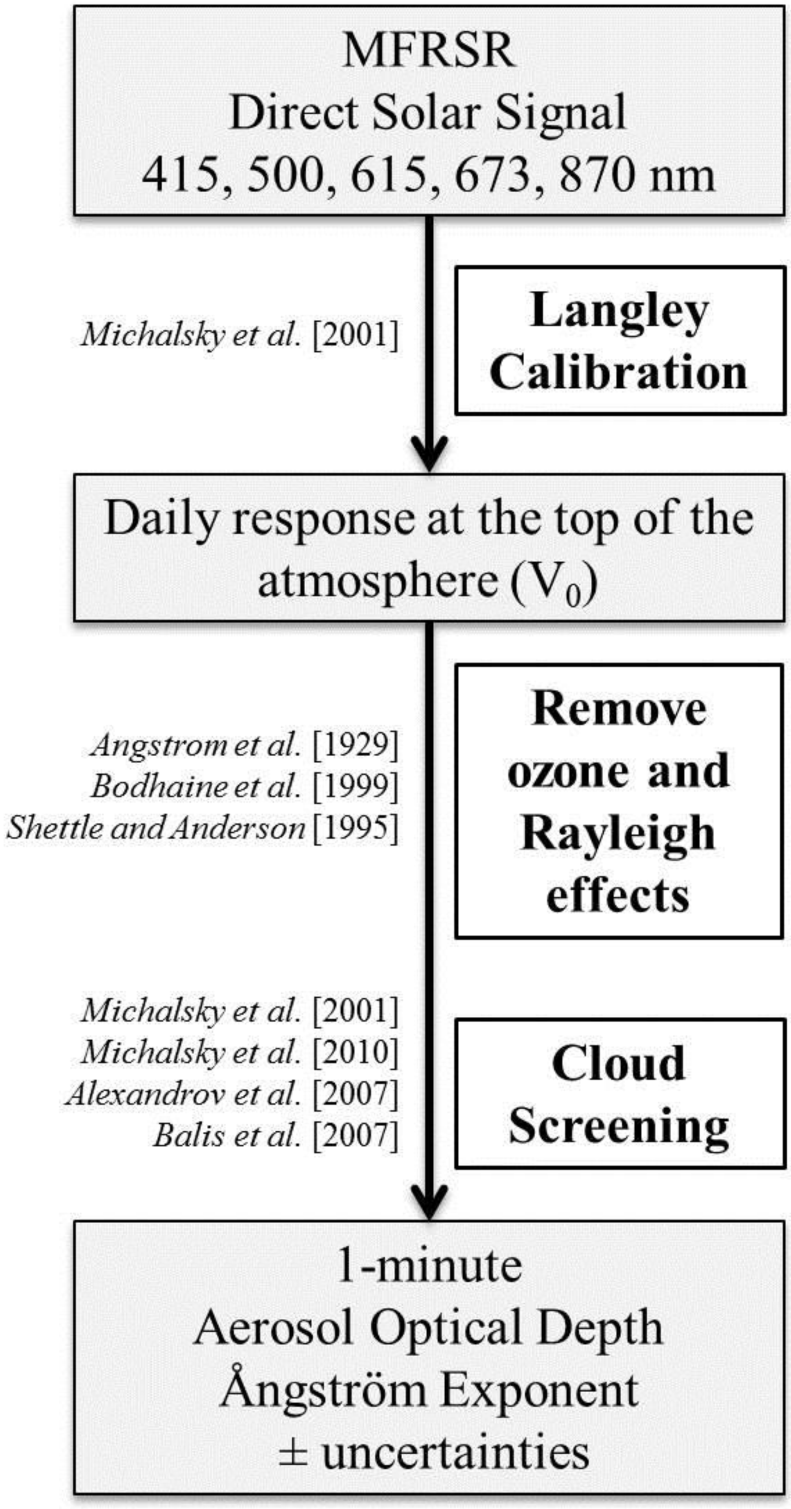
MFRSR
Direct Solar Signal
415, 500, 615, 673, 870 nm
Michalsky et al. [2001]
Langley Calibration
Daily response at the top of the atmosphere (V_0)
Angstrom et al. [1929]
Bodhaine et al. [1999]
Shettle and Anderson [1995]
Remove ozone and Rayleigh effects
Michalsky et al. [2001]
Michalsky et al. [2010]
Alexandrov et al. [2007]
Balis et al. [2007]
Cloud Screening
1-minute
Aerosol Optical Depth
Ångström Exponent
± uncertainties

Figure 6.2. Summary of the steps to obtain AOD and AE from MFRSR. The references for each step are also shown in the figure.

where $V(\lambda)$ is the response of the radiometer at the surface and $V_0(\lambda)$ would be the response at the top of the atmosphere; τ is the total column optical depth due to scattering and absorption by the different components of the atmosphere; and m_A is the air mass traversed by the direct solar beam relative to the air mass in the zenith direction. Taking the natural logarithm of each side in Eq. 6.1 gives,

$$\log[V(\lambda)] = \log[V_0(\lambda)] - \tau(\lambda) m_A \qquad \text{(Eq. 6.2)}$$

Then, when plotting values of $\log[V(\lambda)]$ obtained during a certain period versus m_A, a straight line can be fitted: the Langley regression line. The slope of this line is the total optical depth $\tau(\lambda)$, and the intercept corresponds to $\log[V_0(\lambda)]$ (i.e., the calibration for the channel). For the MFRSR the values of V_0 and τ are determined by applying the algorithm of *Harrison and Michalsky* [1994] to measurements performed during half a day (morning or afternoon) within a range of air mass $2 < m_A < 6$ and for periods with enough suitable data (at least 1/3 of the initial data points have to be retained after applying the method). For the period of study, we obtained, on average, one Langley regression each 3-4 days.

The Langley plot method is usually only applied in very stable, cloud-free atmospheric conditions. The ideal location for using the Langley method is high-altitude remote mountainous regions, or regions with pristine atmospheric conditions or at least regions where stable and low AODs frequently occur. Otherwise, several factors increase the uncertainty of a single Langley plot, such as the atmospheric variability over the course of the day (especially at low altitudes). Such problems suggest that a single Langley plot for a particular morning or afternoon may result in inaccurate derived products, such as AOD retrievals [*Michalsky et al.,* 2001]. Variants of the Langley technique, using a large set of calibration values measured on various days, for relatively stable atmospheric transmittance conditions, seem to offer the advantage of achieving a more extended set of data and, hence, a reliable statistical estimation of the calibration constant.

The procedure used in our study is explained in *Michalsky et al.* [2001], and is based on the studies of *Forgan* [1994]. To find the robust estimate of the calibration on a given day, we process the 20 nearest successful Langley plots in time. From these, the retrieval calibration constant V_0 is obtained from the average of the values of $\log[V_0(\lambda)]$ for which the ratio of the 415 nm to 870 nm intercepts (considered to be an indicator of stability) fall in the interquartile range. *Michalsky and LeBaron* [2013] demonstrate that this technique produces plausible calibrations compared to Mauna Loa Observatory calibrations. Calibration for the 500 nm channel of the MFRSR located at Girona is illustrated in Figure 6.3. The initial rapid decrease in the sensitivity for the first few months (see the red line in Figure 6.3) is common to all channels but the exact rate depends on wavelength (from 1% per month for 870 nm to 2.5% per month for 415 nm). This change indicates some diffuser and interference filter aging over the instrument lifetime. The same effect was found by *Augustine et al.* [2003], *Mazzola et al.* [2010], and *Michalsky and LeBaron* [2013] for other MFRSR instruments. Moreover, these authors found also a seasonal variability that was correlated with the temperature of the sensor. For the instrument at Girona, this seasonal variation in V_0 is not clearly apparent, probably due to the short period of time elapsed after installation.

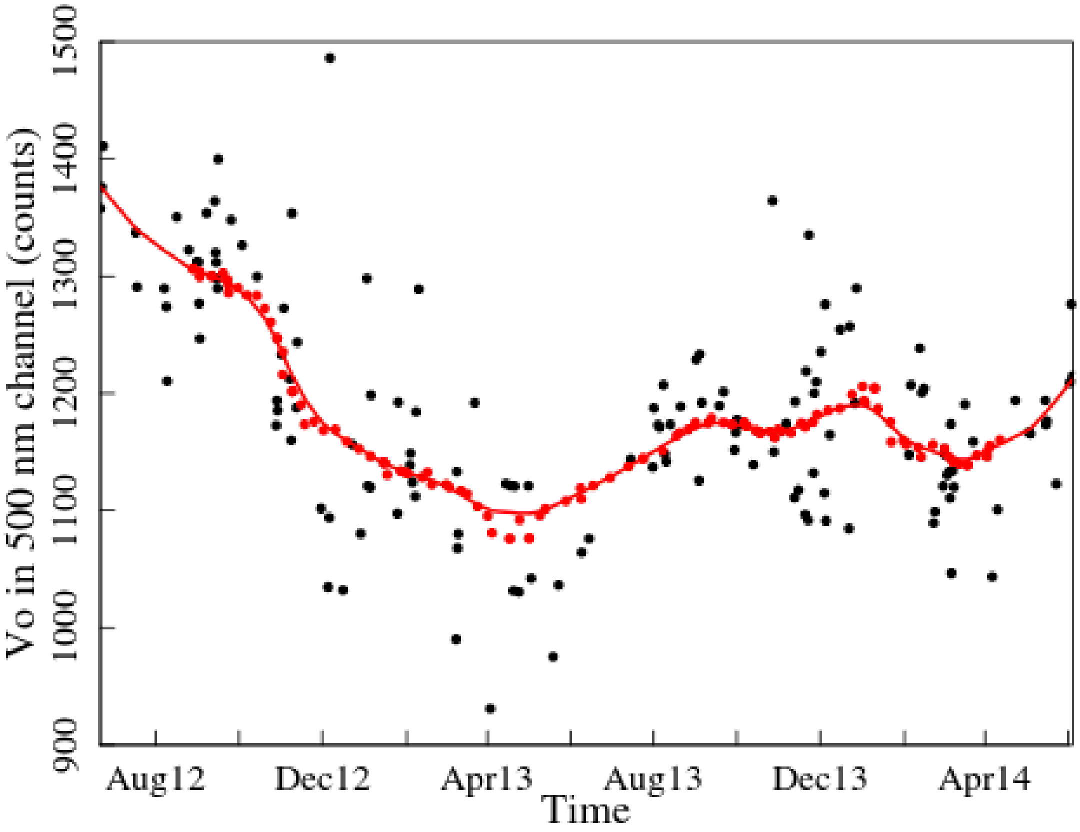

Figure 6.3. Time patterns of V_0 in the 500-nm channel of the MFRSR from June 2012 to June 2014. The black dots are the retrieved Langley plot intercepts. The red dots are robust estimates of V_0 based on a moving window of 20 Langley plot intercepts. The red line is a smooth curve fit to these data, based on Gaussian filter of 30-day width, from which daily V_0 values may be obtained.

6.2.2. Computing AOD and AE

Having calibrated each MFRSR channel, a straightforward application of Eq. 6.2 allows us to solve for the total optical depth τ corresponding to each minute and each channel. For the five channels selected (415, 500, 615, 673 and 870 nm) the effect of water vapor is negligible, so when clouds are absent, AOD (denoted τ_A in the equations) can be obtained from τ by using:

$$\tau = \tau_R + \tau_{O3} + \tau_{NO2} + \tau_A \qquad \text{(Eq. 6.3)}$$

where τ_R (Rayleigh optical depth) is calculated with the formulation of *Bodhaine et al.* [1999], using the pressure measured at the station and considering a concentration of CO_2 equal to 400 ppm. For the ozone optical depth τ_{O3}, we use the absorption coefficient tables developed by *Shettle and Anderson* [1995] for the Chappuis and Wulf ozone bands in the visible and near-infrared, and the total ozone column from the Ozone Monitoring Instrument (OMI, see, for example, *McPeters et al.*, 2008). Because only one total ozone value is available per day, the retrieved value is assumed to be applicable and constant for the entire day. The contribution to the optical depth by NO_2 absorption, τ_{NO2}, is only significant in high-pollution environments, so it is negligible for all channels in Girona and is not considered in our application.

Multi-channel instruments (such as MFRSR) can also provide information about aerosol particle size distributions because the wavelength dependence of scattered light, and hence the wavelength dependence of AOD, depends on the particle size. A simple way of describing the spectral variation of AOD is the Ångström formula [*Ångström*, 1929]:

$$\tau_A(\lambda) = \beta\,\lambda^{-\alpha} \qquad \text{(Eq. 6.4)}$$

The coefficient β corresponds to the AOD at 1 μm and quantifies the total aerosol loading in the atmosphere, and the Ångström exponent AE (α in the equations) is related to the size of the aerosol particles. Specifically, for optically predominant columnar contents of small aerosols (fine particles), such as those generated by pollutants, AE takes rather high values, often close to 2, while for extinction effects of large-size aerosols (coarse particles), as mineral dust or sea spray, it takes lower values, usually ranging between 0 and 0.5. From Eq. 6.4, AE can be derived from measurements of AOD performed over two wavelengths (for the MFRSR usually 500 and 870 nm), with the following expression:

$$\alpha = \frac{\ln(\tau_{A,870}/\tau_{A,500})}{\ln(500/870)} \qquad \text{(Eq. 6.5)}$$

6.2.3. Cloud screening

Time series of AOD obtained with this method can still be contaminated by the presence of clouds in front of the Sun, which can attenuate the direct solar irradiance, or the solar aureole, thus producing more diffuse solar radiation. The cloud screening used in this step is based on *Michalsky et al.* [2010], who assume that a solar beam passing through clouds exhibits much larger temporal variability compared to aerosol. Thus the observed variability of optical depth is frequently a good discriminator of clouds. Specifically, the *Michalsky et al.* [2010] algorithm tests the stability of AOD at 500 nm based on two filters applied in a 10-min moving window. The first, coarser filter takes the difference between each consecutive measurement, generating 9 differences, and also calculates the difference between the maximum and the minimum AOD in the window; the second filter scales the allowed variability according to the magnitude of the AOD. Each surviving datum passing both tests is considered a valid measurement of AOD for any further analysis.

In practice, optically thin clouds are very difficult to “screen out” because of their relatively low optical depth and substantial spatial/temporal homogeneity; these properties sometimes make very thin clouds “seem” like aerosols. In order to avoid this problem, *Alexandrov et al.* [2004], *Augustine et al.* [2008], and *Kassianov et al.* [2013] proposed new automated cloud screening algorithms for the MFRSR. More specifically, [*Kassianov et al.*, 2013] improved the method taking into account the value of the AE: the cases of quite high values of AOD combined with values of AE close to 0 were removed because of possible cloud contamination. However, considering the *Michalsky et al.* [2010] method used in this study, which is quite restrictive, and using the Whole Sky Camera, we observe that thin cirrus clouds are well removed. We can see in Figure 6.4 an example of a daily evolution of AOD after applying the whole procedure and this cloud screening method.

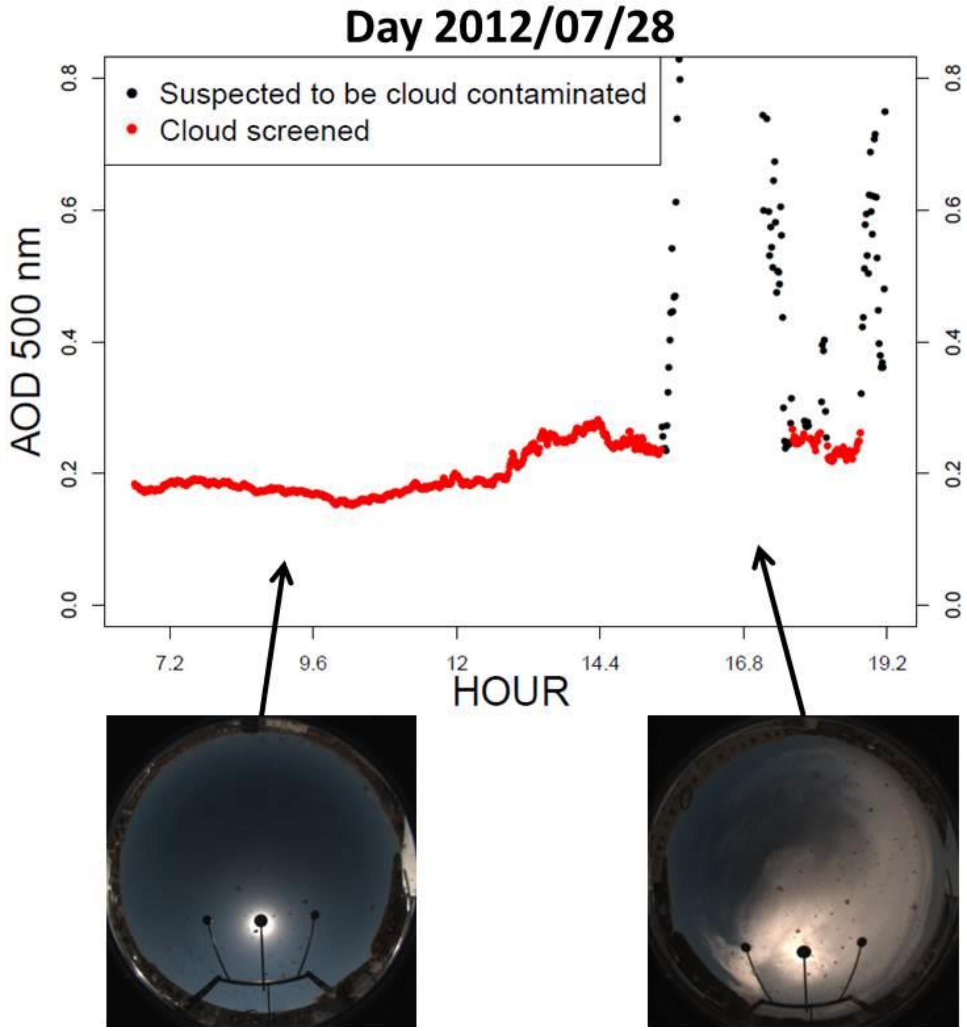

Figure 6.4. An example of the cloud screening results using the technique described in the paper. Red points were deemed true AOD, and black points were considered cloud contaminated. Sample images from the Whole Sky Camera show clear sky and Cirrus clouds, respectively.

6.2.4. Uncertainty of the derived aerosol properties

Uncertainty in the AOD derived from MFRSR measurements can be evaluated from Eq. 6.2 and 6.3, using the propagation of error analysis:

$$\Delta\tau_A(\lambda) = \sqrt{\left[\frac{1}{m_A}\frac{\Delta V_0(\lambda)}{V_0(\lambda)}\right]^2 + \left[\frac{1}{m_A}\frac{\Delta V(\lambda)}{V(\lambda)}\right]^2 + [\Delta\tau_R(\lambda)]^2 + [\Delta\tau_{O3}(\lambda)]^2} \qquad \text{(Eq. 6.6)}$$

The first and the second terms under the square root give estimates of the uncertainties in the calibration constant and the signal, respectively. The third term is the uncertainty due to Rayleigh scattering, and the fourth term due to ozone absorption. We neglect the uncertainty in the NO_2 absorption. Also, the uncertainty in air mass was considered negligible. The first contribution to uncertainty in Eq. 6.6 arises directly from the relative uncertainty of the calibration constant $V_0(\lambda)$, which was estimated as the mean standard deviation of each 20 nearest successful Langley plots in time, per unit air mass [*Michalsky et al.*, 2001; *Augustine et al.*, 2003]. The second contribution, associated with the measurement V, is not easily quantifiable but, following the results of *Alexandrov et al*. [2007], a 1.5% uncertainty in the signal per unit air mass was considered for all channels. For $m_A = 2$ (upper limit of the errors), the contribution of these two terms to the uncertainty in AOD values at the 415, 500, 615, 673 and 870 nm channels is 0.020, 0.015, 0.014, 0.013 and 0.012, respectively.

Each of the other two uncertainties can be separated into a pair of contributions, the first due to the method chosen to evaluate the partial optical depths and the second due to incorrect values of the physical quantities of interest, i.e., pressure and ozone contents respectively. However, based on the results found by *Mazzola et al.* [2010], the uncertainties due to instrument calibration and to signal measurements are at least one order of magnitude greater than the other contributions within all channels. Similar results were found by other authors *[e.g. Bouya et al., 2010; Janjai* *et al.*, 2008; *Vladutescu et al.*, 2013]. Thus, the AOD uncertainties found for MFRSR are similar to the values of 0.01 (0.02) for wavelengths longer than 440 nm (shorter than 440 nm) of the Cimel Sun-photometer used in the AERONET network [*Holben et al.*, 1998].

The uncertainty of AE is evaluated using:

$$\Delta\alpha = \frac{1}{\ln\left(^{870}/_{500}\right)}\left[\frac{\Delta\tau_{A,870}}{\tau_{A,870}} + \frac{\Delta\tau_{A,500}}{\tau_{A,500}}\right] \qquad \text{(Eq. 6.7)}$$

For average values of AOD for the 500 and 870 nm channels (0.14 and 0.07, respectively) and their estimated uncertainties, the uncertainty of AE is approximately 0.5. This value matches the uncertainty of AE found, for example, by *Mazzola et al.* [2010] with a MFRSR and by *Toledano et al.* [2007] with a Cimel Sun-photometer. It is important to remark that uncertainties of AE are quite lower (about 0.15) when we use the highest values of AOD; on the contrary, these uncertainties are much higher when we use values of AOD of the order of their error (i.e. equal or less than 0.02).

6.3. Results and discussion

6.3.1. Evolution of AOD and AE at Girona

In Figure 6.5a, we represent the daily averages of AOD at 500 nm (AOD_{500}) for the 2 years of measurements. There are 560 daily averages, which range between 0.01 and 0.48, with a mean value of 0.14. Higher AOD values are found during afternoon (mean value of 0.15) than during morning (mean value of 0.13). A seasonal pattern is observed: summer values are clearly higher than winter values. For all channels, a similar yearly evolution of AOD, which increases as wavelength decreases, is found. Similar values and evolution of AOD have been found by other authors in other regions of Spain [e.g. *Alados-Arboledas et a*l., 2003; *Estellés et al.*, 2007; *Toledano et al.*, 2007; *Valenzuela et al.*, 2011], as well as in other Mediterranean regions [e.g. *Gerasopoulos et al.*, 2003; *Perrone et al.*, 2005]. Based on the results of the treated period (and in spite of only 2 years of data cannot constitute a climatic study), we have represented the yearly behavior of the AOD_{500} data by boxplots in Figure 6.5b. It is worth noting that the box and the whiskers for July are considerably large if compared with other months (i.e., the variability in AOD is generally greater during summer months). This fact was also found by other authors [*Alados-Arboledas et al.*, 2003; *Toledano et al.*, 2007]. An episode of some days presenting very high AOD will be discussed in Section 6.3.4.

In Figure 6.5c, the daily averages of AE for the 2 years are shown. The mean value is 1.2, and individual values range between 0.0 and 2.2. We notice a strong day-to-day variation, i.e. a large variability in size/type of aerosols. The same was found for other Spanish sites [e.g., *Alados-Arboledas et al.*, 2003; *Prats et al*., 2008; *Toledano et al.*, 2007]. On average, the AE lies in the continental range for aerosol, i.e. between 1.0 and 1.7 [*Hess et al.*, 1998; *Eck et al.*, 2001]. Monthly boxplots for AE are represented in Figure 6.5d. Unlike AOD, AE does not show a clear seasonal pattern, as mean and median monthly values are nearly constant during the year, although a tendency for more fine particles in summer than in winter appears (i.e., AE is slightly higher in summer). The same was also found in other regions of Spain [*Toledano et al.*, 2007; *Obregón et al.*, 2012; *Bennouna et al.*, 2013; *Valenzuela et al.*, 2015]. Due to the large absolute error associated with AE retrievals, these results are less robust than those for AOD.

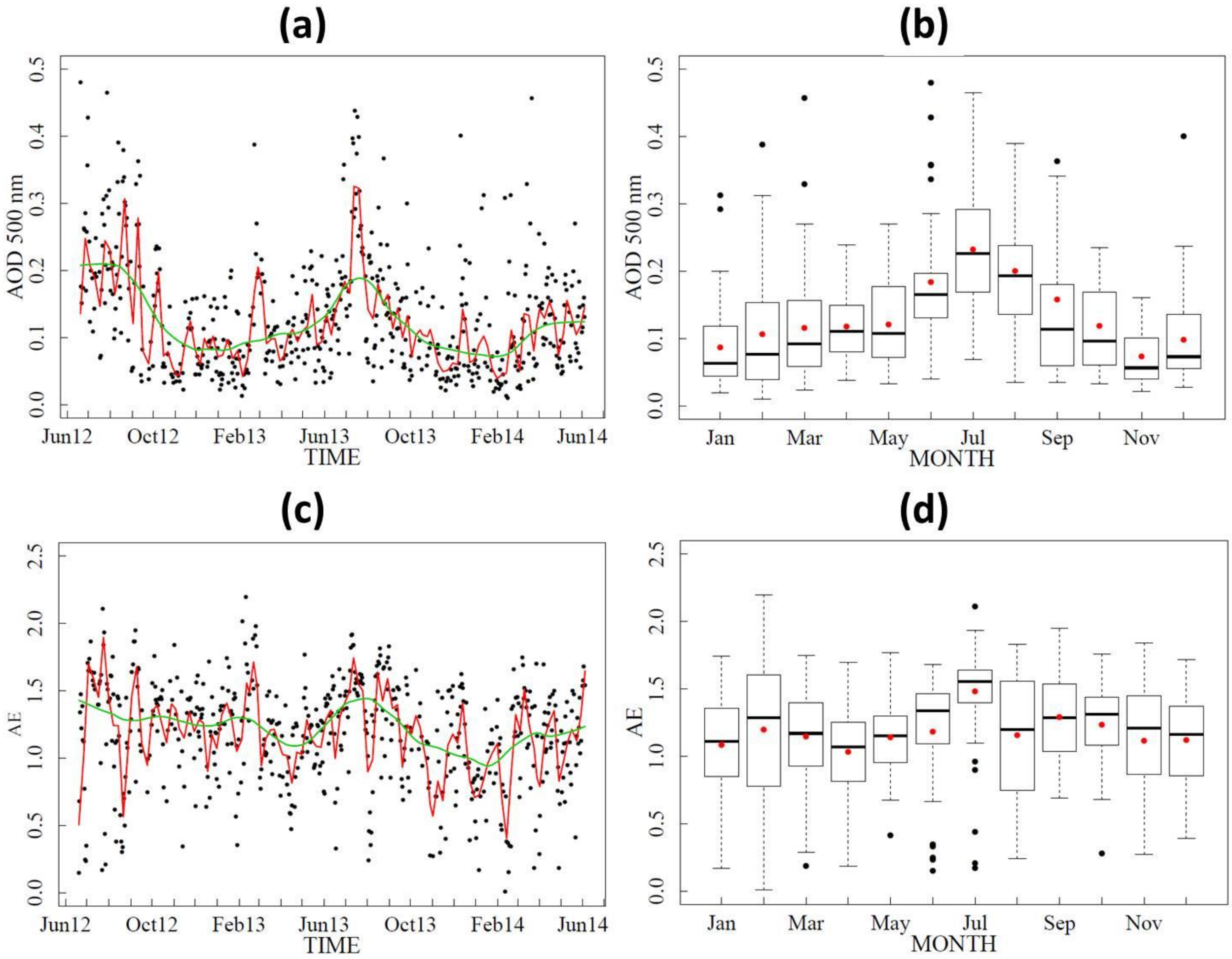

Figure 6.5. (a) Daily averages of AOD at 500 nm anc (c) of AE (black points). Smoothing in windows of ten years (red line) and three months (green line) are also shown. (b) Monthly boxplots of AOD in the 500 nm channel and (d) of AE red; red points represent the monthly mean values, whiskers correspond to 5 and 95 percentiles.

Although climatological conclusions cannot be obtained from our results of AOD and AE, we can state certain evidences. For example, Girona is not a city with a high concentration of aerosols. The seasonal cycle is typical of inland sites worldwide, as it coincides with seasonal variation in the photo-oxidation rates and the sources of aerosols [*Torres et al.*, 2002]. A slight increase of AE in summer seems to indicate that the summer increase in AOD is linked with an enhancement in the number of fine particles, i.e., tropospheric conditions in summer allow abundant sulfates and organic emissions (from increased vegetation activity) to swell through photochemical processes and hygroscopic growth [*Augustine et al.*, 2008]. In addition, considering the short distance from the coast, low values of AE in winter might be due to the contribution from maritime aerosols, which have more weight in the total atmospheric aerosol during winter due to lowered emissions from other sources. Indeed, unlike the common seasonal pattern of AOD, the seasonal pattern for AE depends on the relative contributions of the different types of aerosols (continental particles, desert dust, maritime aerosols, urban pollution, forest fire particles, etc.) on the total concentration of aerosols [*Pereira et al.*, 2011; *Sicard et al.*, 2011; *Obregón et al.*, 2014].

6.3.2. Radiative closure experiment

Achieving agreement between clear-sky shortwave broadband irradiance models and measurements provides a valuable test of in situ and ground based aerosol retrieval techniques [*Kato et al.*, 1997; *Halthore et al.*, 1998]. This type of radiative closure study is important to identify possible shortcomings in aerosol property retrieval algorithms, or in the treatment of aerosol in current radiative transfer models [*Michalsky et al.*, 2006; *Ricchiazzi et al.*, 2006]. Specifically, the measured value of the direct normal irradiance is compared to the value that is simulated by radiative transfer models fed with estimated, measured, or retrieved values of the aerosol optical properties in cloudless conditions. Closure experiments have been successfully conducted at different sites across the world [e.g. *Ge et al.*, 2010; *McFarlane et al.*, 2009; *Wang et al.*, 2009].

In our study, the Simple Model of the Atmospheric Radiative Transfer of Sunshine (SMARTS2) is used to calculate the aerosol effects on the direct broadband shortwave irradiance at the surface. SMARTS2 is a spectral parameterized model for calculating the direct beam, diffuse, and global irradiances incident on the Earth's surface [*Gueymard*, 1995]. The model covers the whole shortwave solar spectrum (280 to 4000 nm), and can be used to simulate the spectral or broadband irradiance that would be measured by a radiometer, such as a spectroradiometer, a pyranometer, or a pyrheliometer. The output of the model is compared in our study against pyrheliometer measurements obtained at the same site where AOD is evaluated.

Different inputs are used in the modeling. Surface pressure, relative humidity, and atmospheric temperature at the site level are obtained from the meteorological station. Integrated water vapor for the column above the site is taken from the ERA-Interim reanalysis [*Dee et al.*, 2011]. As we did with the MFRSR method explained before, the total ozone column above the site is taken from OMI [*McPeters et al.*, 2008]. To describe turbidity and aerosol type we feed the model with AOD_{500} and AE derived from MFRSR measurements. Finally, to define the conditions for gaseous absorption and atmospheric pollution we selected default pristine atmospheric conditions, as the radiometric and weather station is located just outside Girona (a small city with no relevant pollution sources around).

Modeled flux is compared with the observed 1-minute resolution solar broadband direct normal flux in Figure 6.6a, for all minutes with an available MFRSR estimation of AOD and AE. The scatterplot shows that there is an excellent agreement, especially for high values of direct solar irradiance, which results in a large correlation (R = 0.99), with a slope almost 1 (0.98) and a relatively small intercept value (17 W m^{-2}). Blue line in Figure 6.6b shows the histogram of the differences between simulated and observed direct solar irradiance; the mean bias (MB, model minus measurements) is 5.9 W m^{-2} (0.77% in relative terms considering the mean value of 768 W m^{-2}), with a root mean square deviation (RMSD) of 23 W m^{-2} (3.0%). These deviations are only slightly higher than results obtained by other authors [*Kassianov et al.*, 2007; *Wang et al.*, 2009b; *Ge et al.*, 2011], but it is important to remark that we perform the comparison for a large dataset (i.e., including very different atmospheric conditions and sun geometries) and not for some particular cases of some carefully selected days, as the authors mentioned before did.

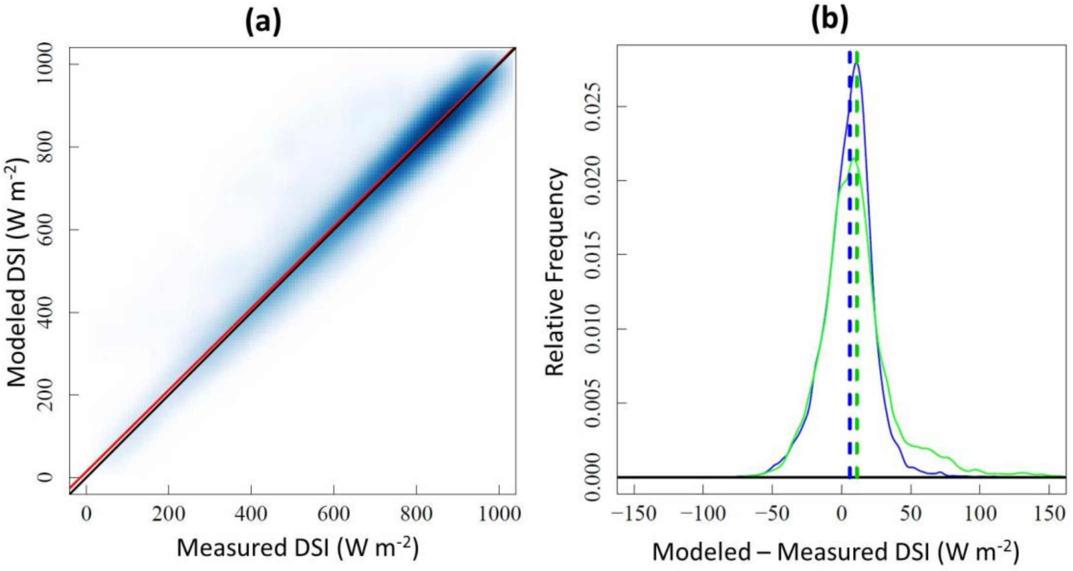

Figure 6.6. (a) Density representation of the scatterplot of simulated solar direct normal irradiance (DSI) using AOD and AE from MFRSR with respect to measurements (1-min averages); the 1:1 line (black line) and the linear regression fit (red line) are also represented. (b) Histogram of the differences between simulated and observed direct solar irradiance, using bins of 1.3 W m^{-2} (blue line for simulated data using AE from MFRSR and green line for simulated values using the rural aerosol model); dashed lines represent the mean bias.

Gueymard [2003] showed a sensitivity study for direct beam (examining sources of uncertainty in the radiative transfer modeling) and found that the primary contributions to uncertainty arise from AOD, followed by integrated water vapor and ozone. For our data, by adding 0.01 units to all AOD values used as input in the model (note that this is approximately the uncertainty of the MFRSR AOD$_{500}$ measurements) the mean difference in the direct flux reduces to 2.1 W m^{-2} (0.3%). This value is well within the instrumental uncertainty of 1% of the Kipp & Zonen CH1 pyrheliometer. So, the AOD uncertainty is confirmed as a principal source of the discrepancies between simulated and measured solar direct flux.

Nevertheless, other aerosol properties, such as AE, must also have an effect. In order to explore the sensitivity of the direct flux to this variable, and to know if the measured AE, despite its associated uncertainty, adds some useful information into the modeling, we perform an additional experiment. There, the rural aerosol proposed by *Shettle and Fenn* [1979] is considered, so the AE only depends on relative humidity and not using aerosol observations from the MFRSR. The agreement between modeled direct irradiances and measurements becomes slightly worse (see green line in Figure 6.6b): MB = 11 W m^{-2} (1.4%) and RMSD = 32 W m^{-2} (4.2%), but we can still conclude that the rural model describes quite well the typical seasonal evolution of aerosol for a site like Girona. The worsening is more apparent in the right tail of the histogram; these large model-measurement differences may be related to extreme values of AE. We will treat some particular cases of these large differences in Section 6.3.4.

The performed closure test confirms the suitability of the method for retrieving aerosol properties from MFRSR measurements, or at least its reliability when used to retrieve the AOD and AE at some particular site; consequently, we will use the dataset obtained at Girona as a reference for other methods of assessing AOD and AE.

6.3.3. Assessment of other aerosol products

In this section the MFRSR-based dataset is used as a reference for other alternative methods of assessing the aerosol properties at Girona. Concretely, we have used daily AOD and AE retrievals from the nearest Cimel Sun-photometer of the AERONET network and also from MISR and MODIS.

The Cimel sun-photometer is located in Barcelona (41.39 ºN, 2.12 ºE, 125 m asl), a city 100 km southwestward from Girona. This check is performed to assess the suitability of using a nearby site when aerosol data is needed, in other words, we intend to assess the spatial variability of the aerosol properties in the region. Barcelona, which unlike Girona is located on the coast, has a metropolitan area with a population of around 3.2 million inhabitants (>30 times that of Girona). We have used AERONET level 2.0 data, i.e. cloud-screened data with improved quality control. In the case of the Barcelona site, data are available for four channels: 440, 675, 870 and 1020 nm. Therefore, 675 and 870 nm channels are common to both instruments. To compare with the 500-nm channel of the MFRSR, we interpolate all channels of Cimel in order to estimate AOD at this wavelength and, subsequently, AE between 500 and 870 nm. Note that the instruments are different (spectral channels, sampling frequency, etc.), and algorithms applied to extract aerosol characteristics are also different (calibration method, cloud-screening, etc.). Despite this, the uncertainty in the retrieved aerosol properties is similar. See *Holben et al.* [1998, 2001] for more about the Cimel instrument and its characteristics.

In Figure 6.7a, we represent the evolution of AOD_{500} along the two years of data for both sites/instruments. Observing the dashed lines (which correspond to averaging on a 3-month running window), it is clear that both show the same seasonal pattern, with a summer maximum and a winter minimum. The MB for each of the three channels (500 nm, 675 nm and 870 nm) is shown in Table 6.1, besides other statistical indexes. The MB is very low compared to the uncertainty estimated for individual measurements, thus it can be argued that both stations present a similar mean AOD. However, a more detailed analysis exhibits some important differences between Girona and Barcelona. Solid lines in Figure 6.7a (which correspond to 10-day windows) show some disagreements between Girona and Barcelona for certain periods:

there appear peaks in one site that are not matched in the other (e.g., September 2012, May 2013). Further, in Figure 6.7b we represent the daily AOD_{500} at Barcelona against daily AOD_{500} at Girona, for the days when such information is available for both sites/instruments (differences in cloudiness conditions in Girona and Barcelona produce differences in the availability of aerosol outputs). It is noticeable that many days present differences in AOD between Girona and Barcelona much higher than the instrumental uncertainty (0.015). Correlation coefficients (see Table 6.1) for the three channels are around 0.82-0.84, showing again the differences in the daily values of AOD at both stations. This is also evidenced by the RMSD, which is well above the instrumental uncertainty of AOD measurements. Other authors that compared Cimel and MFRSR data with both instruments installed at the same place [e.g. *Alexandrov et al., 2008*; *Lee et al.*, 2010; *do Rosário et al.*, 2008; *Vladutescu et al.*, 2013] found better regressions (higher values of R and lower values of RMSD). Therefore, we conclude that, even if both cities are quite close to each other, the differences in the retrieved values of AOD at Girona and Barcelona are not caused by differences in the instruments, but they correspond to real differences in aerosol conditions (at least when simultaneous daily retrievals are considered). Note also that slope (A) and intercept (B) of the regressions in Figure 6.7b indicate that, for very clean conditions at Girona, AOD is slightly higher at Barcelona (maybe caused by the latter being a much larger – and more polluted – city than the former), whereas AOD is slightly lower at Barcelona when AOD is high at Girona. Finally, the few days showing large differences in AOD (that is, AOD in Girona two times higher than AOD in Barcelona, or vice versa), may be contaminated by clouds, since the daily averages of AOD for these particular days were performed with only a small number of cloudless moments (not shown).

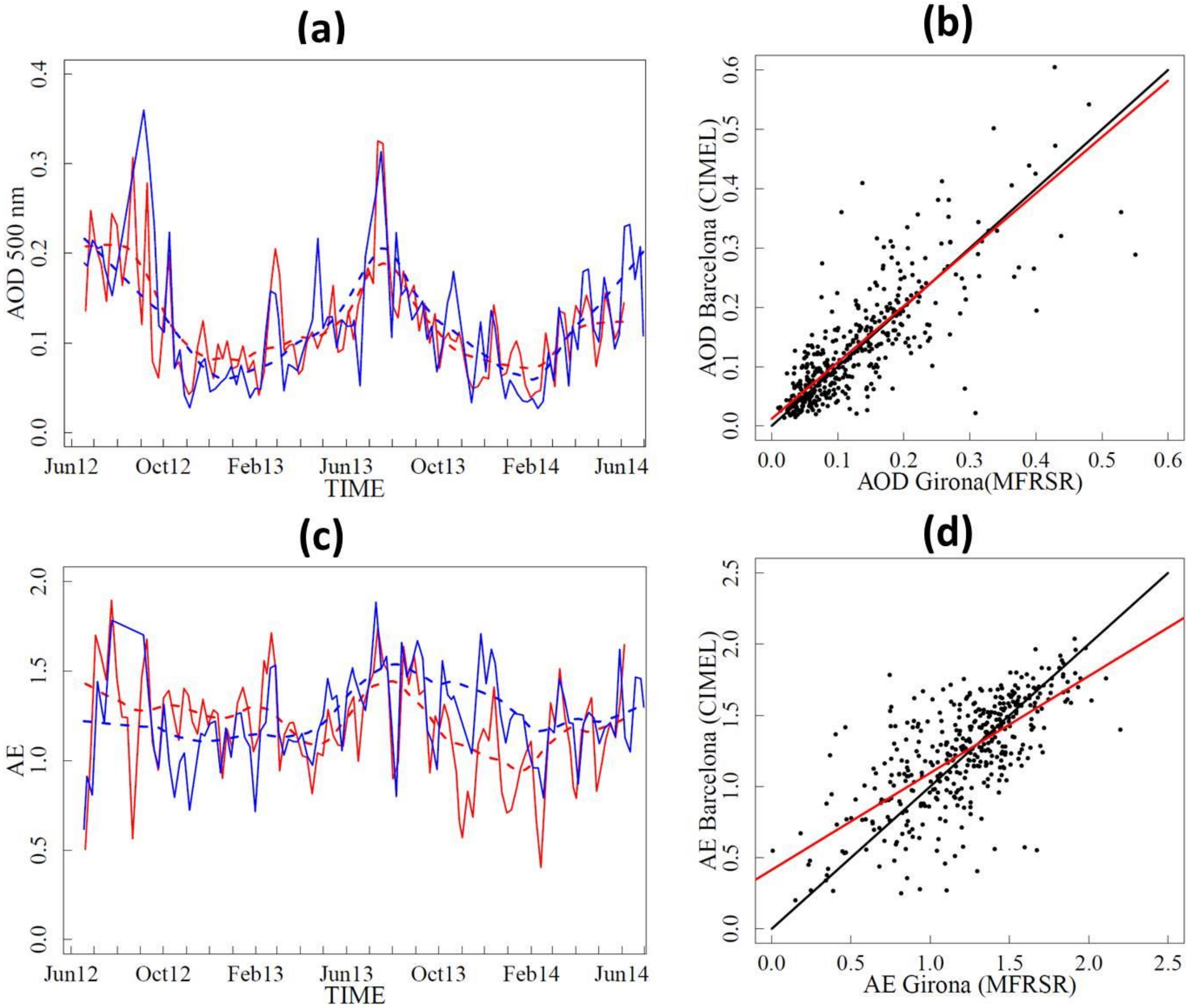

Figure 6.7. (a,c) Behavior of AOD at 500 nm and AE, respectively. Values from MFRSR are in red, those from Cimel are in blue. Solid lines correspond to smoothing in windows of ten days, dashed lines represent fits in windows of three months. (b,d) Scatterplots of the daily values of AOD at 500 nm and AE, respectively, obtained by Cimel versus obtained by MFRSR. The 1:1 line (black lines) and the linear regression fits (red lines) are also shown.

Table 6.1. Statistical comparison of daily AOD/AE retrievals from Cimel (in Barcelona) and satellite instrument (MISR and MODIS onboard Terra/Aqua, for the cells containing Girona) retrievals with that from MFRSR (in Girona). N is the number of days used in each comparison; MB is the mean bias of Cimel or satellite data with respect to MFRSR; RMSD is the root mean square deviation; R, A and B refer respectively to the correlation coefficient, slope and intercept of the regression line.

		Channel	N	MB	RMSD	R	A	B
AERONET	AOD Cimel	500	413	0.004	0.06	0.82	0.95	0.012
	AOD Cimel	675	413	0.001	0.04	0.82	0.94	0.014
	AOD Cimel	870	413	0.001	0.03	0.84	0.94	0.015
	AE Cimel	500-870	413	0.03	0.29	0.69	0.68	0.41
SATELLITE	AOD MISR	555	61	-0.027	0.04	0.92	0.81	0.002
	AOD MODIS T	550	493	-0.008	0.08	0.70	0.87	0.010
	AOD MODIS A	550	505	0.009	0.08	0.70	0.91	0.021

Results for the retrievals of AE can be found in Figures 6.7c and 6.7d, and also in Table 6.1. As for AOD data, evolutions built with a 3-month smoothing show a similar behavior, with values of AE in the continental range. In Table 6.1 we observe that the agreement between both sites/instruments when retrieving AE is similar to that found in other studies having the instruments at the same place [*Alexandrov et al.*, 2008; *Augustine et al.*, 2008; *Ge et al.*, 2010; *Vladutescu et al.*, 2013], i.e. MB of 0.03 and R of about 0.7. The MB is considerably lower than the uncertainty of around 0.5 in the derivation of AE, and thus we must consider both stations as representative of the same mean conditions, at least to the level allowed by the uncertainty, as for AOD. However, important discrepancies are found again for certain periods: the 10-day smoothing shows differences close to the uncertainty level. At the daily resolution, as is shown in Figure 6.7c, differences between AE in Barcelona and Girona are more noticeable. This is confirmed by a value of R = 0.7, and the RMSD, which is close to 0.3. From Figure 6.7d (and from the values of slope A and intercept B of the regression) we see that there is a tendency to find lower values of AE in Barcelona when AE is high in Girona, and higher values in Barcelona when AE is low in Girona.

Regarding satellite observations, they are acknowledged as an effective way to estimate global coverage of AOD. However, satellite aerosol retrievals are complicated by the fact that upward radiance received by the satellite is composed of light reflected by the surface and light scattered by atmospheric constituents, both particles and molecules. Accurate determination of AOD requires the separation of these radiation components, as well as discriminating between aerosols and clouds. This procedure is difficult over land, as the Girona location is, because land surface reflectance is often varying with location and time. In addition, the lower the spatial resolution, the less representative is this measurement for any particular site; for example MISR and MODIS have spatial resolutions of 0.5° and 1° respectively for daily aggregated data (Level 3), so for this location we would expect better results from MISR. The cells for Girona are represented in Figure 6.1 (see that an important part of the MODIS cell is occupied by water, which increases the difficulty of extracting a truly representative value of AOD for the entire cell). At mid-latitudes, MISR, because of its orbital cycle, will generally observe a given ground site only 3 to 5 times each 16 days; on the contrary, MODIS instruments scan the entire Earth's surface every 1 to 2 days. So, more cases are available for comparison against our dataset from MODIS than from MISR. Some authors stated that the MODIS Terra instrument is known to have degraded over time more than MODIS Aqua [e.g. *Levy et al*., 2013; *Lyapustin et al.*, 2014], but as we only use 2 years of data, we will ignore this effect. Notice that the spatial aggregation of MODIS and MISR from Level 2 to Level 3 influences the uncertainty in the Level-3 AOD [e.g. *Ruiz-Arias et al*., 2013].

In Figure 6.8a there is a representation of the temporal evolution of AOD for MFRSR, MISR and MODIS Terra/Aqua, all at 500 nm. In order to transform the AOD measured by MISR and MODIS to this wavelength, we consider an AE of 1.2 (mean value for Girona) and the original AOD values at 550 nm (MODIS) and 555 nm (MISR). Despite clear differences, all instruments give similar seasonal behavior (maximum values in summer and lower values in winter) and in the same range of values (0.0 – 0.4). Comparing daily values of AOD from MISR with that from MFRSR in the left scatterplot of Figure 6.8b and in Table 6.1, we can see that the correlation is quite good. Similar correlation coefficients (~0.9) were found by *Kahn* [2005] for other continental sites. Comparing AOD from MODIS with MFRSR, we can see in the middle and right scatterplots of Figure 6.8b and Table 6.1 that slightly worse relationships are found than with MISR (observe R and RMSD). Although the dataset of MODIS and MISR are different, using exactly the same days (those with MISR data), the results (not shown) indicate the same: MODIS does not agree as well as MISR with MFRSR data. The same conclusion was reached by *Ge et al*. [2010]. So, besides the higher spatial resolution, MISR is better than MODIS, at least over the analyzed area. Observe that the site of ground-based MFRSR measurements (Girona) is in the edges of the cells for both satellites; thus, an interpolation among different cells might enhance the ground-satellite comparison. It is true that in other parts of the world better correlation between ground-based and MODIS-derived AOD have been found [*More*, 2013], but it seems that MODIS algorithm does not perform well in certain areas, as for example *Wang et al*. [2007] have found even negative values for R. On the other hand, the comparison of AE between ground-based and satellite observations shows large disagreements (R values are as low as 0.4-0.5, and RMSD values are higher than 0.40), which are nevertheless within the uncertainty of the ground-based measurement.

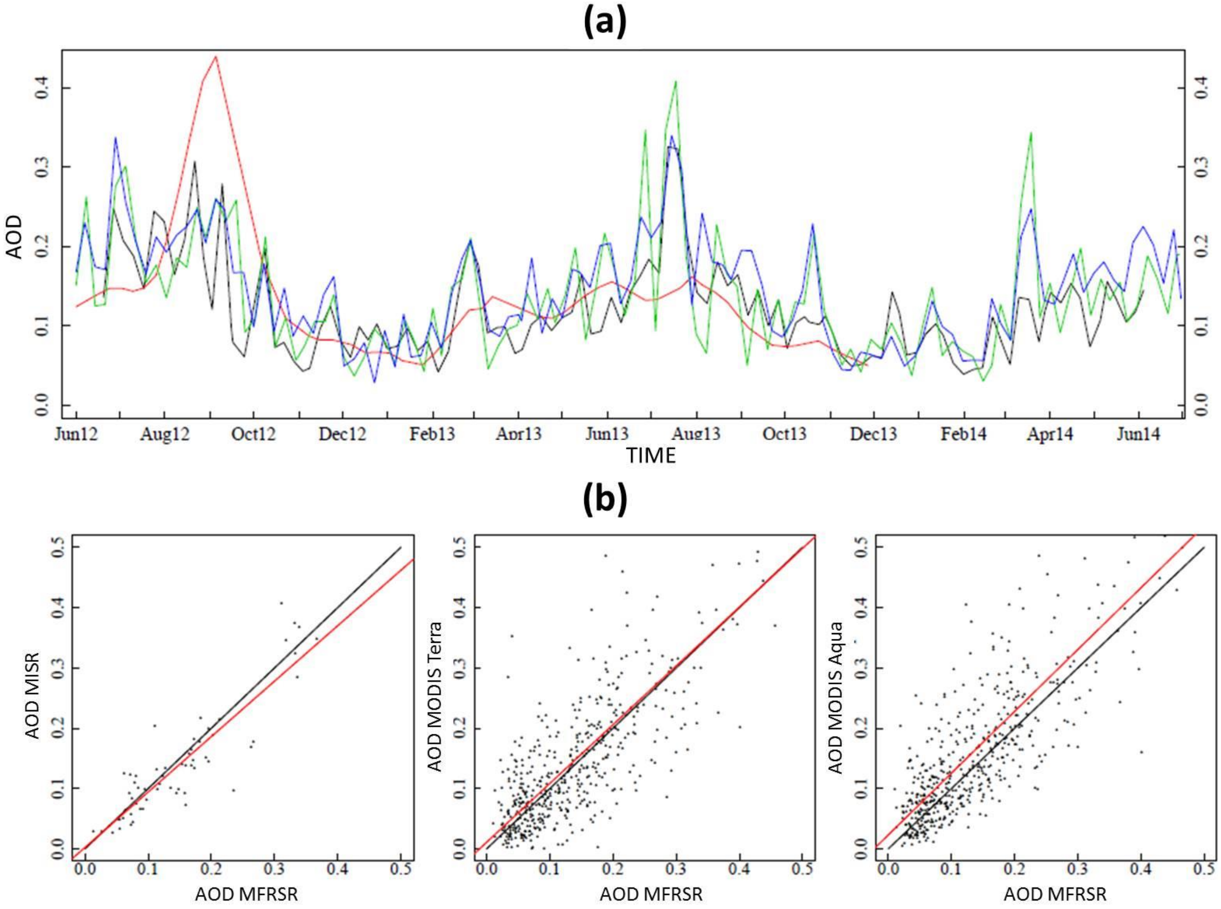

Figure 6.8. (a) Behavior of AOD at 500 nm derived from MFRSR (black line), MISR (red line), and MODIS Terra/Aqua (green/blue lines), in windows of ten days. (b) Scatterplots of daily AOD derived from MISR and MODIS Terra/Aqua against those from MFRSR; the 1:1 line (black lines) and the linear fits (red lines) for each case are also represented.

The ability of the two independent MODIS instruments onboard Terra and Aqua to produce the same results has been examined by *Remer et al.* [2006] but, due to different acquisition times, Terra and Aqua MODIS sensors cannot measure exactly the same conditions. Specifically, Terra and Aqua satellites overpass the study site approximately at 10:30 am (LST) and at 13:30 pm (LST), respectively. In our case, the mean bias is positive for both satellites, but larger for MODIS Aqua (see Table 6.1), i.e., there is a higher overestimation during afternoons with respect to the daily averages of AOD from MFRSR. This result is compatible with the fact that

AOD in Girona usually follows a diurnal variation with lower values in the morning and higher values in the afternoon (recall the mean values during morning and afternoon, section 6.3.1). Finally, another important result is that the MFRSR correlation is better with MISR than with the AERONET data from Barcelona (observe R in Table 6.1). Thus, MISR data represents better the variability of the aerosol load in Girona than extrapolating AERONET observations from Barcelona.

6.3.4. High aerosol event

At midday on 22 July 2012, two wildfires started in a region 60 km north of Girona and on the following days the burnt area reached almost 14,000 ha. The strong north winds that enhanced the fire also produced smoke that passed over Girona and reached Barcelona in the morning of the second day (Figure 6.9a). After the fire was extinguished, the same synoptic situation produced two completely cloudless, and clear (in the sense of low aerosol content) days. After that, in the last days of July (starting on 25 July), the synoptic situation changed, and there was an intense episode of Saharan dust intrusion over the whole Iberian Peninsula that also affected Girona. This situation was initiated by the establishment of meridional winds caused by the presence of a depression centered on the Portuguese coast and a center of high pressure over eastern Algeria (Figure 6.9b). Between these two systems, a powerful south flow drove warm winds and suspended dust into the region, increasing the AOD. We study this whole episode by using MFRSR aerosol retrievals, as well as comparing with MODIS data and validating with outputs of the SMARTS2 model (Figure 6.10). Only one day during the whole episode (26 July) is available from MISR, while only 3 days (afternoon of 23, 24 and morning of 25 July) are available from the AERONET site in Barcelona. So, we do not represent MISR and AERONET data in Figure 6.10, even if we comment their values below.

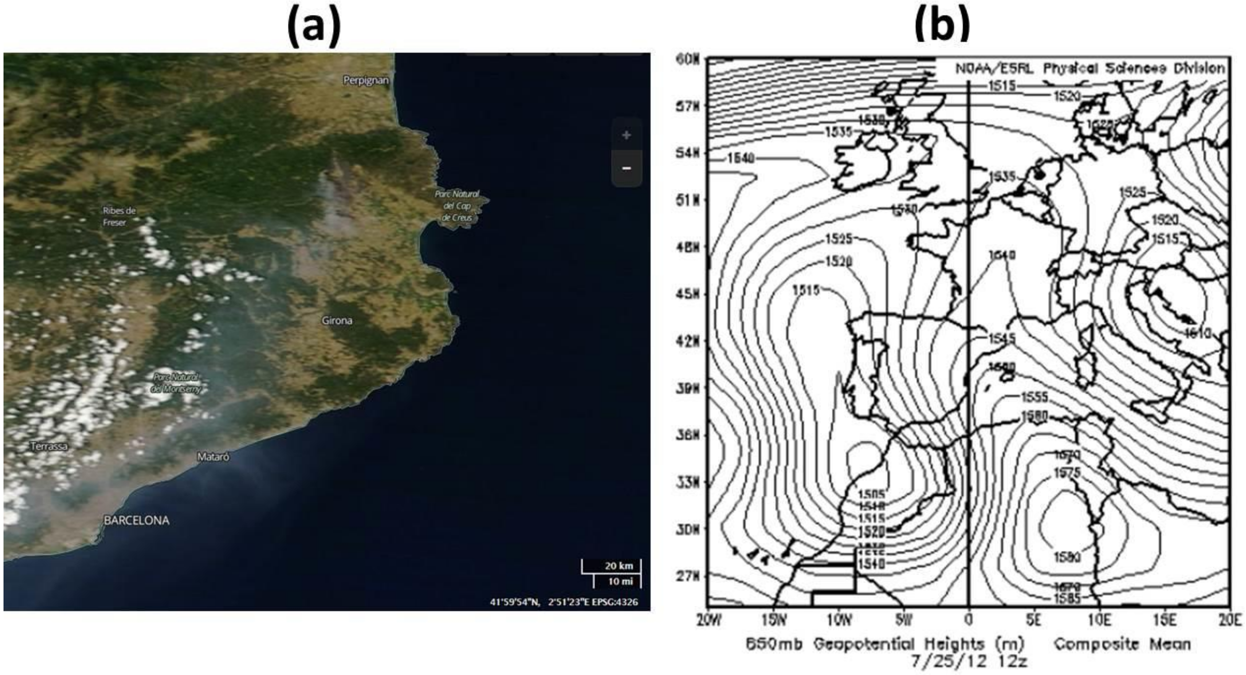
(a)
(b)
Perpignan
Parc Natural del Cap de Creus
Ribes de Freser
Girona
Parc Natural del Montseny
Terrassa
Mataró
BARCELONA
20 km
10 mi
41°59'54"N, 2°51'23"E EPSG:4326
NOAA/ESRL Physical Sciences Division
60N
57N
54N
51N
48N
45N
42N
39N
36N
33N
30N
27N
20W
15W
10W
5W
0
5E
10E
15E
20E
850mb Geopotential Heights (m) Composite Mean
7/25/12 12z

Figure 6.9. (a) Image of MODIS Terra (corrected reflectance) for 23 July 2012, 10.30 LST, showing the plume caused by the forest fire. (b) Geopotential height at 850 hPa for 25 July 2012 at 12 UTC according NOAA-CIRES Climate Diagnostics Center.

Figure 6.10 (next page). (a,b) Evolution of AOD (at 500 nm) and AE, from MFRSR (red), during the episode of the end of July 2012; bid dots correspond to 1-minute AOD and AE values; small dots correspond to cloud contaminated to 1-minute AOD and AE values; small dots correspond to cloud contaminated values; the green line corresponds to AOD (at 550 nm) and AE from MODIS Terra and blue line to MODIS Aqua. Several images of the Whole Sky Camera for these days are included to illustrate different sky conditions. (c) Direct solar irradiance evolution during the whole episode, directly measured (red line), calculated using a rural aerosol model (green line) and calculated using AE obtained by MFRSR in the model (blue line). (d) Relative differences between model and observed direct irradiance. Note that for large solar zenith angles, very high relative differences (beyond the represented scale) are reached when the rural aerosol is used (green line).

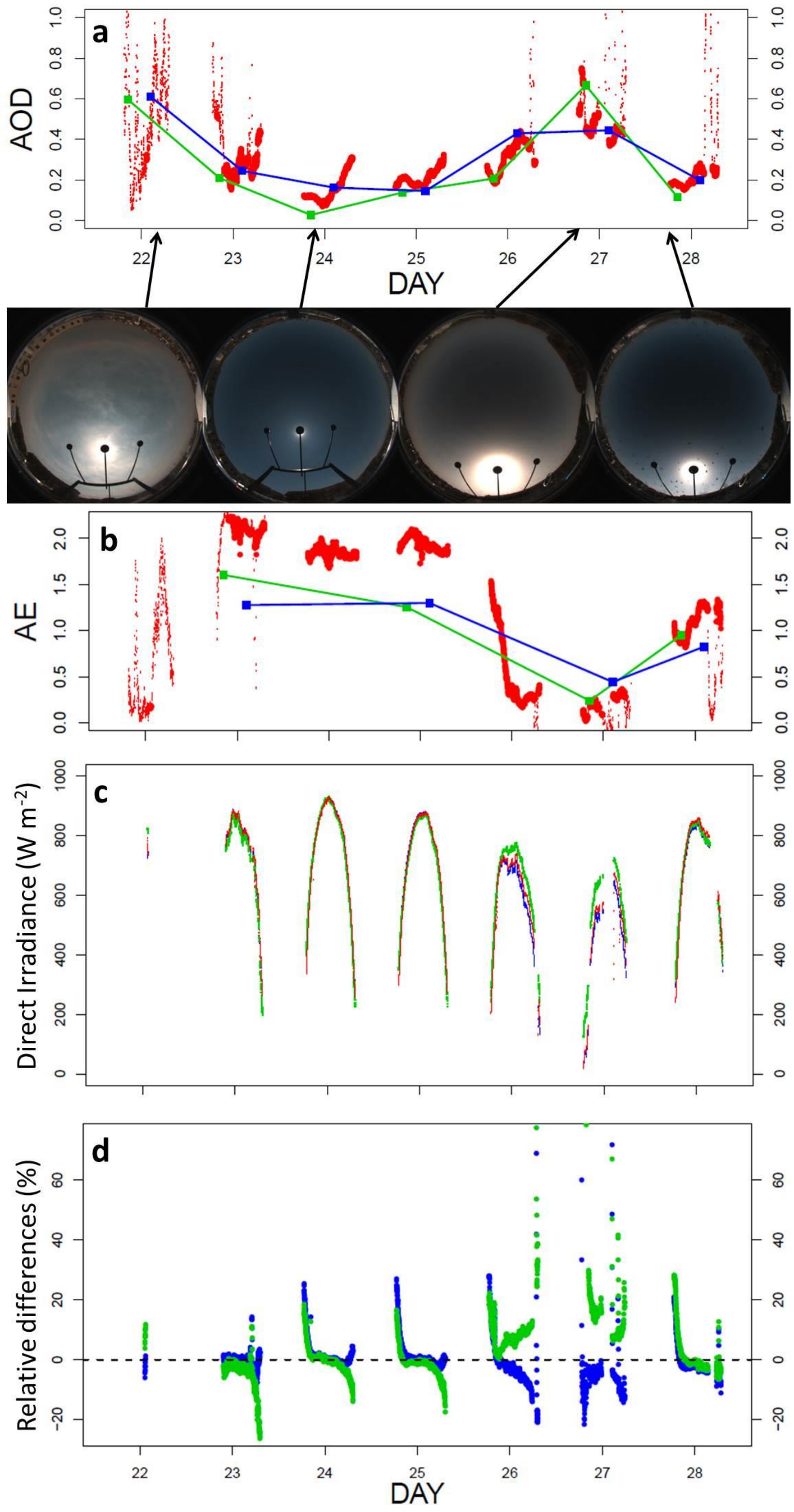
a
AOD
0.0
0.2
0.4
0.6
0.8
1.0
22
23
24
25
26
27
28
DAY
b
AE
0.0
0.5
1.0
1.5
2.0
c
Direct Irradiance (W m-2)
0
200
400
600
800
1000
d
Relative differences (%)
-20
0
20
40
60
22
23
24
25
26
27
28
DAY

Figure 6.10a shows the evolution of AOD from MFRSR (at 500 nm) and MODIS (at 550 nm) during the whole episode. There is an increase of AOD during the afternoon/evening of 22 July that the method considers as cloud contamination, but it is possibly due to the smoke coming from the wildfire, as the AE (Figure 6.10b) also increases simultaneously (see also a sky image of that afternoon in Figure 6.10). In fact, the AOD values from MODIS are very high (0.6). The next three days are almost completely cloudless and present low AOD values as the sample sky image of 24 July shows (note also that the agreement between MFRSR and satellite values of AOD is quite good during these days). AERONET data gives similar values as MFRSR and MODIS for these three days (mean daily values of 0.35, 0.18 and 0.13 for 23, 24 and 25 July, respectively). During 26 July there was a huge increase in AOD for both MFRSR and MODIS (MISR gives 0.36 for this day, a value that is between MODIS Terra and MODIS Aqua), and high AOD values (0.4-0.8) remained during the next day (27 July), while the AE values decreased and took low values (0.2-0.4) simultaneously. This corresponds to the Saharan dust episode (see sky image for 27 July). It is worth noting the good agreement between the morning (afternoon) values of AOD from MFRSR with MODIS Terra (Aqua) during these two days. Finally, on 28 July AOD returned to usual values of both AOD and AE in summer while it is clearly seen in the sky image for 28 July that the dust was gone. As commented, MODIS AOD captures very similar values as MFRSR AOD. Regarding AE, there are no MODIS values for July 22 and 26, but for the other days, despite some differences, the evolution is also well captured, with highest values in the cleanest days (23-25), lowest during the dust episode (27) and normal values later on (28); remember the comparison of AE between MODIS and MFRSR in section 6.3.3.

Finally, the simulated and measured solar broadband direct normal flux is shown for the cloudless moments of the whole episode in Figure 10c. When using the rural aerosol included in the model to describe AE, there appear to be discrepancies during the fire episode (22-23 July) and especially during the dust episode (26-27 July). Contrarily, the agreement is extremely good for the clear days (24-25 July and, in a lesser degree, 28 July). If we use AE obtained from MFRSR, the modeling results are as good as the previous results for the “normal” days (July 24, 25, 28), while they are clearly better for the “special” cases (fire smoke on July 22-23; desert dust on July 26-27). Specifically, the MB is close to 10 W m^{-2} and RMSD is close to 25 W m^{-2} for both flux closure comparisons during 24, 25 and 28 July. In contrast, the flux comparison using rural aerosol for days 22, 23, 26 and 27 July gives MB ~ 45 W m^{-2} and RMSD ~ 50 W m^{-2}, which are reduced to less than 17 W m^{-2} and 33 W m^{-2}, respectively, when using the retrieved AE from MFRSR in the modeling. The impact of using the measured AE instead of that derived from using a rural aerosol model is even clearer in the representation of the relative model-measurement errors (Figure 6.10d). These are quite large at both extremes of each day (i.e. when the solar zenith angle is large), but the use of measured AE reduces significantly the errors, in particular in days 26 and 27. Thus the description of the direct solar irradiance is very accurate when using the MFRSR measurements of AOD and AE (even in special events such as dust and fire episodes), so this is a further demonstration that these measurements are correct.

6.4. Conclusions and future research

This paper describes the retrievals of aerosol optical depth (AOD) and Ångström exponent (AE) from the analysis of two years of data taken with a Multifilter Rotating Shadowband Radiometer

(MFRSR) in a western Mediterranean site (Girona, NE Spain). The method is able to estimate 1-minute values of AOD for the first five spectral channels of the MFRSR, and estimates the AE from two of these channels (500 and 870 nm). Even if we only have two years of AOD and AE values, we can preliminarily state that AOD_{500} in Girona is low to moderate, with daily values ranging from 0.01 to 0.48 and an annual mean of 0.14. A second feature of the data is the clear seasonal cycle in AOD, with higher AODs in summer, and lower AODs in winter; this is consistent with previously published aerosol climatologies for nearby regions. Third, AE has an annual mean of 1.2 (typical of continental particles), but the wide range of values (from 0.0 to 2.2) indicates a large variability in aerosol size/type (though the instrumental uncertainty in this magnitude is high). The annual variation in particle size as inferred from the AE is small with slightly higher values in summer.

The reliability of MFRSR measurements is confirmed by means of a radiative closure experiment using SMARTS2, which is fed with the measured AOD and AE. The good agreement between simulations and observations for 2 years of data (mean bias 5.9 W m^{-2}, 0.77 %) verifies that the retrieved aerosol optical properties and the other input parameters in the SMARTS2 model are appropriate to represent real atmospheric conditions. We anticipate extending this validation in the future by analyzing the diffuse irradiance, but for this, it would be convenient to know other aerosol properties (e.g., the single-scattering albedo and the asymmetry parameter) either from MFRSR measurements or from satellite data.

The MFRSR retrievals of AOD and AE were then used as a reference with which other observations of aerosols were compared. With this, an assessment of the suitability of these other observations (in case no in-situ measurements had been available) was performed. First, the comparison between the MFRSR measurements at Girona and those obtained by a Cimel sunphotometer belonging to an AERONET station in Barcelona showed that fairly homogenous optical properties characterize the aerosol loading over the area (NE Spain). Secondly, we compared satellite products with the AOD retrieved for Girona. Both MISR and MODIS Level 3 products give similar seasonal evolution, despite clear differences in day to day comparisons (R = 0.92 and R = 0.70, respectively). From these results, we conclude that MISR performs better than MODIS, at least over a land site like Girona. The poorer results of MODIS compared to MISR can be attributed to lower spatial resolution and, in consequence, to difficulties of the MODIS algorithm when dealing with highly complex surface conditions and aerosol types. In addition, our results suggest that, in the case of the studied area, using MISR AOD is also better than extrapolating from a nearby AERONET site, at least regarding the variability.

Finally, when analyzing the data we found some episodes of high AOD. One of these episodes, between July 22 and 28, 2012, was then studied in detail to determine the sources of the aerosols. This particular episode was caused, firstly, by a forest fire, and then by a Saharan dust intrusion. These events, broadly noticed by local news reports, have been confirmed by AOD and AE evolution, and also by MODIS and ground based sky images. Under these extreme conditions, the use of AE extracted from MFRSR produces a good agreement between simulated and measured direct irradiances, unlike using a standard rural aerosol model (which otherwise describes quite well the typical seasonal evolution of AE for a site like Girona). So, aerosol optical retrievals from MFRSR are good to describe the direct flux, not only for normal atmospheric conditions, but also for special cases, such as these fire and dust episodes.

In summary, this research has confirmed, from MFRSR measurements, a robust methodology to derive continuous, high temporal resolution, columnar aerosol properties over a site. If no such ground measurements are available, data from satellites or from a nearby site can be used. The former (particularly from MISR) produce better estimations, but lack a continuous temporal coverture; the latter capture the overall seasonal evolution and average conditions, but may not capture some particular episodes, even for quite the next sites as those tested in the present study. In addition, this research has described the behavior of aerosols over a low polluted western Mediterranean site, showing the overall low aerosol content, pointing to the diversity of aerosol types that may be found, and describing particular high aerosol events that may occur sporadically. The description will be enhanced in the future, thanks to the continuous measurements taken at this site that will allow extending the database.

Chapter 7.

Effect of aerosols on burn width

This chapter, which contains not yet published material, deals with relating the measurements of AOD and burn width at a sub-daily resolution. The following sections are devoted to explaining the methodology and the results, as we consider that the topic has already been introduced, in particular in the review of the stat-of-the-art (Chapter 4) and in the introduction of Chapter 5. Specially, we have shown in Chapter 5 [*Sanchez-Romero et al.*, 2015] how DSI can be estimated from burn width of CSSR bands. Then, based on the extensive bibliography relating DSI with AOD, we hypothesize that the burn width is affected by AOD, in such a way that CSSR cards may be used to derive atmospheric aerosol content information at high temporal resolution. Section 7.1 provides a brief description of the instruments and methods used here for measuring burn width and AOD, as well as the specific data used in this research. In Section 7.2 there is a detailed presentation and examination of the results, that is the relationship between AOD and burn width of CSSR bands at a high temporal resolution, as well as a discussion of these results. Finally, we present the conclusions of this chapter in Section 7.3.

7.1. Data and method

As in Chapters 5 and 6, the measurements for the present work are performed at the weather and radiometric station located on the roof of a building of the University of Girona (41.96 ºN, 2.83 ºE, 115 m asl). Data used cover the period from June 2012 to January 2014.

The burn width from the Thies Clima CSSR has been used. It has been obtained with the semi-automatic method for retrieving the burn width at a resolution of 1-minute from the burnt CSSR cards, explained in Chapter 5. The MFRSR has been used to measure AOD; this instrument is fully described in the work of *Harrison et al.* [1994]. The 1-min time series of AOD at 500 nm has been obtained with the method explained in Chapter 6. Furthermore, we would also expect that the relationship of burn width with AOD would depend on the air mass and the different amounts of water vapor in the atmosphere. The air mass relative to that in the zenith direction, m_A, is calculated using the formula proposed by *Kasten and Young* [1989]. Only cases with m_A higher than 2 and smaller than 6 have been considered (see Chapter 6.2). Integrated water vapor for the column above the site is taken from the ERA-Interim reanalysis [*Dee et al.*, 2011]. At the end, we get a file with 6 variables: Julian day (and the fraction of the day), AOD from MFRSR, m_A, solar elevation, burn width from CSSR cards, and total column water vapor. Hereafter, AOD refers to the 500 nm channel.

Then, a comparison has been performed by starting from the 1-minute data of AOD and the 1-minute data of burn width of CSSR cards. In order to remove the cloud effects, the cloud-screening of MFRSR is used, i.e. we only use the records of burn width that correspond to moments when the MFRSR gives a value of AOD, which means that it is not affected by clouds.

We expect to find that the relationship of burn width with AOD would depend on m_A, as for the same conditions of AOD, the higher the m_A, the lower the DSI and the burn width. See, for example, Figure 7.1, which shows the relationship between AOD and burn width for two different ranges of m_A. Indeed, the range of burn width depends on m_A as there is a certain shift to the lower widths for high values of m_A, which matches with our hypothesis. The shape of the relation between burn width and AOD also changes with m_A. We would also expect some effect of different amounts of water vapor in the atmosphere, so we have plotted the points in different colors depending on the water vapor column. However, given the distribution of the points across the plot we can say that water vapor has not an important effect on the relationship of burn width with AOD. In summary, there is a certain relation between the two variables represented, with m_A as an important third variable, i.e. within a certain range of m_A, the less the AOD; the more the burn width. The relationship, however, is relatively weak as the dispersion of the points is quite important; moreover, it does not seem to be linear.

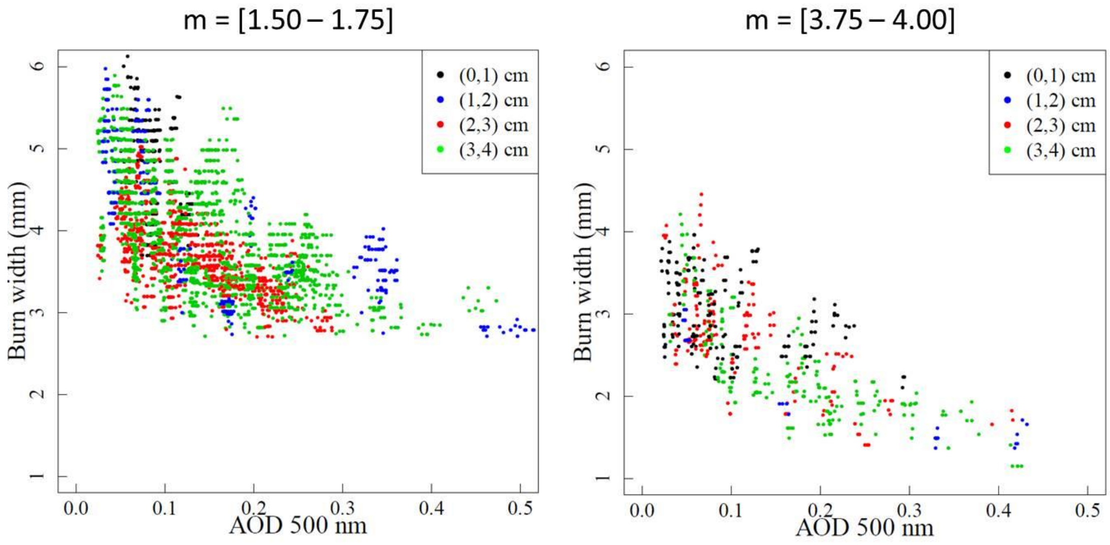

Figure 7.1. Scatterplot of AOD at 500 nm against burn width, in two different ranges of air mass. The colors of the points are related to the range of water vapor.

Although Figure 7.1 uses 1-minute data to show the relationship between AOD and burn width, we must recall that assuring the synchronicity between both measurements is not obvious. In order to avoid misalignments of the burn cards from their correct position in the CSSR device, which may produce an error of synchronization between burn width and AOD data, 10-minutes averages of both variables will be used onwards (remember that the comparison between DSI and burn width in Chapter 5 has been done at hourly resolution in order to avoid this misalignment). The average has been applied to 10 continuous minutes that passed the cloud-screening. For the other magnitudes, we also performed 10-minutes averages, except for m_A, which is computed as the mean value of the first and last value in the 10-minute interval.

Then, in order to describe the relation between AOD with burn width and m_A, we have built a look-up-table (Table 7.1). Intervals of 0.25 for both burn width and m_A have been used to bin the data. The AOD values in each cell of the table are the mean of all AOD values for the data within each range of m_A and burn width. In addition, each AOD value in the look-up-table has been smoothed with the values in the nearest cells using the equation 7.1,

$$AOD = \frac{1}{2}AOD_1 + \frac{3}{32}\sum_{i=1}^{4} AOD_{2,i} + \frac{1}{32}\sum_{i=1}^{4} AOD_{3,i} \qquad \text{(Eq. 7.1)}$$

where AOD_1 refers to the value of the central cell, AOD_2 to the values of the four adjacent cells, and AOD_3 to those from the four diagonal cells (this equation is modified when we refer to values in the edges of the table).

Green (red) values in Table 7.1 refer to the highest (lowest) AOD values, and dashes mean that there exist no cases with this combination of burn width and m_A at 10-minutes resolution. Note the correlation of AOD with burn width, for each range of m_A, and also the correlation of AOD with m_A for each range of burn width. It is important to remark that, before building the look-up-table, we had tried to find some empirical equation $AOD = f(burn\, widht, m_A)$ based on the Linke's turbidity factor, but the non-linearity of the relation made difficult to obtain a reliable equation (more discussion in Chapter 9).

7.2. Results and discussion

From this point, we use $\text{AOD}_{\text{MFRSR}}$ to express the AOD obtained by MFRSR and AOD_{CSSR} to express the AOD estimated from burn width of CSSR cards by using the look-up-table. We use $\text{AOD}_{\text{MFRSR}}$ as the "true" value, which is used as a reference to validate our estimation based on sunshine records.

In Figure 7.2, we show daily AOD evolutions during four different days at 10-minutes resolution. We chose to represent these days because their SD fraction is quite high (i.e. there are uninterrupted sunny conditions). In addition, we chose days that present a noticeable variation from morning to afternoon. Excepting the last one (Figure 7.2d), there is quite good agreement between both data and the daily evolutions are also very similar in all cases. Furthermore, it is possible to see, in particular in the first and last days, that for high values of $\text{AOD}_{\text{MFRSR}}$, the value of AOD_{CSSR} is remarkably lower, i.e., there is a certain underestimation for high AOD values. The apparent absence of AOD_{CSSR} to some sudden changes of AOD could be related to the resolution of air mass and burn width (0.25 for both cases).

Table 7.1. Look-up-table of AOD values from burn width (rows) and air mass (columns). The color code refers to the value of AOD: green (red) colors for high (low) values.

	1.125	**1.375**	**1.625**	**1.875**	**2.125**	**2.375**	**2.625**	**2.875**	**3.125**	**3.375**	**3.625**	**3.875**	**4.125**	**4.375**	**4.625**	**4.875**	**5.125**	**5.375**	**5.625**	**5.875**
0.125	NA	NA	NA	NA	NA	NA	NA	NA	NA	NA	NA	NA	NA	NA	NA	NA	NA	NA	NA	NA
0.375	NA	NA	NA	NA	NA	NA	NA	NA	NA	NA	NA	NA	NA	NA	NA	NA	NA	NA	NA	NA
0.625	NA	NA	NA	NA	NA	NA	NA	NA	NA	NA	NA	NA	NA	NA	NA	NA	NA	NA	NA	NA
0.875	NA	NA	NA	NA	NA	NA	NA	NA	NA	NA	NA	NA	NA	NA	NA	0.207	0.239	0.230	0.241	0.193
1.125	NA	NA	NA	NA	NA	NA	NA	NA	NA	NA	NA	NA	NA	NA	0.244	0.165	0.234	0.227	0.195	0.211
1.375	NA	NA	NA	NA	NA	NA	NA	NA	NA	NA	NA	NA	0.298	0.361	0.212	0.181	0.209	0.203	0.169	0.193
1.625	NA	NA	NA	NA	NA	NA	NA	NA	NA	0.368	0.218	0.295	0.273	0.243	0.204	0.171	0.185	0.159	0.138	0.174
1.875	NA	NA	NA	NA	NA	NA	NA	NA	0.216	0.305	0.254	0.221	0.184	0.187	0.172	0.150	0.157	0.120	0.118	0.162
2.125	NA	NA	NA	NA	NA	NA	0.214	0.314	0.222	0.188	0.200	0.165	0.153	0.158	0.144	0.134	0.126	0.095	0.125	0.093
2.375	NA	NA	NA	NA	NA	0.243	0.212	0.202	0.193	0.175	0.169	0.135	0.133	0.130	0.124	0.095	0.102	0.087	0.096	0.071
2.625	0.228	0.354	0.419	0.324	0.221	0.186	0.187	0.171	0.157	0.149	0.121	0.106	0.104	0.103	0.103	0.088	0.098	0.096	0.095	0.093
2.875	0.226	0.280	0.254	0.199	0.181	0.155	0.142	0.142	0.116	0.102	0.093	0.099	0.076	0.077	0.075	0.069	0.087	0.092	0.080	0.086
3.125	0.220	0.222	0.197	0.176	0.159	0.130	0.115	0.101	0.087	0.078	0.088	0.088	0.070	0.053	0.057	0.053	0.075	0.053	0.069	0.061
3.375	0.164	0.185	0.175	0.159	0.125	0.115	0.101	0.083	0.091	0.081	0.072	0.063	0.053	0.057	NA	NA	NA	NA	NA	NA
3.625	0.141	0.168	0.150	0.131	0.109	0.100	0.091	0.083	0.106	0.086	0.067	0.075	0.057	NA	NA	NA	NA	NA	NA	NA
3.875	0.117	0.134	0.126	0.101	0.082	0.083	0.098	0.060	0.099	0.074	0.059	0.049	NA	NA	NA	NA	NA	NA	NA	NA
4.125	0.076	0.101	0.097	0.087	0.080	0.089	0.066	0.092	NA	NA	NA	NA	NA	NA	NA	NA	NA	NA	NA	NA
4.375	0.069	0.084	0.091	0.083	0.088	0.083	0.078	NA	NA	NA	NA	NA	NA	NA	NA	NA	NA	NA	NA	NA
4.625	0.061	0.074	0.081	0.075	0.086	0.064	0.076	NA	NA	NA	NA	NA	NA	NA	NA	NA	NA	NA	NA	NA
4.875	0.061	0.065	0.077	0.066	0.084	0.075	NA	NA	NA	NA	NA	NA	NA	NA	NA	NA	NA	NA	NA	NA
5.125	0.063	0.060	0.072	0.069	0.078	0.084	NA	NA	NA	NA	NA	NA	NA	NA	NA	NA	NA	NA	NA	NA
5.375	0.039	0.043	0.047	0.083	0.071	NA	NA	NA	NA	NA	NA	NA	NA	NA	NA	NA	NA	NA	NA	NA
5.625	NA	NA	NA	NA	NA	NA	NA	NA	NA	NA	NA	NA	NA	NA	NA	NA	NA	NA	NA	NA
5.875	NA	NA	NA	NA	NA	NA	NA	NA	NA	NA	NA	NA	NA	NA	NA	NA	NA	NA	NA	NA

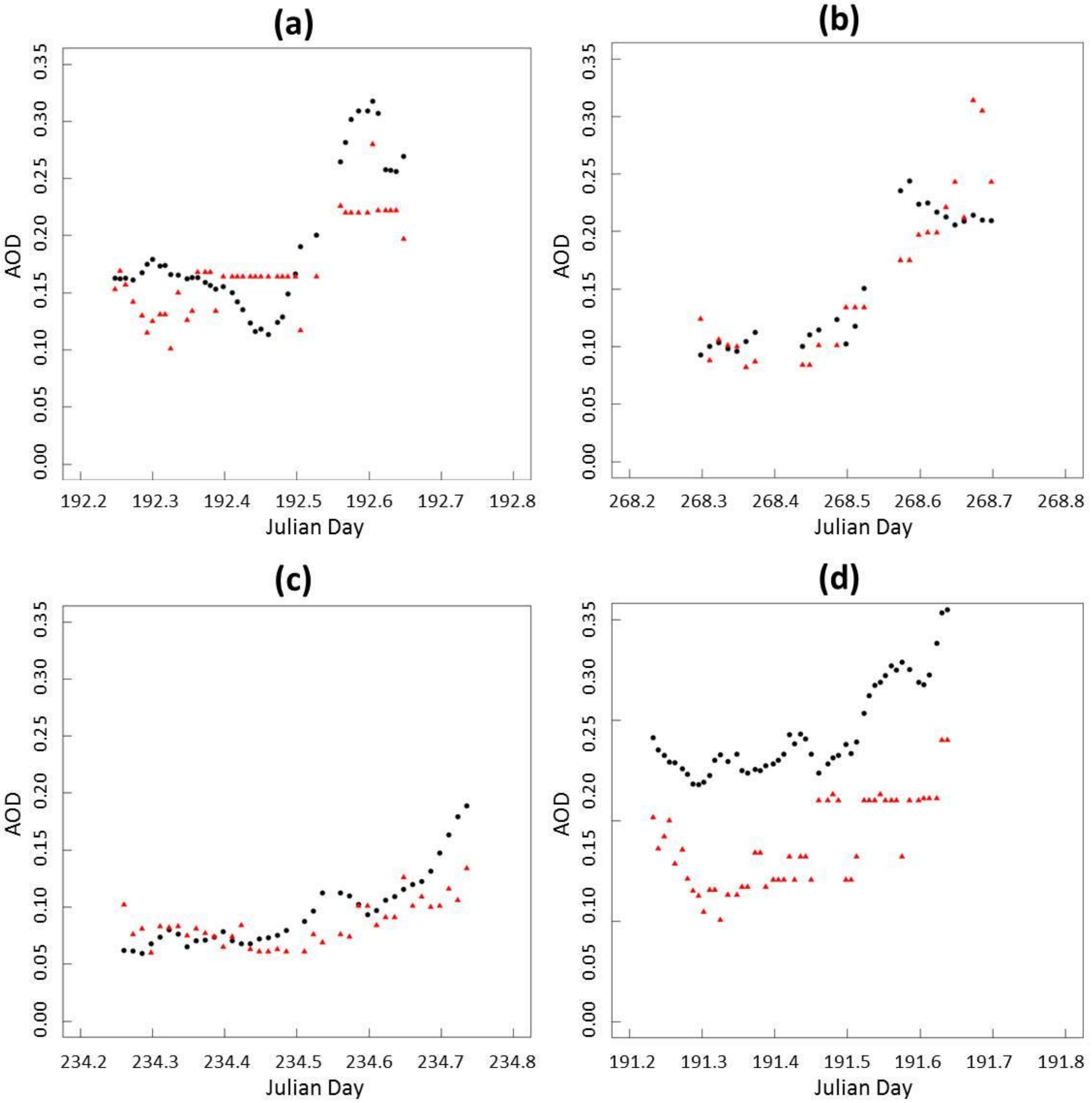

Figure 7.2. Four examples of daily evolution of AOD obtained from MFRSR (black points) or estimated from burn width (red triangles), at 10-min resolution. These days correspond to (a) 10th of July 2012, (b) 25th of September 2013, (c) 22nd of August 2013, and (d) 10th of July 2013 (d).

In order to show the overall comparison between measured and estimated AOD, the scatterplot between AOD_{CSSR} and AOD_{MFRSR} at 10-minutes resolution is represented in Figure 7.3a. The colors are related with the number of points in each region (note the legend in the right side).

There are 2,084 points, with a correlation coefficient of 0.65 and a RMSE of 0.067. Setting the intercept equal to 0, the slope is 0.83. Furthermore, the dispersion of the points of the scatterplot is quite high; especially, there is a clear underestimation of AOD for high values of AOD_{MFRSR}. This matches with what we saw in Figure 7.2. Note that we represent values for all seasons of the year, despite the CSSR uses different cards (see Figure 4.2).

In Figure 7.3b, box plots for the residuals between AOD_{CSSR} and AOD_{MFRSR} in 0.05-width bins are represented. Note that, even if the mean residual value is 0, there is a certain increase in the dispersion of AOD residuals when AOD_{CSSR} increases. We also indicate the number of points that are included in each bin, with almost 85% having AOD_{CSSR} values lower than 0.20. In addition, the data is evenly distributed over the total range (i.e., around the mean value), particularly for values of AOD lower than 0.3 (AODs ≥ 0.3 are non-significant).

If we represent similar boxplot of the residuals depending on solar elevation, which is directly related to m_A (Figure 7.3c), the figure shows a median and mean residual near 0 and dispersion almost constant for the different ranges of solar elevation. Nevertheless, there seems to be a slight increase of the dispersion for high values of solar elevation (low values of m_A), as well as some asymmetry around the median value (observe the line in the middle of the rectangle and the red triangles).

Figure 7.3 (next page). (a) Scatterplot of AOD_{CSSR} versus AOD_{MFRSR} at 10-minutes resolution. We also represent the 1:1 line (dotted line) and the linear regression fit (black line). (b) Boxplot of the differences between estimated and true AOD (centered in the values of the x-axis), where the top and bottom lines of the rectangle are the 3rd and 1st quartiles, and the line in the middle is the median (or the 2nd quartile); red triangles refer to mean values, and numbers on the top of each rectangle refer to the number of points of each box. (c) The same boxplot of (B) but depending on solar elevation.

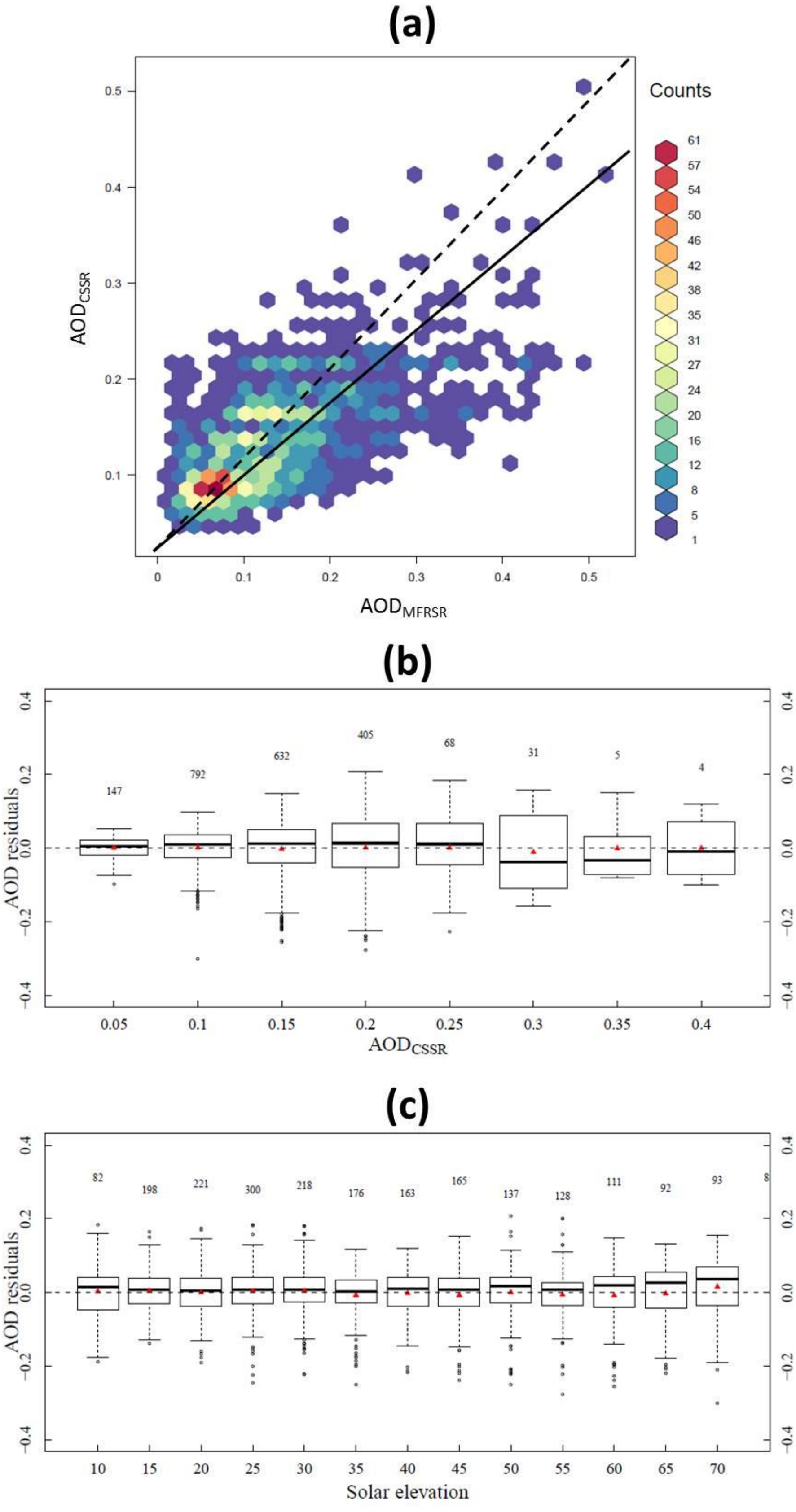
(a)
Counts
61
57
54
50
46
42
38
35
31
27
24
20
16
12
8
5
1
AOD$_{CSSR}$
AOD$_{MFRSR}$
0
0.1
0.2
0.3
0.4
0.5
(b)
AOD residuals
AOD$_{CSSR}$
147
792
632
405
68
31
5
4
0.05
0.1
0.15
0.2
0.25
0.3
0.35
0.4
−0.4
−0.2
0.0
0.2
0.4
(c)
AOD residuals
Solar elevation
82
198
221
300
218
176
163
165
137
128
111
92
93
8
10
15
20
25
30
35
40
45
50
55
60
65
70

To prove that the effect of AOD on CSSR cards is more visible on low solar elevations (Chapter 4), we reduce the dataset to cases with solar elevation lower than 15º (high values of m_A). Note that this study is also limited by the condition of $m_A < 6$ (solar elevation higher than around 10º). Moreover, we consider only evening values, as the effect of water deposits on the glass sphere of CSSR, producing losses of burning records, is more noticeable in the early morning than in the late evening (see section 4.2.2). The scatterplot between AOD_{CSSR} and AOD_{MFRSR} is represented in Figure 7.4a. There are 98 points, with a correlation coefficient of 0.80 (so quite improved with respect that for the whole dataset) and a RMSE of 0.055 (slightly lower than for the whole dataset); setting an intercept equal to 0, the slope is 0.84. So, the improved values of R and RMSE using these cases instead of the whole dataset verify that the effect of AOD on CSSR cards is more important on low solar elevations. As we observed before, there is a clear underestimation of AOD for high values of AOD_{MFRSR}, resulting in the slope being lower than 1.

These 98 points correspond to 43 different days. Figure 7.4b shows the scatterplot of mean burn width against mean $AOD_{MFRSR,}$ for these days assuming only evening cases from solar elevation < 15º and until the burn disappears (i.e., without the restriction of $m_A < 6$). In fact, another reason for using only evening cases is that the local horizon is higher than 5º for the sunrise directions (except during summer period) while the horizon for the sunset is much lower during most months. This figure is similar to Figure 7.1, but here each point represents a day. From the 43 points, it is possible to see a good correlation between both variables: the higher the "mean daily AOD", the narrower the "mean burn width" near sunset. Concretely, the correlation coefficient is –0.75. This matches with the studies of *Jaenicke and Kasten* (1978), *Helmes and Jaenicke* (1984, 1985, 1986), and *Horseman et al.* (2008), which stated that the impact of aerosols on SD occurs particularly just after sunrise and before sunset because of the long distances that the direct beam travels to reach the Earth’s surface, so being much more affected by the presence of aerosols.

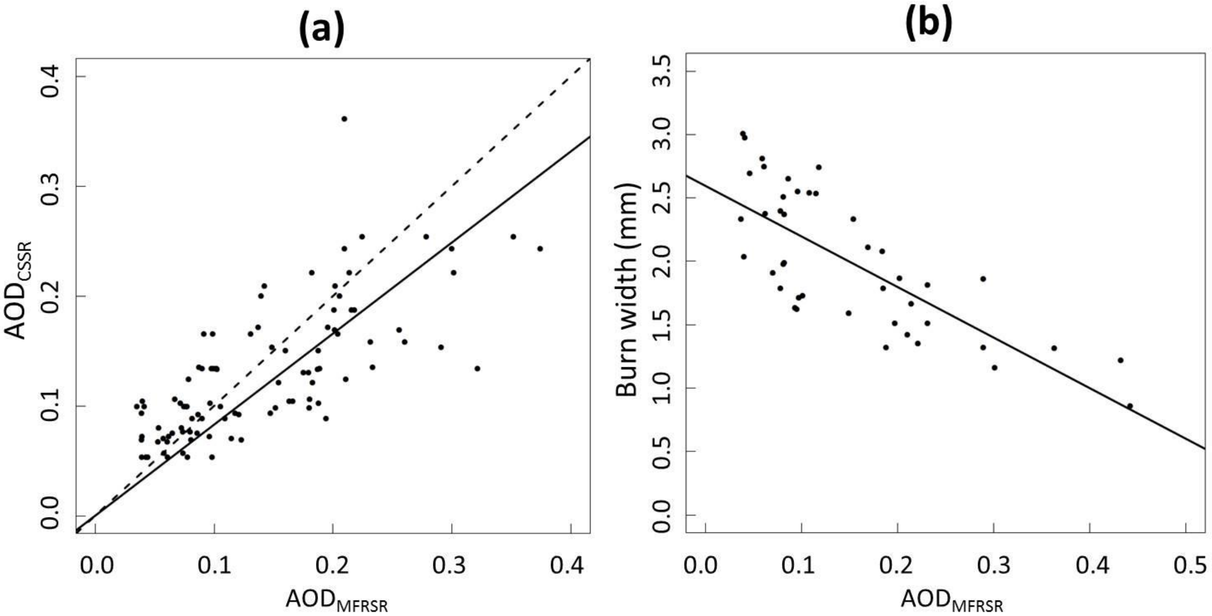

Figure 7.4. (a) Scatterplot of AOD_{CSSR} versus AOD_{MFRSR} on 10-minutes resolution (solar elevation < 15º); we also represent the 1:1 line (dotted line) and the linear regression fit (black line). (b) Scatterplot of mean burn width versus AOD_{MFRSR} (solar elevation < 15º) for each evening; we also represent the linear regression fit (black line).

7.3. Conclusions

The objective of this chapter was to make evident that the burn width is affected by AOD, so to check if CSSR cards can be used to derive atmospheric aerosol content at high temporal resolution. We found that there is a non-linear relation between both variables which in turn depends on the value of m_A. Then, we have built a look-up-table in order to describe the relation between AOD with burn width and m_A. This description has been done at 10-minutes resolution, in order to avoid the problem of possible misalignments of the burn cards from their correct position in the CSSR device.

The scatterplot between AOD_{CSSR} (AOD estimated from burn width of CSSR cards by using the look-up-table) and AOD_{MFRSR} (AOD obtained by MFRSR) gives a correlation coefficient of 0.65 and a RMSE of 0.067. With these results, we can confirm that AOD leaves some signal in the CSSR cards, more concretely, in the burn width. Thus, it is possible to reconstruct AOD variations at a high resolution (10 minutes) using burn width, although we must recognize the high dispersion of the estimates and the clear underestimation for high values of AOD. Indeed, the magnitude of the effect of aerosols on burn width is a complex issue and further research may consider taking into account the perforated part of the burn besides the burn width (perforated plus scorch parts). In addition, the inclusion of the meteorological variables (wind, humidity, temperature, etc.) could give better AOD estimations from burn width.

We also considered burn width only during cloudless sunsets, in order to proof the studies of *Jaenicke and Kasten* (1978), *Helmes and Jaenicke* (1984, 1985, 1986), and *Horseman et al.* (2008), which stated that the impact of aerosols on CSSR cards occurs particularly just after sunrise and before sunset. Thus, considering only sunsets, the mean burn width, for solar elevation values lower than 15º, matches quite nicely with AOD values from MFRSR. Concretely, the reduction of burn width when AOD increases shows a correlation coefficient of –0.75.

We conclude that detailed studies of the burn in CSSR cards (in particular during cloudless sunrises and sunsets) provide the possibility to determine variations in the atmospheric aerosol loading. This can be done for short time scales but, as long-term records of CSSR cards are available at some historical meteorological stations, it would be possible to obtain variations in atmospheric aerosol loading for long time scales.

Chapter 8.

Reconstruction of long-term aerosol optical depth series with sunshine duration records

This chapter is a transcription of the paper:

Sanchez-Romero, A., A. Sanchez-Lorenzo, J. A. González, and J. Calbó (2016), Reconstruction of long-term aerosol optical depth series using sunshine duration records, *Geophysical Research Letters*, 43, 1296–1305, doi:10.1002/2015GL067543.

The paper reports the suitability of sunshine duration records as a proxy for the reconstruction of atmospheric aerosol content in long temporal scales. Specifically, we have treated cloudless summer days in 16 stations throughout Spain. These reconstructed series show an increase in AOD from the mid-1960s to the 1980s, followed by a decrease until the present, in agreement with changes in anthropogenic aerosol emissions and with opposite trends of solar irradiance.

8.1. Introduction

Atmospheric aerosols play a key role in the global energy balance and therefore in modulating climate through its direct effect on radiation [e.g., *Charlson et al.*, 1992; *Hansen et al.*, 1997] and its indirect effects associated with interaction with clouds [e.g., *Twomey*, 1977; *Ramanathan et al.*, 2001; *Rosenfeld et al.*, 2014]. Determining the evolution of the atmospheric aerosol load in the past is thus of capital importance with regard to quantifying its effects on radiation and other climatic variables and consequently to furthering our knowledge of the global climate system [*Hartmann et al.*, 2013].

One of the major pieces of evidence supporting the crucial role played by atmospheric aerosol in modulating surface solar radiation is provided by the dimming and brightening phenomenon [*Stanhill and Cohen*, 2001; *Wild*, 2009]. The changes in atmospheric transmissivity since the midtwentieth century, which result from variations in anthropogenic aerosol emissions, are considered to constitute the main factor causing the trends observed in surface solar radiation [*Wild*, 2009, 2012]. The limited availability of systematic measurements hinders the study of the evolution of surface solar radiation before the dimming-brightening period (i.e., 1960s): these only started subsequent to the 1957–1958 International Geophysical Year, becoming worldwide much more recently.

Furthermore, widespread quantification of the aerosol load in the atmosphere (or at least of its radiative characteristics) had not commenced until the late 1970s, with the development of ground- and satellite-based instruments. The aerosol series obtained by satellite were started in 1978 with the Nimbus platform, while spectral Sun photometers also started to be used in the 1970s [*Shaw et al.*, 1973; *Voltz*, 1974]. These old data sets often present inhomogeneities and/or conflicting results at the beginning [*Cermak et al.*, 2010]. In addition, they had a low spatial resolution, while the limited number of ground-based measurements prevented them from being useful for fully explaining the effect of aerosols on climate.

At present, the global network of Cimel Sun photometers called AErosol RObotic NETwork (AERONET) is considered to be the main reference for measuring aerosol characteristics from the ground [*Holben et al.*, 1998; *Dubovik et al.*, 2000], but most of the stations were established after the 1990s. Moderate Resolution Imaging Spectroradiometer (MODIS) and Multiangle Imaging Spectroradiometer (MISR) [*King et al.*, 1992; *Diner et al.*, 1998] constitute the current satellite instruments most commonly used for aerosol observation but also started measuring at the end of the 1990s. They provide global coverage, but with low temporal resolution as compared to ground-based observations. The latter are assumed to give more accurate aerosol retrievals and usually involve measurements of direct solar radiation in distinct spectral bands.

Herein we advocate the use of sunshine duration (SD) as a proxy of aerosol optical depth (AOD) and hence of atmospheric turbidity for studying the evolution of the atmospheric aerosol load in the past. According to the World Meteorological Organization (WMO) [2008], the SD for a given period is defined as the sum of the subperiods for which direct solar irradiance exceeds 120 W m^{-2}. One of the instruments used to measure SD is the Campbell-Stokes sunshine recorder (CSSR). It was invented in the late nineteenth century to provide a measurement of the duration of bright sunlight by means of a burn mark on a piece of specially treated cardboard [*Stanhill*, 2003; *Sanchez-Lorenzo et al.*, 2013b]. Although in recent years some stations have changed CSSR for new models of automatic sunshine recorders, the long record of SD measurements endow them with remarkable historical value; their series are much longer than those of aerosol and surface solar radiation.

The effect of atmospheric turbidity (caused by the presence of aerosol) on SD has been addressed in several studies. *Cohen and Kleiman* [2005] observed that on some cloudless mornings (afternoons), the Sun cannot be seen after the previously calculated sunrise (before the sunset), so the length of the day is apparently shortened due to a higher aerosol content. Recently, *Magee et al.* [2014] observed that SD variability is associated with a wide variety of natural and anthropogenic processes (e.g., industrial activity and regional air quality). In this direction, some authors [*Jaenicke and Kasten*, 1978; *Helmes and Jaenicke*, 1984, 1985, 1986; *Horseman et al.*, 2008] claim that aerosols reduce daily SD due to their effect at low solar elevations (i.e., at the beginning and the end of the day): a high aerosol content can reduce the incident direct solar irradiance and, in consequence, the burn time is reduced on the CSSR cards (or the time reaching the threshold irradiance in the automatic devices).

We assume that SD can be used as a proxy for AOD, which may be useful for reconstructing aerosol-related series in time and then for explaining long-term aerosol effects. We test this hypothesis with data from some stations on the Iberian Peninsula (southern Europe) and in the Canary Isles.

8.1. Data and methods

We used data from 16 stations of the Spanish Meteorological Agency (AEMET) and 16 stations associated with AERONET and distributed throughout Spain (Figure 8.1 and Table 8.1). It should be noted that two stations are located in the Canary Isles, much farther south of the Iberian Peninsula, facing the coast of West Africa. At all these selected sites, an AEMET station is close to the AERONET station or is even located in the same place. The mean horizontal distance for each pair of stations is 12.6 km (with a maximum of 42.3 km).

Daily records of SD (in hours) are available from the AEMET stations, mostly measured by CSSR, although some stations have recently changed to an automatic sensor (Table 8.1). The uncertainty of this measurement is 0.1 h [*WMO*, 2008]. We calculated the SD fraction, which is the ratio of SD to the total length of the day defined as the time from sunrise to sunset. In addition, total cloud cover (TCC) records were obtained for these stations. These data correspond to ground level visual observations measured in oktas and are available for observations taken 3 times a day (at 7, 13, and 18 UTC). In order to screen out the clouds, we only considered cloudless days, i.e., days on which mean daily TCC from the 3-daily observations is rounded to 0 oktas (a maximum of one observation with a maximum of 1 okta is therefore allowed).

The AERONET stations provide mean daily values of AOD in several channels (440, 500, 675, and 870 nm). Specifically, we used in this study mean daily values of AOD in the 440nm channel (this channel is available at all sites), AOD_{440}, by using the cloud-screened and quality-assured level 2.0 data. The uncertainty of AOD in this channel is 0.02 [*Holben et al.*, 1998]. The period of time with availability of SD, TCC, and AOD data is also shown in Table 8.1 for each pair of stations. This period depends mainly on the starting date of the AERONET station, as most of the SD and TCC data from AEMET started prior to the 1980s. It should be noted that we use at least two years of data for each site.

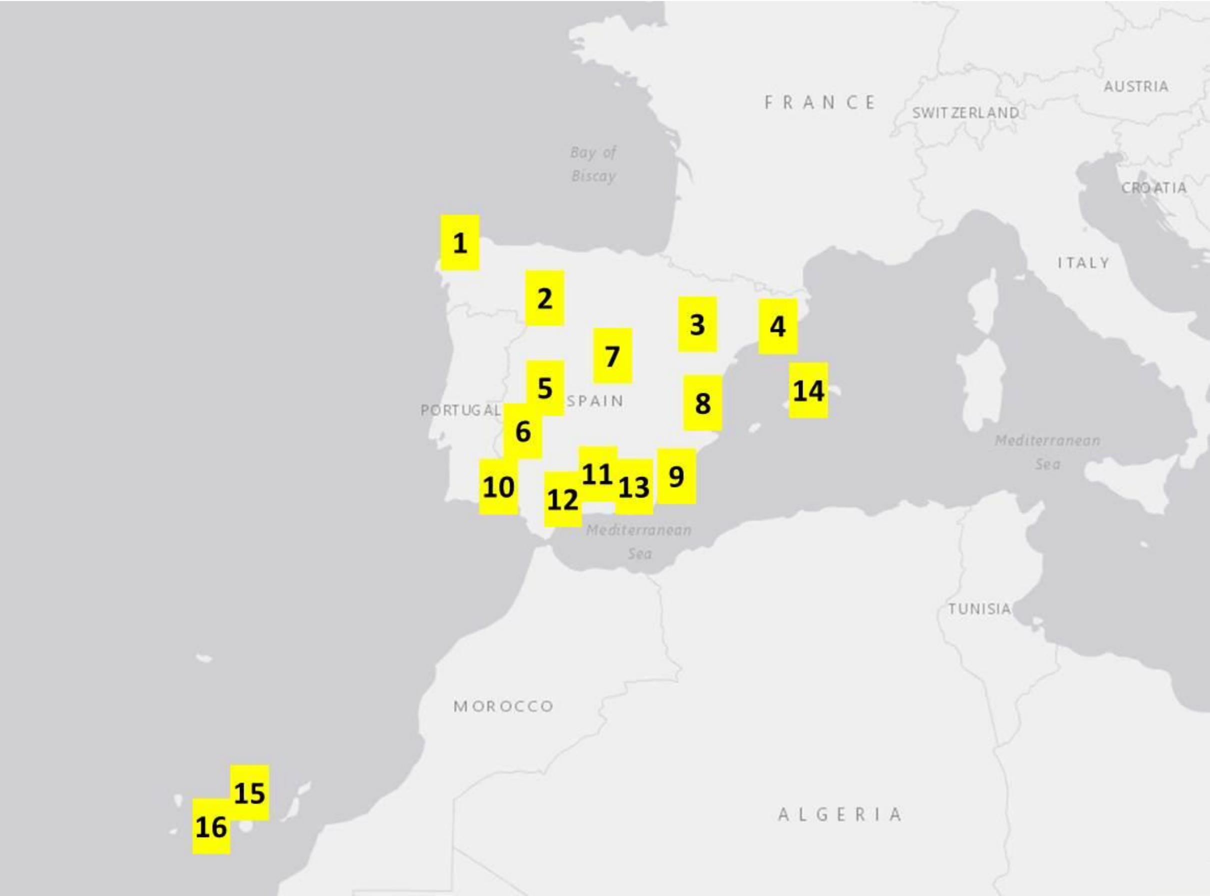

Figure 8.1. Map of the distribution of the 16 sites studied in our research. Each number is associated with one AEMET and one AERONET station, as defined in Table 8.1.

Table 8.1 **(next page)**. Summary of Locations of the 16 stations in Spain[a]

[a] For each station, latitude, longitude and elevation above sea level are specified, as well as the distance between AEMET and AERONET station. The initial date for historic SD and TCC that is available and the period used for establishing the relationships are also specified. N is the number of days used (only summer cloudless days) and R is the correlation coefficient between SD and AOD. In SD versus AOD columns, we include intercept and slope of the linear regression of SD fraction depending on daily AOD_{440}. In AOD versus SD columns, we include intercept and slope of the linear regression of daily AOD_{440} depending on SD fraction for the eight sites used in the long-term reconstruction of AOD. The uncertainty in the regression parameters (shown in parentheses) is calculated as their standard errors. RMSD refers to root-mean-square deviation between estimated and observed AOD_{440}.

[b] Stations which still measure SD with CSSR.

[c] Station where CSSR has been replaced with automatic sensors (Izaña-2001).

[d] Stations where the instrument may have been changed, but for which this information is unavailable.

[e] Urban site.

[f] Rural site.

[g] Marine site, i.e., island.

[h] (S) Correlation coefficient is statistically significant at a confidence level higher than 95%. (NS) Correlation coefficient is not statistically significant with the same level.

#	**AEMET (SD)**	**Started**	**AERONET (AOD)**	**Dist. (km)**	**Period time**	**N**	**R[h]**	**SD vs AOD**		**AOD vs SD**		
								Intercept	**Slope**	**Intercept**	**Slope**	**RMSD**
1	Coruña[b] 43.37 ºN, 8.42 ºW, 58 m	01/1961	Coruña 43.63 ºN, 8.42 ºW, 67 m	28.9	01/2012 – 03/2014	16	−0.48 (NS)	0.962 (0.018)	−0.16 (0.08)	–	–	–
2	Valladolid (Villanubla)[b] 41.70ºN, 4.85 ºW, 846 m	01/1961	Palencia[f] 41.99 ºN, 4.52 ºW, 750 m	42.3	02/2003 – 12/2014	146	−0.48 (S)	0.959 (0.004)	−0.20 (0.03)	–	–	–
3	Zaragoza (Airport)[b] 41.66 ºN, 1.01 ºW, 247 m	01/1961	Zaragoza 41.63 ºN, 0.88 ºW, 250 m	11.3	06/2012 – 07/2014	30	−0.81 (S)	0.971 (0.006)	−0.28 (0.04)	2.33 (0.30)	–2.36 (0.32)	0.045
4	Barcelona (Fabra Obs.)[b] 41.42 ºN, 2.12 ºE, 412 m	01/1983	Barcelona[e] 41.39 ºN, 2.12 ºE, 125 m	3.3	01/2005 – 01/2015	21	−0.75 (S)	0.932 (0.009)	−0.15 (0.03)	–	–	–
5	Caceres[d] 39.50 ºN, 6.37 ºW, 459 m	01/1983	Cáceres[f] 39.48 ºN, 6.34 ºW, 397 m	3.4	07/2005 – 06/2012	142	−0.59 (S)	0.948 (0.003)	−0.19 (0.02)	–	–	–
6	Badajoz (Talavera la Real)[b] 38.83 ºN, 6.83 ºW, 185 m	01/1961	Badajoz[f] 38.88 ºN, 7.01 ºW, 186 m	16.5	06/2012 – 10/2014	87	−0.51 (S)	0.961 (0.006)	−0.18 (0.03)	1.24 (0.22)	–1.18 (0.24)	0.071
7	Madrid (Cuatro Vientos)[b] 40.38ºN, 3.79ºW, 687 m	01/1961	Madrid[e] 40.45 ºN, 3.72 ºW, 680 m	13.7	03/2012 – 05/2014	63	−0.63 (S)	0.942 (0.005)	−0.28 (0.03)	1.96 (0.34)	–2.01 ()	0.074
8	Valencia[d] 39.48 ºN, 0.37 ºW, 11 m	02/1938	Burjassot 39.51 ºN, 0.42 ºW, 30 m	5.4	04/2007 – 04/2013	67	−0.29 (S)	0.820 (0.010)	−0.11 (0.04)	–	–	–
9	Murcia[d] 38.00 ºN, 1.17 ºW, 61 m	01/1961	Murcia[f] 38.00 ºN, 1.17 ºW, 69 m	0.0	09/2012 – 10/2014	37	−0.52 (S)	0.938 (0.009)	−0.17 (0.03)	1.67 (0.31)	–1.62 (0.45)	0.077
10	Huelva (Ronda del Este)[d] 37.28 ºN, 6.91 ºW, 19 m	01/1960	El Arenosillo[f] 37.11 ºN, 6.73 ºW, 0 m	24.7	02/2000 - 12/2009	210	−0.67 (S)	0.949 (0.004)	−0.21 (0.02)	–	–	–
11	Granada (Airport)[b] 37.19 ºN, 3.79 ºW, 567 m	11/1972	Granada 37.16 ºN, 3.60 ºW, 680 m	17.1	12/2004 – 06/2013	161	−0.92 (S)	0.950 (0.002)	−0.36 (0.01)	–	–	–
12	Malaga (Airport)[b] 36.67 ºN, 4.49 ºW, 7 m	12/1947	Málaga 36.72 ºN, 4.48 ºW, 40 m	5.6	02/2009 – 09/2013	143	−0.71 (S)	0.941 (0.005)	−0.25 (0.02)	–	–	–
13	Almeria (Airpot)[b] 36.85 ºN, 2.36 ºW, 21 m	02/1968	Tabernas (PSA-DLR)[f] 37.09 ºN, 2.36 ºW, 500 m	26.7	02/2011 - 10/2014	73	−0.75 (S)	0.952 (0.007)	−0.33 (0.03)	1.72 (0.16)	–1.72 (0.18)	0.067
14	Palma de Mallorca (CMT)[d] 39.56 ºN, 2.63 ºE, 3 m	08/1972	Palma de Mallorca[g] 39.55 ºN, 2.63 ºE, 10 m	1.1	08/2011 – 12/2013	31	−0.90 (S)	0.970 (0.007)	−0.33 (0.03)	2.39 (0.20)	–2.42 (0.22)	0.047
15	Sta. Cruz de Tenerife[d] 28.46 ºN, 16.26 ºW, 35 m	01/1931	Sta. Cruz de Tenerife[g] 28.47 ºN, 16.25 ºW, 52 m	1.5	07/2005 – 02/2014	73	−0.93 (S)	0.958 (0.006)	−0.28 (0.01)	2.99 (0.12)	–3.07 (0.14)	0.051
16	Izaña[c] 28.31 ºN, 16.50 ºW, 2371 m	01/1920	Izaña[g] 28.31ºN, 16.50ºW, 2391 m	0.0	01/2005 – 01/2010	231	−0.89 (S)	0.959 (0.001)	−0.30 (0.01)	2.53 (0.08)	–2.62 (0.09)	0.037

We first explored the relationship between AOD_{440} and SD fraction for the summer months (June, July, and August), as this season presents the maximum number of cases with clear-sky conditions and the lowest effect of dew or precipitation on the glass sphere or on the CSSR cards [*Sanchez-Romero et al.*, 2014]. In addition, higher amounts of aerosols are sometimes present in this region during summer, which increases the range of AOD values employed [*Bennouna et al.*, 2013]. Moreover, for the range of latitudes covered by the studied stations (from 28° to 43°) the apparent trajectories of the Sun in the sky (which has some effect on the expected and observed SD) are very similar in this season. Results of this part of the study are reported in section 8.3.1.

In order to study the long-term changes of AOD in Spain, we selected those sites with SD series that proved to be homogeneous. Specifically, the temporal homogeneity of each of the 16 SD series was checked by means of the Standard Normal Homogeneity Test (SNHT) [*Alexandersson and Moberg*, 1997]. Our approach rejects the a priori assumption of nonexistence of homogenous reference series and consists of testing each of the 16 series against the others, normally in subgroups of the highest correlated series (i.e., using as reference the series that present $R>0.7$). In short, the SNHT test derives a statistic T where changes in the standardized difference series between candidate and reference time series over the whole period are calculated. Large changes in the mean values before and after a time step, which indicate the possibility of breaks in the time series, provide high values of T. For further details, see, e.g., *Alexandersson and Moberg* [1997]. Only seven series proved to be homogeneous: Zaragoza, Badajoz, Madrid, Murcia, Santa Cruz de Tenerife, Palma de Mallorca, and Almería. The other series show evidence of inhomogeneity with at least one significant break ($p<0.05$) since the 1960s, except for Izaña, where the only inhomogeneity is detected around 1953. Consequently, for the subsequent analyses we used only the seven homogeneous series, as well as the records from Izaña since the mid-1950s.

Subsequently, since the goal is to be able to estimate AOD from SD data, we fitted daily AOD_{440} with respect to daily SD for the summer cloudless days at these eight sites. We used here the orthogonal-distance regression method weighted by the measurement uncertainty ratio. The obtained relationships were then applied to the historical data of SD, and the daily series of estimated AOD_{440} were converted into summer values, by averaging all daily values of each summer. In order to detect a general signal in the mean anomalies over Spain that is not affected by local conditions (e.g., differences in absolute mean values), we computed the relative anomalies of estimated AOD for each station with respect to the 1971–2000 period (which is common for all eight series) and then averaged all available anomaly series. This also reduces the bias resulting from the fact that the number of available series varies over time. Results of this part of the study are shown in section 8.3.2.

8.1. Results and discussion

8.1.1. Effect of AOD on SD

Figure 8.2 shows the scatterplot of SD fraction versus AOD_{440} for eight selected cases (which are the sites having homogenous SD series that will be used in the next section to reconstruct AOD). The relationship is clearly linear, so in Table 8.1 we present the parameters of the linear fit between SD fraction and AOD_{440} for each location. The negative slopes mean that an increase in AOD causes a decrease in SD.

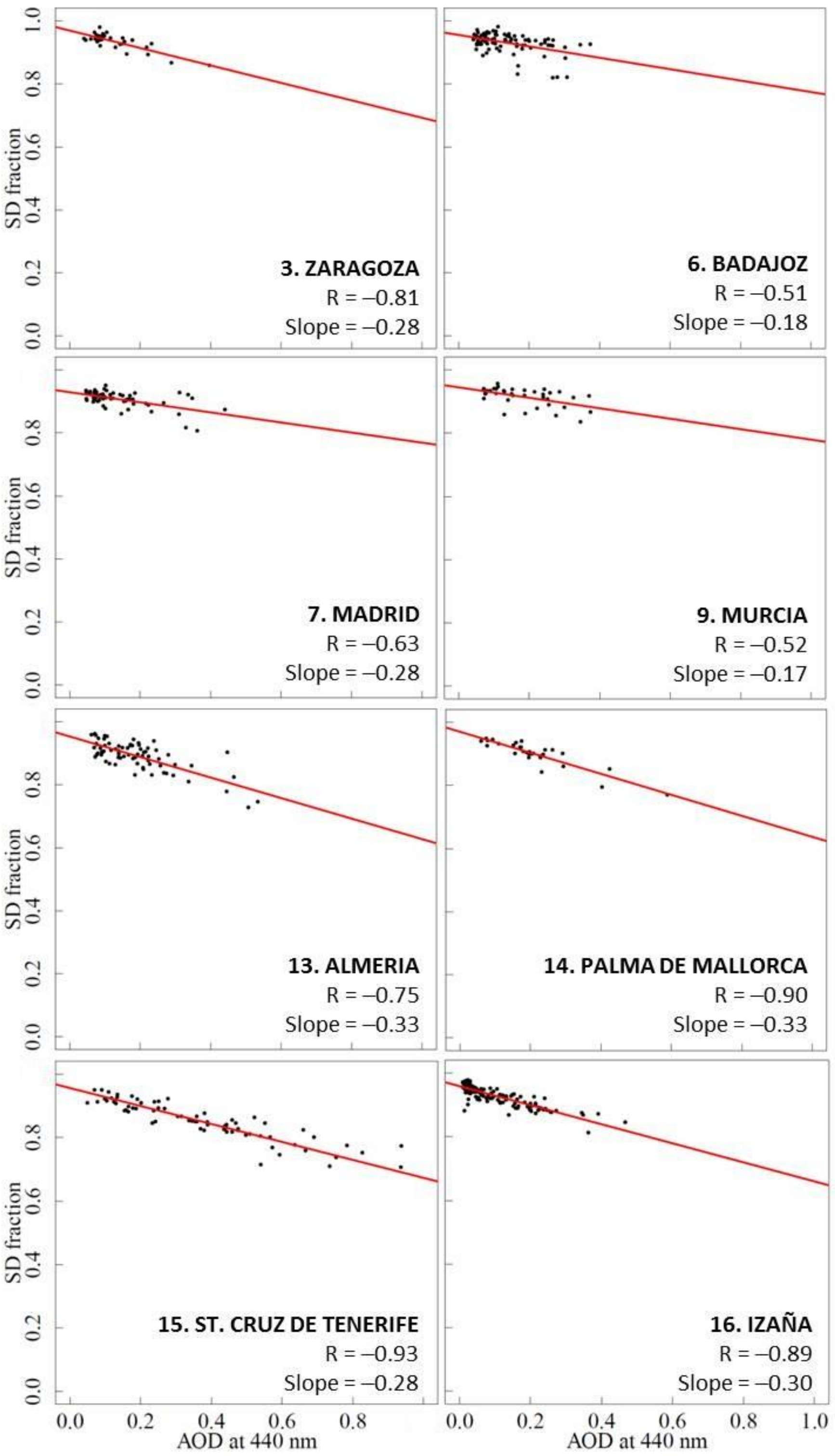

Figure 8.2. Scatterplot of SD fraction versus AOD_{440} for summer (June, July and August) at eight sites. Each point represents one day of measurements. We also show the correlation coefficients and slope values.

Taking into account the uncertainties involved and that cloudless days are selected upon only three TCC observations during each day, the correlations obtained may be considered to be remarkable. More concretely, all 16 sites treated, except Coruña, show significant correlation coefficients at a confidence level higher than 95%. The weighted average (accounting for the number of points of each case) of the correlation coefficient is –0.72. For some sites, e.g., Granada and Santa Cruz de Tenerife, the correlation coefficient is even greater (in absolute terms) than –0.9. The different values of correlation (and of the other parameters of the regression) could be explained partially by the uncertainties in the observations used. In addition, in some cases, the AEMET and AERONET stations are quite distant, e.g., Valladolid (from Palencia) and Huelva (from El Arenosillo); or at different altitudes, e.g., Barcelona and Almeria.

Intercept values of the linear regression are close to 1 (a weighted mean value of 0.96), which agrees with the fact that for AOD (and TCC) close to 0, the SD fraction must be close to 1 (i.e., SD approaching the length of the daytime). Slope values present some variability (Table 8.1), even if all are negative, with a weighted (i.e., depending on the number of points used in the linear regression) mean value of –0.28. This mean value implies a change in SD of around 3% per 0.1 units of AOD. It should be noted that even if we consider the associated uncertainty, all slope values maintain negative values. As expected, closer sites show similar slope values (Izaña and Santa Cruz de Tenerife, in the Canary Isles, and Caceres and Badajoz, both inland locations in the West of Spain). The variability in slope values may be explained with different types of aerosol depending on the region of Spain. Different aerosol types exhibit different optical properties (that is, they have different effects on the scattering and absorption along the spectrum of solar radiation, although they may present the same AOD_{440} value) and, consequently, could affect SD measurement in a different manner. We speculate that the different classes of particles found in Spain [*Pereira et al.*, 2011; *Sicard et al.*, 2011; *Obregón et al.*, 2014] could affect SD in different ways: the high slope values in Table 8.1 could correspond to the presence of desert dust (from the Sahara desert and from arid regions of the Iberian Peninsula) and marine aerosol (southern and Canary Isles sites), while dominant continental aerosol could be related to lower slopes (Mediterranean and western sites).

The effect of AOD on SD provided herein by means of empirical observations is also supported by theoretical results. Specifically, we studied the effect of AOD upon SD using the Santa Barbara Discrete ordinates radiative transfer Atmospheric Radiative Transfer model (SBDART) [*Ricchiazzi et al.*, 1998]: a series of runs was performed with different aerosol conditions, including type (rural, urban, oceanic, and tropospheric aerosol) and AOD (from 0 to 1). The model was run in order to find the value of solar height needed for the direct solar irradiance to reach 120 W m^{-2}, depending on aerosol conditions, for a certain unspecific site located at a latitude of 40°N (mean latitude of the Iberian Peninsula). This solar height is then transformed into time by simple astronomical relations, and an SD fraction depending on aerosol conditions is finally established. The range of slope values obtained in the regression between such simulated SD fraction and AOD is compatible with those shown in Table 8.1. Low values of the slope were obtained for tropospheric aerosol (–0.13), whereas increasingly higher values were obtained for rural (–0.17), urban (–0.20), and oceanic aerosols (–0.30). The concrete values of slope depend on the range of AOD values used in the linear regression between relative SD and AOD_{440}.

8.1.2. Reconstruction of AOD series

The coefficients of the fit between AOD_{440} and SD fraction (the latter used as the predictor variable), performed with the orthogonal-distance method, for the eight selected sites, are given in Table 8.1. These fits are then used to estimate daily AOD_{440} for all summer cloudless days since the beginning of the corresponding SD and TCC series (except for Izaña, where we start after the break detected in 1953). It should be noted that the fits for the other sites could be derived as well, but they would be useless as we are not intending to reconstruct AOD series from inhomogeneous SD data. For the eight selected sites and for the period used to develop the fit, the root-mean-square deviation (RMSD) between daily estimated and measured AOD_{440} is also given in Table 8.1. The agreement between estimations and measurement is further confirmed when comparing the averaged summer values (for all sites together, see Figure 8.3), with a RMSD of 0.035.

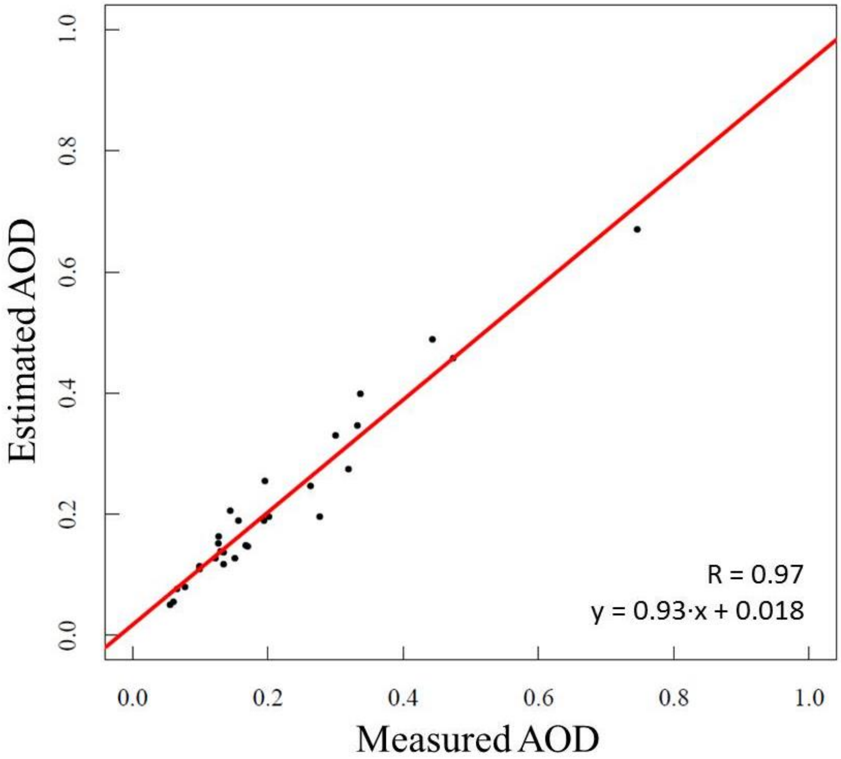

Figure 8.3. Scatterplot of AOD estimated from SD and AOD measured by Cimel for the eight selected stations and for summer values (average of the available days of June, July and August). Each point represents one summer mean value for one site. The fitted line and the correlation coefficient illustrate the remarkable agreement.

In Figure 8.4a we represent the evolution of the mean relative anomalies (with respect to a mean value of 0.26 for the 1971–2000 period) of estimated AOD_{440} for summer and for the eight homogenous series, during the period 1961–2014. See Table 8.2 for the absolute values of the evolution of mean summer estimated AOD_{440}. It is worth noting that the smoothed evolution of the AOD is very similar if we use only data from the Canary Isles sites (Figure 8.5a) or the other sites (Iberian Peninsula and Mallorca, Figure 8.5b). This means that the decadal evolution observed does not reflect local anomalies, but is quite representative of the whole region. There is a clear increase in AOD from the mid-1960s to the 1980s, with a maximum during the 1982–1984 period. A decrease in AOD then becomes apparent from the 1980s to the 2010s, which almost results in a recovery of AOD levels to those of the mid-1960s. The linear trend, estimated over the whole 1961–2014 period, is not statistically significant at the 95% confidence level as assessed by means of the Mann-Kendall nonparametric test. If the whole period is subdivided into the 1961–1984 and 1985–2014 subperiods, both linear trends are significant positive (32% per decade) and negative (–22% per decade), respectively. The latter is in agreement with [*Ruckstuhl et al.* [2008] and *Chiacchio et al.* [2011], who found AOD decreases of about 60% since the 1980s in Europe.

In order to validate our approach, we compared our AOD_{440} estimation for Izaña during the 1955 to 2010 period (as an inhomogeneity can be observed around 1953) with AOD at 500nm obtained by *García et al.* [2015]. They estimated the long-term AOD time series at Izaña using Artificial Neural Networks techniques and, as input parameters, in situ meteorological observations (visibility, SD, TCC, relative humidity, and temperature) and day of year. Both methods agree very well, as they present a minimum (~0.1) around 1955, and then an increase in AOD until 1982 (~0.3), followed by a decrease until the present (~0.1). The peaks of 1968 and

1982 are also in concordance. So our simpler method (which uses only SD and TCC data) provides results similar to those of that more complex technique.

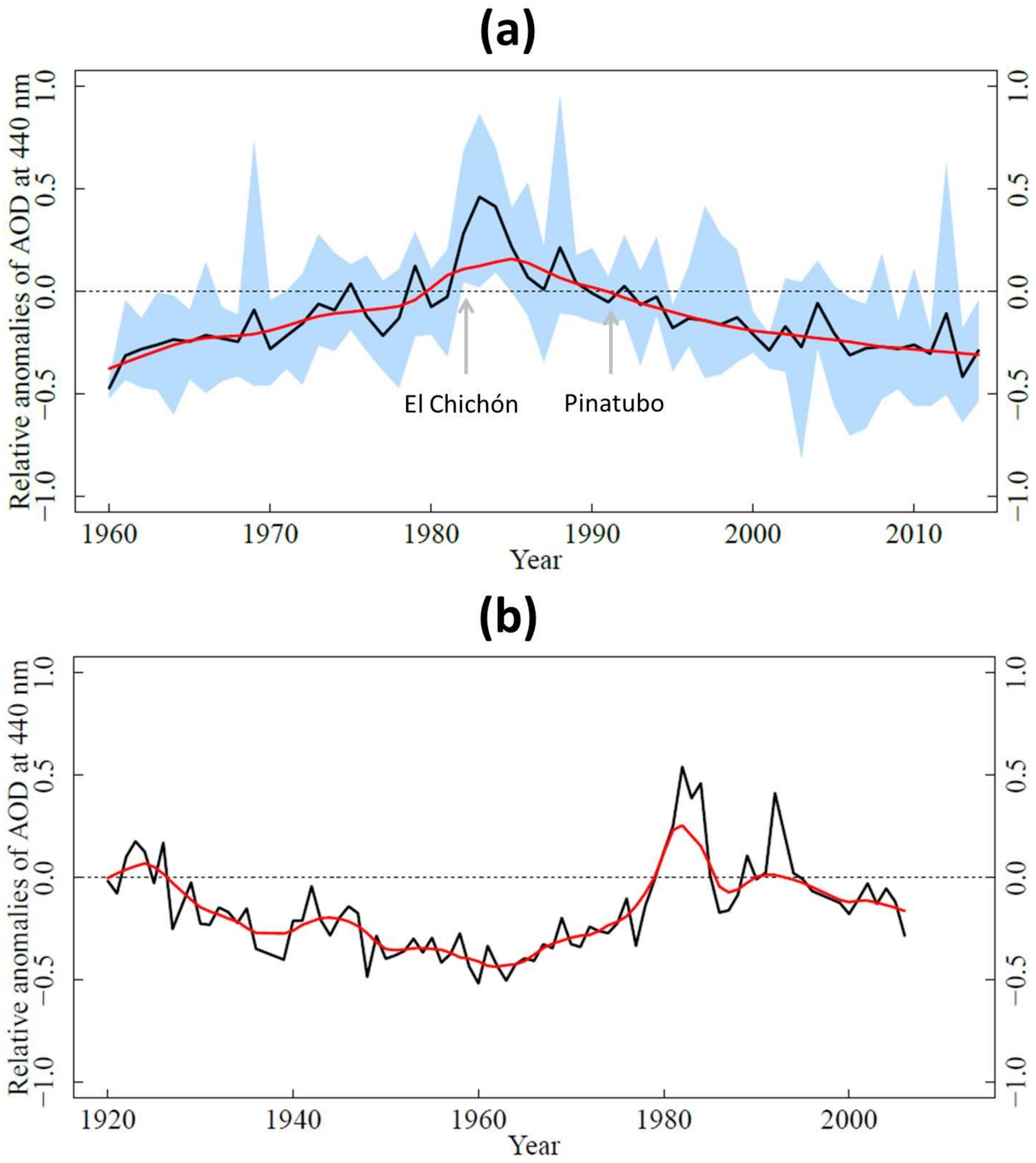

Figure 8.4. (a) Evolution (1961-2014 period) of the mean relative anomalies of estimated AOD_{440} for summer (black line) for eight sites distributed throughout Spain (including two in the Canary Isles); smoothing by a moving window of 11 years (red line) is also shown; blue area refers to range between the maximum and minimum values of the different series for each year. (b) Evolution (1920-2007 period) of the relative anomalies of estimated AOD_{440} (black line) for Madrid in summer; smoothing by a moving window of 11 years (red line) is also shown.

Table 8.2. Reconstructed time series of average summer AOD for Spain from 1961 to 2014, obtained from 8 sites distributed throughout Spain (including two in the Canary Isles).

Year	AOD	Year	AOD	Year	AOD	Year	AOD	Year	AOD	Year	AOD
1961	0.08	**1971**	0.20	**1981**	0.23	**1991**	0.22	**2001**	0.12	**2011**	0.09
1962	0.09	**1972**	0.19	**1982**	0.34	**1992**	0.26	**2002**	0.17	**2012**	0.20
1963	0.10	**1973**	0.20	**1983**	0.42	**1993**	0.22	**2003**	0.13	**2013**	0.09
1964	0.12	**1974**	0.20	**1984**	0.39	**1994**	0.22	**2004**	0.21	**2014**	0.10
1965	0.11	**1975**	0.26	**1985**	0.29	**1995**	0.18	**2005**	0.19		
1966	0.11	**1976**	0.20	**1986**	0.24	**1996**	0.20	**2006**	0.14		
1967	0.09	**1977**	0.17	**1987**	0.25	**1997**	0.19	**2007**	0.13		
1968	0.13	**1978**	0.28	**1988**	0.30	**1998**	0.18	**2008**	0.15		
1969	0.22	**1979**	0.30	**1989**	0.24	**1999**	0.19	**2009**	0.13		
1970	0.13	**1980**	0.20	**1990**	0.23	**2000**	0.15	**2010**	0.13		

The results shown in Figure 8.4a are also in agreement with the dimming and brightening phenomenon described elsewhere for the Iberian Peninsula [*Sanchez-Lorenzo et al.*, 2009, 2013a; *Román et al.*, 2014] and Europe [*Sanchez-Lorenzo et al.*, 2015], while the continued decrease in AOD, even after the 2000s, is in line with the results shown in [*Mateos et al.*, 2014]. In addition, the maximum values of AOD during the summers of 1982–1984 are in concordance with the eruption of the El Chichón volcano (spring 1982). The eruption of Pinatubo (summer 1991) was bigger than that of El Chichón, but its signal is not clearly visible in Figure 8.4a; taking into account that an increase of AOD decreases SD, other studies of SD series in Europe also found a stronger signal of the El Chichón compared with that of the Pinatubo eruption [*Sanchez-Lorenzo et al.*, 2009; *Manara et al.*, 2015]. Further research is needed about other causes associated with the observed trends of AOD, especially in relation to the trends of dust over the region. Indeed, it is intriguing that the maximum in the early 1980s, as well as the decadal variability of AOD since 1960, is in agreement with the drought in the Sahel region [e.g., *Held et al.*, 2006], which is one of the main source areas of dust [*Prospero*, 2014], especially over the Mediterranean region. In addition, when only the Canary Isles sites are considered (Figure 8.5a), the eruptions of El Arenal and Fernandina Island volcanoes (summer 1968) are also visible [*García et al.*, 2014], whereas they are unappreciable at the Iberian Peninsula stations. Finally, a certain amount of the aerosol evolution could also be explained by the trend of anthropogenic emissions in Western Europe [*Stern*, 2006; *Streets et al.*, 2009; *Nabat et al.*, 2014; *Turnock et al.*, 2015].

The evolution of AOD should be noticeable in the surface solar radiation measurements in the region. According to [*Sanchez-Lorenzo et al.*, 2013a], summer global solar radiation on the Iberian Peninsula increased at a rate of 6.5 W m^{-2} per decade over the 1985–2010 period, i.e., 17 W m^{-2} during the whole period. The decrease in cloud cover in summer during this period was almost negligible and statistically nonsignificant [*Sanchez-Lorenzo et al.*, 2012], i.e., cloudiness played an unimportant role in the variation in summer radiation. We have calculated how the temporal variability of AOD found with our method would affect the temporal variability of solar irradiance. To this end, once again we used a radiative model (SBDART) to calculate the daily mean irradiance for a characteristic summer day, with high and low conditions of aerosol content. These are defined as 20% higher and 30% lower than the mean value of the period of reference 1971–2000 (see red line in Figure 8.4a). The differences between daily mean irradiances for low and high aerosol levels are around 10–23 W m^{-2} (depending on the aerosol type). In conclusion, these results demonstrate the suitability of our estimated AOD evolution and confirm that aerosols may have played an important role in the brightening over Spain, despite the fact that there is still some discussion regarding the relative importance of natural and anthropogenic aerosols on the total aerosol content.

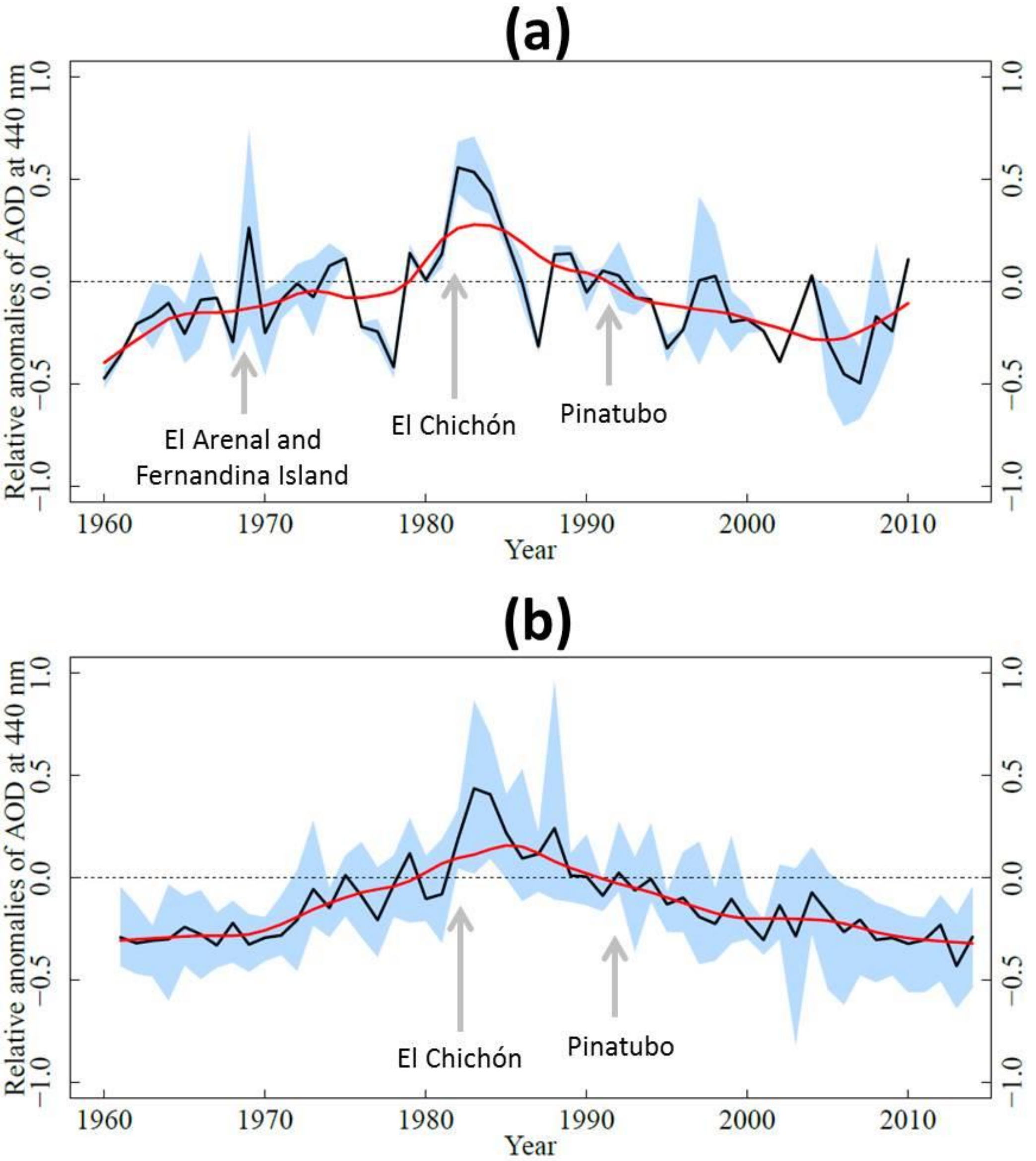

Figure 8.5 (previous page). (a) Evolution of the mean relative anomalies of estimated AOD_{440} for summer for the two Canary Isles sites (1961-2014 period, black line). (b) Evolution of the relative anomalies of estimated AOD_{440} for summer for the six sites distributed throughout the Iberian Peninsula and Mallorca (1961-2014 period, black line). In both panels, smoothing by a moving window of eleven years (red line) is also shown; blue are refers to the range between the maximum and minimum values of the different series for each year.

Finally, the reconstruction of AOD for Madrid is presented in Figure 8.4b. SD and TCC data have been available since the 1920s (specifically, in the Madrid Retiro station, for the 1920–2007 period). It should be noted that Madrid Retiro no longer has SD records in recent times in which AOD measurements are, however, available. Nevertheless, this observatory is close to the Madrid Cuatro Vientos station (Table 8.1) which presents very similar values of SD (R>0.9). Consequently, we used the expression derived from the latter station (Table 1) to convert the SD fraction in Madrid Retiro into AOD_{440}. It is worth noting that the Madrid Retiro SD series has proven to be homogeneous since the 1920s following verification by means of the SNHT test. Figure 8.4b shows that the AOD has a tendency to a decrease from the 1920s to the midtwentieth century, especially from the mid-1940s to the late 1950s. This trend is in line with the early brightening phenomenon reported in some regions of Europe, detected by means of SD and solar radiation series, especially from around the 1930s to the 1950s [*Sanchez-Lorenzo et al.*, 2009, 2015; *Founda et al.*, 2014; *Matuszko*, 2014b; *Manara et al.*, 2015] Although there is no definitive explanation of this aerosol reduction and of the early brightening phenomenon, a possible cause involves the observed decrease in black carbon emissions since the early twentieth century [*McConnell et al.*, 2007].

8.2. Conclusion

We studied the relationship between AOD and daily SD for cloudless days and for some stations in southern Europe with the aim of performing a long-term reconstruction of AOD. We found a negative correlation with some spatial variability (including cases with correlation coefficients higher than –0.90 on a daily basis). The reconstructed AOD series are compatible with the dimming and brightening phenomenon: the increase in AOD from the mid-1960s to the 1980s is followed by a decrease until the present. A reconstructed AOD series starting in 1920 is also presented for Madrid, where a decrease in AOD from the mid-1940s to 1960 is observed. This is compatible with the early brightening phenomenon observed in other parts of Europe.

As a vast network of instruments exists that enables AOD to be measured, as well as SD and TCC measurements since the late nineteenth century, this type of study can be performed in other parts of the world in order to provide more information on changes in aerosol concentration in the atmosphere, especially prior to the 1980s. In addition, as the burn width in CSSR bands has been associated with direct solar irradiance [*Horseman et al.*, 2013; *Sanchez-Romero et al.*, 2015], in a future study we intend to relate burn width to aerosol load at subdaily resolution.

PART III.

DISCUSSION
AND
CONCLUSIONS

Chapter 9.

Discussion

In chapters 5 to 8, we have presented not only the methodology and results, but also discussions of these results, which we will not repeat in chapter 9. Nevertheless, there are some topics that we didn’t discuss and others for which the discussion was not complete due to, for example, lack of space in the published paper. In this chapter we recover these topics and present a discussion about them. In addition, we also argue about the applicability of the different suggestions that we make to study AOD from CSSR cards. Finally, we try to present this discussion in an integrated way, giving a sense of unity to the thesis.

9.1. Aerosol characterization at high temporal resolution

As far as the methodology is concerned, to prove and quantify the effect of aerosols on the burn width of CSSR cards at a high temporal resolution, there are two issues that we have to take into account: the measurement of burn width and the measurement of AOD.

The method based on digital image processing of scanned CSSR cards has proved the possibility to determine variations in DSI for both short and long times scales. Further research may consider taking into account the perforated part of the burn besides the burn width (perforated plus scorch parts), in particular during cloudless sunrises and sunsets; a priori, this would help in the estimation of DSI and would give some light to explain the reasons of the mean overestimation in daily SD and underestimation in the threshold value (lower than the 120 W m^{-2} proposed by WMO) derived from this method. If we intend to use this method to reconstruct long time series of DSI (and/or AOD), it should be noted that at some sites, the reconstruction can reach as much as around 120 years from the present days. Therefore, it would be also useful to make the method totally automatic (without the need of manual intervention, except for the process of scanning).

As a result of the characterization of CSSR devices, we found that it is important to know which CSSR had been used, especially for those before the standardization of the worldwide CSSR network [*WMO*, 1962]: different CSSR have different sensitivity and, in consequence, different threshold values and different burn width measurements. This is also reflected in the equation that relates burn width with DSI (see Chapter 5). It is true that, unlike we did in our study, the threshold applied in the image processing to distinguish between burnt and intact sections of the card could be defined differently for each card type. Although this difference of sensitivity is very small and of the same order of the instrumental uncertainty, this could be important if we are interested in burn width during cloudless sunrises and sunsets, which, recall, are the periods most affected by the changing aerosol load in the atmosphere.

Regarding the need of obtaining reliable measurements of AOD at a high temporal resolution, by using a MFRSR device, there are two points that require more attention. The first one is related to the Langley plot method to find the absolute calibration; we found an initial rapid decrease in the sensitivity for the first few months but, after that, it is difficult to explain the behavior of V_0, as the period of time elapsed after installation is too short. Referring to other authors that studied V_0, they found that, after the rapid decrease, V_0 suffer seasonal changes quite correlated with the temperature of the sensor [*Mazzola et al.*, 2010; *Michalsky and LeBaron*, 2013]. As we now have almost 4 years of data, we could update the V_0 series, as a future research, in order to extract robust conclusions on V_0 evolution.

Secondly, we used a single daily value of total ozone column from the Ozone Monitoring Instrument, as continuous measurements of concentration of atmospheric ozone are not available. Thus, the retrieved value is assumed to be constant for the entire day. There are some authors that retrieve ozone estimations at sub-daily resolution from spectral measurements of MFRSR [e.g., *Michalsky et al.*, 1995; *Taha and Box*, 1999], other possibility would be to use the measurement of the nearly Brewer Spectrophotometer, situated in Zaragoza (310 km from Girona). However, some authors tried to characterize diurnal variations of total ozone column for improving ozone trend estimates but didn't find important variability. For example, *Sakazaki et al.* [2013] investigated the contribution of diurnal variations in stratospheric ozone to those in the total column ozone and found that the peak-to-peak difference may reach 1% over the course of a day, for sites in similar latitudes as our area. In consequence, the error associated to the diurnal variation of ozone optical depth, τ_{O3}, is of the order of 10^{-4}–10^{-5}, depending on the channel; thus, it can be considered negligible compared with the uncertainties in the calibration constant and the measured signal (see Equation 6.6).

The relationship between burn width of CSSR cards and AOD, at high resolution, is not immediate but, for a given value of m_A, higher burn width means lower AOD (see Table 7.1).

Although our method of extracting burn width and obtaining AOD allows retrieving 1-minute values, we explored the relationship at 10-minutes resolution in order to avoid problems derived from the possible slight misalignments of the cards from their correct position in the CSSR device (which lead to shift in the time attributed to the measurements), as well as from the spatial dimensions of scorch area during changing atmospheric conditions. In fact, when we compared burn width and DSI (Chapter 5), we found a mean time shift of 0.28 minutes, with a standard deviation of 2.36 minutes. This jeopardizes the comparison at higher resolution (e.g., 1-minute), especially in cases of intermittent burning, i.e. cloudy days.

Although we created a look-up table of AOD values from burn width and m_A, we had first tried to find empirical expressions linking AOD with burn width and m_A. More specifically, we had converted burn width data of CSSR cards into DSI by using the equation proposed in Chapter 5 (see Equation 5.1). For a given wavelength, DSI depends exponentially on AOD and m_A according to the Bouguer-Lambert-Beer law. In our case, we have a broadband measurement (or estimate) of DSI, but we propose a similar equation based on the definition of Linke's turbidity factor (see Equation 4.1). This expression links DSI with atmospheric aerosol loading:

$$DSI_W = L \cdot e^{-k \cdot AOD \cdot m_A} \qquad \text{(Eq. 9.1)}$$

where DSI_W is the estimation of DSI from burn width of CSSR and L is related to the maximum DSI that can be measured (i.e., if AOD were null). It should be noted the similarities with Linke's turbidity factor, T_L, which is almost the same equation just changing AOD (spectral magnitude) for T_L (broadband magnitude) and k for the optical thickness of the clean dry atmosphere (δ_{CD}). Note that T_L depends on AOD and water vapor; in particular, some authors presented conversion functions between T_L, the atmospheric water vapor and AOD [e.g., *Ineichen,* 2008]. This is a first approximation, as we don't consider water vapor, but an improved method could consider it using climatological averages depending on the time and site. So, taking the natural logarithm of each side of the equation, we can obtain a relationship between burn width (which is used to calculate DSI_W) and AOD (Equation 9.2).

$$\log[DSI_W] = \log[L] - k \cdot AOD \cdot m_A \qquad \text{(Eq. 9.2)}$$

We did some research with this expression, that is, trying to fit the data (DSI_W, AOD, m_A) to determine L and k, but we just found rough linear relationships. In fact, we found better results using the look-up-table instead of the empirical equation. Improving the methods to extract burn width and/or taking into account water vapor could be two different lines of research in order to find better empirical expressions that relate AOD with burn width and m_A but, at present, the look-up-table has shown as the best option. In addition, it would be useful to apply the same method to other sites with different aerosol conditions in order to extract more robust conclusions.

The cloud-screening routine is an important aspect in the whole method. In our case, the cloud-screening method applied in the MFRSR data is based on the observed variability of optical depth. However, we saw in Chapter 6 that there would be errors in special cases (as dust and fire episodes) due to the complexity of defining the edge between cloud and atmospheric aerosol. Indeed, there is certain lack of knowledge about the description of the aerosol-cloud system as a continuum or considering an exclusionary distinction between cloud and aerosol [e.g., *Charlson et al.*, 2007; *Koren et al.*, 2007; *Marshak et al.*, 2008]. Therefore, one of the goals of the new research project of the Environmental Physics Group (in the framework of which this thesis has been conducted) is to establish the importance of the intermediate region between cloud and aerosol.

Nevertheless, if we want to take advantage of CSSR cards, it is important to define a method of cloud-screening from the information contained in them, so for example from burn width or sunshine duration. In fact, the look-up-table could be used as a cloud-screening method, using only those combinations of burn width and m_A for which a value of AOD exists. This would assume that unusual combinations of burn width and m_A must correspond to cloudy conditions. In addition, we can impose some condition over the daily SD fraction, for example that it must be higher than 0.9. Although DSI (in our case, burn width) is the best variable to discriminate clouds, this method of extracting cloud-contaminated periods from the CSSR cards would be a first approximation. The authors that studied how clear skies can be identified from broadband radiation measurements have also used diffuse irradiances [e.g., *Long and Ackerman*, 2000] or global irradiances [*Kudo et al.*, 2010a, 2010b], in order to discriminate the moments when there are clouds without blocking the Sun. Another option, even if we lose temporal resolution and extra data is necessary, is to use only burn width data centered in the times of the day when visual observations available at the same meteorological station report cloudiness conditions.

As we studied in detail the CSSR cards, we observed some anomalies in burn width. These cases are unusual and do not represent significant contribution to the whole dataset. Concretely, there are cases when certain “flashes” or sudden increases in the burn width appear, without matching an increase in DSI. For example, see Figure 9.1, which shows two temporal evolution of the burn in two different CSSR cards (see Chapter 5.2 to know more about the models of CSSR) corresponding to two different days. We propose some explanations in order to explain these anomalies, even if more research is needed. One possible explanation for the big burn widths of the first case (Figure 9.1a) could be related to an increase of the circumsolar radiation (for example, under broken clouds) and, in consequence, the burn width in CSSR cards would also increase. The possible explanation for the second case (Figure 9.2b) could be related to the rain during the previous night that wet the corresponding CSSR card. Other explanations could be related to certain defects (unhomogeneities) in CSSR cards that produce different burn patterns.

(a)
18/02/2013

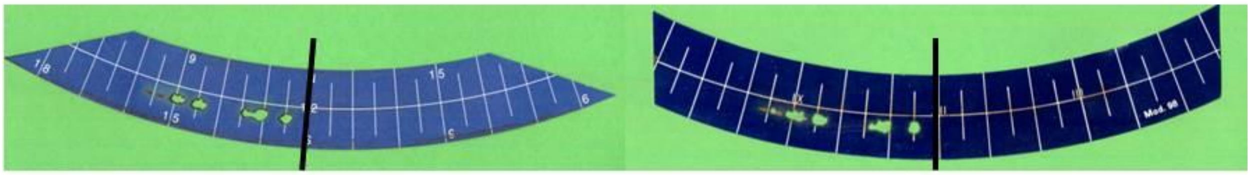

(b)
19/03/2013

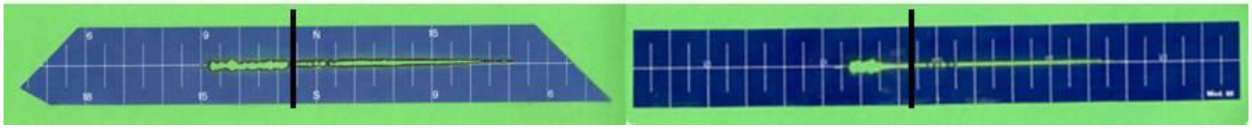

Figure 9.1. Two different CSSR cards for two different cases. Black lines separate the days, as we change the CSSR card near midday: the afternoon data is for the previous day of the morning data.

In conclusion, it is possible to prove and quantify the effect of aerosols on burn width of CSSR cards at a high temporal resolution. In consequence, AOD estimations are possible using burn width as a proxy when the CSSR cards are available (as scanning these cards is the first step of the method to measure burnt width). However, the cloud-screening and the availability of the original CSSR cards in the historical meteorological stations are some of the limitations of this method.

9.2. Aerosol characterization in long temporal scales

As we stated before, our initial hypothesis is that one cause of the decadal changes observed in SD records involves variations in atmospheric aerosol load. In this direction, the effect of atmospheric turbidity (caused by the presence of aerosol) on SD has been addressed in several studies. In particular, some authors [*Jaenicke and Kasten*, 1978; *Helmes and Jaenicke*, 1984, 1986; *Horseman et al.*, 2008] claim that aerosols reduce daily SD due to their effect at low solar elevations (i.e. at the beginning and the end of the day): a high aerosol content can reduce the incident direct solar irradiance and, in consequence, the burn time is reduced on the CSSR cards (or the time reaching the threshold irradiance in the automatic devices). In our case, we have shown the effect of AOD on burn width (see Chapters 5 and 7), but most stations do not store the CSSR cards and only register SD data. So, we have explained a method that uses SD as a proxy for AOD (see Chapter 8), which may be useful for reconstructing aerosol-related series in time.

In principle, the signal of AOD in SD is weak. Thus, a change in the way to measure SD could affect the homogeneity of the series and give rise to errors when evaluating trends. This is related to the problem of characterization of CSSR, which was discussed in Chapter 5. So, the homogeneity of the long-term sunshine records is an important factor (in fact this is one of the reasons why we only used 8 of the 16 series presented in Chapter 8), as well as the availability of the cloudiness data. There are other limitations inherent in the method; some are related with the uncertainty in the measurement of SD, and others are related with cloudiness, as the availability of cloudiness observations or the difficulty in selecting cloudless days from only a few observations per day. In our study, we also have the problem of the distance (including also different altitudes) between the AEMET and the AERONET stations.

Nevertheless, to extract information on the trends of AOD, seasonal or monthly basis are more suitable than annual basis because the origin of particles can vary along the year. For example, in developed countries, more pollution particles are usually caused by space-heating-related emissions during winter, whereas photochemical processes dominate during summer. In our case, we only performed the reconstruction of AOD for summer months and, as mentioned, the results match quite well with dimming and brightening evolution of solar radiation in Spain and in other regions in southern Europe. Although it is not shown in Chapter 8, we had performed the analysis for the other seasons, but the number of cloudless cases was considerable lower at certain stations. Thus, the results found for some stations were not statistically significant. This is one of the limitations of this method: it is necessary to have simultaneous daily measurements of AOD and SD in cloudless conditions, and this is particularly difficult for winter studies and northern stations.

Slope values of the linear regressions between SD fraction and AOD present some variability, depending on the site, even if all are negative. In order to explain the different slope values, apart of the instrumental behavior (we stated before that different CSSR could have different sensitivity), we speculate that the different classes of particles found in Spain could affect SD in different ways (through AE, single scattering albedo or asymmetry parameter). Nevertheless, we are aware that this part would require more work for obtaining some robust conclusions, studying in detail, and empirically, how the relationship between SD and AOD depend on the actual aerosol characteristics.

Finally, it is important to remark that, when we started this thesis, significant studies had been carried out to quantify atmospheric turbidity using SD data but we were not aware of any report on retrieving AOD based on SD observations. In the meantime, however, at least another research group has explored and found that SD is a good proxy for AOD. Concretely, a recent paper studies the trends in AOD in northern China as retrieved from SD data [*Li et al.*, 2015]. Their method is more complex than ours (as atmospheric column water vapor content and air pressure data is necessary) and is based on the Bouguer-Lambert-Beer's law:

$$DSI = (R/R_0)^2 I_0 \tau_R \tau_w \tau_{O3} \tau_g e^{-m_A BAOD} \quad \text{(Equation 9.3)}$$

where $(R/R_0)^2$ denotes the dependence of the solar constant on the Sun-Earth distance and *BAOD* corresponds to the so-called broadband AOD. Taking into account that SD is defined as the daily sunshine duration during which beam solar irradiance is greater than 120 W m^{-2}, and the assumption of diurnal uniformity of AOD, they establish that:

$$BAOD = -\ln\left\{120/\left[(R/R_0)^2 I_0 \tau_R \tau_w \tau_{O3} \tau_g\right]\right\}/m_A \quad \text{(Equation 9.4)}$$

The latter assumption implies also a diurnal uniformity of SD (i.e., it is equally divided between morning and afternoon) and, in consequence, the air mass is obtained taking into account the solar zenith angle at the beginning and end of the burnt track of the SD instrument each day. This assumption can be the major source of uncertainty for this method (that the authors estimated to be approximately 30%), as well as considering 120 W m^{-2} as a constant threshold value. However, according with the study, retrieved AODs from SD agree reasonably well with AODs retrieved from MODIS observations. Values and trends in AOD retrieved from SD also agree with those retrieved from solar radiation and visibility [*Daren et al.*, 2001; *Xu et al.*, 2009; *Zhang et al.*, 2015]. Note that the assumption of diurnal uniformity could be avoid if the CSSR cards were available; in that case, it would be possible to know the exact solar elevation angle when the burnt trace starts/ends for each day. This is similar to what Helmes and Jaenicke applied in their studies [*Helmes and Jaenicke*, 1984, 1985, 1986].

In conclusion, our method using SD as a proxy for AOD is a simple way to reconstruct aerosol-related series in time. SD and TCC measurements exist at many stations all over the world since the late nineteenth century, so it would be possible to obtain long AOD reconstructions for many sites. The main limitation of the method, however, is the possible inhomogeneity of the long-term SD and cloudiness data.

Chapter 10.

General conclusions

In the present thesis we have demonstrated that sunshine observations performed with the use of CSSR instruments can be employed to estimate AOD and its variability and trends both quantitatively and at high temporal resolution and for long-timescales.

The theoretical basis is quite simple: one cause of the changes observed in the CSSR cards, and therefore in the SD records, involves variations in atmospheric aerosol loading. According to the reviewed literature, there is evidence that SD records contain signals of the direct effects of aerosols on the solar beam and, in consequence, SD records can be used as a proxy for studying aerosol trends and their radiative forcing.

To prove and quantify the effect of aerosols on the burn width of CSSR cards at a high temporal resolution (e.g., sub-daily), we first characterized CSSR and their cards. We found that different CSSR devices present different sensitivities and, in consequence, show different threshold values and different burn widths for the same atmospheric conditions. This affects the measurement of burn width, but also of the retrieved SD.

We then developed a semiautomatic method to obtain the temporal evolution of burn width and length in CSSR cards, using automated digital image processing techniques. We observed that hourly direct solar irradiance (DSI) can be satisfactorily estimated from the burn width measurements more accurately than when SD is used as an estimator. This result shows that burn width provides more information on the variation of DSI at high temporal resolution, whereas SD is useful only for estimations for longer periods (e.g., longer than daily).

As DSI is affected by atmospheric turbidity, especially at times near sunrise and sunset due to the longer optical path, an estimation of DSI from the burn width may be used to estimate turbidity, i.e. CSSR records can become a proxy measurement for AOD, which in turn is a proxy for the atmospheric aerosol loading.

We designed a robust methodology to derive continuous columnar aerosol properties at high temporal resolution over a site from Multifilter Rotating Shadow band Radiometer (MFRSR) measurements. This aspect of our research also enables us to describe the behavior of aerosols over a western Mediterranean site which shows a low level of pollution and exhibits an overall low aerosol content; moreover it allows us to identify the diversity of aerosol types that may be found and to describe particularly high aerosol events that may occur sporadically. In addition, we have demonstrated the good relationship between our data and other aerosol data (from satellites or from a nearby site), as well as the reliability of our measurements, confirmed by means of a radiative closure experiment.

As it was already established that AOD affects the measurement on CSSR cards, we studied this effect at a high resolution, comparing AOD data with burn width. The results we found confirm that AOD leaves some signal on the CSSR cards, more specifically, in the burn width. Thus, AOD variations can be reconstructed at a high resolution (10 minutes) by means of burn width. In addition, although the magnitude of the effect of aerosols on burn width is a complex issue, detailed studies of the burn (in particular during cloudless sunrises and sunsets) provides the possibility to determine variations in turbidity for both short and long time scales, and therefore to ultimately assess the possible influence of human activities on the Earth radiation budget, with the resulting climatological implications.

If AOD has a certain effect on burn width (especially during cloudless sunrises and sunsets), this effect must also be detectable in SD. Thus, as few stations retain the burnt cards from CSSRs, we studied the suitability of SD records as a proxy for the reconstruction of atmospheric aerosol content. Although at a lower resolution, this method is applicable to more sites, as there is no need to avail of the original CSSR cards or to scan them. Concretely, we studied the relationship between AOD and daily SD for cloudless days and for some stations in southern Europe with the aim of performing a long-term reconstruction of AOD. We found a negative correlation with some spatial variability, which means that the effect of AOD reduces daily SD; this effect, however, depends upon other factors (one of them likely being the type of aerosols).

The reconstructed AOD series are compatible with the dimming and brightening phenomenon: the increase in AOD from the mid-1960s to the 1980s is followed by a decrease until the present. A reconstructed AOD series starting in 1920 is also presented, in which a decrease in AOD from the mid-1940s to 1960 is observed. This is compatible with the early brightening phenomenon observed in other parts of Europe. As a vast network of instruments exists that enables AOD to be measured, as well as SD and TCC since the late 19th century, this type of study can be performed in other parts of the world in order to provide more information on changes in aerosol concentration in the atmosphere, especially prior to the 1980s.

REFERENCES

Ackerman, A. S., O. B. Toon, D. E. Stevens, A. J. Heymsfield, V. Ramanathan, and E. J. Welton (2000), Reduction of tropical cloudiness by soot, *Science*, *288*(5468), 1042–1047, doi:10.1126/science.288.5468.1042.

Aguilar, E., I. Auer, M. Brunet, T. C. Peterson, and J. Wieringa (2003), *Guidelines on climate metadata and homogenization*, Malaga.

Aksoy, B. (1999), Analysis of changes in Sunshine Duration data for Ankara, Turkey, *Theor. Appl. Climatol.*, *64*(3-4), 229–237, doi:10.1007/s007040050125.

Alados-Arboledas, L., H. Lyamani, and F. J. Olmo (2003), Aerosol size properties at Armilla, Granada (Spain), *Q. J. R. Meteorol. Soc.*, *129*(590), 1395–1413, doi:10.1256/qj.01.207.

Albrecht, B. (1989), Aerosols, cloud microphysics, and fractional cloudiness, *Science*, *245*(4923), 1227–1230.

Alexandersson, H., and A. Moberg (1997), Homogenization of Swedish temperature data. Part I: homogeneity test for linear trends, *Int. J. Climatol.*, *17*(1), 25–34, doi:10.1002/(SICI)1097-0088(199701)17:1<25::AID-JOC103>3.0.CO;2-J.

Alexandrov, M. D., A. A. Lacis, B. E. Carlson, and B. Cairns (2002), Remote sensing of atmospheric aerosols and trace gases by means of Multifilter Rotating Shadowband Radiometer. Part I: retrieval algorithm, *J. Atmos. Sci.*, *59*, 524–543, doi:10.1175/1520-0469(2002)059<0524:RSOAAA>2.0.CO;2.

Alexandrov, M. D., A. Marshak, B. Cairns, A. A. Lacis, and B. E. Carlson (2004), Automated cloud screening algorithm for MFRSR data, *Geophys. Res. Lett.*, *31*(4), L04118, doi:10.1029/2003GL019105.

Alexandrov, M. D., P. Kiedron, J. J. Michalsky, G. Hodges, C. J. Flynn, and A. A. Lacis (2007), Optical depth measurements by shadow-band radiometers and their uncertainties, *Appl. Opt.*, *46*(33), 8027–38, doi:10.1364/AO.46.008027.

Alexandrov, M. D., A. A. Lacis, B. E. Carlson, and B. Cairns (2008), Characterization of atmospheric aerosols using MFRSR measurements, *J. Geophys. Res.*, *113*(D8), D08204, doi:10.1029/2007JD009388.

Angell, J. K. (1990), Variation in United States cloudiness and sunshine duration between 1950 and the drought year of 1988, *J. Clim.*, *3*, 296–308.

Angell, J. K., J. Korshover, and G. F. Cotton (1984), Variation in United States cloudiness and sunshine, 1950-82, *J. Clim. Appl. Meteorol.*, *23*, 752–760.

Ångström, A. (1924), Solar and terrestrial radiation, *Q. J. R. Meteorol. Soc.*, *50*, 121–125.

Ångström, A. (1929), On the atmospheric transmission of sun radiation and on dust in the air, *Geogr. Ann.*, *2*, 156–166.

Ångström, A. (1964), The parameters of atmospheric turbidity, *Tellus*, *1*, 64–75.

Augustine, J. A., C. R. Cornwall, G. B. Hodges, C. N. Long, C. I. Medina, and J. J. DeLuisi (2003), An automated method of MFRSR calibration for aerosol optical depth analysis with application to an Asian Dust Outbreak over the United States, *J. Appl. Meteorol.*, *42*, 266–278.

Augustine, J. A., G. B. Hodges, E. G. Dutton, J. J. Michalsky, and C. R. Cornwall (2008), An aerosol optical depth climatology for NOAA's national surface radiation budget network (SURFRAD), *J. Geophys. Res.*, *113*(D11204), doi:10.1029/2007JD009504.

Baker, D. G., and D. A. Haines (1969), *Solar radiation and sunshine duration relationships in the north-central region and Alaska*, Agricultural Experiment Station, University of Minnesota.

Bakirci, K. (2009), Models of solar radiation with hours of bright sunshine: A review, *Renew. Sustain. Energy Rev.*, *13*(9), 2580–2588, doi:10.1016/j.rser.2009.07.011.

Balis, D., M. Kroon, M. E. Koukouli, E. J. Brinksma, G. Labow, J. P. Veefkind, and R. D. McPeters (2007), Validation of Ozone Monitoring Instrument total ozone column measurements using Brewer and Dobson spectrophotometer ground-based observations, *J. Geophys. Res.*, *112*(D24), D24S46, doi:10.1029/2007JD008796.

Balling, R. C., and S. B. Idso (1991), Sulfate aerosols of the stratosphere and troposphere: Combined effects on surface air temperature, *Theor. Appl. Climatol.*, *44*(3-4), 239–241, doi:10.1007/BF00868179.

Barnsley, M. J., J. J. Settle, M. A. Cutter, D. R. Lobb, and F. Teston (2004), The PROBA/CHRIS mission: a low-cost smallsat for hyperspectral multiangle observations of the Earth surface and atmosphere, *IEEE Trans. Geosci. Remote Sens.*, *42*(7), 1512–1520, doi:10.1109/TGRS.2004.827260.

Baynard, T., R. M. Garland, A. R. Ravishankara, M. A. Tolbert, and E. R. Lovejoy (2006), Key factors influencing the relative humidity dependence of aerosol light scattering, *Geophys. Res. Lett.*, *33*(6), 3–6, doi:10.1029/2005GL024898.

Van Beelen, A. J., and A. J. Van Delden (2012), Cleaner air brings better views, more sunshine and warmer summer days in the Netherlands, *Weather*, *67*(1), 21–25, doi:10.1002/wea.836.

Bennouna, Y. S., V. E. Cachorro, C. Toledano, A. Berjón, N. Prats, D. Fuertes, R. Gonzalez, R. Rodrigo, B. Torres, and A. M. de Frutos (2011), Comparison of atmospheric aerosol climatologies over southwestern Spain derived from AERONET and MODIS, *Remote Sens. Environ.*, *115*(5), 1272–1284, doi:10.1016/j.rse.2011.01.011.

Bennouna, Y. S., V. E. Cachorro, B. Torres, C. Toledano, A. Berjón, A. M. de Frutos, and I. Alonso Fernández Coppel (2013), Atmospheric turbidity determined by the annual cycle of the aerosol optical depth over north-center Spain from ground (AERONET) and satellite (MODIS), *Atmos. Environ.*, *67*, 352–364, doi:10.1016/j.atmosenv.2012.10.065.

Benson, R. B. B., M. V. V Paris, J. E. E. Sherry, and C. G. G. Justus (1984), Estimation of daily and monthly direct, diffuse and global solar radiation from sunshine duration measurements, *Sol. Energy*, *32*(4), 523–535, doi:10.1016/0038-092X(84)90267-6.

Bider, M. (1958), Uber die Genauigkeit der Registrierungen des Sonnenscheinautographen Campbell-Stokes, *Arch. Meteor. Geophys. Bioklim.*, *B9*(2), 1922–230.

Bodhaine, B. A., N. B. Wood, E. G. Dutton, and J. R. Slusser (1999), On Rayleigh optical depth calculations, *J. Atmos. Ocean. Technol.*, *16*, 1854–1861.

Boucher, O., D. Randall, P. Artaxo, C. Bretherton, G. Feingold, P. Forster, V. M. Kerminen, Y. Kondo, H. Liao, U. Lohman, P. Rasch, S. K. Satheesh, S. Sherwood, B. Stevens, and X. Y. Zhang (2013), Clouds and Aerosols, in *Climate change 2013: the physical science basis. Contribution of working group I to the Fifth Assessment Report of the Intergovernmental Panel on Climate Change*, pp. 571–658, Cambridge University Press, Cambridge, United Kingdom and New York, NY, USA.

Bourassa, A. E., D. A. Degenstein, R. L. Gattinger, and E. J. Llewellyn (2007), Stratospheric aerosol retrieval with optical spectrograph and infrared imaging system limb scatter measurements, *J.*

Geophys. Res., *112*(D10), D10217, doi:10.1029/2006JD008079.

Bouya, Z., and G. P. Box (2011), Seasonal variation of aerosol size distributions in Darwin, Australia, *J. Atmos. Solar-Terrestrial Phys.*, *73*(13), 2022–2033, doi:10.1016/j.jastp.2011.06.016.

Bouya, Z., G. P. Box, and M. A. Box (2010), Seasonal variability of aerosol optical properties in Darwin, Australia, *J. Atmos. Solar-Terrestrial Phys.*, *72*(9-10), 726–739, doi:10.1016/j.jastp.2010.03.015.

Brázdil, R., A. A. Flocas, and H. S. Sahsamanoglou (1994), Fluctuation of sunshine duration in central and south-eastern Europe, *Int. J. Climatol.*, *14*(9), 1017–1034, doi:10.1002/joc.3370140907.

Brooks, C. F., and E. S. Brooks (1947), Sunshine recorders: A comparative study of the burning-glass and thermometric systems, *J. Meteorol.*, *4*(4), 105–115.

Brunetti, M., G. Lentini, M. Maugeri, T. Nanni, I. Auer, R. Bohm, and W. Schöner (2009), Climate variability and change in the Greater Alpine Region over the last two centuries based on multi-variable analysis, *Int. J. Climatol.*, *29*(15), 2197–2225, doi:10.1002/joc.

Calbó, J., and J. Sabburg (2008), Feature extraction from whole-sky ground-based images for cloud-type recognition, *J. Atmos. Ocean. Technol.*, *25*(1), 3–14, doi:10.1175/2007JTECHA959.1.

Campbell, J. F. (1857), On a new self-registering sun-dial, in *Report of the Council of the Brithish Meteorological Society*, pp. 18–26.

Cermak, J., M. Wild, R. Knutti, M. I. Mishchenko, and A. K. Heidinger (2010), Consistency of global satellite-derived aerosol and cloud data sets with recent brightening observations, *Geophys. Res. Lett.*, *37*(21), 1–5, doi:10.1029/2010GL044632.

Cerveny, R., and R. C. Balling (1990), Inhomogeneities in the long-term United States' sunshine record, *J. Clim.*, *3*, 1045–1048.

Changnon, S. A. (1981), Midwestern cloud, sunshine and temperature trends since 1901: Possible evidence of jet contrail effects, *J. Appl. Meteorol.*, *20*, 496–508.

Charlson, R. J., S. E. Schwartz, J. M. Hales, R. D. Cess, J. A. Coakley, Jr., J. E. Hansen, and D. J. Hofmann (1992), Climate forcing by anthropogenic aerosols, *Science*, *255*, 423–430, doi:10.1126/science.255.5043.423.

Charlson, R. J., A. S. Ackerman, F. A.-M. Bender, T. L. Anderson, and Z. Liu (2007), On the climate forcing consequences of the albedo continuum between cloudy and clear air, *Tellus B*, *59*(4), 715–727, doi:10.1111/j.1600-0889.2007.00297.x.

Che, H. Z., G. Y. Shi, X. Y. Zhang, R. Arimoto, J. Q. Zhao, L. Xu, B. Wang, and Z. H. Chen (2005), Analysis of 40 years of solar radiation data from China, 1961–2000, *Geophys. Res. Lett.*, *32*(6), L06803, doi:10.1029/2004GL022322.

Cheng, T., H. Chen, X. Gu, T. Yu, J. Guo, and H. Guo (2012), The inter-comparison of MODIS, MISR and GOCART aerosol products against AERONET data over China, *J. Quant. Spectrosc. Radiat. Transf.*, *113*(16), 2135–2145, doi:10.1016/j.jqsrt.2012.06.016.

Chiacchio, M., T. Ewen, M. Wild, M. Chin, and T. Diehl (2011), Decadal variability of aerosol optical depth in Europe and its relationship to the temporal shift of the North Atlantic Oscillation in the realm of dimming and brightening, *J. Geophys. Res.*, *116*(D2), D02108, doi:10.1029/2010JD014471.

Ciardini, V., T. Di Iorio, L. Di Liberto, C. Tirelli, G. Casasanta, A. di Sarra, G. Fiocco, D. Fuà, and M. Cacciani (2012), Seasonal variability of tropospheric aerosols in Rome, *Atmos. Res.*, *118*, 205–214, doi:10.1016/j.atmosres.2012.06.026.

Cohen, A., and M. M. Kleiman (2005), Evidence suggesting the shortening of the day from "sunrise" to "sunset" due to global change, in *13th International Workshop on Lidar Multiple Scattering Experiments*, vol. 5829, edited by A. G. Borovoi, p. 274 pp, St Petersburg, Russia.

Cutforth, H. W., and D. Judiesch (2007), Long-term changes to incoming solar energy on the Canadian Prairie, *Agric. For. Meteorol.*, *145*(3-4), 167–175, doi:10.1016/j.agrformet.2007.04.011.

D'Almeida, G. A., P. Koepke, and E. P. Shettle (1991), *Atmospheric aerosols. Global climatology and radiative characteristics*, Deepak, Hampton, Va.

Daren, L., Y. F. Luo, D. R. Lu, X. J. Zhou, W. L. Li, and Q. He (2001), Characteristics of the spatial distribution and yearly variation of aerosol optical depth over China in last 30 years, *J. Geophys. Res.*, *106*(D13), 14501, doi:10.1029/2001JD900030.

Dee, D. P., S. M. Uppala, A. J. Simmons, P. Berrisford, P. Poli, S. Kobayashi, U. Andrae, M. A. Balmaseda, G. Balsamo, P. Bauer, P. Bechtold, A. C. M. Beljaars, L. van de Berg, J. Bidlot, N. Bormann, C. Delsol, R. Dragani, M. Fuentes, A. J. Geer, L. Haimberger, S. B. Healy, H. Hersbach, E. V. Hólm, L. Isaksen, P. Kållberg, M. Köhler, M. Matricardi, A. P. McNally, B. M. Monge-Sanz, J. J. Morcrette, B. K. Park, C. Peubey, P. de Rosnay, C. Tavolato, J. N. Thépaut, and F. Vitart (2011), The ERA-Interim reanalysis: configuration and performance of the data assimilation system, *Q. J. R. Meteorol. Soc.*, *137*(656), 553–597, doi:10.1002/qj.828.

Diner, D. J., J. C. Beckert, T. H. Reilly, C. J. Bruegge, J. E. Conel, R. A. Kahn, J. V. Martonchik, T. P. Ackerman, R. Davies, S. A. W. Gerstl, H. R. Gordon, J. Muller, R. B. Myneni, P. J. Sellers, B. Pinty, and M. M. Verstraete (1998), Multi-angle Imaging SpectroRadiometer (MISR) instrument description and experiment overview, *IEEE Trans. Geosci. Remote Sens.*, *36*(4), 1072–1087, doi:10.1109/36.700992.

Diner, D. J., B. H. Braswell, R. Davies, N. Gobron, J. Hu, Y. Jin, R. A. Kahn, Y. Knyazikhin, N. Loeb, J. P. Muller, A. W. Nolin, B. Pinty, C. B. Schaaf, G. Seiz, and J. Stroeve (2005), The value of multiangle measurements for retrieving structurally and radiatively consistent properties of clouds, aerosols, and surfaces, *Remote Sens. Environ.*, *97*(4), 495–518, doi:10.1016/j.rse.2005.06.006.

Döll, P., F. Kaspar, and B. Lehner (2003), A global hydrological model for deriving water availability indicators: model tuning and validation, *J. Hydrol.*, *270*(1-2), 105–134, doi:10.1016/S0022-1694(02)00283-4.

Dubovik, O., M. D. King, O. Dubovikl, and D. King (2000), A flexible inversion algorithm for retrieval of aerosol optical properties from sun and sky radiance measurements, *J. Geophys. Res.*, *105*(D16), 20673–20696, doi:10.1029/2000JD900282.

Eck, T. F., B. N. Holben, D. E. Ward, O. Dubovik, J. S. Reid, A. Smirnov, M. M. Mukelabai, N. C. Hsu, N. T. O'Neill, and I. Slutsker (2001), Characterization of the optical properties of biomass burning aerosols in Zambia during the 1997 ZIBBEE field campaign, *J. Geophys. Res.*, *106*(D4), 3425–3448.

Eltbaakh, Y. A., M. H. Ruslan, M. A. Alghoul, M. Y. Othman, K. Sopian, and T. M. Razykov (2012), Solar attenuation by aerosols: An overview, *Renew. Sustain. Energy Rev.*, *16*(6), 4264–4276, doi:10.1016/j.rser.2012.03.053.

Estellés, V., J. A. Martínez-Lozano, M. P. Utrillas, and M. Campanelli (2007), Columnar aerosol properties in Valencia (Spain) by ground-based sun photometry, *J. Geophys. Res.*, *112*(D11), D11201, doi:10.1029/2006JD008167.

Fan, Q., and Y. Zhang (2013), A scorch extraction method for the Campbell-Stokes sunshine recorder based on multivariable thresholding, in *International Conference on Imaging Systems and*

Techniques, Beijing.

Fan, X., H. Chen, L. Lin, Z. Han, and P. Goloub (2009), Retrieval of aerosol optical properties over the Beijing area using POLDER/PARASOL satellite polarization measurements, *Adv. Atmos. Sci.*, *26*(6), 1099–1107, doi:10.1007/s00376-009-8103-x.

Folini, D., and M. Wild (2011), Aerosol emissions and dimming/brightening in Europe: Sensitivity studies with ECHAM5-HAM, *J. Geophys. Res. Atmos.*, *116*(21), 1–15, doi:10.1029/2011JD016227.

Forgan, B. W. (1994), General method for calibrating sun photometers., *Appl. Opt.*, *33*(21), 4841–50.

Foster, N. B., and L. W. Foskett (1953), A photoelectric sunshine recorder, *Bull. Am. Meteorol. Soc.*, *34*, 212–215.

Founda, D., A. Kalimeris, and F. Pierros (2014), Multi annual variability and climatic signal analysis of sunshine duration at a large urban area of Mediterranean (Athens), *Urban Clim.*, *10*, 815–830, doi:10.1016/j.uclim.2014.09.008.

Fox, R. L. (1961), Sunshine-cloudiness relationships in the United-States, *Mon. Weather Rev.*, *89*, 543–548.

Galindo Estrada, I. G., and E. M. Fournier d'Albe (1960), The use of the Campbell-Stokes sunshine recorder as an integrating actinometer, *Q. J. R. Meteorol. Soc.*, *86*(368), 270–272.

Galindo, I., and A. Chavez (1978), Thermal and radiation aspects of the Christmas Eve 1977 air pollution episode in Mexico city, *Geofísica Int.*, *17*, 71–82.

García, R. D., E. Cuevas, O. E. García, V. E. Cachorro, P. Pallé, J. J. Bustos, P. M. Romero-Campos, and A. M. de Frutos (2014), Reconstruction of global solar radiation time series from 1933 to 2013 at the Izaña Atmospheric Observatory, *Atmos. Meas. Tech.*, *7*(4), 3139–3150, doi:10.5194/amtd-7-4191-2014.

García, R. D., O. E. García, E. Cuevas, V. E. Cachorro, A. Barreto, C. Guirado-Fuentes, N. Kouremeti, J. J. Bustos, P. M. Romero-Campos, and A. M. de Frutos (2015), Aerosol optical depth retrievals at the Izaña Atmospheric Observatory from 1941 to 2013 by using artificial neural networks, *Atmos. Meas. Tech. Discuss.*, *8*(9), 9075–9103, doi:10.5194/amtd-8-9075-2015.

Ge, J. M., J. Su, T. P. Ackerman, Q. Fu, J. P. Huang, and J. S. Shi (2010), Dust aerosol optical properties retrieval and radiative forcing over northwestern China during the 2008 China-U.S. joint field experiment, *J. Geophys. Res.*, *115*, D00K12, doi:10.1029/2009JD013263.

Ge, J. M., J. P. Huang, J. Su, J. R. Bi, and Q. Fu (2011), Shortwave radiative closure experiment and direct forcing of dust aerosol over northwestern China, *Geophys. Res. Lett.*, *38*(24), doi:10.1029/2011GL049571.

Gerasopoulos, E., M. O. Andreae, C. S. Zerefos, T. W. Andreae, D. Balis, P. Formenti, P. Merlet, and V. Amiridis (2003), Climatological aspects of aerosol optical properties in Northern Greece, *Atmos. Chem. Phys.*, *3*, 2025–2041.

Gilgen, H., M. Wild, and A. Ohmura (1998), Means and trends of shortwave irradiance at the surface estimated from global energy balance archive data, *J. Clim.*, *11*, 2042–2061.

Good, E. (2010), Estimating daily sunshine duration over the UK from geostationary satellite data, *Weather*, *65*(12), 324–328.

Gordon, H. R., and M. Wang (1994), Retrieval of water-leaving radiance and aerosol optical thickness over the oceans with SeaWiFS: a preliminary algorithm, *Appl. Opt.*, *33*(3), 443, doi:10.1364/AO.33.000443.

Grey, W. M., P. R. North, and S. O. Los (2006), Computationally efficient method for retrieving aerosol optical depth from ATSR-2 and AATSR data, *Appl. Opt.*, *45*(12), 2786–95.

Gueymard, C. (1993), Analysis of monthly average solar radiation and bright sunshine for different thresholds at Cape Canaveral, Florida, *Sol. Energy*, *51*(2), 139–145.

Gueymard, C. (1995), *SMARTS2, A Simple Model of the Atmospheric Radiative Transfer of Sunshine: Algorithms and performance assessment*, Florida Solar Energy Center, Cocoa, Florida.

Gueymard, C. A. (1998), Turbidity determination from broadband irradiance measurements: a detailed multicoefficient approach, *J. Appl. Meteorol.*, *37*, 414–435.

Gueymard, C. A. (2003), Direct solar transmittance and irradiance predictions with broadband models. Part II: validation with high-quality measurements, *Sol. Energy*, *74*, 381–395.

Guijarro, J. A. (2007), Cambios en la medida de las horas de insolación: Análisis de su impacto en dos observatorios de las Islas Baleares (España), *Rev. Climatol.*, *7*, 27–32.

Halthore, N., S. Nemesure, S. E. Schwartz, D. G. Imre, A. Berk, E. G. Dutton, and M. H. Bergin (1998), Models overestimate diffuse clear-sky surface irradiance: A case for excess atmospheric absorption, *Geophys. Res. Lett.*, *25*(19), 3591–3594.

Hansen, J., M. Sato, and R. Ruedy (1997), Radiative forcing and climate response, *J. Geophys. Res.*, *102*(D6), 6831–6864.

Harrison, L., and J. Michalsky (1994), Objective algorithms for the retrieval of optical depths from ground-based measurements, *Appl. Opt.*, *33*(22), 5126–32.

Harrison, L., J. Michalsky, and J. Berndt (1994), Automated multifilter rotating shadow-band radiometer: an instrument for optical depth and radiation measurements, *Appl. Opt.*, *33*(22), 5118–25.

Hartmann, D., M. E. Ockert-Bell, and M. L. Michelsen (1992), The effect of cloud type on Earth's energy balance: Global analysis, *J. Clim.*, *5*(11), 1281–1304.

Hartmann, D. L., A. M. G. Klein Tank, M. Rusticucci, L. V. Alexander, S. Brönniamann, Y. Charabi, F. J. Dentener, E. J. Dlugokency, D. R. Easterling, A. Kaplan, B. J. Soden, P. W. Thorne, M. Wild, and P. M. Zhai (2013), Observations: Atmosphere and Surface, in *Climate change 2013: The physical science basis. Contribution of working group I to the Fifth Assessment Report of the Intergovernmental Panel on Climate Change*, pp. 159–254, Cambridge University Press, Cambridge, United Kingdom and New York, NY, USA.

Haurwitz, B. (1948), Insolation in relation to cloud type, *J. Meteorol.*, *5*, 110–113.

Haywood, J., and O. Boucher (2000), Estimates of the direct and indirect radiative forcing due to tropospheric aerosols: A review, *Rev. Geophys.*, *38*(4), 513–543, doi:10.1029/1999RG000078.

Held, I. M., T. L. Delworth, J. Lu, K. L. Findell, and T. R. Knutson (2006), Simulation of Sahel drought in the 20th and 21st century, *PNAS*, *102*(50), 17891–17896.

Helmes, L., and R. Jaenicke (1984), Experimental verification of the determination of atmospheric turbidity from sunshine recorders, *J. Clim. Appl. Meteorol.*, *23*, 1350–1353.

Helmes, L., and R. Jaenicke (1985), Hidden information within series of measurements - Four examples from atmospheric sciences, *J. Atmos. Chem.*, *3*, 171–185.

Helmes, L., and R. Jaenicke (1986), Atmospheric turbidity determined from sunshine records, *J. Aerosol Sci.*, *17*(3), 261–263.

Hess, M., P. Koepke, and I. Schult (1998), Optical properties of aerosols and clouds : the software package OPAC, *Bull. Am. Meteorol. Soc.*, *79*(5), 831–844.

Hinssen, Y. B. L. (2006), *Comparison of different methods for the determination of sunshine duration*, De Bilt.

Hinssen, Y. B. L., and W. H. Knap (2007), Comparison of pyranometric and pyrheliometric methods for the determination of sunshine duration, *J. Atmos. Ocean. Technol.*, *24*(5), 835–846, doi:10.1175/JTECH2013.1.

Holben, B. N., T. F. Eck, I. Slutsker, D. Tanre, J. P. Buis, A. Setzer, E. Vermote, J. A. Reagan, Y. J. Kaufman, T. Nakajima, F. Lavenu, I. Jankowiak, and A. Smirnov (1998), AERONET-A federated instrument network and data archive for aerosol characterization, *Remote Sens. Environ.*, *66*, 1–16.

Holben, B. N., D. Tanre, A. Smirnov, T. F. Eck, I. Slutsker, N. Abuhassan, W. W. Newcomb, J. S. Schafer, B. Chatenet, F. Lavenu, Y. J. Kaufman, J. Vande Castle, A. Setzer, B. Markham, D. Clark, R. Frouin, R. Halthore, A. Karneli, N. T. O'Neill, C. Pietras, R. T. Pinker, K. Voss, and G. Zibordi (2001), An emerging ground-based aerosol climatology: Aerosol optical depth from AERONET, *J. Geophys. Res.*, *106*(D11), 12067–12097.

Horseman, A., A. R. MacKenzie, and R. Timmis (2008), Using bright sunshine at low-elevation angles to compile an historical record of the effect of aerosol on incoming solar radiation, *Atmos. Environ.*, *42*(33), 7600–7610, doi:10.1016/j.atmosenv.2008.06.033.

Horseman, A. M., T. Richardson, A. T. Boardman, W. Tych, R. Timmis, and A. R. MacKenzie (2013), Calibrated digital images of Campbell–Stokes recorder card archives for direct solar irradiance studies, *Atmos. Meas. Tech.*, *6*(5), 1371–1379, doi:10.5194/amt-6-1371-2013.

Ignatov, A., and L. Stowe (2000), Physical Basis, Premises, and Self-Consistency Checks of Aerosol Retrievals from TRMM VIRS, *J. Appl. Meteorol.*, *39*(12), 2259–2277, doi:10.1175/1520-0450(2001)040<2259:PBPASC>2.0.CO;2.

Ineichen, P. (2008), Conversion function between the Linke turbidity and the atmospheric water vapor and aerosol content, *Sol. Energy*, *82*(11), 1095–1097, doi:10.1016/j.solener.2008.04.010.

Iqbal, M. (1983), *An Introduction To Solar Radiation*, Elsevier.

Jaenicke, R., and F. Kasten (1978), Estimation of atmospheric turbidity from the burned traces of the Campbell-Stokes sunshine recorder, *Appl. Opt.*, *17*(16), 2617–2621.

Janjai, S., S. Suntaropas, and M. Nunez (2008), Investigation of aerosol optical properties in Bangkok and suburbs, *Theor. Appl. Climatol.*, *96*(3-4), 221–233, doi:10.1007/s00704-008-0026-4.

Jaswal, A. K. (2009), Sunshine duration climatology and trends in association with other climatic factors over India for 1970-2006, *MAUSAM*, *60*(4), 437–454.

Jones, P. A., and A. Henderson-Sellers (1991), Historical records of cloudiness and sunshine in Australia, *J. Clim.*, *5*, 260–267.

Jordan, J. B. (1888), Jordan's new pattern photographic sunshine recorder, *Q. J. R. Meteorol. Soc.*, *14*(67), 212–217.

Jordan, J. B., and F. Gaster (1886), Notes as to the principle and working of Jordan's improved photographic sunshine recorder, *Quaterly J. R. Meteorol. Soc.*, *12*, 21–25.

Kahn, R. A. (2005), Multiangle Imaging Spectroradiometer (MISR) global aerosol optical depth validation based on 2 years of coincident Aerosol Robotic Network (AERONET) observations, *J. Geophys. Res.*, *110*(D10), D10S04, doi:10.1029/2004JD004706.

Kaiser, D. P. (2000), Decreasing cloudiness over China: An updated analysis examining additional variables, *Geophys. Res. Lett.*, *27*(15), 2193–2196.

Kaiser, D. P. (2001), Assessing observed temperature and cloud amount trends for China over the last half of the Twentieth Century: What can the sunshine duration record tell us?, in *Eighty-First Annual Meeting of the American Meteorological Society, Twelfth Symposium on Global Change and Climate Variations*, Alburquerque , New Mexico.

Kaiser, D. P., and Y. Qian (2002), Decreasing trends in sunshine duration over China for 1954–1998: Indication of increased haze pollution?, *Geophys. Res. Lett.*, *29*(21), 2042, doi:10.1029/2002GL016057.

Kanniah, K. D., H. Q. Lim, D. G. Kaskaoutis, and A. P. Cracknell (2014), Investigating aerosol properties in Peninsular Malaysia via the synergy of satellite remote sensing and ground-based measurements, *Atmos. Res.*, *138*, 223–239, doi:10.1016/j.atmosres.2013.11.018.

Karl, T. R., and P. M. Steuer (1990), Increased cloudiness in the United States during the first half of the twentieth century: Fact or fiction, *Geophys. Res. Lett.*, *17*(11), 1925–1928.

Kassianov, E., C. Flynn, A. Koontz, C. Sivaraman, and J. Barnard (2013), Failure and redemption of Multifilter Rotating Shadowband Radiometer (MFRSR)/Normal incidence Multifilter Radiometer (NIMFR) cloud screening: contrasting algorithm performance at Atmospheric Radiation Measurement (ARM) North Slope of Alaska (NSA) and Sout, *Atmosphere (Basel).*, *4*(3), 299–314, doi:10.3390/atmos4030299.

Kassianov, E. I., C. J. Flynn, T. P. Ackerman, and J. C. Barnard (2007), Aerosol single-scattering albedo and asymmetry parameter from MFRSR observations during the ARM Aerosol IOP 2003, *Atmos. Chem. Phys.*, *7*(12), 3341–3351, doi:10.5194/acp-7-3341-2007.

Kasten, F., and A. T. Young (1989), Revised optical air mass tables and approximation formula, *Appl. Opt.*, *28*(22), 4735–4738.

Kato, S., P. Ackerman, E. Clothiaux, H. Mather, G. Mace, M. L. Wesely, F. Murcray, and J. Michalsky (1997), Uncertainties in modeled and measured clear-sky surface shortwave irradiances, *J. Geophys. Res.*, *102*(D22), 25881–25898.

Katsuyama, M. (1987), On comparison between rotating mirror sunshine recorders and Jordan sunshine recorders, *Weather Serv. Bull.*, *54*, 169–183.

Kerr, A., and R. Tabony (2004), Comparison of sunshine recorded by Campbell–Stokes and automatic sensors, *Weather*, *59*(4), 90–95, doi:10.1256/wea.99.03.

Kharol, S. K., K. V. S. Badarinath, A. R. Sharma, D. G. Kaskaoutis, and H. D. Kambezidis (2011), Multiyear analysis of Terra/Aqua MODIS aerosol optical depth and ground observations over tropical urban region of Hyderabad, India, *Atmos. Environ.*, *45*(8), 1532–1542, doi:10.1016/j.atmosenv.2010.12.047.

King, M. D., Y. J. Kaufman, W. P. Menzel, and D. Tanre (1992), Remote Sensing of Cloud, Aerosol, and Water Vapor Properties from the Moderate Resolution Imaging Spectrometer (MODIS), *IEEE Trans. Geosci. Remote Sens.*, *30*(1), 2–27.

Kircher, A. (1646), *Ars Magna Lucis et Umbrae*, Scheus, Rome.

Kitsara, G., G. Papaioannou, A. Papathanasiou, and A. Retalis (2013), Dimming/brightening in Athens: Trends in Sunshine Duration, Cloud Cover and Reference Evapotranspiration, *Water Resour. Manag.*, *27*(6), 1623–1633, doi:10.1007/s11269-012-0229-4.

Knapp, K. R. (2002), Aerosol optical depth retrieval from GOES-8: Uncertainty study and retrieval validation over South America, *J. Geophys. Res.*, *107*(D7), doi:10.1029/2001JD000505.

Kokhanovsky, A. A., J. L. Deuzé, D. J. Diner, O. Dubovik, F. Ducos, C. Emde, M. J. Garay, R. G. Grainger, A. Heckel, M. Herman, I. L. Katsev, J. Keller, R. Levy, P. R. J. North, A. S. Prikhach, V. V. Rozanov, A. M. Sayer, Y. Ota, D. Tanré, G. E. Thomas, and E. P. Zege (2010), The inter-comparison of major satellite aerosol retrieval algorithms using simulated intensity and polarization characteristics of reflected light, *Atmos. Meas. Tech.*, *3*, 909–932.

Koren, I., L. A. Remer, Y. J. Kaufman, Y. Rudich, and J. V. Martins (2007), On the twilight zone between clouds and aerosols, *Geophys. Res. Lett.*, *34*(8), L08805, doi:10.1029/2007GL029253.

Kothe, S., E. Good, A. Obregón, B. Ahrens, and H. Nitsche (2013), Satellite-Based Sunshine Duration for Europe, *Remote Sens.*, *5*(6), 2943–2972, doi:10.3390/rs5062943.

Kudo, R., A. Uchiyama, A. Yamazaki, T. Sakami, and E. Kobayashi (2010a), From solar radiation measurements to optical properties: 1998-2008 trends in Japan, *Geophys. Res. Lett.*, *37*(4), doi:10.1029/2009GL041794.

Kudo, R., A. Uchiyama, A. Yamazaki, and E. Kobayashi (2010b), Seasonal characteristics of aerosol radiative effect estimated from ground-based solar radiation measurements in Tsukuba, Japan, *J. Geophys. Res.*, *115*(D1), D01204, doi:10.1029/2009JD012487.

Lally, M. J. (2008), Solar beam intensity inferred from Campbell-Stokes Sunshine Records, University of Reading, UK.

Lee, K. H., Z. Li, Y. J. Kim, and A. Kokhanovsky (2009), Atmospheric aerosol monitoring from satellite observations: a history of three decades, edited by Y. J. Kim, U. Platt, M. B. Gu, and H. Iwahashi, *Atmos. Biol. Environ. Monit.*, doi:10.1007/978-1-4020-9674-7.

Lee, K. H., Z. Li, M. C. Cribb, J. Liu, L. Wang, Y. Zheng, X. Xia, H. Chen, and B. Li (2010), Aerosol optical depth measurements in eastern China and a new calibration method, *J. Geophys. Res.*, *115*, D00K11, doi:10.1029/2009JD012812.

Levy, R. C., S. Mattoo, L. A. Munchak, L. A. Remer, A. M. Sayer, F. Patadia, and N. C. Hsu (2013), The Collection 6 MODIS aerosol products over land and ocean, *Atmos. Meas. Tech.*, *6*(11), 2989–3034, doi:10.5194/amt-6-2989-2013.

Li, H., Y. Lian, X. Wang, W. Ma, and L. Zhao (2011), Global solar radiation estimation with sunshine duration in Tibet, China, *Energy*, *36*(11), 3141–3145, doi:10.1016/j.renene.2011.03.019.

Li, J., R. Liu, S. C. Liu, C.-J. Shiu, J. Wang, and Y. Zhang (2015), Trends in Aerosol Optical Depth in Northern China Retrieved from Sunshine Duration Data, *Geophys. Res. Lett.*, (JANUARY), doi:10.1002/2015GL067111.

Li, R., L. Zhao, T. Wu, Y. Ding, Y. Xin, D. Zou, Y. Xiao, Y. Jiao, Y. Qin, and L. Sun (2012), Temporal and spatial variations of global solar radiation over the Qinghai–Tibetan Plateau during the past 40 years, *Theor. Appl. Climatol.*, *113*(3-4), 573–583, doi:10.1007/s00704-012-0809-5.

Li, Z., X. Zhao, M. Mishchenko, L. Remer, K.-H. Lee, M. Wang, I. Laszlo, T. Nakajima, and H. Maring (2009), Uncertainties in satellite remote sensing of aerosols and impact on monitoring its long-term trend: A review and perspective, *Ann. Geophys.*, *27*, 2755–2770.

Liang, F., and X. A. Xia (2005), Long-term trends in solar radiation and the associated climatic factors over China for 1961-2000, *Ann. Geophys.*, *23*(7), 2425–2432, doi:10.5194/angeo-23-2425-2005.

Liepert, B. G. (1997), Recent changes in solar radiation under cloudy conditions in Germany, *Int. J.*

Climatol., *17*(14), 1581–1593, doi:10.1002/(SICI)1097-0088(19971130)17:14<1581::AID-JOC214>3.0.CO;2-H.

Liepert, B. G., and G. J. Kukla (1997), Decline in global solar radiation with increased horizontal visibility in Germany between 1964 and 1990, *J. Clim.*, *10*(9), 2391–2401.

Liley, J. B., and B. W. Forgan (2009), Aerosol optical depth over Lauder, New Zealand, *Geophys. Res. Lett.*, *36*(7), doi:10.1029/2008GL037141.

Lindfors, A. V., N. Kouremeti, A. Arola, S. Kazadzis, a. F. Bais, and A. Laaksonen (2013), Effective aerosol optical depth from pyranometer measurements of surface solar radiation (global radiation) at Thessaloniki, Greece, *Atmos. Chem. Phys.*, *13*(7), 3733–3741, doi:10.5194/acp-13-3733-2013.

Linke, F. (1922), Transmissions-Koeffizient und Trübungsfaktor, *Beitr. Phys. fr. Atmos.*, *10*, 91–103.

Liu, S. C., C.-H. Wang, C.-J. Shiu, H.-W. Chang, C.-K. Hsiao, and S.-H. Liaw (2002), Reduction in Sunshine Duration over Taiwan: Causes and Implications, *Terr. Atmos. Ocean. Sci.*, *13*(4), 523–545.

Long, C. N., and T. P. Ackerman (2000), Identification of clear skies from broadband pyranometer measurements and calculation of downwelling shortwave cloud effects, *J. Geophys. Res.*, *105*(D12), 15609, doi:10.1029/2000JD900077.

Louche, A., G. Notton, P. Poggi, and G. Simonnot (1991), Correlations for direct normal and global horizontal irradiation on a French Mediterranean site, *Sol. Energy*, *46*(4), 261–266, doi:10.1016/0038-092X(91)90072-5.

Lyapustin, A., Y. Wang, X. Xiong, G. Meister, S. Platnick, R. Levy, B. Franz, S. Korkin, T. Hilker, J. Tucker, F. Hall, P. Sellers, A. Wu, and A. Angal (2014), Science impact of MODIS C5 calibration degradation and C6+ improvements, *Atmos. Meas. Tech. Discuss.*, *7*(7), 7281–7319, doi:10.5194/amtd-7-7281-2014.

Maduekwe, A. A. L., and M. A. C. Chendo (1995), Predicting the components of the total hemispherical solar radiation from sunshine duration measurements in Lagos, Nigeria, *Renew. Energy*, *6*(7), 807–812.

Magee, N. B., E. Melaas, P. M. Finocchio, M. Jardel, A. Noonan, and M. J. Iacono (2014), Blue Hill Observatory Sunshine - Assesment of climate signals in the longest continuous meteorological record in North America, *Bull. Am. Meteorol. Soc.*, *in press*, doi:10.1175/BAMS-D-12-00206.1.

Manara, V., M. C. Beltrano, M. Brunetti, M. Maugeri, A. Sanchez-Lorenzo, C. Simolo, and S. Sorrenti (2015), Sunshine duration variability and trends in Italy from homogenized instrumental time series (1963-2013), *J. Geophys. Res. Atmos.*, *120*(9), 3622–3641.

Maring, D. T. (1897), An improved sunshine recorder, *Mon. Weather Rev.*, *25*, 485–490.

Marshak, A., G. Wen, J. A. Coakley, L. A. Remer, N. G. Loeb, and R. F. Cahalan (2008), A simple model for the cloud adjacency effect and the apparent bluing of aerosols near clouds, *J. Geophys. Res.*, *113*(D14), D14S17, doi:10.1029/2007JD009196.

Martínez-Lozano, J. A., F. Tena, J. E. Onrubia, and J. De La Rubia (1984), The historical evolution of the Ångström formula and its modifications: Review and bibliography, *Agric. For. Meteorol.*, *33*(2-3), 109–128.

Masmoudi, M., M. Chaabane, D. Tanré, P. Gouloup, L. Blarel, and F. Elleuch (2003), Spatial and temporal variability of aerosol: size distribution and optical properties, *Atmos. Res.*, *66*(1-2), 1–19, doi:10.1016/S0169-8095(02)00174-6.

Massen, F. (2011), *Sunshine duration from pyranometer readings*, Luxemburg.

Mateos, D., A. Sanchez-Lorenzo, M. Antón, V. E. Cachorro, J. Calbó, M. J. Costa, B. Torres, and M. Wild (2014), Quantifying the respective roles of aerosols and clouds in the strong brightening since the early 2000s over the Iberian Peninsula, *J. Geophys. Res. Atmos.*, *119*(17), 10,382–10,393, doi:10.1002/2014JD022076.

Matuszko, D. (2014a), A comparison of sunshine duration records from the Campbell-Stokes sunshine recorder and CSD3 sunshine duration sensor, *Theor. Appl. Climatol.*, *34*(1), 228–234, doi:10.1007/s00704-014-1125-z.

Matuszko, D. (2014b), Long-term variability in solar radiation in Krakow based on measurements of sunshine duration, *Int. J. Climatol.*, *34*(1), 228–234, doi:10.1002/joc.3681.

Maurer, J., and C. Dorno (1914), On the progress and geographical distribution of the atmospheric optical disturbance of 1912-13, *Mon. Weather Rev.*, *42*, 214–216.

Mazzola, M., C. Lanconelli, A. Lupi, M. Busetto, V. Vitale, and C. Tomasi (2010), Columnar aerosol optical properties in the Po Valley, Italy, from MFRSR data, *J. Geophys. Res.*, *115*(D17), D17206, doi:10.1029/2009JD013310.

McConnell, J. R., R. Edwards, G. L. Kok, M. G. Flanner, C. S. Zender, E. S. Saltzman, J. R. Banta, D. R. Pasteris, M. M. Carter, and J. D. W. Kahl (2007), 20th century industrial black carbon emissions altered artic climate forcing, *Science (80-.).*, *317*, 1381–1384.

McCormick, R. A., and J. H. Ludwig (1967), Climate modification by atmospheric aerosols, *Science (80-.).*, *156*, 1358–1359.

McFarlane, S. A., E. I. Kassianov, J. Barnard, C. Flynn, and T. P. Ackerman (2009), Surface shortwave aerosol radiative forcing during the Atmospheric Radiation Measurement Mobile Facility deployment in Niamey, Niger, *J. Geophys. Res.*, *114*(May 2008), D00E06, doi:10.1029/2008JD010491.

McPeters, R., M. Kroon, G. Labow, E. Brinksma, D. Balis, I. Petropavlovskikh, J. P. Veefkind, P. K. Bhartia, and P. F. Levelt (2008), Validation of the Aura Ozone Monitoring Instrument total column ozone product, *J. Geophys. Res.*, *113*(D15), D15S14, doi:10.1029/2007JD008802.

de Meij, A., and J. Lelieveld (2011), Evaluating aerosol optical properties observed by ground-based and satellite remote sensing over the Mediterranean and the Middle East in 2006, *Atmos. Res.*, *99*(3,Äì4), 415–433, doi:http://dx.doi.org/10.1016/j.atmosres.2010.11.005.

Michalsky, J., and B. LeBaron (2013), Fifteen-year aerosol optical depth climatology for Salt Lake City, *J. Geophys. Res. Atmos.*, *118*(8), 3271–3277, doi:10.1002/jgrd.50329.

Michalsky, J., F. Denn, C. Flynn, G. Hodges, P. Kiedron, A. Koontz, J. Schlemmer, and S. E. Schwartz (2010), Climatology of aerosol optical depth in north-central Oklahoma: 1992–2008, *J. Geophys. Res.*, *115*(D07203), doi:10.1029/2009JD012197.

Michalsky, J. J. (1992), Comparison of a National Weather Service Foster Sunshine Recorder and the World Meteorological Organization Standard for sunshine duration, *Sol. Energy*, *48*(2), 133–141.

Michalsky, J. J., J. C. Liljegren, and L. C. Harrison (1995), A comparison of Sun photometer derivations of total column water vapor and ozone to standard measures of same at the Southern Great Plains Atmospheric Radiation Measurement site, *J. Geophys. Res.*, *100*(D12), 25995–26003, doi:10.1029/95JD02706.

Michalsky, J. J., J. A. Schlemmer, W. E. Berkheiser, J. L. Berndt, L. C. Harrison, N. S. Laulainen, N. R. Larson, and J. C. Barnard (2001), Multiyear measurements of aerosol optical depth in the Atmospheric Radiation Measurement and Quantitative Links programs, *J. Geophys. Res.*, *106*(D11), 12099–12107.

Michalsky, J. J., G. P. Anderson, J. Barnard, J. Delamere, C. Gueymard, S. Kato, P. Kiedron, A. McComiskey, and P. Ricchiazzi (2006), Shortwave radiative closure studies for clear skies during the Atmospheric Radiation Measurement 2003 Aerosol Intensive Observation Period, *J. Geophys. Res.*, *111*(D14), D14S90, doi:10.1029/2005JD006341.

Middleton, W. E. K. (1969), *Invention of the meteorological instruments*, John Hopki., The Johns Hopkins University Press, Baltimore.

Mishchenko, M. I., I. V Geogdzhayev, B. Cairns, W. B. Rossow, and A. A. Lacis (1999), Aerosol retrievals over the ocean by use of channels 1 and 2 AVHRR data: sensitivity analysis and preliminary results., *Appl. Opt.*, *38*(36), 7325–7341, doi:10.1364/AO.38.007325.

Monteith, J. L. (1977), Climate and the efficiency of crop production in Britain, *Philos. Trans. R. Soc. London*, *281*, 277–294.

Moosmüller, H., R. K. Chakrabarty, and W. P. Arnott (2009), Aerosol light absorption and its measurement: A review, *J. Quant. Spectrosc. Radiat. Transf.*, *110*(11), 844–878, doi:10.1016/j.jqsrt.2009.02.035.

Morawska-Horawska, M. (1985), Cloudiness and sunshine in Cracow, 1861-1980, and its contemporary tendencies, *J. Climatol.*, *5*(6), 633–642, doi:10.1002/joc.3370050605.

More, S. (2013), Comparison of Aerosol Products Retrieved from AERONET, MICROTOPS and MODIS over a Tropical Urban City, Pune, India, *Aerosol Air Qual. Res.*, 107–121, doi:10.4209/aaqr.2012.04.0102.

Nabat, P., S. Somot, M. Mallet, A. Sanchez-Lorenzo, and M. Wild (2014), Contribution of anthropogenic sulfate aerosols to the changing Euro-Mediterranean climate since 1980, *Geophys. Res. Lett.*, *41*(15), 5605–5611, doi:10.1002/2014GL060798.

Nfaoui, H., and J. Buret (1993), Estimation of daily and monthly direct, diffuse and global solar radiation in Rabat (Morocco), *Renew. Energy*, *3*(8), 923–930.

Obregón, M. A., S. Pereira, F. Wagner, A. Serrano, M. L. Cancillo, and A. M. Silva (2012), Regional differences of column aerosol parameters in western Iberian Peninsula, *Atmos. Environ.*, *62*, 208–219, doi:10.1016/j.atmosenv.2012.08.016.

Obregón, M. A., A. Serrano, M. L. Cancillo, V. E. Cachorro, and C. Toledano (2014), Aerosol radiometric properties at Western Spain (Cáceres station), *Int. J. Climatol.*, *35*(6), 981–990, doi:10.1002/joc.4031.

Oguz, E., M. D. Kaya, and Y. Nuhoglu (2003), Interaction between air pollution and meteorologicalparameters in Erzurum, Turkey, *Int. J. Environ. Pollut.*, *19*(3), 292, doi:10.1504/IJEP.2003.003312.

Ohvril, H., H. Teral, L. Neiman, M. Kannel, M. Uustare, M. Tee, V. Russak, O. Okulov, A. Jõeveer, A. Kallis, T. Ohvril, E. I. Terez, G. A. Terez, G. K. Gushchin, G. M. Abakumova, E. V. Gorbarenko, A. V. Tsvetkov, and N. Laulainen (2009), Global dimming and brightening versus atmospheric column transparency, Europe, 1906–2007, *J. Geophys. Res.*, *114*(2), D00D12, doi:10.1029/2008JD010644.

Olseth, J. A., and A. Skartveit (2001), Solar irradiance, sunshine duration and daylight illuminance derived from METEOSAT data for some European sites, *Theor. Appl. Climatol.*, *69*(3-4), 239–252, doi:10.1007/s007040170029.

Pace, G., A. di Sarra, D. Meloni, S. Piacentino, and P. Chamard (2006), Aerosol optical properties at

Lampedusa (Central Mediterranean). 1. Influence of transport and identification of different aerosol types, *Atmos. Chem. Phys.*, *6*(3), 697–713, doi:10.5194/acp-6-697-2006.

Painter, H. E. (1981), The performance of a Campbell-Stokes sunshine recorder compared with a simultaneous record of a normal incidence irradiance, *Meteorol. Mag.*, *110*, 102–109.

Pallé, E., and C. J. Butler (2001), Sunshine records from Ireland: cloud factors and possible links to solar activity and cosmic rays, *Int. J. Climatol.*, *21*(6), 709–729, doi:10.1002/joc.657.

Pereira, S. N., F. Wagner, and A. M. Silva (2011), Seven years of measurements of aerosol scattering properties, near the surface, in the southwestern Iberia Peninsula, *Atmos. Chem. Phys.*, *11*(1), 17–29, doi:10.5194/acp-11-17-2011.

Perrone, M. R., M. Santese, A. M. Tafuro, B. Holben, and A. Smirnov (2005), Aerosol load characterization over South–East Italy for one year of AERONET sun-photometer measurements, *Atmos. Res.*, *75*(1-2), 111–133, doi:10.1016/j.atmosres.2004.12.003.

Plantico, M. S., T. R. Karl, G. Kukla, and J. Gavin (1990), Is recent climate change across the United States related to rising levels of anthropogenic greenhouse gases?, *J. Geophys. Res.*, *95*(D10), 16617–16637.

Popp, C., A. Hauser, N. Foppa, and S. Wunderle (2007), Remote sensing of aerosol optical depth over central Europe from MSG-SEVIRI data and accuracy assessment with ground-based AERONET measurements, *J. Geophys. Res.*, *112*(D24), D24S11, doi:10.1029/2007JD008423.

Powell, G. L. (1983), Instrumental effects on the sunshine record, *J. Clim. Appl. Meteorol.*, *22*, 962–963.

Power, H. C. (2001), Estimating clear-sky beam irradiation from sunshine duration, *Sol. Energy*, *71*(4), 217–224.

Power, H. C. (2003a), The geography and climatology of aerosols, *Prog. Phys. Geogr.*, *27*(4), 502–547, doi:10.1191/0309133303pp393ra.

Power, H. C. (2003b), Trends in solar radiation over Germany and an assessment of the role of aerosols and sunshine duration, *Theor. Appl. Climatol.*, *76*(1-2), 47–63, doi:10.1007/s00704-003-0005-8.

Prats, N., V. Cachorro, M. Sorribas, S. Mogo, A. Berjon, C. Toledano, A. Defrutos, J. Delarosa, N. Laulainen, and B. Delamorena (2008), Columnar aerosol optical properties during “El Arenosillo 2004 summer campaign,” *Atmos. Environ.*, *42*(11), 2643–2653, doi:10.1016/j.atmosenv.2007.07.041.

Prescott, J. (1940), Evaporation from a water surface in relation to solar radiation, *Trans. R. Soc. Sci. Aust.*, *64*, 114–125.

Prospero, J. M. (2014), Characterizing the temporal and spatial variability of African dust over the Atlantic, *PAGES Mag.*, *22*(2), 68–69.

Qi, Y., J. Ge, and J. Huang (2013), Spatial and temporal distribution of MODIS and MISR aerosol optical depth over northern China and comparison with AERONET, *Chinese Sci. Bull.*, *58*(20), 2497–2506, doi:10.1007/s11434-013-5678-5.

Qian, Y., D. P. Kaiser, L. R. Leung, and M. Xu (2006), More frequent cloud-free sky and less surface solar radiation in China from 1955 to 2000, *Geophys. Res. Lett.*, *33*(1), L01812, doi:10.1029/2005GL024586.

Qian, Y., W. Wang, L. R. Leung, and D. P. Kaiser (2007), Variability of solar radiation under cloud-free skies in China: The role of aerosols, *Geophys. Res. Lett.*, *34*(12), L12804, doi:10.1029/2006GL028800.

Qiu, J. (1998), A Method to Determine Atmospheric Aerosol Optical Depth Using Total Direct Solar Radiation, *J. Atmos. Sci.*, *55*, 744–757.

Raichijk, C. (2012), Observed trends in sunshine duration over South America, *Int. J. Climatol.*, *32*(5), 669–680, doi:10.1002/joc.2296.

Ramachandran, S., and A. Jayaraman (2003), Balloon-borne study of the upper tropospheric and stratospheric aerosols over a tropical station in India, *Tellus*, *55B*, 820–836.

Ramanathan, V., R. D. Cess, E. F. Harrison, P. Minnis, B. R. Barkstrom, E. Ahmad, and D. Hartmann (1989), Cloud-radiative forcing and climate: Results from the Earth Radiation Budget Experiment, *Science*, *243*(4887), 57–63, doi:10.1126/science.243.4887.57.

Ramanathan, V., P. J. Crutzen, J. T. Kiehl, and D. Rosenfeld (2001), Aerosols, climate, and the hydrological cycle, *Science*, *294*(5549), 2119–2124, doi:10.1126/science.1064034.

Randall, C. E., R. M. Bevilacqua, J. D. Lumpe, and K. W. Hoppel (2001), Validation of POAM III aerosols: Comparison to SAGE II and HALOE, *J. Geophys. Res.*, *106*(D21), 27525, doi:10.1029/2001JD000528.

Rebetez, M., and M. Beniston (1998), Changes in sunshine duration are correlated with changes in daily temperature range this century: An analysis of Swiss climatological data, *Geophys. Res. Lett.*, *25*(19), 3611–3613.

Remer, L. A., Y. J. Kaufman, D. Tanré, S. Mattoo, D. A. Chu, J. V. Martins, R. R. Li, C. Ichoku, R. C. Levy, R. G. Kleidman, T. F. Eck, E. Vermote, and B. N. Holben (2005), The MODIS Aerosol Algorithm, Products, and Validation, *J. Atmos. Sci.*, *62*, 947–973.

Remer, L. A., D. Tanré, Y. J. Kaufman, R. Levy, and S. Mattoo (2006), *Algorithm for Remote Sensing of Tropospheric Aerosol from MODIS: Collection 005, Product ID MOD04/MYD04*.

Ricchiazzi, P., S. Yang, C. Gautier, and D. Sowle (1998), SBDART: A Research and Teaching Software Tool for Plane-Parallel Radiative Transfer in the Earth's Atmosphere, *Bull. Am. Meteorol. Soc.*, *79*(10), 2101–2114, doi:10.1175/1520-0477(1998)079<2101:SARATS>2.0.CO;2.

Ricchiazzi, P., C. Gautier, J. A. Ogren, and B. Schmid (2006), A comparison of aerosol optical properties obtained from in situ measurements and retrieved from Sun and sky radiance observations during the May 2003 ARM Aerosol Intensive Observation Period, *J. Geophys. Res.*, *111*(D5), D05S06, doi:10.1029/2005JD005863.

Roberts, C. J. (2012), Recovering Direct Solar Downwelling Flux Time Series from the Campbell-Stokes Sunshine Card Archive, University of Birmingham.

Roldán, A., R. Righini, and H. Grossi Gallegos (2005), Preliminary analysis of tghe Behaviour of the cards used in the Argentine sunshine recorders, *Av. en Energías Renov. y Medio Ambient.*, *9*(2), 9–13.

Román, R., J. Bilbao, and A. de Miguel (2014), Reconstruction of six decades of daily total solar shortwave irradiation in the Iberian Peninsula using sunshine duration records, *Atmos. Environ.*, *99*, 41–50, doi:10.1016/j.atmosenv.2014.09.052.

do Rosário, N., M. A. Yamasoe, A. Sayão, and R. Siqueira (2008), Multifilter rotating shadowband radiometer calibration for spectral aerosol optical depth retrievals over São Paulo City, Brazil., *Appl. Opt.*, *47*(9), 1171–6.

Rosenfeld, D., U. Lohmann, G. B. Raga, C. D. O'Dowd, M. Kulmala, S. Fuzzi, A. Reissell, and M. O. Andreae (2008), Flood or drought: how do aerosols affect precipitation?, *Science*, *321*(5894), 1309–1313, doi:10.1126/science.1160606.

Rosenfeld, D., M. O. Andreae, A. Asmi, M. Chin, G. Leeuw, D. P. Donovan, R. Kahn, S. Kinne, N. Kivekäs,

M. Kulmala, W. Lau, K. S. Schmidt, T. Suni, T. Wagner, M. Wild, and J. Quaas (2014), Global observations of aerosol-cloud-precipitation-climate interactions, *Rev. Geophys.*, *52*(4), 750–808, doi:10.1002/2013RG000441.

Ruckstuhl, C., R. Philipona, K. Behrens, M. Collaud Coen, B. Dürr, A. Heimo, C. Mätzler, S. Nyeki, A. Ohmura, L. Vuilleumier, M. Weller, C. Wehrli, and A. Zelenka (2008), Aerosol and cloud effects on solar brightening and the recent rapid warming, *Geophys. Res. Lett.*, *35*(12), L12708, doi:10.1029/2008GL034228.

Ruiz-Arias, J. A., J. Dudhia, C. A. Gueymard, and D. Pozo-Vázquez (2013), Assessment of the Level-3 MODIS daily aerosol optical depth in the context of surface solar radiation and numerical weather modeling, *Atmos. Chem. Phys.*, *13*(2), 675–692, doi:10.5194/acp-13-675-2013.

Sakazaki, T., M. Fujiwara, C. Mitsuda, K. Imai, N. Manago, Y. Naito, T. Nakamura, H. Akiyoshi, D. Kinnison, T. Sano, M. Suzuki, and M. Shiotani (2013), Diurnal ozone variations in the stratosphere revealed in observations from the Superconducting Submillimeter-Wave Limb-Emission Sounder (SMILES) on board the International Space Station (ISS), *J. Geophys. Res. Atmos.*, *118*(7), 2991–3006, doi:10.1002/jgrd.50220.

Salomonson, V. V, W. L. Barnes, P. W. Maymon, H. E. Montgomery, and H. Ostrow (1989), MODIS: advanced facility instrument for studies of the Earth as a system, *IEEE Trans. Geosci. Remote Sens.*, *27*(2), 145–153.

Sanchez-Lorenzo, A., and M. Wild (2012), Decadal variations in estimated surface solar radiation over Switzerland since the late 19th century, *Atmos. Chem. Phys.*, *12*(18), 8635–8644, doi:10.5194/acp-12-8635-2012.

Sanchez-Lorenzo, A., M. Brunetti, J. Calbó, and J. Martin-Vide (2007), Recent spatial and temporal variability and trends of sunshine duration over the Iberian Peninsula from a homogenized data set, *J. Geophys. Res.*, *112*(D20), D20115, doi:10.1029/2007JD008677.

Sanchez-Lorenzo, A., J. Calbó, and J. Martin-Vide (2008), Spatial and temporal trends in sunshine duration over Western Europe (1938–2004), *J. Clim.*, *21*(22), 6089–6098, doi:10.1175/2008JCLI2442.1.

Sanchez-Lorenzo, A., J. Calbó, M. Brunetti, and C. Deser (2009), Dimming/brightening over the Iberian Peninsula: Trends in sunshine duration and cloud cover and their relations with atmospheric circulation, *J. Geophys. Res.*, *114*, D00D09, doi:10.1029/2008JD011394.

Sanchez-Lorenzo, A., J. Calbó, and M. Wild (2012), Increasing cloud cover in the 20th century: review and new findings in Spain, *Clim. Past*, *8*(4), 1199–1212, doi:10.5194/cp-8-1199-2012.

Sanchez-Lorenzo, A., J. Calbó, and M. Wild (2013a), Global and diffuse solar radiation in Spain: Building a homogeneous dataset and assessing their trends, *Glob. Planet. Change*, *100*, 343–352, doi:10.1016/j.gloplacha.2012.11.010.

Sanchez-Lorenzo, A., J. Calbó, M. Wild, C. Azorin-Molina, and A. Sanchez-Romero (2013b), New insights into the history of the Campbell-Stokes sunshine recorder, *Weather*, *68*(12), 327–331, doi:10.1002/wea.2156.

Sanchez-Lorenzo, A., M. Wild, M. Brunetti, J. A. Guijarro, M. Z. Hakuba, J. Calbó, S. Mystakidis, and B. Bartok (2015), Reassessment and update of long-term trends in downward surface shortwave radiation over Europe (1939-2012), *J. Geophys. Res. Atmos.*, *120*(18), doi:10.1002/2015JD023321.

Sanchez-Romero, A., A. Sanchez-Lorenzo, J. Calbó, J. A. González, and C. Azorin-Molina (2014), The signal of aerosol-induced changes in sunshine duration records: A review of the evidence, *J. Geophys.*

Res. Atmos., *119*(8), 4657–4673, doi:10.1002/2013JD021393.

Sanchez-Romero, A., J. A. González, J. Calbó, and A. Sanchez-Lorenzo (2015), Using digital image processing to characterize the Campbell–Stokes sunshine recorder and to derive high-temporal resolution direct solar irradiance, *Atmos. Meas. Tech.*, *8*(1), 183–194, doi:10.5194/amt-8-183-2015.

Sanchez-Romero, A., J. A. González, J. Calbó, A. Sanchez-Lorenzo, and J. Michalsky (2016a), Aerosol optical depth in a western Mediterranean site: An assessment of different methods, *Atmos. Res.*, *174-175*, 70–84, doi:10.1016/j.atmosres.2016.02.002.

Sanchez-Romero, A., A. Sanchez-Lorenzo, J. A. González, and J. Calbó (2016b), Reconstruction of long-term aerosol optical depth series with sunshine duration records, *Geophys. Res. Lett.*, *43*, 1296–1305, doi:10.1002/2015GL67543.

Sanroma, E., E. Palle, and A. Sanchez-Lorenzo (2010), Long-term changes in insolation and temperatures at different altitudes, *Environ. Res. Lett.*, *5*(2), 024006, doi:10.1088/1748-9326/5/2/024006.

Scott, R. H. (1885), On the measurement of sunshine, *Quaterly J. R. Meteorol. Soc.*, *11*(55), 205–216.

Sears, R. D., R. G. Flocchini, and J. L. Hatfield (1981), Correlations of total, diffuse and direct solar radiation with the percentage of possible sunshine for Davis, California, *Sol. Energy*, *27*(4), 357–360, doi:10.1016/0038-092X(81)90070-0.

Segura, S., V. Estellés, A. R. Esteve, F. Tena, M. P. Utrillas, and J. A. Martínez-Lozano (2015), Assessment and application of MODIS ocean and land algorithms for the characterization of aerosol properties over a Mediterranean coastal site, *Atmos. Res.*, *157*, 66–73, doi:10.1016/j.atmosres.2015.01.019.

Sellers, W. D. (1965), *Physical Climatology*, University of Chicago Press, Chicago.

Shaw, G. E., J. a. Reagan, and B. M. Herman (1973), Investigations of atmospheric extinction using direct solar radiation measurements made with a multiple wavelength radiometer, *J. Appl. Meteorol.*, *12*, 374–380, doi:10.1175/1520-0450(1973)012<0374:IOAEUD>2.0.CO;2.

Shettle, E. P., and S. Anderson (1995), New visibile and near IR ozone absorption cross-sections for MODTRAN, in *Proceedings of the 17th Annual Review Conference on Atmospheric Transmission Models*, vol. 2060, edited by G. P. Anderson, R. H. Picard, and J. H. Chetwynd, pp. 335–345, PL-TR-92-2060, Phillips Lab., Hanscom Air Force Base, Mass.

Shettle, E. P., and R. W. Fenn (1979), *Models for the aerosols of the lower atmosphere and the effects of humidity variations on their optical properties*, Massachusetts.

Shi, G.-Y., T. Hayasaka, A. Ohmura, Z.-H. Chen, B. Wang, J.-Q. Zhao, H.-Z. Che, and L. Xu (2008), Data quality assessment and the long-term trend of ground solar radiation in China, *J. Appl. Meteorol. Climatol.*, *47*(4), 1006–1016, doi:10.1175/2007JAMC1493.1.

Sicard, M., F. Rocadenbosch, M. N. M. Reba, A. Comerón, S. Tomás, D. García-Vízcaino, O. Batet, R. Barrios, D. Kumar, and J. M. Baldasano (2011), Seasonal variability of aerosol optical properties observed by means of a Raman lidar at an EARLINET site over Northeastern Spain, *Atmos. Chem. Phys.*, *11*(1), 175–190, doi:10.5194/acp-11-175-2011.

Smith, S. J., J. Van Aardenne, Z. Klimont, R. J. Andres, a. Volke, and S. Delgado Arias (2011), Anthropogenic sulfur dioxide emissions: 1850-2005, *Atmos. Chem. Phys.*, *11*(3), 1101–1116, doi:10.5194/acp-11-1101-2011.

Solomon, S., D. Qin, M. Manning, Z. Chen, M. Marquis, K. Averyt, M. Tignor, and H. Miller (2007), *Climate Change 2007: The Physical Science Basis. Contribution of Working Group I to the Fourth Assessment Report of the Intergovernmental Panel on Climate Change*, Cambridge, Univ. Press, Cambridge, U.K. and New York.

Soni, V. K., G. Pandithurai, and D. S. Pai (2012), Evaluation of long-term changes of solar radiation in India, *Int. J. Climatol.*, *32*(4), 540–551, doi:10.1002/joc.2294.

Stanhill, G. (1998a), Estimation of direct solar beam irradiance from measurements of the duration of bright sunshine, *Int. J. Climatol.*, *18*(3), 347–354, doi:10.1002/(SICI)1097-0088(19980315)18:3<347::AID-JOC239>3.0.CO;2-O.

Stanhill, G. (1998b), Long-term trends in, and spatial variation of, solar irradiances in Ireland, *Int. J. Climatol.*, *18*(9), 1015–1030, doi:10.1002/(SICI)1097-0088(199807)18:9<1015::AID-JOC297>3.0.CO;2-2.

Stanhill, G. (2003), Through a glass brightly: Some new light on the Campbell-Stokes sunshine recorder, *Weather*, *58*(1), 3–11.

Stanhill, G. (2005), Global dimming: A new aspect of climate change, *Weather*, *60*(1), 11–14.

Stanhill, G., and S. Cohen (2001), Global dimming: a review of the evidence for a widespread and significant reduction in global radiation with discussion of its probable causes and possible agricultural consequences, *Agric. For. Meteorol.*, *107*(4), 255–278, doi:10.1016/S0168-1923(00)00241-0.

Stanhill, G., and S. Cohen (2005), Solar radiation changes in the United States during the Twentieth Century: Evidence from sunshine duration measurements, *J. Clim.*, *18*(10), 1503–1512.

Stanhill, G., and S. Cohen (2008), Solar radiation changes in Japan during the 20th Century: Evidence from sunshine duration measurements, *J. Meteorol. Soc. Japan*, *86*(1), 57–67.

Stanhill, G., and J. D. Kalma (1995), Solar dimming and urban heating at Hong Kong, *Int. J. Climatol.*, *15*(8), 933–941, doi:10.1002/joc.3370150807.

Stern, D. I. (2006), Reversal of the trend in global anthropogenic sulfur emissions, *Glob. Environ. Chang.*, *16*(2), 207–220, doi:10.1016/j.gloenvcha.2006.01.001.

Steurer, P. M., and T. R. Karl (1991), *Historical sunshine and cloud data in the United States*, Oak Ridge National Laboratory, Pennsylvania State University, United States.

Stocker, T. F., D. Qin, G. K. Plattner, M. Tignor, S. K. Allen, J. Boschung, A. Nauels, Y. Xia, V. Bex, and P. M. Midley (2013), *IPCC, 2013: Climate Change 2013: The physical sciences basis. Contribution of working group I to the Fifth Assessment Report of the Intergovernmental Panel on Climate Change*, Cambridge University Press, Cambridge, United Kingdom and New York, NY, USA.

van der Stok, J. P. (1913), *On the relation between the cloudiness of the sky and the duration of sunshine*, Amsterdam.

Streets, D. G., F. Yan, M. Chin, T. Diehl, N. Mahowald, M. Schultz, M. Wild, Y. Wu, and C. Yu (2009), Anthropogenic and natural contributions to regional trends in aerosol optical depth, 1980-2006, *J. Geophys. Res. Atmos.*, *114*(14), 1–16, doi:10.1029/2008JD011624.

Suehrcke, H. (2000), On the relationship between duration of sunshine and solar radiation on the Earth’s surface: Ångström’s equation revisited, *Sol. Energy*, *68*(5), 417–425.

Taha, G., and G. P. Box (1999), New method for inferring total ozone and aerosol optical thickness from multispectral extinction measurements using eigenvalue analysis, *Geophys. Res. Lett.*, *26*(20), 3085–3088, doi:10.1029/1999GL010823.

Tang, I. N. (1996), Chemical and size effects of hygroscopic aerosols on light scattering coefficients, *J.*

Geophys. Res., *101*(D14), 19245, doi:10.1029/96JD03003.

Toledano, C., V. E. Cachorro, A. Berjon, A. M. de Frutos, M. Sorribas, B. A. de la Morena, and P. Goloub (2007), Aerosol optical depth and Angström exponent climatology at El Arenosillo AERONET site (Huelva, Spain), *Quaterly J. R. Meteorol. Soc.*, *133*, 795–807, doi:10.1002/qj.

Torres, O., P. K. Bhartia, J. R. Herman, A. Sinyuk, P. Ginoux, B. Holben, A. Sinyu, P. Ginoux, and B. Holben (2002), A long-term record of aerosol optical depth from TOMS observations and comparison to AERONET measurements, *J. Atmos. Sci.*, *59*(3), 398–413, doi:10.1175/1520-0469(2002)059<0398:ALTROA>2.0.CO;2.

Torres, O., A. Tanskanen, B. Veihelmann, C. Ahn, R. Braak, P. K. Bhartia, P. Veefkind, and P. Levelt (2007), Aerosols and surface UV products from Ozone Monitoring Instrument observations: An overview, *J. Geophys. Res.*, *112*(D24), D24S47, doi:10.1029/2007JD008809.

Turnock, S. T., D. V. Spracklen, K. S. Carslaw, G. W. Mann, M. T. Woodhouse, P. M. Forster, J. Haywood, C. E. Johnson, M. Dalvi, N. Bellouin, and a. Sanchez-Lorenzo (2015), Modelled and observed changes in aerosols and surface solar radiation over Europe between 1960 and 2009, *Atmos. Chem. Phys.*, *15*(16), 9477–9500, doi:10.5194/acp-15-9477-2015.

Twomey, S. (1977), The influence of pollution on the shortwave albedo of clouds, *J. Atmos. Sci.*, *34*, 1149–1152.

Unsworth, M. H., and J. L. Monteith (1972), Aerosol and solar radiation in Britain, *Q. J. R. Meteorol. Soc.*, *98*, 778–797.

Valenzuela, A., F. J. Olmo, H. Lyamani, A. Quirantes, and L. Alados-Arboledas (2011), Aerosol radiative properties retrieved during Saharan dust events in Southeastern Spain from 2005 to 2008, *Óptica pura y Apl.*, *1516*(2008), 661–664.

Valenzuela, A., F. J. Olmo, H. Lyamani, M. Antón, G. Titos, A. Cazorla, and L. Alados-Arboledas (2015), Aerosol scattering and absorption Angström exponents as indicators of dust and dust-free days over Granada (Spain), *Atmos. Res.*, *154*, 1–13, doi:10.1016/j.atmosres.2014.10.015.

Veefkind, J. P., G. de Leeuw, P. A. Durkee, P. B. Russell, P. V. Hobbs, and J. M. Livingston (1999), Aerosol optical depth retrieval using ATSR-2 and AVHRR data during TARFOX, *J. Geophys. Res.*, *104*(D2), 2253, doi:10.1029/98JD02816.

Vignola, F., J. Michalsky, and T. Stoffel (2012), *Solar and Infrared Radiation Measurements*, CRC Press.

Vladutescu, D. V., B. L. Madhavan, B. M. Gross, A. Aguirre, F. Moshary, S. A. Ahmed, L. Member, M. Razani, and R. A. Blake (2013), Assessment of Langley and NASA-GISS calibration techniques for MFRSR aerosol retrieval, *IEEE Trans. Geosci. Remote Sens.*, *84*, 1–16.

Voltz, F. E. (1974), Economical multispectral sun photometer for measurements of aerosol extinction from 0.44 µm to 1.6 µm and precipitable water, *Appl. Opt.*, *13*, 1732–1733.

Vuerich, E., J. P. Morel, S. Mevel, and J. Oliviéri (2012), Updating and development of methods for worldwide accurate measurements of sunshine duration, in *TECO - 2012*, vol. 1984, Brussels.

Wang, K., R. E. Dickinson, and S. Liang (2009a), Clear sky visibility has decreased over land globally from 1973 to 2007., *Science*, *323*(5920), 1468–1470, doi:10.1126/science.1167549.

Wang, K. C., R. E. Dickinson, M. Wild, and S. Liang (2012a), Atmospheric impacts on climatic variability of surface incident solar radiation, *Atmos. Chem. Phys.*, *12*(20), 9581–9592, doi:10.5194/acp-12-9581-2012.

Wang, L., J. Xin, Y. Wang, Z. Li, G. Liu, and J. Li (2007), Evaluation of the MODIS aerosol optical depth retrieval over different ecosystems in China during EAST-AIRE, *Atmos. Environ.*, *41*(33), 7138–7149, doi:10.1016/j.atmosenv.2007.05.001.

Wang, P., W. H. Knap, P. Kuipers Munneke, and P. Stammes (2009b), Clear-sky shortwave radiative closure for the Cabauw Baseline Surface Radiation Network site, Netherlands, *J. Geophys. Res.*, *114*(D14), D14206, doi:10.1029/2009JD011978.

Wang, Y., Y. Yang, N. Zhao, C. Liu, and Q. Wang (2012b), The magnitude of the effect of air pollution on sunshine hours in China, *J. Geophys. Res. Atmos.*, *117*(D00V14), doi:10.1029/2011JD016753.

Wang, Y., Y. Yang, S. Han, Q. Wang, and J. Zhang (2013), Sunshine dimming and brightening in Chinese cities (1955-2011) was driven by air pollution rather than clouds, *Clim. Res.*, *56*(1), 11–20, doi:10.3354/cr01139.

Weber, G. R. (1990), Spatial and temporal variation of sunshine in the Federal Republic of Germany, *Theor. Appl. Climatol.*, *41*, 1–9.

Wheeler, D., and J. Mayes (1997), *Regional Climate of the British Isles*, Routledge, Londond and New York.

Whipple, G. M. (1878), On the relative duration of sunshine at the Royal Observatory, Greenwich, and at the Kew Observatory, during the year 1877, *Quaterly J. R. Meteorol. Soc.*, *4*(28), 201–207.

Wild, M. (2009), Global dimming and brightening: A review, *J. Geophys. Res.*, *114*, D00D16, doi:10.1029/2008JD011470.

Wild, M. (2012), Enlightening Global Dimming and Brightening, *Bull. Am. Meteorol. Soc.*, *93*(1), 27–37, doi:10.1175/BAMS-D-11-00074.1.

Wild, M., H. Gilgen, A. Roesch, A. Ohmura, C. N. Long, E. G. Dutton, B. Forgan, A. Kallis, V. Russak, and A. Tsvetkov (2005), From dimming to brightening: decadal changes in solar radiation at Earth's surface., *Science*, *308*(5723), 847–50, doi:10.1126/science.1103215.

Wild, M., D. Folini, C. Schär, N. Loeb, E. G. Dutton, and G. König-Langlo (2013), The global energy balance from a surface perspective, *Clim. Dyn.*, *40*(11-12), 3107–3134, doi:10.1007/s00382-012-1569-8.

WMO (1962), *Abridged Final Report of the Third Season of the Commission for Instruments and Methods of Observations, WMO-No. 116*, Geneva, Switzerland.

WMO (2008), *Guide to Meteorological Instruments and Methods of Observation, 7th Edition*, Geneva, Switzerland.

Wood, J., T. Muneer, and J. Kubie (2003), Evaluation of a new photodiode sensor for measuring global and diffuse irradiance, and sunshine duration, *J. Sol. Energy Eng.*, *125*(1), 43, doi:10.1115/1.1531149.

Wood, R. C., and R. G. Harrison (2011), Scorch marks from the sky, *Weather*, *66*(2), 39–41, doi:10.1002/wea.664.

Wright, H. L. (1935), *Some notes on readings at Kew Observatory of the Gorczynski pyrheliometer the sunshine recorder and the black bulb thermometer*, Vol. V, London.

Wu, Z., R. E. Newell, and J. Hsiung (1990), Possible factors controlling global marine temperature variations over the past century, *J. Geophys. Res.*, *95*(D8), 11799–11810.

Xia, X. (2010), Spatiotemporal changes in sunshine duration and cloud amount as well as their relationship in China during 1954–2005, *J. Geophys. Res.*, *115*, D00K06, doi:10.1029/2009JD012879.

Xia, X. (2013), Variability and trend of diurnal temperature range in China and their relationship to total cloud cover and sunshine duration, *Ann. Geophys.*, *31*(5), 795–804, doi:10.5194/angeo-31-795-2013.

Xu, X., X. Shi, S. Zhang, G. Ding, Q. Miao, and L. Zhou (2006), Aerosol influence domain of Beijing and peripheral city agglomeration and its climatic effect, *Chinese Sci. Bull.*, *51*(16), 2016–2026, doi:10.1007/s11434-006-2066-4.

Xu, X., J. Qiu, S. Niu, and L. Tang (2009), Optical depth of the atmospheric aerosol at 12 stations in CHina over the past 45 years, *Chin. Acta. Sci. Circum.*, *29*, 488–495.

Yang, K., B. Ding, J. Qin, W. Tang, N. Lu, and C. Lin (2012), Can aerosol loading explain the solar dimming over the Tibetan Plateau?, *Geophys. Res. Lett.*, *39*, L20710, doi:10.1029/2012GL053733.

Yang, Y., N. Zhao, Y. Hu, and X. Zhou (2009a), Effect of wind speed on sunshine hours in three cities in Northern China, *Clim. Res.*, *39*(2), 149–157, doi:10.3354/cr00820.

Yang, Y. H., N. Zhao, X. H. Hao, and C. Q. Li (2009b), Decreasing trend of sunshine hours and related driving forces in North China, *Theor. Appl. Climatol.*, *97*(1-2), 91–98, doi:10.1007/s00704-008-0049-x.

You, Q., S. Kang, W.-A. Flügel, A. Sanchez-Lorenzo, Y. Yan, J. Huang, and J. Martin-Vide (2010), From brightening to dimming in sunshine duration over the eastern and central Tibetan Plateau (1961–2005), *Theor. Appl. Climatol.*, *101*(3-4), 445–457, doi:10.1007/s00704-009-0231-9.

You, Q., A. Sanchez-Lorenzo, M. Wild, D. Folini, K. Fraedrich, G. Ren, and S. Kang (2013), Decadal variation of surface solar radiation in the Tibetan Plateau from observations, reanalysis and model simulations, *Clim. Dyn.*, *40*(7-8), 2073–2086, doi:10.1007/s00382-012-1383-3.

Zhang, X., X. Xia, and C. Xuan (2015), On the drivers of variability and trend of surface solar radiation in Beijing metropolitan area, *Int. J. Climatol.*, *35*(3), 452–461, doi:10.1002/joc.3994.

Zhang, Y. L., B. Q. Qin, and W. M. Chen (2004), Analysis of 40 year records of solar radiation data in Shanghai, Nanjing and Hangzhou in Eastern China, *Theor. Appl. Climatol.*, *78*(4), 217–227, doi:10.1007/s00704-003-0030-7.

Zheng, X., W. Kang, T. Zhao, Y. Luo, C. Duan, and J. Chen (2008), Long-term trends in sunshine duration over Yunnan-Guizhou Plateau in Southwest China for 1961–2005, *Geophys. Res. Lett.*, *35*(15), L15707, doi:10.1029/2008GL034482.

Zheng, X., T. Zhao, Y. Luo, C. Duan, and J. Chen (2011), Trends in sunshine duration and atmospheric visibility in the Yunnan-Guizhou Plateau, 1961–2005, *Sci. Cold Arid Reg.*, *3*(2), 179–184, doi:10.3724/SP.J.1226.2011.00179.

Zongxing, L., F. Qi, Z. Wei, H. Yuanqing, W. Xufeng, N. Catto, A. Wenlin, D. Jiankuo, C. Aifang, L. Li, and H. Meng (2012), Decreasing trend of sunshine hours and related driving forces in Southwestern China, *Theor. Appl. Climatol.*, *109*(1-2), 305–321, doi:10.1007/s00704-012-0583-4.

UdG